

The Influence of Particle Morphology and Breakage on the Strength of Sandy Soil

A Thesis Submitted for the Degree of Doctor of Philosophy

By

SHUODONG ZHANG

Department of Civil and Environmental Engineering

Brunel University London

October 2024

Declaration

I hereby declare that, except where specific reference is made to the works of others, the contents of this thesis are original and have not been submitted, in whole or in part, to any other university for any degree or qualification. This thesis, except where specific statement is made, solely reflects the outcomes of my independent research endeavours, devoid of any collaborative contributions.

A handwritten signature in black ink that reads "Shuodong Zhang". The signature is written in a cursive style with a clear, legible font.

Shuodong Zhang

October 2024

Acknowledgements

First and foremost, I would like to express my deepest gratitude to my principal supervisor, Dr. Tao Zhao, for affording me the invaluable opportunity to pursue a doctoral degree programme subsequent to the completion of my master's program at Brunel University London. All the academic milestones attained, and the completion of this thesis could not have been achieved without his meticulous guidance and unwavering support. He has served as an exemplary role model, inspiring me to embody diligence and meticulousness in the realm of academic research. This work would not have been completed without his constant support and encouragement.

My sincere gratitude extends to Prof. Houzhen Wei, for providing me with the precious opportunity to carry out all my laboratory experiments at the Institute of Rock and Soil Mechanics (IRSM), Chinese Academy of Sciences. Beyond granting me access to all the experimental equipment, Professor Wei also offered invaluable guidance on the design of experimental procedures, the design, manufacturing, and troubleshooting of experimental equipment, which enabled all the experiments to be successfully completed as planned.

I would like to sincerely thank my supervisor, Prof. Yadong Bian at Zhongyuan University of Technology (ZUT), for his support and guidance. I am especially grateful for his understanding that my presence at ZUT has not been continuous, owing to the need to perform experiments at IRSM. I would like to thank ZUT for providing me the scholarship to carry out my research.

My sincere thanks go to Yongjie Wu, and Xiaoxiao Li from IRSM, and to the technicians from the equipment manufacturer, without whose suggestions and instructions my experiments could not have been completed so successfully. My thanks are extended to all my fellow researchers, for their friendship and support during the past few years.

Finally, I wish to express my heartfelt gratitude to my parents and my beloved wife, for your unconditional support, encouragement, and love.

Abstract

With the increasing global energy shortages and the expanding exploitation of marine energy resources, geotechnical engineers have encountered numerous challenges related to pile driving in calcareous sand-dominant offshore seafloors. These issues are related to the low strength and high susceptibility to particle breakage of calcareous sands when used as a foundation material. Additionally, large quantities of calcareous sands are utilized in offshore land reclamation projects, serving as the primary foundation material for various infrastructural developments. The unique properties of calcareous sands, such as high susceptibility to particle breakage, can significantly influence the settlement behaviour, impacting the long-term stability of such structures.

The primary objective of this study is to examine the influence of both particle breakage and morphology on the strength and settlement behavior of calcareous sands. To provide a comparative framework, river sand—one of the most commonly used construction materials from terrestrial sources—was also included in the analysis. While both calcareous (CS) and river sands (RS) are originated from aquatic environments, they exhibit significant differences in their morphological features and susceptibility to crushing, offering valuable insights into how these factors could affect their mechanical performance. Sand specimens with different initial relative densities, and in different particle size ranges were prepared. To investigate the influence of particle breakage and morphology on the deformation of sandy soils under load, a series of one-dimensional consolidation tests under the vertical effective stress of up to 7.2 MPa were carried out. To investigate the influence of particle breakage and particle morphology on the shear strength of sandy soils, a series of consolidated drained (CD) triaxial compression tests were conducted under the effective confining pressure of up to 800 kPa.

To achieve a more precise and comparable quantification of particle morphology, specimens were analysed using the dynamic image analysis (DIA) techniques both before and after the tests. This approach allows for a detailed assessment of morphological parameters and offers an alternative approach to quantify particle breakage. The quantified particle breakage results can then be compared with those obtained from traditional sieving methods, ensuring a more comprehensive and accurate analysis of particle behaviour. To analyse the initiation and

progression of micro-mechanical processes such as particle breakage, acoustic emission (AE) recording techniques were employed in conjunction with the one-dimensional consolidation experiments. This innovative application allowed for a detailed examination of the deformation behaviour of calcareous sand samples, offering insights into distinguishing different micro-activities such as particle sliding and breakage. Furthermore, the technique enabled the quantification of the intensity of these micro-activities, providing a novel method to assess the internal processes that influence the mechanical response of calcareous sands.

The main contributions of this research include a comprehensive analysis of the mechanical behaviour of calcareous sands under varying initial relative densities and particle sizes. The influence of particle breakage on compressibility and strength have been quantitatively evaluated. Additionally, the study advances the quantification of morphological changes occurring during both compression and shearing of sandy soil, and validates a novel method for assessing particle breakage based on morphological parameters. An innovative aspect of this research is the application of AE recording technique, which facilitated the differentiation and quantification of microscopic activities in calcareous sands. This research also offers valuable insights into how particle breakage and morphology affect the overall strength characteristics of sandy soil.

Keywords: Sandy soil; particle breakage; particle morphology; dynamic image analysis; one-dimensional consolidation; consolidated drained triaxial compression; calcareous sands; acoustic emission

Table of Contents

| | |
|---|--------------|
| Declaration | i |
| Acknowledgements | ii |
| Abstract | iii |
| Table of Contents | v |
| List of Figures | ix |
| List of Tables | xvi |
| Abbreviations | xvii |
| Symbols | xviii |
| Chapter 1 Introduction | 1 |
| 1.1 Background..... | 1 |
| 1.2 Objectives | 5 |
| 1.3 Thesis outline..... | 6 |
| Chapter 2 Literature Review | 9 |
| 2.1 The strength of sandy soils | 9 |
| 2.1.1 <i>Definition of shear strength of sandy soils</i> | 9 |
| 2.1.2 <i>Factors influencing the strength of sandy soils</i> | 10 |
| 2.2 Influence of initial relative density on soil strength | 14 |
| 2.2.1 <i>Influence of initial relative density on the consolidation of sandy soil</i> | 15 |
| 2.2.2 <i>Influence of initial relative density on strength of sandy soil</i> | 18 |
| 2.3 Particle morphology and its influence on the strength of sandy soil | 23 |
| 2.3.1 <i>Definition and determination of particle morphology</i> | 23 |
| 2.3.2 <i>Quantification of particle morphology</i> | 33 |
| 2.3.3 <i>Influence of particle morphology on soil strength</i> | 36 |
| 2.4 Particle breakage and its influence on the strength of sandy soils..... | 42 |
| 2.4.1 <i>Definition and types of particle breakage</i> | 42 |
| 2.4.2 <i>Quantification of particle breakage</i> | 44 |

| | |
|---|-----------|
| 2.4.3 Influence of particle breakage on soil strength | 49 |
| 2.5 Summary..... | 54 |
| Chapter 3 Research Methodology | 56 |
| 3.1 Testing materials..... | 56 |
| 3.1.1 Calcareous sands | 56 |
| 3.1.2 River sands | 58 |
| 3.1.3 Material preparation..... | 60 |
| 3.1.4 The physical parameters of the tested samples | 61 |
| 3.2 Determination of the basic physical parameters..... | 62 |
| 3.2.1 Minimum dry index density (ρ_{dmin})..... | 62 |
| 3.2.2 Maximum dry index density (ρ_{dmax})..... | 64 |
| 3.2.3 Specific gravity (G_s) | 66 |
| 3.3 Dynamic image analysis..... | 68 |
| 3.4 Quantification of particle breakage | 72 |
| 3.5 Acoustic emission testing | 73 |
| 3.5.1 Technique principle | 73 |
| 3.5.2 Testing apparatus | 76 |
| 3.5.3 Operational procedure | 76 |
| 3.6 One-dimensional consolidation test..... | 78 |
| 3.6.1 Testing apparatus | 79 |
| 3.6.2 Testing procedure | 79 |
| 3.7 Consolidated drained triaxial compression test | 82 |
| 3.7.1 Testing apparatus | 83 |
| 3.7.2 Sample preparation | 84 |
| 3.7.3 Saturation..... | 85 |
| 3.7.4 Consolidation | 89 |
| 3.7.5 Drained shear loading | 89 |
| Chapter 4 One-Dimensional Consolidation Tests..... | 91 |
| 4.1 Experimental setup | 91 |

| | |
|---|------------|
| 4.2 Relationship between void ratio and effective normal stress..... | 92 |
| 4.2.1 Influence of initial relative density on the evaluation of void ratio during compression | 92 |
| 4.2.2 Influence of particle size on the evaluation of void ratio during compression | 94 |
| 4.3 Yield characteristics..... | 96 |
| 4.4 Particle breakage characteristics..... | 98 |
| 4.4.1 Influence of initial relative density on particle size distribution change..... | 98 |
| 4.4.2 Influence of particle size on the particle size distribution change | 100 |
| 4.4.3 Relationship between relative breakage and initial relative density | 103 |
| 4.4.4 Relationship between particle breakage and compression deformation | 104 |
| 4.5 Acoustic emission characteristics | 106 |
| 4.5.1 Evolutions of AE ringdown counts | 106 |
| 4.5.2 Evolutions of AE peak frequency..... | 109 |
| 4.6 Changes of particle morphological characteristics | 110 |
| 4.7 Summary..... | 112 |
| Chapter 5 Consolidated and Drained Triaxial Compression Tests..... | 114 |
| 5.1 The mechanical behaviour of soil..... | 114 |
| 5.1.1 Influence of initial relative density on the shear response | 114 |
| 5.1.2 Influence of particle size on shear response..... | 115 |
| 5.1.3 Influence of effective confining pressure on shear response | 117 |
| 5.2 Particle breakage..... | 119 |
| 5.2.1 Changes in particle size distribution..... | 119 |
| 5.2.2 Statistics of particle size distribution | 121 |
| 5.2.3 Changes in particle size distribution obtained by applying sieving analysis..... | 126 |
| 5.2.4 Quantification of particle breakage | 128 |
| 5.3 Changes of particle morphological characteristics | 131 |
| 5.3.1 Morphological characteristics of calcareous sands..... | 131 |
| 5.3.2 Morphological characteristics of river sands | 133 |
| 5.3.3 Comparison of particle morphological characteristics | 135 |
| 5.4 Influence on shear strength characteristics | 137 |

| | |
|--|------------|
| 5.4.1 <i>Influence on peak friction angle and cohesion</i> | 137 |
| 5.4.2 <i>Influence on dilatancy angle</i> | 138 |
| 5.5 Summary..... | 141 |
| Chapter 6 Conclusions and Future Research | 144 |
| 6.1 Conclusions | 144 |
| 6.1.1 <i>One-dimensional consolidation tests</i> | 144 |
| 6.1.2 <i>Consolidated drained triaxial compression tests</i> | 145 |
| 6.2 Publications | 147 |
| 6.3 Future research | 147 |
| 6.3.1 <i>Data already collected</i> | 147 |
| 6.3.2 <i>New experiments</i> | 148 |
| References | 150 |

List of Figures

| | |
|--|----|
| Figure 1.1. Global distribution of calcareous sands..... | 2 |
| Figure 1.2. Schematic diagram illustrating the influence of particle morphology on the arrangement behaviour of sandy soils: The packing arrangement and inter-particle contacts within a) unsaturated sands; saturated sands with b) high roundness, and c) low roundness. | 4 |
| Figure 2.1. Mohr-Coulomb failure criterion. | 10 |
| Figure 2.2. a) interlocked soil particles; b) the occurrence of dilatancy during shear failure. | 12 |
| Figure 2.3. Typical deviatoric stress-axial strain, and volumetric strain-axial strain relationships for loose sands (a, c); dense sands (b, d) in consolidated drained triaxial compression tests. | 13 |
| Figure 2.4. Schematic diagram of the positional rearrangement of the a) loose; and b) dense sand particles during shearing..... | 14 |
| Figure 2.5. Conceptual interpretation of 1-D compression for cohesionless soils (modified after Vesic and Clough (1968)). | 15 |
| Figure 2.6. Relationship between peak friction angle and relative density (modified after Jamiolkowski et al. (2003))..... | 20 |
| Figure 2.7. a) “convexity gage” used by Wentworth (1923) to quantify the curvature of particle corners; b) apparatus devised by Szadeczky-Kardoss (1933) to trace the particle outline; c) “sliding rod caliper” developed by Krumbein (1941) to measure the particle length in different directions; d) circle scale employed by Wadell (1935) to determine sphericity and roundness of quartz particles..... | 25 |
| Figure 2.8. Comparison chart developed by Krumbein (1941) for visual determination of roundness. | 26 |
| Figure 2.9 Visual chart proposed by Powers (1953) to characterise particle sphericity and roundness. | 27 |
| Figure 2.10. Comparison chart proposed by Krumbein and Sloss (1963) to characterise particle sphericity and roundness..... | 27 |
| Figure 2.11. Two radiuses acquired at one angle when employing Fourier mathematical | |

| | |
|--|----|
| technique on particle shape with re-entrant angles..... | 29 |
| Figure 2.12. The parallel-line method employed in the fractal analysis (modified after Hyslip and Vallejo (1997)). | 30 |
| Figure 2.13. a) a PTS-A series (binocular) photographic white light 3D scanner produced by Shenzhen Stereo3D Technology (2023); b) particle surface presented by point cloud; c) local enlarged image of the point cloud; d) reconstructed particle surface (Shen et al., 2020). | 31 |
| Figure 2.14. Schematic diagram of laser-aided tomography (Matsushima et al., 2003). | 32 |
| Figure 2.15. Shape descriptors at different scales..... | 34 |
| Figure 2.16. Relationship between friction angle and roundness (modified after Zavala (2012)). | 40 |
| Figure 2.17. Schematic representation illustrating particle breakage under three different mechanisms (modified after Wang et al. (2022b))..... | 44 |
| Figure 2.18. Calculation method of particle breakage indices proposed by various researchers (modified after Yu (2021)). | 45 |
| Figure 2.19. Calculation of ballast breakage index, <i>BBI</i> (modified after Indraratna et al. (2005)). | 46 |
| Figure 2.20. The mechanical sieving analysis (MSA, black lines) and dynamic image analysis (DIA, red curves) of PSD before (dashed lines) and after (solid lines) the CD triaxial compression tests. | 48 |
| Figure 3.1. a) The location of the Spratly Islands in the South China Sea; b) Enlarged view of the Spratly Islands, showing the location of the Yongshu Reef (modified after Dong et al. (2019))..... | 57 |
| Figure 3.2. a) Calcareous sand particles of very diverse shapes, such as b) blocky; c) branched; d) flaky; and e) rodlike..... | 58 |
| Figure 3.3. River sands with a round particle shape and a smooth surface. | 59 |
| Figure 3.4. Series of sieves installed on the mechanical sieve shaker. | 60 |
| Figure 3.5. Tested materials: a) calcareous sands and b) river sands of particle size range of 5, 1-2, and 0.5-1 mm. | 61 |
| Figure 3.6. a) apparatuses for determining the ρ_{dmin} , including a glass graduated cylinder, a long | |

| | |
|--|----|
| neck funnel and a rod with tapered stopper; b) the glass cylinder loaded with 700 g of calcareous sands..... | 63 |
| Figure 3.7. Apparatuses for determining the ρ_{dmax} , including a) a vibrating table, a mould, and a hoist; b) vibrator controller; c) surcharge weight..... | 65 |
| Figure 3.8. a) gas pycnometry system; b) sample chamber loaded with calcareous sands on a balance. | 67 |
| Figure 3.9. Schematic diagram of the measurement of specific gravity by gas pycnometry. . | 67 |
| Figure 3.10. a) Particle size and shape analyser, PartAn ^{3D} Maxi (modified after Wei et al. (2020)); b) schematic view of the particle size and shape analysing system..... | 69 |
| Figure 3.11. Successive snapshots of 3 particles (one row for each particle) during free falling. | 70 |
| Figure 3.12. An image of digitized particle and definitions of a series of basic dimensions. . | 71 |
| Figure 3.13. The calculation of relative breakage, B_r proposed by Hardin (1985)..... | 73 |
| Figure 3.14. Schematic of an acoustic emission testing system. | 74 |
| Figure 3.15. Parameters of an AE hit. | 75 |
| Figure 3.16. Acoustic emission testing set-up. | 76 |
| Figure 3.17. Cable connection of the preamplifier. | 77 |
| Figure 3.18. Typical real-time results of cumulative AE hits, hits, and amplitude by using AEwin. | 78 |
| Figure 3.19. One-dimensional compression test set-up. | 79 |
| Figure 3.20. Components of a consolidometer. | 80 |
| Figure 3.21. Consolidated and drained triaxial compression test set-up. | 83 |
| Figure 3.22. Illustration of specimen preparation for triaxial tests..... | 84 |
| Figure 3.23. a) Sample preparation; b) Vacuumed specimen for triaxial tests. | 85 |
| Figure 3.24. A prepared sand specimen before shearing. | 86 |
| Figure 3.25. Pressure variation during stages of a) Specimen saturation; b) B -check..... | 87 |
| Figure 3.26. Set up of the “ B -check” step in the triaxial testing system using the software GeoSmartLab. | 88 |
| Figure 3.27. Pressure variation during the consolidation of test specimen. | 89 |
| Figure 4.1. Effective normal stress-time relationships for calcareous sands with initial relative | |

| | |
|--|-----|
| density of 0.7 in the size range of 2–5 mm during 1-D consolidation test. (b)(c): enlarged views. | 92 |
| Figure 4.2. One-dimensional compression curves for (a) calcareous sands; and (b) river sands with different initial relative densities in the size range of 2-5 mm. | 93 |
| Figure 4.3. 1-D compression curves for CS in different size ranges. The initial relative density is 0.6..... | 95 |
| Figure 4.4. Yield points and fitting curves of (a) calcareous sands (CS) and (b) river sands (RS) with different initial relative densities and particle size of 2-5 mm, CS with different initial relative densities and particle size of (c) 1-2 mm and (d) 0.5-1 mm. | 97 |
| Figure 4.5. Influence of initial relative density and particle size on yield stress of calcareous sands (CS) and river sands (RS). | 98 |
| Figure 4.6. Initial (dashed curves) and final (solid curves) particle size distributions for (a) calcareous and (b) river sand samples with different initial relative densities in the particle size range of 2-5 mm..... | 99 |
| Figure 4.7. Statistics of particle sizes for calcareous sand specimens with the initial particle size range of 2-5 mm and initial relative density of (a) 0.55, and (b) 0.8 before and after the oedometer tests..... | 100 |
| Figure 4.8. The initial (dashed curves) and final (solid curves) particle size distributions for calcareous sand samples of different particle size ranges. The initial relative density was 0.65..... | 101 |
| Figure 4.9. Statistics of individual particle size of calcareous sand specimens with the initial relative density of 0.7 and the particle size range of (a) 2-5 mm, and (b) 1-2 mm before and after the tests. | 102 |
| Figure 4.10. PSD of CS specimens with initial relative density of 0.5, 0.75, and 0.8 in particle size range of (a) 2-5 mm, and (b) 1-2 mm before and after the tests obtained by applying MSA..... | 103 |
| Figure 4.11. Relative breakage of CS specimen obtained by applying MSA and DIA. | 103 |
| Figure 4.12. Definition of the change in void ratio due to particle rearrangement and breakage. | 104 |
| Figure 4.13. The change in void ratio due to breakage under the normal stress ranging from 0.3 | |

| | |
|--|-----|
| to 7.2 MPa of CS with the initial relative density of 0.5 and in particle size range of 2-5 mm. | 106 |
| Figure 4.14. Evolutions of AE ringdown counts and vertical effective stress over time of CS specimen with an initial relative density of 0.6 and in particle size range of 1-2 mm. . | 107 |
| Figure 4.15. Evolutions of cumulative AE RDC with vertical effective stress during of CS (a) with different initial relative densities in the same particle size range of 1-2 mm, (b) with the same initial relative density of 0.7 in different particle size ranges..... | 108 |
| Figure 4.16. Evolutions of AE peak frequency and vertical effective stress with time of calcareous sands with particle size range of 1-2 mm and initial relative density of (a) 0.6, and (b) 0.8. | 110 |
| Figure 4.17. Frequency counts of particle shape descriptors including (a) sphericity, (b) convexity, (c) aspect ratio, and (d) flatness before and after the one-dimensional consolidation tests..... | 111 |
| Figure 5.1. Evolutions of a) deviatoric stress; and b) volumetric strain with axial strain of CS specimen in particle size range of 2-5 mm under the effective confining pressures of 200 kPa..... | 115 |
| Figure 5.2. Evolutions of a) deviatoric stress; and b) volumetric strain with axial strain of calcareous sand (CS) and river sand (RS) specimens, at the initial relative density of 0.7 under the effective confining pressure of 200 kPa..... | 116 |
| Figure 5.3. Evolutions of a) deviatoric stress; and b) volumetric strain with axial strain for calcareous sand (CS) and river sand (RS) specimens, at an initial relative density of 0.7 and in particle size range of 2-5 mm under different effective confining pressures..... | 118 |
| Figure 5.4. Initial (dashed curves) and final (solid curves) PSD for (a) CS with different initial relative densities but uniform particle size in the range of 2-5 mm; (b) CS and RS with initial relative density of 0.7 but different particle size ranges under the effective confining pressure of 200 kPa..... | 120 |
| Figure 5.5. Initial (dashed curves) and final (solid curves) PSD for (a) CS samples, and (b) RS samples with initial relative density of 0.7 and in particle size range of 2-5 mm under different effective confining pressures..... | 121 |
| Figure 5.6. Statistics of individual particle size of calcareous sands with the initial particle size | |

| | |
|---|-----|
| range of 2-5 mm and initial relative density of (a) 0.6, and (b) 0.7 before and after the tests under the effective confining pressure of 200 kPa..... | 122 |
| Figure 5.7. Statistics of individual particle size of calcareous sands with initial relative density of 0.7 in initial particle size range of (a) 2-5 mm, and (b) 1-2 mm before and after the tests under the effective confining pressure of 200 kPa..... | 123 |
| Figure 5.8. Statistics of individual particle size of river sands with initial relative density of 0.7 in initial particle size range of (a) 2-5 mm, and (b) 1-2 mm before and after the tests under the effective confining pressure of 200 kPa..... | 123 |
| Figure 5.9. Statistics of individual particle size of calcareous sands with initial relative density of 0.7 in initial particle size range of 2-5 mm before and after the tests under the effective confining pressure of (a) 50 kPa, and (b) 800 kPa..... | 124 |
| Figure 5.10. Statistics of individual particle size of river sands with initial relative density of 0.7 in initial particle size range of 2-5 mm before and after the tests under the effective confining pressure of (a) 50 kPa, and (b) 800 kPa..... | 125 |
| Figure 5.11. PSD for (a) calcareous sands in particle size range of 2-5 mm but with different initial relative densities; (b) calcareous and river sands with initial relative density of 0.7 but in different particle size ranges before (dashed lines) and after (solid lines) the tests under the effective confining pressure of 200 kPa. The results were obtained by applying sieving analysis. | 126 |
| Figure 5.12. PSD for (a) calcareous sands; and (b) river sands in particle size range of 2-5 mm and with initial relative density of 0.7 before (dashed lines) and after (solid lines) the tests under different effective confining pressures. . The results were obtained by applying sieving analysis. | 127 |
| Figure 5.13. Relative breakage for calcareous sands with different initial relative densities (a) in particle size range of 2-5 mm and 1-2 mm after the tests under the effective confining pressure of 100, 200 and 300 kPa; and (b) in different particles size ranges after the tests under the same effective confining pressure of 300 kPa obtained by applying sieving analysis..... | 129 |
| Figure 5.14. Evolutions of B_r with effective confining pressure for CS and RS in particle size range of 2-5 mm with initial relative density of 0.7. The data was obtained by applying | |

| | |
|---|-----|
| MSA..... | 131 |
| Figure 5.15. Frequency of particle shape descriptors: (a) sphericity, (b) convexity, (c) aspect ratio, and (d) flatness for calcareous sands before and after the tests. The specimens were in particle size range of 2-5 mm, initial relative density of 0.7 and under an effective confining pressure of 400 kPa..... | 132 |
| Figure 5.16. Frequency distribution of particle shape descriptors of (a) sphericity, (b) convexity, (c) aspect ratio, and (d) flatness for river sand specimens. The specimens have the particle size in the range of 2-5 mm, initial relative density of 0.7, under the effective confining pressure of 400 kPa..... | 134 |
| Figure 5.17. Variation of a) peak friction angle; and b) apparent cohesion with particle size for calcareous sand specimen with initial relative density of 0.5 and 0.6. | 137 |
| Figure 5.18. Variation of dilatancy angle in calcareous sand specimens: (a) in different initial particle size ranges, but under the effective confining pressure of 100 kPa; (b) in the same initial particle size range of 0.5-1 mm, but under different effective confining pressures. | 140 |
| Figure 5.19. Variation of soil dilatancy angle with the effective confining pressure for CS and RS specimens. The initial relative density was 0.7 and initial particle size range was 2-5 mm. | 141 |

List of Tables

| | |
|--|-----|
| Table 1.1. Classification of marine sediments. | 2 |
| Table 2.1. Solid classification by relative densities. | 22 |
| Table 2.2. The fitting parameters of coral sands with different initial relative densities. | 51 |
| Table 3.1. The main minerals of calcareous sands (modified after Wang et al. (2017b)). | 58 |
| Table 3.2. Quantitative mineralogy analysis results of river sands. | 59 |
| Table 3.3. The basic physical parameters of calcareous and river sands. | 62 |
| Table 3.4. Parameter settings by using AEWin. | 77 |
| Table 3.5. Weight added and cumulative weight in each stage of the oedometer tests. | 81 |
| Table 4.1. Yield stress (unit: kPa) of calcareous and river sands. | 97 |
| Table 4.2. Experimental parameters of Eq. 4.6. | 105 |
| Table 5.1. Relative breakage for CS in different particle size ranges and with different initial relative densities after the tests under different effective confining pressures obtained by applying MSA. | 128 |
| Table 5.2. Relative breakage of calcareous and river sand specimens in the particle size range of 2-5 mm and with initial relative density of 0.7 after the tests under different effective confining pressures obtained by applying MSA. | 130 |
| Table 5.3. Dilatancy angle of CS and RS specimens with different initial relative densities and initial particle size ranges after the tests under different effective confining pressures. | 139 |
| Table 5.4. Dilatancy angle of CS and RS specimens with the initial relative density of 0.7 and in initial particle size range of 2-5 mm under different effective confining pressures. | 141 |

Abbreviations

| | |
|------------|------------------------------------|
| AE | acoustic emission |
| AF | normalised angularity factor |
| AST | automatic sensor test |
| <i>BBI</i> | ballast breakage index |
| CCD | charge-coupled device |
| CD | consolidated drained |
| COD | coefficient of determination |
| CS | calcareous sand |
| CN | coordination number |
| DEM | discrete element method |
| DIA | dynamic image analysis |
| FIR | finite impulse response |
| KSPS | kilo samples per second |
| LAT | laser-aided tomography |
| LBS | Leighton Buzzard sands |
| LCC | limiting compression curve |
| MSA | mechanical sieving analysis |
| MSPS | mega samples per second |
| NCL | normal compression line |
| NDT | non-destructive testing |
| PLB | pencil lead break |
| PSD | particle size distribution |
| RDC | ringdown counts |
| RS | river sand |
| SCS | South China Sea |
| SF | normalised shape factor |
| SMB | SubMiniature version B |
| RDC | ringdown counts |
| rpm | round per minute |
| SD | standard deviation |
| SP | poorly graded |
| USCS | unified soil classification system |
| XRD | X-ray diffraction |
| 2D | two-dimensional |
| 3D | three-dimensional |
| μ CT | X-ray micro-computed tomography |

Symbols

| | |
|-----------|---|
| A | particle area |
| A_{BBI} | parameter for ballast breakage index calculation |
| A_c | area of convex hull |
| A_{cs} | cross-sectional area of the specimen |
| A_{ema} | major axis of best-fit ellipse |
| A_{emi} | minor axis of best-fit ellipse |
| A_o | specimen area during oedometer test |
| A_s | particle surface area |
| A | cross-sectional area of axial load piston |
| a_n | Fourier coefficient |
| a_1 | fitting parameter in Equation 2.30 |
| B_{BBI} | parameter for ballast breakage index calculation |
| B_f | particle breakage index proposed by Nakata et al. (1999) |
| B_g | particle breakage index proposed by Marsal (1967) |
| B_{r-p} | particle breakage index proposed by Wei et al. (2020) |
| B_r | relative breakage |
| B_{10} | particle breakage index proposed by Lade et al. (1996) |
| B_{15} | particle breakage index proposed by Lee and Farhoomand (1967) |
| B | difference between void ratio and initial void ratio under the vertical stress of 1 MPa |
| b_n | Fourier coefficient |
| b_1 | fitting parameter in Equation 2.30 |
| C | convexity |
| C | cohesion |
| c_p | peak cohesion |
| C_u | coefficient of uniformity |
| Da | area equivalent diameter |
| D_b | particle breakage index proposed by Yu (2018) |
| D_c | current fractal dimension of the current PSD |
| D_f | fragmentation fractal dimension |
| D_i | initial fractal dimension of the initial PSD |
| D_R | roughness fractal dimension of the curve |
| D_r | initial relative density |
| D_{ult} | ultimate fractal dimension of the ultimate PSD |
| D_{10} | sieve opening size (mm) through which 10% (by weight) of the aggregate passes |
| D_{10i} | particle size (diameter) at which 10 percent of the material is finer before test |
| D_{10f} | particle size (diameter) at which 10 percent of the material is finer after test |

| | |
|------------------------|---|
| D_{15i} | particle size (diameter) at which 15 percent of the material is finer before test |
| D_{15f} | particle size (diameter) at which 15 percent of the material is finer after test |
| D_{50} | sieve opening size (mm) through which 50% (by weight) of the aggregate passes |
| D_{60} | sieve opening size (mm) through which 60% (by weight) of the aggregate passes |
| d | particle size |
| e | void ratio |
| e_b | change in void ratio due to particle breakage |
| e_c | void ratio corresponding to the vertical stress of 1 MPa |
| e_i | residual value |
| e_{max} | maximum void ratio |
| e_{min} | minimum void ratio |
| e_r | change in void ratio due to particle rearrangement |
| e_{skps} | skeleton void ratio |
| e_0 | initial void ratio |
| FL | particle length |
| FT | particle thickness |
| FW | particle width |
| F_{max} | the largest Feret size |
| F_{min} | the smallest Feret size |
| F_o | weight applied on beam during oedometer test |
| ΔF_c | increase of fine contents |
| f | test parameter in Equation 4.5 for compression curve |
| f_i | fitted value corresponding to dataset value g_i |
| G_s | specific gravity |
| g_i | dataset value |
| \bar{g} | mean of the dataset value |
| H_c | specimen height after consolidation |
| h_s | equivalent height of solids |
| h_0 | initial specimen height |
| ΔH_ε | height change from beginning of shear |
| I_B | brittleness index |
| I_g | grading state index |
| J | sieve size fraction |
| K | proportionality constant |
| L_s | diameter of a sphere with the same volume as the particle |
| M | sample mass |
| M_d | dry mass of specimen |
| M_r | mass required |

| | |
|-----------------|--|
| N | intercept of NCL |
| $N(R_r > r)$ | number of particles with the radius of R_r larger than the given value r |
| N_f | number of features examined |
| N_s | number of sampling points |
| N_h | total number of harmonics |
| N | harmonic number |
| n_1 | proportionality constant |
| P | value obtained by the submersible force sensor |
| P_a | total particle perimeters after test |
| P_{at} | atmospheric pressure |
| P_b | total particle perimeters before test |
| P_c | convex hull perimeter |
| P_o | stress applied on the specimen during oedometer test |
| P_p | particle perimeter |
| P_1 | gas pressure when only sample cell is pressurized |
| P_2 | gas pressure after expansion |
| $P(\lambda_l)$ | polygon perimeter |
| p' | effective normal stress |
| Δp_{ij} | difference of percentages finer on the initial gradings at sieve size fraction j |
| Δp_{if} | difference of percentages finer on the final gradings at sieve size fraction j |
| Q | deviatoric stress |
| q_{max} | peak deviatoric stress |
| q_{rse} | residual deviatoric stress |
| R | a given value of particle radius |
| R_A | particle breakage index proposed by Nakata et al. (2001a) |
| R_p | difference between the percentage of particle finer after test and the minimum particle size of the specimen before test |
| R_r | particle radius |
| $R(\theta)$ | radius at angle θ |
| R^2 | coefficient of determination |
| R_1 | roundness determined by comparing the chart proposed by Krumbein and Sloss (1963) as shown in Figure 2.10 |
| R_2 | roundness determined by employing the equation proposed by Wadell (1932) |
| r_{max} | radius of the largest inscribed circle |
| r_i | radius of curvature of surface features |
| S | sphericity |
| S_a | cross-sectional area of the particle after test |
| S_b | cross-sectional area of the particle before test |
| S_h | modified shape parameter |
| SS_{res} | residual sum of squares |

| | |
|--------------------|---|
| SS_{tot} | total sum of squares |
| S | number of values |
| V | volume of specimen |
| V_c | specimen volume after consolidation |
| V_{cell} | volume of sample chamber |
| V_{exp} | volume of expansion chamber |
| V_m | volume of the mould |
| V_{max} | maximum volume of the tested-dry soil |
| V_{min} | minimum volume of the tested-dry soil |
| V_s | volume of solids |
| V_{sample} | calculated sample volume by using gas pycnometry method |
| ΔV_e | volume change from beginning of shear |
| W | plastic work done |
| x_i | Sukumaran coefficients |
| y_i | Sukumaran coefficients |
| α | aspect ratio |
| α_i | distortion angle |
| α_{i-fp} | value of distortion angle corresponding to a thin flat particle |
| B | flatness |
| β_i | internal angles of the particle corner |
| ε_a | axial strain |
| ε_v | volumetric strain |
| Γ | model parameter used by Yu (2017d) |
| λ | rate parameter of the exponential distribution |
| λ_c | slope of compression curve within e - $\log(p')$ plot |
| λ_p | model parameter used by Yu (2017d) |
| λ_{NCL} | gradient of NCL |
| λ_l | unit measurement length |
| φ | internal friction angle |
| φ_{AF} | friction angle calculated based on AF |
| φ_{cs} | critical-state friction angle |
| φ_{excess} | excess friction angle |
| φ_{MC} | friction angle at maximum contraction |
| φ_p | peak friction angle |
| φ_{rep} | angle of repose |
| φ_{SF} | friction angle calculated based on SF |
| ψ | dilatancy angle |
| ψ_{max} | maximum dilatancy angle |
| ρ_d | dry density |

| | |
|---------------|---|
| ρ_{dmax} | maximum (dry) index density |
| ρ_{dmin} | minimum (dry) index density |
| ρ_w | density of water, 1.0 g/cm ³ |
| σ_1 | major principal stress |
| σ_3 | minor principal stress (confining stress) |
| τ | shear strength |
| μ | x-coordinate of the centre of the Gaussian distribution |

Chapter 1 Introduction

1.1 Background

Throughout history, humans have utilized a range of energy sources, including wood, coal, oil, petroleum, and nuclear power for the purpose of generating electricity and heat. However, the uncontrolled utilization of these resources and the absence of strategic planning in development initiatives have resulted in severe energy crisis. Due to the constraints on their availability, oil, gas, and electricity have escalated costs across many regions in the world (IEA, 2022). Surging oil and gas price have led human to turn to the oceans for natural resources, which drives the growth of offshore drilling. It is predicted that the offshore drilling industry will continue to expand at a compounded annual growth rate of approximately 7.54% during the forecast period spanning from 2023 to 2035, ultimately resulting in an estimated market size of roughly USD 237.19 Billion (Research Nester, 2023).

In parallel with the expansion of traditional energy extraction, there is a growing focus on the development and implementation of clean and sustainable energy resources. As one of the renewable energy resources, the offshore wind energy is gaining escalated consideration and is being extensively deployed, owing to its greater capacity factor, and its reduced impact on people and the landscape in comparison to onshore wind power. According to Det Norske Veritas (2022), the total installed capacity of offshore wind turbines is anticipated to persistently expand on a global scale, and is expected to reach 1550 GW in 2050, thereby contributing to 9% of the total global electricity output, as opposed to the current portion of 0.3%. Such a rapid rate of development places an even higher demand on the design safety and installation stability of the offshore foundations. In addition to the exploitation of offshore energy resources, coastal reclamation projects have also been carried out in large numbers to address the growing demand for land resources, serving purposes such as recreational activities, real estate development, and the establishment of public infrastructure (Tamsir et al., 2020). These aforementioned engineering activities cannot be carried out successfully without adequate knowledge of the engineering properties of the foundation soil.

As presented in Table 1.1, Keller (1967) concludes that marine sediments can be divided into 6 categories. In these categories, the fluvial sediments are predominantly confined along the shelf break, exhibit minimal dispersal across the oceanic seabed. The oozes and inorganic pelagic are widely distributed in deep ocean, which have not presented significant challenges to offshore development (Houston and Herrmann, 1980). In contrast, calcareous sands, silts, and gravels, which are predominantly located in the shallower waters of continental shelves and coastal regions, have posed significant challenges to offshore foundation engineering.

Table 1.1. Classification of marine sediments.

| Marine Sediments | Description |
|------------------------------|---|
| Fluvial marine sand and silt | Predominantly sourced from terrestrial runoff and are typically deposited in shallow marine environments. |
| Fluvial marine silt and clay | |
| Inorganic pelagic clay | Deep ocean inorganic deposits. |
| Siliceous ooze | Generally found in the deep ocean, these deposits consist primarily of fine-grained skeletal remains. |
| Calcareous ooze | |
| Calcareous sand and silt | Primarily composed of shell fragments and coralline debris. |

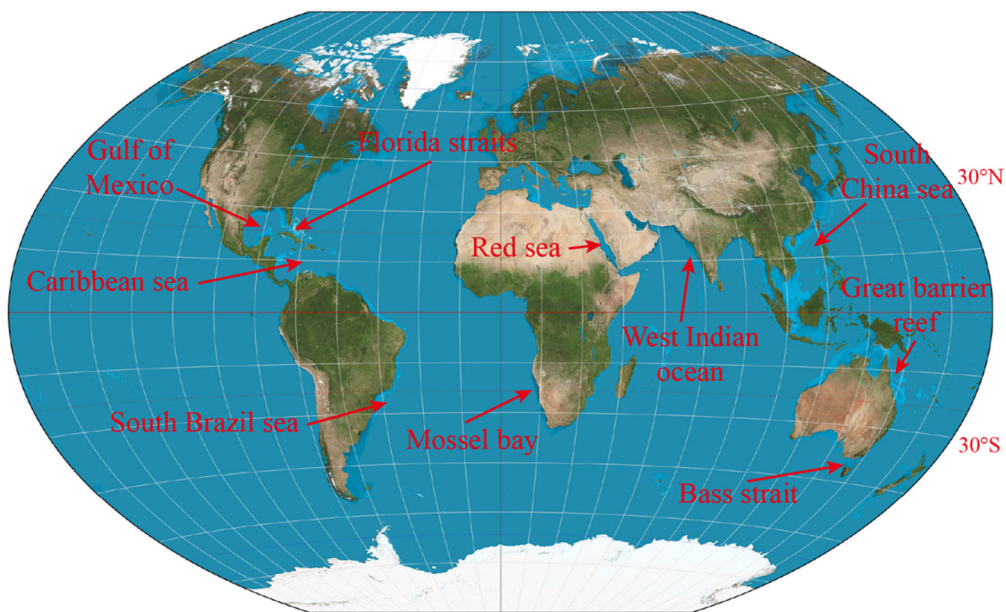


Figure 1.1. Global distribution of calcareous sands.

As shown in Figure 1.1, calcareous sands are primarily distributed in the coastline and continental shelf with tropical or subtropical climate between 30° N and 30° S of the equator. They are widespread across the islands and reefs and north coast, such as the South China Sea, the Red Sea, continental shelves in west Australia and the Bass Strait (Spalding et al., 2001).

Soil particles located at the base of large structures (such as lighthouses, aircraft runways, and ports) on the shoreline or at the tip of piles supporting high-rise offshore structures (such as oil platforms, and wind farms), particularly during the process of soil penetration, are subjected to immense pressures, leading to high potential of particle breakage (Yu, 2017a, Gao and Ye, 2023). Engineering activities conducted on calcareous sands can be traced back to World War II, when a runway was built on Los Negros Island in Papua New Guinea, marking one of the earliest recorded instances of large-scale construction on such fragile marine sediments (Xu et al., 2022). In the middle of nineteen sixties, submarine sediment layers composed of shell fragments and sandy limestones were revealed in the oil exploration hole in the Arabian Gulf, but it was not realized by engineers how they differed from other land-based sands. During the construction of the Lavan oil platform in Iran in 1968, a pile with diameter of approximately 1 m fell freely for a height of 15 m after passing through an 8-meter strata under the mudline, which marked the first recorded engineering problem caused by the extensive breakage of calcareous sands (McClelland, 1988). Subsequently, calcareous sands have been responsible for a range of engineering settlement and instability problems with significant financial losses during the construction of offshore oil platforms in various areas including the North West Continental Shelf of Australia (Dolwin et al., 1988), the Bass Strait (Wiltsie et al., 2021), the Great Barrier Reef and White Tip Reef on the eastern continental shelf of Australia, the Campos Basin and Sergipe Basin on south-eastern Brazil (De Mello et al., 1989), Quiou, Pisiou, and Plouasne sites in western France (Nauroy and Le Tirant, 1983), the Gulf of Mexico in central America, and the Caribbean Sea (Dutt et al., 2021), and the Red Sea in the Middle East (Hagenaar, 2021).

In recent years, engineering failures due to inadequate understanding of the unique properties of calcareous sands have continued to occur worldwide. Lessons such as the large-scale settlement of Kansai Airport in Japan (Mesri and Funk, 2015), the collapse of harbour construction at Nice Airport in France (Dan et al., 2007), and the serious damage to the protective structure of the Maldives by the Indian Ocean tsunami (Fujima et al., 2006) have shown that reclaimed artificial islands are also facing many threats such as settlement after construction and during the maintenance stage.

Several factors could contribute to particle breakage, such as the material inherent strength

and the effective stress state (Yamamuro and Lade, 1996). Extensive research has been conducted on the influences of mineralogy (Lobo-Guerrero and Vallejo, 2005b, Bono et al., 2014), loading condition (Indraratna et al., 2015, Thakur, 2011), particle size (Marsal, 1973, Hardin, 1985, Rozenblat et al., 2011), and the coordination number (Lobo-Guerrero and Vallejo, 2005b, Mishra and Thornton, 2001, Cil and Alshibli, 2012) on particle breakage. However, the impact of particle morphology on the crushing process remains less thoroughly explored. In geotechnical engineering, as a non-negligible factor of micro-mechanisms, the morphology of sand particles plays an important role in influencing the mechanical macroscopic performances, such as compressibility, stiffness, packing, shear response, and critical state parameters (Santamarina and Cho, 2004, Cho et al., 2006, Cavarretta et al., 2010, Altuhafi et al., 2016). The significance of particle morphology, particularly in granular materials such as sand, is illustrated in Figure 1.2. In such a granular packing, the solid skeleton and pore spaces can significantly influence the consolidation state of sands under both saturated and unsaturated conditions. This relationship is intricately linked to the ground settlement, playing a crucial role in determining the overall stability of structures built upon them.

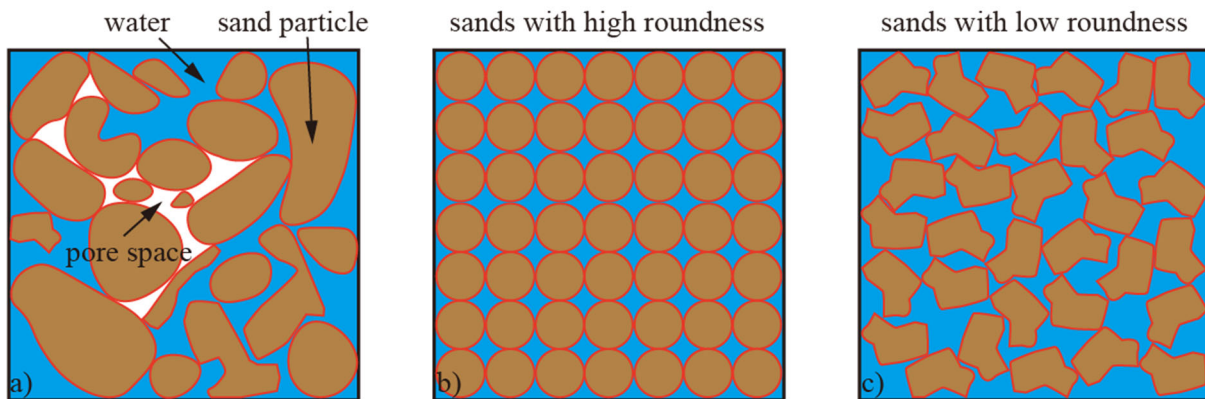


Figure 1.2. Schematic diagram illustrating the influence of particle morphology on the arrangement behaviour of sandy soils: The packing arrangement and inter-particle contacts within a) unsaturated sands; saturated sands with b) high roundness, and c) low roundness.

However, the current methodologies for characterizing particle morphology rely largely on manual measurements or chart-based analysis, both of which are not only cumbersome but also subject to individual interpretation (Anusree and Latha, 2023). Furthermore, the absence of standardized protocols for quantification and their application in engineering design further complicates the process. Developing precise techniques for particle classification and

morphology characterization, alongside establishing a robust correlation between particle morphology and mechanical behaviour, will significantly enhance the accuracy of material selection and utilization in geotechnical engineering practices.

Therefore, it is essential to conduct thorough research on the impacts of the unique properties of calcareous sands, such as their highly irregular shapes and vulnerability to crushing, on the strength. This is of great significance for understanding the mechanical properties of calcareous sands, as well as to advance the research on particle breakage and particle morphology of granular soil materials.

1.2 Objectives

The aim of this research is to experimentally investigate the influence of particle breakage and morphology on the strength of sandy soil. Two types of laboratory experiments including the one-dimensional (1-D) consolidation tests, and consolidated drained (CD) triaxial compression tests were conducted on calcareous and river sands, respectively. The main research objectives are listed as follows:

1-D consolidation tests were conducted to investigate the particle breakage characteristics and its morphological changes under various loading conditions. The objectives include:

- To obtain the evolution of void ratio with effective normal stress for calcareous and river sands under the one-dimensional consolidation.
- To analyse the evolution of particle size distribution and quantify the relative breakage by the mechanical sieving analysis (MSA).
- To employ innovative methods to characterise the evolution of morphological parameters after test based on the statistical results.
- To analyse the changes in particle size distribution before and after the test by statistically evaluating particle morphology. These findings can be then compared with the results obtained via MSA.
- To quantify particle breakage by analysing morphological parameters and subsequently comparing these findings with results obtained via MSA.
- To employ innovative technological methods to monitor the entire experimental process, enabling the differentiation and quantification of distinct microscopic activities, such as

particle sliding and breakage, and assessing their intensities.

- To propose a computational model for predicting the settlement of calcareous sand under specific loading conditions.

CD triaxial compression tests were conducted to examine how particle breakage influences the strength parameters of calcareous sands and the associated changes in particle morphology.

The corresponding research objectives include:

- To analyse the deviatoric stress-axial strain, and volumetric strain-axial strain relationships of calcareous and river sands.
- To analyse the evolution of particle size distribution before and after the test by statistical analysis, and quantify the relative breakage obtained by using the MSA.
- To employ innovative methods to characterise the evolution of morphological parameters after test based on the statistical results.
- To analyse the variation in peak friction angle and apparent cohesion of calcareous sands under diverse experimental conditions.
- To quantify the dilatancy angle and analyse its variation for calcareous and river sands under diverse experimental conditions.
- To present relationships between dilatancy angle and effective confining pressure for calcareous and river sands.

1.3 Thesis outline

The thesis is structured as follows:

Chapter 2 presents a critical review of the literature relevant to the key research topics relevant to this research. Section 2.1 provides an overview of the Mohr-Coulomb theory, along with an explanation of two key factors that significantly affect the shear strength: the friction angle and cohesion. Subsequently, there is an examination and evaluation of strain softening, strain hardening, shear dilation, and shear contraction behaviour of soil. Section 2.2 is divided into two subsections that provide an overview of the advancements in research concerning the influence of initial relative density on the consolidation and strength characteristics of sandy soils. In Section 2.3, the concept of particle morphology is first introduced. Then, a summary of the existing literature on methods and tools used to describe particle morphology, as well as

the shape descriptors in different scales are presented. Finally, the literature about the influence of particle morphology on consolidation and shear strength of sandy soil is reviewed. In Section 2.4, first, the definition of particle breakage is introduced. Then, a summary of the existing literature on methods to quantify particle breakage is presented. Finally, the literature with regards to the influence of particle breakage on consolidation and shear strength of sandy soil is reviewed. Finally, Section 2.5 aims to critically assess and summarize the limitations identified in contemporary research, as highlighted in the review of relevant literature.

Chapter 3 details the testing materials, methods, and the testing apparatus used throughout the study. In Section 0, first, the calcareous and river sands are introduced. Then, the preparation for testing material is described, which is followed by a summary of the physical parameters of the sand samples. In Section 3.2, the methods and apparatus employed for the determination of physical parameters including minimum and maximum dry index density, and specific gravity are described. In Section 3.3, first, the particle size and shape analyser, PartAn^{3D} Maxi is introduced. Then, the testing procedure for dynamic image analysis is described in detail. Finally, the calculation methods for shape descriptors including the area equivalent diameter, aspect ratio, flatness, roundness, sphericity, and convexity are presented. In Section 3.4, the quantification of particle breakage by applying DIA and MSA are described, respectively. In Section 3.5, first, the methodology for AE testing is introduced. The key parameters of an AE signal are illustrated and explained. Then, the main components of the testing system are presented. The specifications for each part are summarized. Finally, the operational procedure for AE testing is described. In Section 3.6, the consolidometer is introduced, as well as its specifications. Then, the testing procedure including the calibration of equipment, the preparation and loading of sand sample, the loading and unloading process, calculation of the key parameters such as void ratio are described in detail. In Section 3.7, first, the triaxial testing system are described, as well as the main specifications. Then, the preparation and loading of sand samples are illustrated and explained. Finally, the testing procedures for saturation, consolidation, and drained shear loading are described.

Chapter 4 provides a thorough summary of the outcomes obtained in the one-dimensional consolidation tests. Section 0 presents the relationships between effective normal stress and loading time. Section 4.2 presents the relationships between void ratio and effective normal

stress. Section 4.3 focuses on the yield stress of sand specimens. Section 4.4 presents the evolution of PSD, statistics of individual particle size obtained by using DIA. The evolution of PSD obtained by using MSA is also presented and compared with the results obtained by using DIA. Then, particle breakage quantified by using MSA and DIA is compared. Finally, the numerical results for the relationships between the change in void ratio due to particle breakage and vertical stress are presented. In Section 4.5, the evolutions of AE ringdown counts and vertical effective stress over time is first introduced. Then, the evolutions of cumulative AE RDC with vertical effective stress are presented. Finally, the evolutions of AE peak frequency and vertical effective stress with time are presented. Section 4.6 presents the evolution of morphological parameters, including sphericity, convexity, aspect ratio, and flatness of calcareous sands after test based on the statistical results obtained by using DIA. Section 4.7 concludes with a comprehensive summary of the key findings discussed in Chapter 4.

Chapter 5 summarizes the outcomes obtained in the consolidated drained triaxial compression tests. Section 5.1 presents the influence of sample initial relative density, particle size, and effective confining pressure on the deviatoric stress-axial strain and volumetric strain-axial strain relationships. In Section 5.2, first, the influence of initial relative density, particle size, and effective confining pressure on the evolutions of particle size distribution by using the DIA are discussed. The influence of initial relative density, particle size, and effective confining pressure on the evolutions of particle size distribution and relative breakage by using MSA are also presented. Finally, the relationships between relative breakage obtained by using MSA and effective confining pressure for calcareous and river sands are presented. In Section 5.3, the evolution of morphological parameters including sphericity, convexity, aspect ratio, and flatness of calcareous and river sands after the test based on the statistical results obtained by using DIA are characterised and compared. In Section 5.4, the influence of initial relative density, particle size, and effective confining pressure on the peak friction angle, apparent cohesion, and dilatancy angle are analysed. The dilatancy angle-initial relative density and dilatancy angle-effective confining pressure relationships are presented. Section 5.5 concludes with a comprehensive summary of the key findings discussed in this chapter.

Chapter 6 concludes the thesis by detailing the main conclusions of the research and opportunities for future works.

Chapter 2 Literature Review

This chapter begins by defining the concept of shear strength in sandy soils and identifies two key parameters that significantly influence this property: the initial relative density and particle morphology. These factors play a crucial role in determining the degree of particle interlocking, thereby influencing the macro-mechanical behaviour of soil. This chapter provides a detailed summary of studies examining the impact of these parameters on consolidation and strength characteristics. In addition, a thorough discussion of particle morphology, including its definition and quantification, is presented. The chapter also addresses the phenomenon of particle breakage, which alters both the particle size distribution and the morphological properties of individual grains. These changes, in turn, have a profound effect on the macro-mechanical behaviour of sandy soils. Consequently, this chapter concludes by summarizing the reviews on the quantification of particle breakage and its influence on soil strength characteristics.

2.1 The strength of sandy soils

2.1.1 Definition of shear strength of sandy soils

The soil shear strength is an important parameter to control the mechanical behaviour and deformation of geotechnical structures. Soil usually fails in the form of “shearing” along a continuous surface within the soil mass. At failure state, the shear stress along the failure surface, i.e., the mobilized shear resistance, reaches the shear strength. According to the classical soil mechanics, the shear strength of a soil mass is the internal resistance per unit area that the soil mass can offer to resist the failure and sliding along any plane inside it. It is a measure of the soil resistance to deformation by continuous displacement of the constituent soil particles. Therefore, the determination of soil shear strength is a crucial aspect in geotechnical engineering practices. In addition, the understanding of shear strength provides the basis for analysing soil stability problems (Xu et al., 2011), such as the measurement of lateral earth pressure on retaining structures (Li et al., 2019), determination of loading capacity of ground foundations (Smith, 1982), and analysis of slope stability (Zheng, 2012).

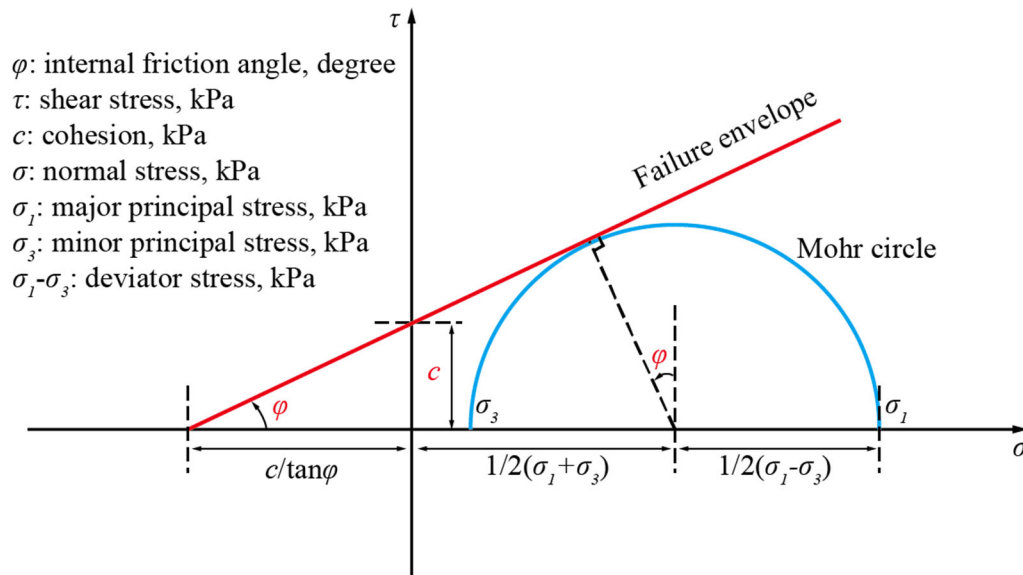


Figure 2.1. Mohr-Coulomb failure criterion.

The Mohr-Coulomb theory is the oldest but still widely used failure criteria for calculating soil shear strength, which combines the Coulomb's shear stress equation (Coulomb, 1773) and the Mohr's failure theory (Mohr, 1900). As illustrated in Figure 2.1, the Mohr-Coulomb failure criterion refers to the linear envelope derived from the plotting of the shear strength of a given material against the normal stress that is applied to it. Such a relationship is mathematically expressed as follows:

$$\tau = \sigma \tan(\varphi) + c \quad (2.1)$$

where τ is the shear stress on the shear failure plane, namely the shear strength; σ is the normal stress acting on the failure plane; $\tan(\varphi)$ is the friction factor and its value is expressed as the slope of the failure envelope, and c is defined as the shear strength at the zero normal stress on the failure plane, which is shown in Figure 2.1 as the intercept on the ordinate.

In Eq. (2.1), c is independent of σ , which is also known as cohesion, and φ is the internal friction angle. $\sigma \cdot \tan(\varphi)$ is the frictional strength and its magnitude is proportional to the normal stress, σ . When the above relationship between shear strength (τ) and normal stress (σ) is satisfied, failure will occur.

2.1.2 Factors influencing the strength of sandy soils

The strength parameters, c and φ , are usually considered as constant under the same testing conditions for the same type of soil. They can be determined through laboratory tests, such as the direct shear (Fannin et al., 2005, Nam et al., 2011), simple shear, triaxial compression (Shi

et al., 2010), or triaxial extension tests. However, their values can vary significantly when different testing methods are used.

2.1.2.1 Cohesion

Cohesion is the soil shear strength in the absence of any effective stress, which is usually generated through interparticle physicochemical forces and interlocking (Lu et al., 2009). Factors contributing to physicochemical forces mainly include cementation from chemical compounds (e.g. carbonate, alumina and silica), electrostatic attraction and electromagnetic attraction (van der Waals force), primary valence bonding and adhesion (Mitchell and Soga, 2005, Lu and Likos, 2006). In addition, the capillary force sometimes emerges as a result of the presence of gas-liquid interfaces and causes cohesion for variably saturated granular materials. The aforementioned physicochemical and capillary forces are collectively referred to as suction stress (Lu and Likos, 2006). Most of the suction stresses are noticeable in fine granular materials such as clay (Van Olphen, 1964, Lu et al., 2007). The interlocking resistance refers to the restraining effect of adjacent particles on relative movement caused by the uneven particle surface morphology (Rowe, 1954).

Regarding the cohesionless granular material, it is generally accepted that sandy soil has no cohesive strength. However, numerous experimental results in geotechnics have shown that sand specimens could have certain values of cohesion due to particle interlocking, which is defined as the “apparent cohesion”. By conducting large-scale direct shear tests, Wang et al. (2017b) concluded that the apparent cohesion of calcareous sands is larger than that of quartz sands, which can be attributed to their angular and elongated particle shapes. Therefore, the cohesion of sandy soil is significantly influenced by particle morphology.

2.1.2.2 Internal friction angle

The internal friction angle holds a macroscopic physical significance with regards to the resistance exhibited by granular materials towards the shear deformation. It represents the maximum angle at which a granular material can maintain its stability and resist sliding when subjected to shear stress (Holtz et al., 1981). A higher internal friction angle indicates a greater resistance to shear deformation, implying that the soil mass can withstand larger shear stresses before it starts to deform or fail. At the micro level, the internal friction angle characterizes the

resistance to relative motion between individual soil particles. When shear stress is applied to a granular material, particles interact with each other through friction and interlocking.

The internal friction angle quantifies the efficiency of these interparticle forces in transmitting and resisting shear stresses, thereby influencing the overall behaviour and stability of the soil (Terzaghi and Peck, 1948). It involves relative sliding between soil particles, and its physical process includes the sliding friction caused by interparticle sliding and the interlocking. The sliding frictional resistance is mainly influenced by surface roughness and surface adsorption. The particle surface roughness is significantly impacted by the presence of asperities and depressions. Especially for particles with an extremely irregular shape, which increases the interparticle friction considerably. The effect of surface adsorption is small compared to that of surface roughness. For a given granular material, the value of its sliding friction angle is basically constant. For example, for saturated quartz, the value is between 22° and 24.5° (Jang et al., 2018).

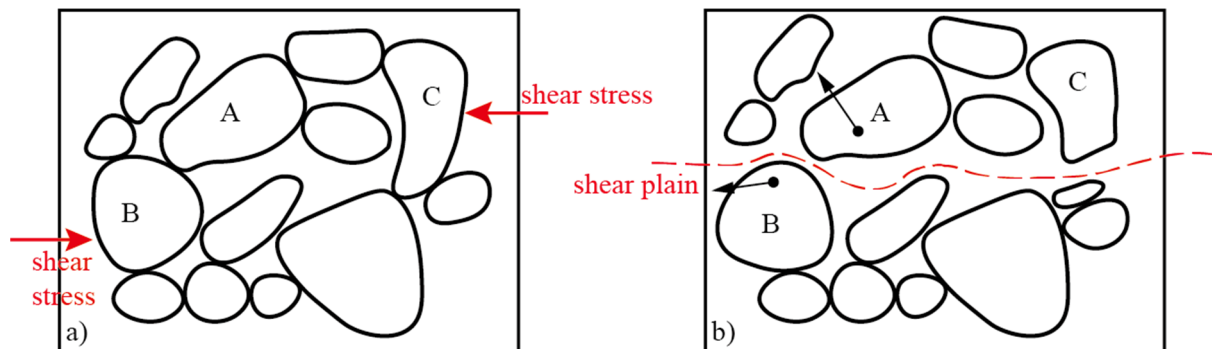


Figure 2.2. a) interlocked soil particles; b) the occurrence of dilatancy during shear failure.

Interlocking friction refers to the restraining effect of adjacent particles on relative particle movement. Figure 2.2(a) shows a typical arrangement of interlocked particles. When shear failure occurs along a certain shear plane in the soil, the interlocked particles must be lifted from the original position (particle A in Figure 2.2(b)), to pass the adjacent particles (particle B), or be cut at the sharp angle (particle C). In short, the original interlocking state must be destroyed first, which is generally manifested as volume expansion, namely the so-called phenomenon of soil dilation, before the shear failure can happen. The term “dilatancy” was first named by Reynolds (1885). He observed that the looser sands contracted, while the denser specimens expanded during shearing induced failure. Dilatancy will consume part of the energy,

which needs to be compensated by the work done by the shear stress, which is manifested as an increase in the internal friction angle. The denser the soil and the smaller the roundness is, the stronger the interlocking effect can be, and the greater the internal friction angle would be. In addition, the particles in the soil are rearranged during shearing, which also consumes or releases a certain amount of energy and affects the internal friction angle.

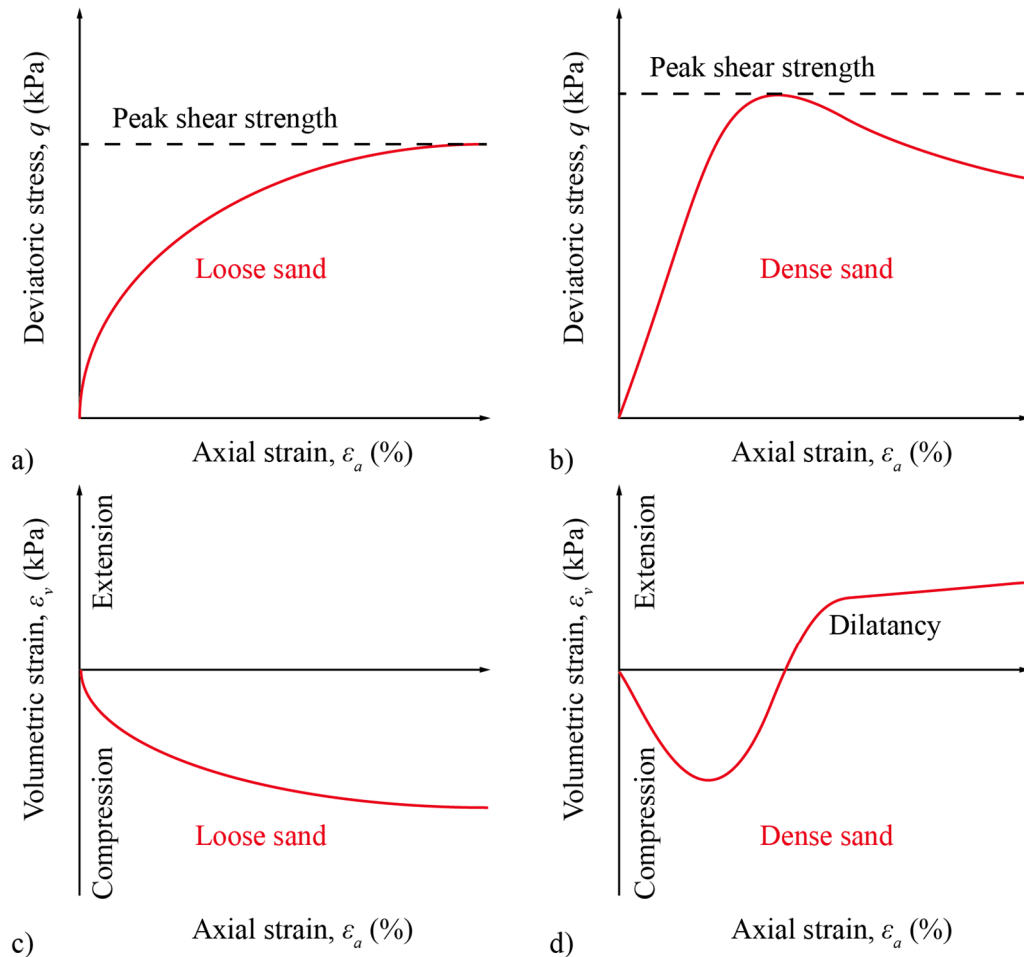


Figure 2.3. Typical deviatoric stress-axial strain, and volumetric strain-axial strain relationships for loose sands (a, c); dense sands (b, d) in consolidated drained triaxial compression tests.

Figure 2.3(a) and (b) present the deviatoric stress-axial strain relationships of loose and dense sand samples, respectively. As shown in Figure 2.3(a), the deviatoric stress of the loose specimen increases at a decreasing rate with the increase of the axial strain, eventually peaking at a relatively large axial strain. The behaviour observed in loose sands is referred to as strain hardening (Cuccovillo and Coop, 1999, Zhang et al., 2021). However, for dense sand samples, its deviatoric stress (presented in Figure 2.3(b)) experiences a rapid increase, reaching a significantly higher peak value, and then it starts to decrease gradually, exhibiting strain

softening (Wood and Belkheir, 1994). The reason for this is that the particles within the dense specimen are already in close contact with each other at the beginning of the shearing, forming a more stable force chain network to resist the onset of shear deformation. Before reaching the peak shear strength, the particles achieve complete interlocking with each other by continuously adjusting their positions (particle sliding and particle rearrangement). As shearing continues, the particle breakage gradually begins to occur, causing a reduction in the strength of the specimen and eventually reaching the residual strength.

Figure 2.3(c) and (d) present the volumetric strain-axial strain relationships of loose and dense sand samples, respectively. As shown in Figure 2.3(c), the volumetric strain of the loose specimen increases gradually with the increase of the axial strain, indicating that the volume of the specimen is decreasing due to shear contraction (Atkinson, 1993). As illustrated in Figure 2.3(d), the dense sand sample shows a shear contraction during the initial phase of shearing, followed by shear dilatancy (Yang et al., 2022). This can be attributed to the interlocking particle state when densely compacted. Particles along the shear plane have to climb over adjacent particles (lever effect) as shown in Figure 2.4(b), leading to a bulk expansion of the soil assembly, i.e., the occurrence of dilatancy (Siang et al., 2013). This is the reason why dense sands have a peak shear stress.

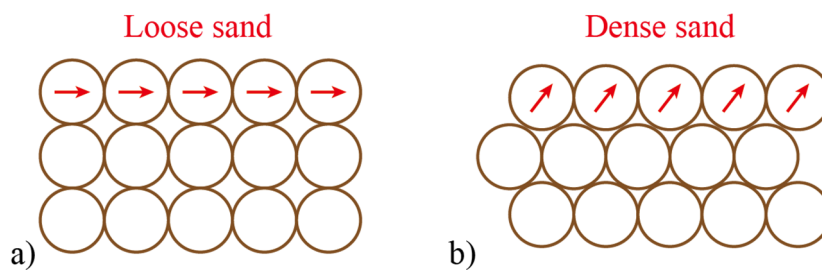


Figure 2.4. Schematic diagram of the positional rearrangement of the a) loose; and b) dense sand particles during shearing.

2.2 Influence of initial relative density on soil strength

From the above analysis, it is clear that the initial relative density (i.e. loose or dense state) has a significant effect on the strength and deformation of sandy soils (Jin et al., 2017, Wu et al., 2019). In real engineering practices, the average in-place relative density of cohesionless soils should be at least 0.85 for compaction of the drainage or filter layers of dams (US Army

Corps of Engineers, 2004). In addition, extensive laboratory experiments and numerical studies have been carried out to investigate the role of relative density on soil responses (Yao et al., 2008, Tsegaye and Benz, 2014, Amirpour Harehdasht et al., 2017, Hanley et al., 2018).

2.2.1 Influence of initial relative density on the consolidation of sandy soil

The initial relative density, as a key state parameter, has a significant impact on the compressive behaviour of coarse-grained soils. It indicates the average number of interparticle contact points per particle, which governs the distribution and magnitude of contact stresses within the soil matrix (Zheng et al., 2017). A higher relative density corresponds to an increased number of contact points, enhancing the interparticle friction and resistance to deformation (Dunlop et al., 2003). Furthermore, this parameter reflects the availability of void spaces, into which particles may shift or embed, influencing the material's ability to compact under load and its overall compressibility.

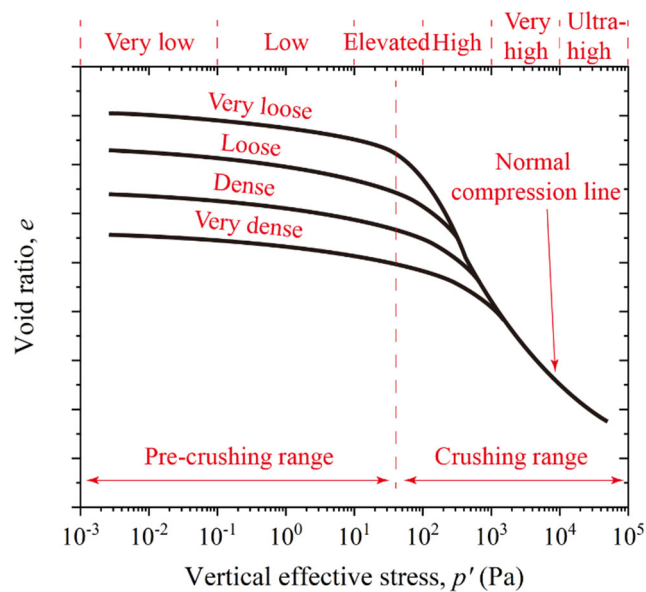


Figure 2.5. Conceptual interpretation of 1-D compression for cohesionless soils (modified after Vesic and Clough (1968)).

As early as 1968, the idealised one-dimensional (1-D) compressive behaviour of cohesionless sand particles with different initial relative densities in a e - $\log(p')$ plot was proposed by Vesic and Clough (1968). As depicted in Figure 2.5, the compression curve can be delineated into two distinct ranges: the pre-crushing range and the crushing range. In the pre-crushing range, where particle breakage has not yet occurred, the compressibility of the

sand specimens remains relatively low. However, as the vertical stress increases significantly, particle breakage begins to occur, leading to a convergence of compression lines for specimens of different initial relative densities. The result of a unique normal compression line reflects the characteristic response of the sandy soil under high stress conditions.

In the literature, dedicated studies solely focusing on the influence of initial relative density on the 1-D compression behaviour of sandy soils are still limited. Several investigations incorporate this state parameter are within broader research area on the compressive properties of sandy soils. A series of traditional one-dimensional consolidation tests were conducted by Uygur and Doven (2006) on dry sandy soil with varying initial relative densities ranging from 0.14 to 0.85. The compression lines of the specimens with different initial relative densities did not show a tendency to converge for the vertical pressures of up to 14 MPa. As the sand particles are rich in quartz in addition to calcite, the vertical pressures applied in the experiment are not high enough to reach the strength of the particles. The existing result illustrated that the compression index decreases almost linearly with increasing relative densities.

By performing oedometer tests under the vertical pressure up to 2 MPa on calcareous sands with varying initial relative densities (e.g. 0.2, 0.4, and 0.6), Karimpour-Fard et al. (2021) concluded that the compression index increased with the vertical stress. However, the effect of initial relative density on the compression index is more difficult to be observed from the results presented. Xiao et al. (2017) conducted a series of 1-D consolidation tests on carbonate sands with six different initial relative densities ranging from 0.2 to 0.85, subjected to vertical pressures up to 3.2 MPa. Although the applied vertical pressure was insufficient to observe a convergence in the compression curves for specimens with varying initial relative densities, the study revealed a clear trend that the rate of volumetric deformation decreased as the increase of initial relative density. In Murison (2023)'s study on the impact of oedometer sample aspect ratio on the 1-D compression behaviour of silica sands, two distinct initial relative densities were examined under the maximum vertical effective stress of 1.5 MPa. The initial void ratio for loose and medium-dense specimen is 0.92-0.93, and 0.78-0.79, respectively. The results revealed that the compression and rebound lines of the loose specimens were almost linear, while the compression lines for the medium-dense specimens exhibited an accelerated decreasing trend.

By conducting the oedometer tests under the maximum vertical pressure of no more than 2 MPa on both soaked and unsoaked (dry) poorly graded dune sands with five different initial relative densities (ranging from 0.1 to 0.9), Al-Taie and Al-Shakarchi (2017) found that both the axial strain and collapse potential decreased with the increase of relative density. Similarly, Ovalle et al. (2015) performed a series of 1-D oedometer tests on loose and dense angular sands at dry, saturated, or flooded conditions under the vertical pressures up to 2.1 MPa, and found that in the e - $\log(p')$ plot, the compression line of the dense sands lies below that of the loose sands. As vertical pressure increases, the compression curves for sands with varying relative densities tend to converge.

To investigate the compressibility of sands of various geologic origins at pre-crushing stress levels, a series of oedometer tests under the vertical stress up to 0.3 MPa were conducted by Zheng et al. (2017) at dry conditions. The specimens were compared in loose (D_r is about 0.1), medium dense (D_r is about 0.5), and dense (D_r is about 0.9) conditions to analyse the effect of relative density on soil responses. The results indicated that the slope of the compression line in the e - $\log(p')$ plot (commonly represented by the compression index) decreased as the initial relative density increased. The same findings were also obtained by Lee et al. (2020) by performing oedometer tests under the vertical stress up to 0.64 MPa on dense ($D_r = 0.8$) and loose ($D_r = 0.4$) silica sands. Furthermore, a linear relationship was observed between the compression index and $(1 - D_r/2)$, suggesting a direct correlation between the compressibility of the material and its compactness.

In the study conducted by Gao et al. (2021), the vertical stresses up to 35 MPa were applied to characterize the compressibility of sandy loess samples with initial void ratios ranging from 0.736 to 0.803. Although the presentation of results is somewhat unclear due to the overlapping compression lines in the same graph, it is evident that, at higher vertical pressures, the compression lines of sandy loess with varying relative densities eventually became asymptotic, reaching a unique normal compression line (NCL). For a specific combination of specimen volume and normal loading pressure, the compression lines would converge to a unique NCL which is influenced by the initial degree of specimen densification. This is primarily due to its effect on the coordination number (CN)—the number of inter-particle contacts (Shipton and Coop, 2012). For clean quartz sands, it is typical for the NCL to be reached at specific volumes

within the range of 1.3 to 1.6, and at stress levels generally between 10 and 100 MPa (Mesri and Vardhanabhuti, 2009). However, for weaker sands with higher specific volumes, the NCLs can be found under significantly lower stress levels. For instance, Coop and Lee (1992) reported that the Dog's Bay carbonate sands reached their NCLs at specific volumes between 2.2 and 2.6, under a much lower stress in the range of 1 to 3 MPa.

In addition to laboratory tests, numerical simulations have also been conducted to explore the influence of varying relative densities on the compressive behaviour of sandy soils. The finite element model was used by Aldefae (2016) to predict the 1-D compressive behaviour of dense (D_r is about 0.25) and loose (D_r is about 0.75) silica sands at the normal stress up to 0.6 MPa. A comparison between the simulation outcomes and indoor experimental results reveals that, while the simulations effectively captured the general trends by the compression curves for specimens of varying relative densities, discrepancies were observed. Specifically, the simulations tended to underestimate the compression behaviour of dense specimens, whereas they overestimated the compressive response of loosely packed specimens.

2.2.2 Influence of initial relative density on strength of sandy soil

The influence of initial relative density on the relationship between deviatoric stress and axial strain has been investigated by various researchers. By conducting triaxial tests on poorly graded (SP) unreinforced and fibre-reinforced river sands of different D_r (0.35, 0.65 and 0.85) under the confining pressure ranging from 100 to 400 kPa, Patel and Singh (2019) concluded that both the deviatoric stress (initial stiffness and peak deviatoric stress) and dilation increased with D_r . In contrast, the axial strain at failure exhibited an inverse relationship, decreasing with the increasing D_r . Consistent response in terms of volumetric strain behaviour was also observed by Mashiri et al. (2015) by performing monotonic drained triaxial tests on sand-tyre chip mixtures with varying D_r (0.25, 0.5 and 0.75). The axial strain at failure decreased with increasing D_r was also stated by Maeda and Miura (1999) by performing drained triaxial compression tests on natural and reconstituted sand particles with varying D_r (0.5, 0.7 and 0.9). In addition, they also found that the normalized secant modulus (shear stiffness), and volumetric strain at maximum volume contract (dilation) increased with D_r .

By performing triaxial compression tests on uniform quartz sands with D_r of 0.5 and 0.7,

Hamidi and Hooresfand (2013) concluded that both the peak deviatoric stress and deviatoric stress at failure increased with D_r . The relative density also influenced the energy absorption characteristics that particles with higher D_r could absorb more energy. In addition, they claimed that the brittleness index (I_B) proposed by Consoli et al. (1998) increased with D_r . The brittleness index is defined as:

$$I_B = \frac{q_{max}}{q_{res}} - 1 \quad (2.2)$$

where q_{max} and q_{res} are the peak and residual deviatoric stress, respectively.

The influence of initial relative density on strength and volumetric strain-axial strain behaviour has been reported by various researchers. By conducting CD triaxial tests on dense ($D_r = 0.9$) and loose ($D_r = 0.7$) calcareous sands under effective confining pressure up to 800 kPa, Zhang et al. (2023) concluded that only strain softening behaviour can be observed in all tests, and the denser specimen exhibited more obvious strain softening behaviour. In addition, dense specimen showed higher peak deviatoric stress, but smaller strain at failure. Vaid et al. (1990) investigated the resistance to sand liquefaction by performing a series of undrained cyclic triaxial tests on river sands with varying relative densities. The results showed that the poorly graded sands with relative densities ranging from the loosest state to a value of about 0.43 exhibited purely contractive deformation without any dilation. In contrast, the well-graded sands demonstrated a dilative response under similar conditions.

As the relative density increases, there is a corresponding increase in the initial elastic modulus and peak friction angle, while the volumetric strain decreases (Ueng and Chen, 2000). The linear relationship between peak friction angle and relative densities of different types of sands was first proposed by Burmister (1948). Once the relative densities of sand particles are known, their peak friction angle can be approximately estimated by the plots shown in Figure 2.6. However, this method has clear limitations: firstly, it is restricted to specific types of soil particles. Secondly, it is only valid for triaxial tests conducted under confining pressures in the range of 50 to 350 kPa, or for direct shear tests under vertical pressures between 80 and 400 kPa. These constraints limit the generalization of the method to a broader spectrum of soil conditions and stress scenarios.

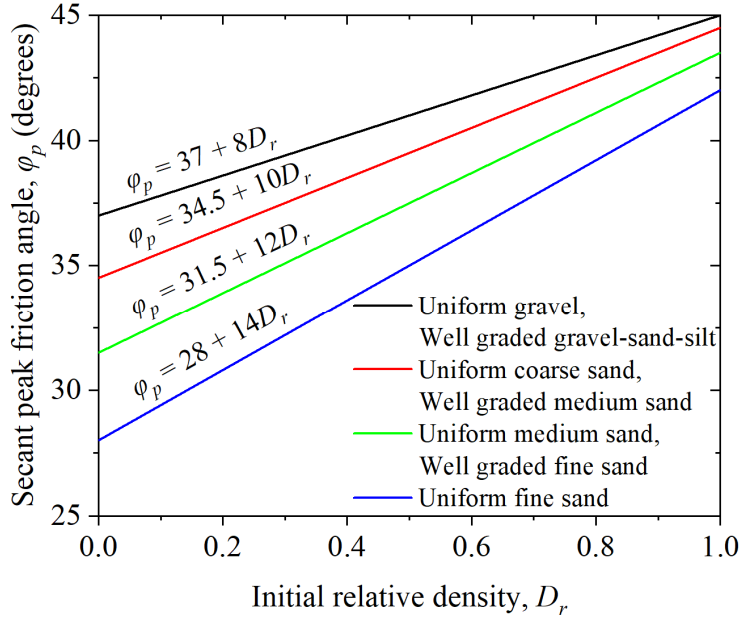


Figure 2.6. Relationship between peak friction angle and relative density (modified after Jamiolkowski et al. (2003)).

A linear relationship between $\log(\tan \phi_p)$ and D_r was presented by Maeda and Miura (1999), based on which, an index $R_D(\tan \phi_p)$ was proposed:

$$R_D(\tan \phi_p) = \frac{\Delta \log \tan \phi_p}{\Delta D_r} \quad (2.3)$$

By analysing the relationship between $R_D(\tan \phi_p)$ and angularity introduced by Lees (1964), Maeda and Miura (1999) concluded that sand particles with high angularity exhibited a significant, but not always distinct, dependency of shear strength on D_r . A positive correlation between $R_D(\tan \phi_p)$ and void ratio extent ($e_{max} - e_{min}$) was also presented, suggesting that the void ratio could serve as a useful parameter for estimating $R_D(\tan \phi_p)$ in engineering applications.

By conducting a series of ring shear tests on silica sands with varying relative densities from 0.29 to 0.77 under the effective normal stress ranging from 98 to 392 kPa, Igwe et al. (2012) concluded that the peak and residual strengths of soil increased with the relative density. The same conclusion was also obtained by Lambe and Whitman (1991), Thevanayagam et al. (1997), and Thevanayagam (1998) who claimed that the more dense granular specimens have higher shear strength. Although Igwe et al. (2012) applied a linear fit to the data, they did not include the corresponding R^2 values, which would have provided a quantitative measure of how well the linear model could fit the data.

The R^2 value is known as the coefficient of determination (COD), it is a statistic parameter

extensively utilized in the realm of statistical models, primarily aimed at forecasting future outcomes or evaluating hypotheses predicated on related variables. It quantifies the proportion of the variation in the dependent variable that is predictable from the independent variable(s), thereby indicating how well observed outcomes are replicated by the model (Carpenter, 1960, Glantz et al., 1990, Draper and Smith, 1998). Typically, the R^2 value ranges from 0 to 1, provides insight into the model's goodness of fit (Casella and Berger, 2024). Specifically, in regression analysis, R^2 assesses the degree of alignment between the predicted values and the actual data points, with an R^2 value of 1 signifying a perfect fit. For a dataset consisting of values denoted as g_1, g_2, \dots, g_s (collectively referred to as g_i), each value is associated with a corresponding fitted (modelled or predicted) value f_i . The residuals are defined as:

$$e_i = g_i - f_i \quad (2.4)$$

The variability within the dataset can be quantified using two sums of squares:

$$SS_{res} = \sum_i e_i^2 \quad (2.5)$$

$$SS_{tot} = \sum_i (g_i - \bar{g})^2 \quad (2.6)$$

where SS_{res} is the residual sum of squares; SS_{tot} is the total sum of squares, which is proportional to the variance of the data; and \bar{g} is the mean of the dataset. Then, the coefficient of determination (R^2) is defined as:

$$R^2 = 1 - \frac{SS_{res}}{SS_{tot}} \quad (2.7)$$

By performing triaxial compression tests under a confining pressure of 100 kPa on Jumunjin standard sands with varying initial relative densities, Park et al. (2008) found out that only specimen at very dense state exhibited strain softening behaviour. In their study, the categorisation of different relative densities follows the classification method proposed by Skempton (1986) as shown in Table 2.1. The relationship between peak friction angle (φ_p) and relative density was expressed by the following quadratic equation with R^2 of 0.998:

$$\varphi_p = 0.0014(D_r)^2 - 0.0159(D_r) + 32.151 \quad (2.8)$$

This finding deviates from the previously established trend, as the peak friction angle does not exhibit a linear relationship with increasing relative densities but instead demonstrates an

accelerated growth.

Table 2.1. Solid classification by relative densities.

| Relative density | < 0.15 | 0.15-0.35 | 0.35-0.65 | 0.65-0.85 | 0.85-1 |
|------------------|------------|-----------|-----------|-----------|------------|
| Description | very loose | loose | medium | dense | very dense |

Chen and Zhang (2016) reported that an increase in D_r can lead to the increase of shear strength and dilation based on the consolidated drained (CD) triaxial tests on crushed granite gravel-clayey sand mixtures of varying D_r (0.3, 0.5, 0.7 and 0.9). The results also showed that the difference between the peak and residual friction angles showed a linear positive correlation with both D_r and the dilatancy angle, although the R^2 values were not presented. The dilatancy angle was calculated by using the following equation proposed by Vaid and Sasitharan (1992) based on Bolton (1986).

$$\psi = \sin^{-1} \left[\frac{-3.3(d\varepsilon_V/d\varepsilon_a)_p}{6.7 - 3.3(d\varepsilon_V/d\varepsilon_a)_p} \right] \quad (2.9)$$

where ψ is the dilatancy angle; $d\varepsilon_V$ and $d\varepsilon_a$ represent the incremental of volumetric and axial strains, respectively; the subscript p denotes the peak state.

Several studies in the literature have documented the internal friction angle and apparent cohesion of sandy soil specimens across varying initial relative densities. Patel and Singh (2019) found that both the internal friction angle and cohesion increased with D_r , and their values for poorly graded fine (0.02-2 mm) river sands with varying D_r (0.35, 0.65 and 0.85) are 32.7°, 35°, 37°, and 11, 18, 24 kPa, respectively. Zhang et al. (2023) reported that the internal friction angle and apparent cohesion of loose ($D_r = 0.7$) and dense ($D_r = 0.9$) non-uniform calcareous sands (average particle size = 0.43 mm) are 41.88°, 39.81°, and 29.67, 81.73 kPa, respectively.

Despite that the initial relative density have a considerable effect on the shear strength of sandy soil, the most fundamental factor affecting the shear strength of sandy soil is still particle interlocking. Particle interlocking is not only closely tied to but is greatly influenced by particle morphology. Under a high compressive or confining pressure exceeding the material strength, partially or fully particle breakage will occur (Ovalle et al., 2015), which will change part or all of the morphological characteristics of the particles and particle size distribution, which in turn has a significant effect on their mechanical behaviours. Therefore, the investigation of the

influence of particle morphology and particle breakage on the shear strength of sandy soil is of utmost importance.

2.3 Particle morphology and its influence on the strength of sandy soil

When the external loading stress does not exceed the strength of the sand particles, it is universally accepted that the uncemented particles interact with each other by interlocking and surface friction during the shearing process. As an important parameter describing particle geometric characteristics, the particle morphology (i.e., particle size, shape, form, sphericity, and surface roughness) carries significant weight in determining the development of these interactions. Different morphological features have dramatic impacts on the particle contact relationship, geometrical arrangement and other fabric (microstructure) characteristics (Estrada et al., 2011, Azéma et al., 2013), which in turn plays a vital role in the macroscopic properties of the granular material such as internal friction angle, dilatancy and non-coaxiality (Yang et al., 2015, Alshibli and Cil, 2018). Therefore, particle morphology is an important factor to be considered when studying the fundamental mechanical properties of sandy soil.

2.3.1 Definition and determination of particle morphology

The definition of “morphology” is “*the study of forms or shapes*” in various discipline areas. According to the Cambridge Dictionary (2023), the term “shape” is defined as “*the particular physical form or appearance of something*”. Every tangible object possesses a visual appearance that represents its shape in three dimensions. The final shape of an object is determined by the mechanical processes it undergoes from its initial formation to the current state. Thus, researchers from various disciplines such as Civil Engineering, Powder Industry, Biology, and Geology have shown great interest in quantifying particle shapes (Tunwal, 2018). This has enabled them to compare different objects based on their physical forms.

The topic of particle morphology was first introduced in the field of geology before it gained attention in geotechnical engineering. Regardless of the type or material, the morphology of particles can reflect the material composition, formation of grains, and how they were released from the mineral matrix. It also provides insights into the transportation and depositional environments (Cho et al., 2006). For example, the characteristics of sandy soil

particles formed by sedimentation depend on the source of the sediment and the deposition conditions, whereas residual soils typically exhibit a diverse range of mineral compositions and grading characteristics as they have not undergone the transportation and sorting processes. Alluvial or beach-deposited quartz soil particles gradually become rounded and smooth with the increase of transport time and distance (Ideozu and Ikoru, 2015), while some soft particles such as volcanic ash, show high angularity due to particle breakage during transportation (Dellino et al., 2012). Accordingly, the investigation of particle morphology is crucial in enhancing researchers' comprehension of the generation and development of wear particles in civil engineering discipline (Büttner et al., 2006, Manga et al., 2011), as well as to forecast the settlement or deformation of the particle assembly (Alfano et al., 2011, Bagheri et al., 2015).

The formation and modification of the morphological characteristics of particles are closely related to the mechanical and chemical process to which they are subjected to once they are detached from the ground matrix (Rahaman, 2017). When the particle size is less than 50 μm , the chemical action is the primary factor shaping the particle morphology. Conversely, for particles exceeding 400 μm in size, the mechanical process becomes the dominant influencing factor. As early as in the 1900's, it was recognised that particle morphology plays a critical role in influencing soil behaviour. Pentland (1927), Wadell (1932) and Riley (1941) were among the first few researchers to propose methods for describing particle form and roundness. Studies have shown that particle morphology affects the engineering properties of gravels (Mora and Kwan, 2000) and soils (Santamarina and Cho, 2004), including the internal friction angle (Shinohara et al., 2000), void ratio (Rousé et al., 2008), and permeability (Witt and Brauns, 1983). Furthermore, particle morphology has been incorporated in geotechnical guidelines such as soil classification in Eurocode 7 (Bond et al., 2013), "Tests for geometrical properties of aggregates" in British Standard: BS EN 933-4:2008 (British Standards Institution, 2008), "Standard Practice for Description and Identification of Soils (Visual-Manual Procedures)" in American Society for Testing and Materials (ASTM) D2488-17e1 (ASTM, 2018).

2.3.1.1 Hand measurement

The technical methods for determining particle morphology include hand measurement, chart comparison, sieve analysis, and image analysis. In the early days of morphological

characterization, it was mainly performed manually and with the help of simple instruments. The “convexity gauge”, as shown in Figure 2.7(a), originally designed for opticians to measure lens curvature, can also be used for determining the curvatures in pebble corners (Wentworth, 1923). As presented in Figure 2.7(b), an apparatus was devised by Szadeczky-Kardoss (1933) to trace the outline, and quantitatively determine the percentage of concave, convex, and plane of sedimentary particles and fragments with the particle size between 2 and 100 mm (Krumbein and Pettijohn, 1938). The “sliding rod caliper”, as illustrated in Figure 2.7(c), was developed by Krumbein (1941) to measure the particle length in different directions. In addition, a “camera lucida” was employed by Wadell (1935) to project the contour of quartz particles onto a circle scale presented in Figure 2.7(d), allowing for the determination of sphericity and roundness. However, it is evident that when the aforementioned method is employed, only one particle can be measured at a time, resulting in a significant reduction in measurement efficiency. Furthermore, the manual measurements yield results that are inevitably influenced by a substantial bias, thereby compromising the reproducibility of the findings.

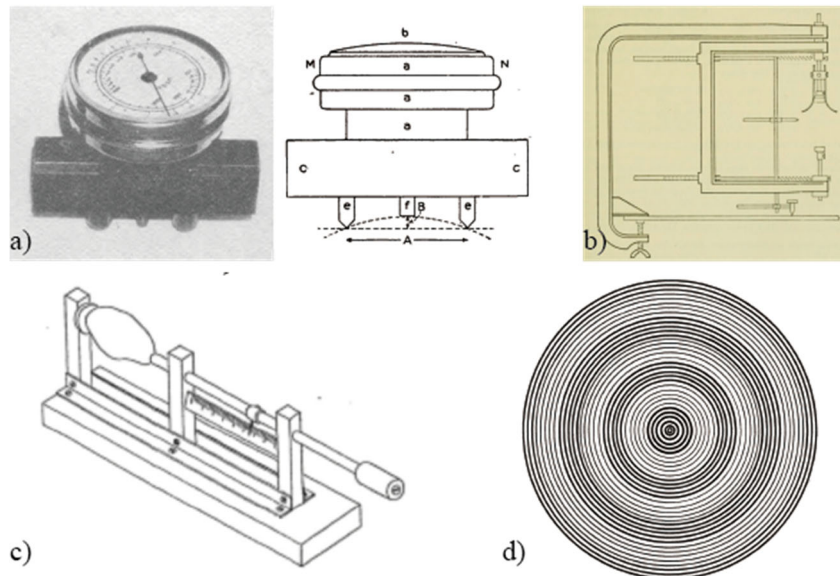


Figure 2.7. a) “convexity gage” used by Wentworth (1923) to quantify the curvature of particle corners; b) apparatus devised by Szadeczky-Kardoss (1933) to trace the particle outline; c) “sliding rod caliper” developed by Krumbein (1941) to measure the particle length in different directions; d) circle scale employed by Wadell (1935) to determine sphericity and roundness of quartz particles.

2.3.1.2 Chart comparison

Visual charts were also created at an earlier stage in order to reduce the time required for

manual measurement (Krumbein, 1941, Aschenbrenner, 1956). A comparison chart for roundness shown in Figure 2.8 was developed by Krumbein (1941). Visual representations of various pebbles with roundness categorized in nine classes determined by using the approach presented by Wadell (1932) are displayed. However, due to the proximity of the roundness values, it is often challenging to determine which roundness value should be assigned to a specific particle (Blatt, 1973, Blatt, 1982).

A qualitative chart shown in Figure 2.9 was proposed by Powers (1953) to characterise particle sphericity and roundness. Based on the photographs of particles, another category, i.e. “very angular” was added to the classification system defined by Russell and Taylor (1937) and Pettijohn (1949), making a total of six grade terms of roundness of particles from very angular to well rounded. In addition, each roundness category is depicted using two particles, one exhibiting a relatively high level of sphericity, and one displaying a lower level of sphericity. Subsequently, as a concern for the errors that inevitably arise when subjective human judgements are made, Folk (1955) validated this method by concluding that the error in determining sphericity by chart comparison is negligible. However, when it came to roundness, he suggested that additional in-depth investigation was still required because of the significant variability observed in his research.

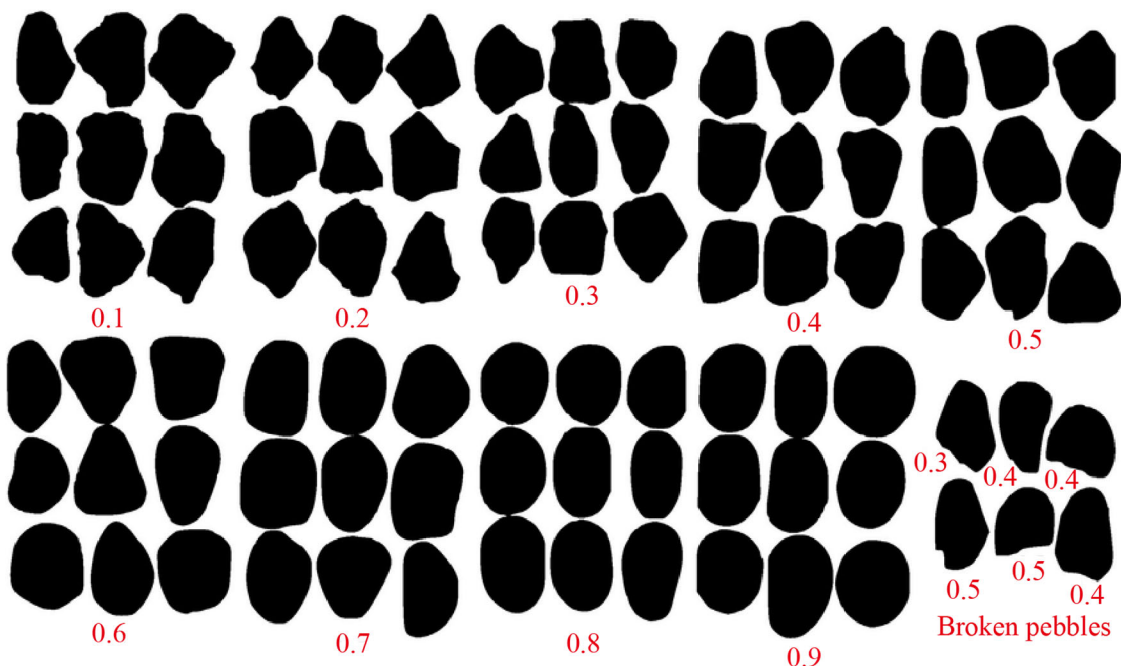


Figure 2.8. Comparison chart developed by Krumbein (1941) for visual determination of roundness.

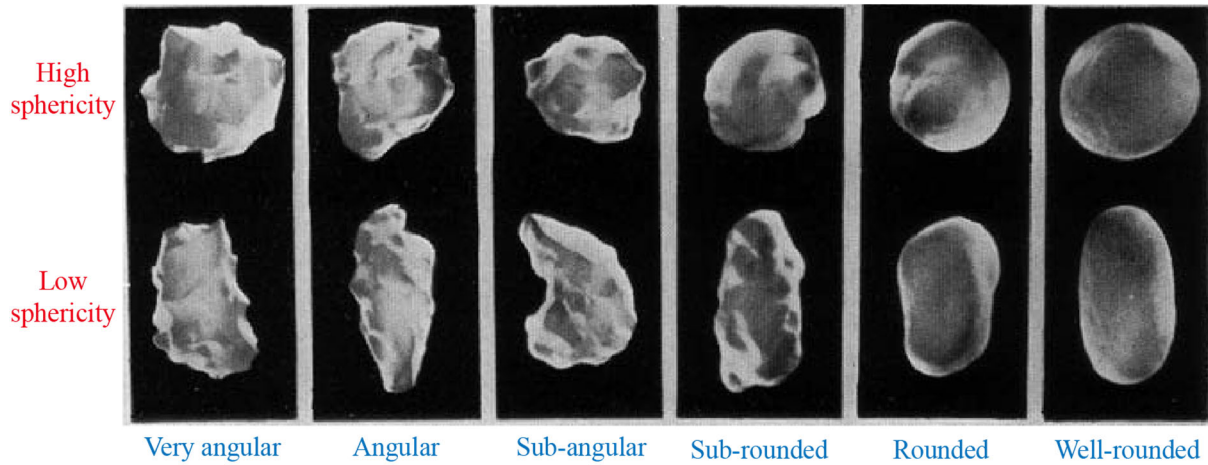


Figure 2.9 Visual chart proposed by Powers (1953) to characterise particle sphericity and roundness.

Another comparison chart as shown in Figure 2.10 was introduced by Krumbein and Sloss (1963) to characterise both particle sphericity and roundness. The simultaneous presentation of numerical values obtained by using the method proposed by Wadell (1932) makes this method more user-friendly, while greatly reducing human subjectivity in the description.

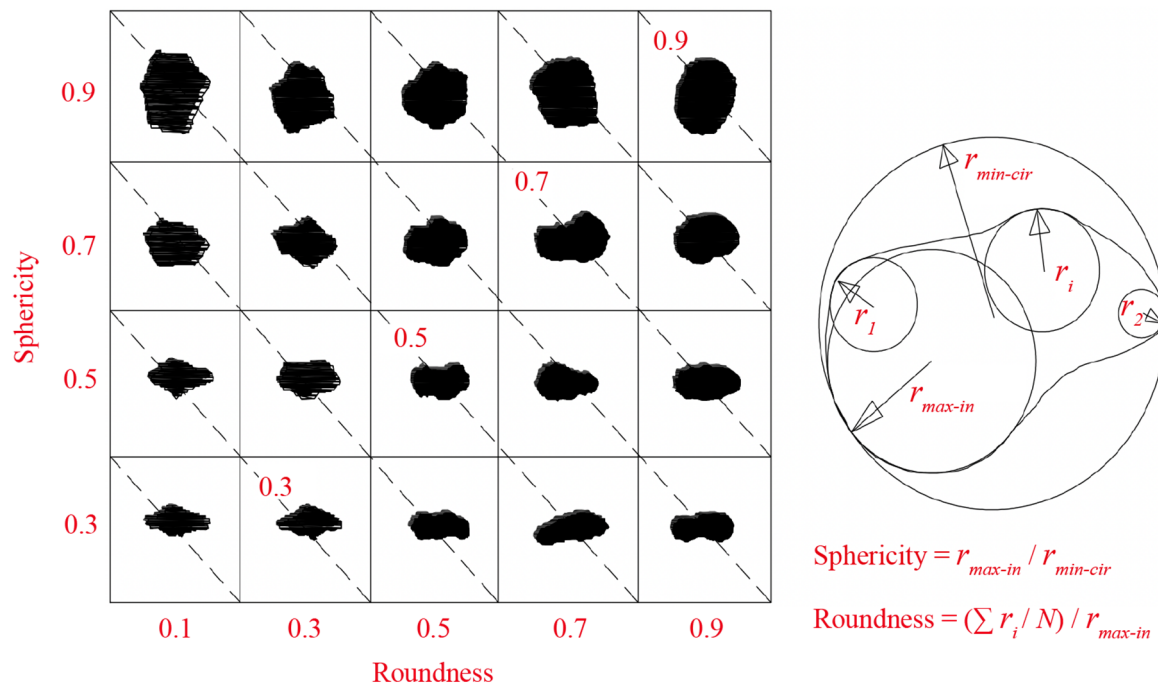


Figure 2.10. Comparison chart proposed by Krumbein and Sloss (1963) to characterise particle sphericity and roundness.

However, the visual chart comparison is achieved through visual examination and subjective evaluation by the individual engineer, which can lead to non-reproducible results. The lack of an objective and quantitative method for characterising particle shape has

significantly hindered the advancement of incorporating particle morphology into geotechnical investigations.

2.3.1.3 Sieve analysis

The traditional sieving analysis, recognized as one of the most commonly employed techniques for determining the particle size distribution (PSD), was also utilized to evaluate the flakiness and elongation index of coarse aggregate particles. A two-step sieving operation is usually required when employing this method. The first sieving separates the particles based on their size fraction, and the average maximum diameter is determined. Bar sieving is then conducted according to BS EN 933-3:2012 (British Standards Institution, 2012) to obtain the shortest axis diameter. Based on the results, the geometrical properties including flakiness and elongation index can be quantified. However, this method is only applicable to aggregates with limited particle size range of 4 to 63 mm, and not to fine materials due to practical constraints (Persson, 1998). Sieving analysis is a method requiring substantial time and cost (Andersson, 2010). Furthermore, the ability of particles to pass through the screen is largely dependent on their morphological characteristics. This dependency leads to marked variations in the average amount of particles with different shapes retained in each size interval (Fernlund, 1998).

2.3.1.4 Image analysis

Despite the inherent inaccuracies caused by the overlapping or partial concealment of the testing particles, the image analysis technology is now prevailing over the other traditional techniques due to its fast speed and automatic execution (Garboczi and Bullard, 2004, Andersson, 2010, Callahan et al., 2012, Heilbronner and Barrett, 2013, Lieberman et al., 2015, Cepuritis et al., 2016, Bales et al., 2017). There are various techniques that can be used to process the particle images, which include the Feret measurement technique, Fourier mathematical technique, fractal dimension, orthogonal image analysis, laser scanning technique, and laser-aided tomography.

The Feret size was computed as the measurement of the distance between two parallel planes that closely bound the particle and keep it perpendicular to the planes (Janoo, 1998). Then, the particle length and particle width can be determined as the largest and smallest Feret size obtained in a range of individual particle photos, respectively.

Based on mathematical relations, the Fourier mathematical technique is applied to trace the profile of 2D particles, so that the roughness and textural features of individual particles can be characterised (Schwarcz and Shane, 1969, Dowdeswell, 1982, Thomas et al., 1995, Suzuki et al., 2015). The profile equation used by the (R, θ) Fourier method is as below:

$$R(\theta) = a_0 + \sum_{n=1}^{N_h} (a_n \cos n\theta + b_n \sin n\theta) \quad (2.10)$$

where $R(\theta)$ is the radius at angle θ ; N_h is the total number of harmonics; n is the harmonic number; a_n, b_n are Fourier coefficients giving magnitude and phase for each harmonic.

Accurately determining the centroid of the particle at the beginning of the analysis is crucial, but this can be challenging when dealing with particles with complex shapes. Furthermore, another challenge with this approach arises when dealing with re-entrant angles as shown in Figure 2.11. In such cases, there can be two potential values for $R(\theta)$, which can be problematic when analysing carbonate particles like Dog's Bay sands, which have irregular shapes with numerous concaves (Thomas et al., 1995, Suzuki et al., 2015).

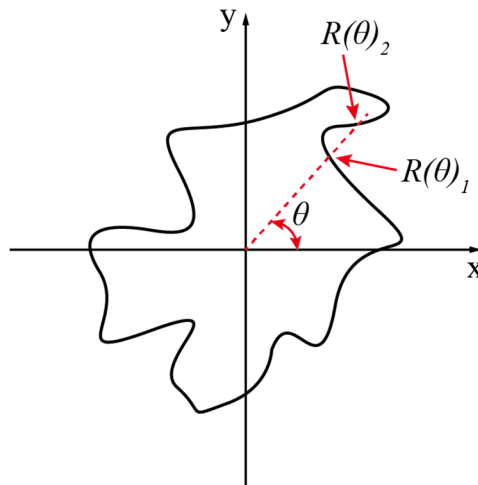


Figure 2.11. Two radiuses acquired at one angle when employing Fourier mathematical technique on particle shape with re-entrant angles.

Based on Richardson's empirical research on coastlines (L.F. Richardson effect) (Kappraff, 1986), Mandelbrot (1983) suggested that a line which appears irregular when examined closely can be defined as a fractal line, and its length can be measured as following:

$$P(\lambda_1) = n_1 \lambda_1^{1-D_R} \quad (2.11)$$

where λ_1 is the unit measurement length; $P(\lambda_1)$ is the polygon perimeter, which equals to the

length of the line or curve based on λ_1 ; n_1 is a proportionality constant, which is equivalent to the actual and indeterminate length of the line; and D_R is the roughness fractal dimension of the curve.

The fractal dimensioning technique was introduced by Hyslip and Vallejo (1997) to quantify both the particle roughness and PSD of granular soils. In the given example as shown in Figure 2.12, the parallel-line method is used in the fractal analysis to measure the polygon perimeter, represented as $P(\lambda_1)$ of individual particles. The measurement step length, denoted as λ_1 , determines the spacing between the parallel lines. The measured $P(\lambda_1)$, will vary depending on the chosen λ_1 .

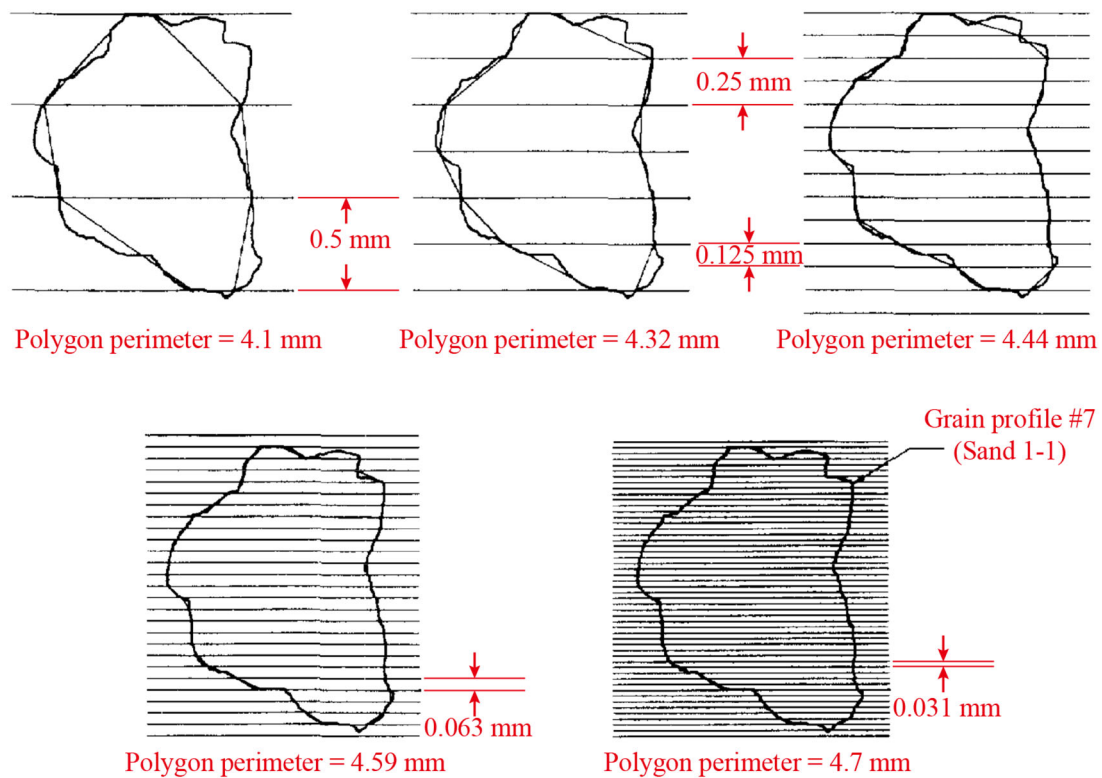


Figure 2.12. The parallel-line method employed in the fractal analysis (modified after Hyslip and Vallejo (1997)).

Orthogonal image analysis method uses two images that are perpendicular to each other to determine the three dimensions of particles (Fernlund, 2005). Testing objects were placed vertically and horizontally on a fluorescent background, and then photographed by a camera located at a height of about 1.5 m directly above them.

As one of the most advanced technological tools to create 3D digital representations, the laser scanning technique is widely applied currently to characterise the morphological features

of particle surface (Lanaro and Tolppanen, 2002). As shown in Figure 2.13(a), the laser sensor emits a narrow strip of light onto the particle surface, creating a "laser plane". Two charge-coupled device (CCD) cameras are employed to obtain particle photos as it intersects with the laser plane. By knowing the position of the reference points fixed on the calibration board, and the location of the cameras in relation to the laser sensor, it is possible to mathematically reconstruct the morphological characteristics of particle for further investigation as presented in Figure 2.13(d).

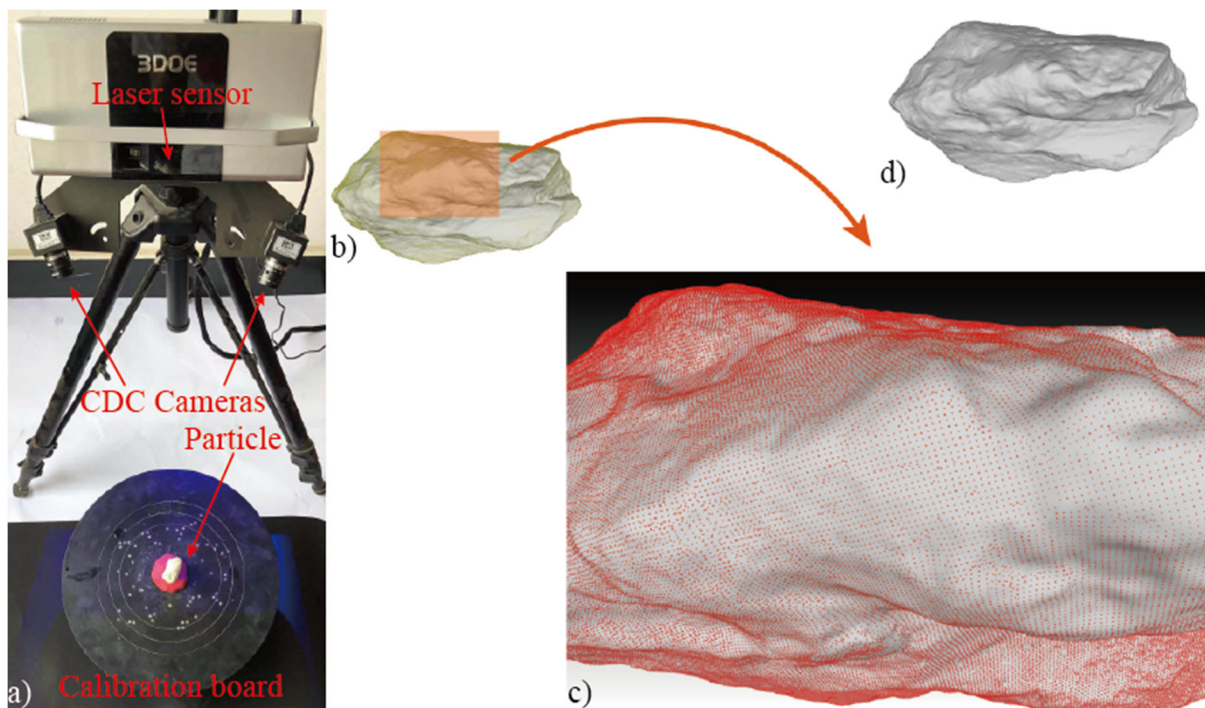


Figure 2.13. a) a PTS-A series (binocular) photographic white light 3D scanner produced by Shenzhen Stereo3D Technology (2023); b) particle surface presented by point cloud; c) local enlarged image of the point cloud; d) reconstructed particle surface (Shen et al., 2020).

In addition, there is another method that also draws on laser technology to obtain morphological information of particles, which is termed as laser-aided tomography (LAT). However, there are specific constraints when using this technique. Specifically, materials to be tested must be immersed in a liquid medium of the same refractive index as the material, and the sample must be exposed to the path of laser light or a certain percentage of light. Additionally, the testing materials must allow the laser or a certain percentage of light to pass through (such as glass grains) (Matsushima et al., 2003, Rodriguez et al., 2013).

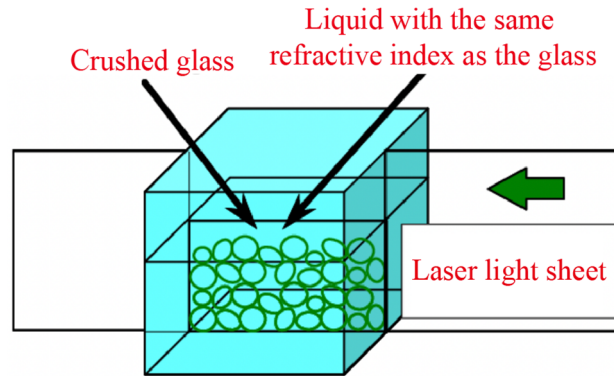


Figure 2.14. Schematic diagram of laser-aided tomography (Matsushima et al., 2003).

However, the application of laser scanning has limitation on the size of the object to be measured. In addition, the accuracy of the outcomes achieved with this technique relies on the resolution of the obtained images (Zeidan et al., 2007). According to Schäfer (2002), there are significant errors associated with the determination of parameters such as particle length based on digital images. These errors can be reduced or eliminated by increasing the resolution, but only suitable for measuring the diameter, not the perimeter of the particles. By employing three different resolutions to measure the same granular material, Johansson and Vall (2011) came to a similar conclusion that there were notable variations in the outcomes related to the measured values of particle perimeter. Therefore, it is important to be cautious when dealing with any calculations on the particle perimeter. Although increasing the equipment resolution can yield more accurate results for the testing object, it can also lead to a substantial increase in the required time and storage capacity. Therefore, it is crucial to configure the device parameters, such as resolution, in accordance with the desired level of fidelity and objectives of the work (Schäfer, 2002).

Furthermore, the vast majority of the image analysis techniques currently available for analysing particle shapes are designed for loose particles (Iwata and Ukai, 2002, Charpentier et al., 2013). The algorithms that are extensively employed at present for automatically identifying and separating particle boundaries in photomicrographs cannot fulfil the task of providing the detailed particle boundary characteristics needed for advanced morphology investigation (Choudhury et al., 2006, Gorsevski et al., 2012, Mingireanov Filho et al., 2013). Therefore, to guarantee the precision of particle morphology quantification results, it is crucial to make multiple attempts using different shape parameters for morphological characterisation

(Blott and Pye, 2008).

2.3.2 Quantification of particle morphology

Particle morphology characterization can be classified as either three-dimensional or two-dimensional. Three-dimensional characterization involves using sophisticated apparatus to scan the particle surface and generate the three-dimensional models. Alternatively, as briefly mentioned in previous sections, two orthogonal images can be employed to demonstrate the three dimensions. However, this method has a limitation on measuring the minimum particle size. Furthermore, it is more challenging to keep particles with irregular shapes in a vertical position, while taking photographs (Fernlund, 2005). Since the two-dimensional morphological characterization only necessitates the utilization of a normal photographic apparatus such as digital camera or microscope to capture particle outlines based on their projections, it is comparatively simple to operate. The projected image is then binarized using digital image processing software such as Matlab or ImageJ based on Fourier analysis, fractal analysis, and other hybrid techniques, which has the capability to present the morphological parameters of particles efficiently and rapidly (Meloy, 1977, Clark, 1987, Bowman et al., 2001).

Nowadays, various parameters are widely applied by researchers (Li et al., 2003, Cho et al., 2006, Arasan et al., 2010) to describe the morphology of soil particles at three scales including the overall particle, local, and micro scale, as shown in Figure 2.15. While the research community generally agrees on the three-scale approach to quantify particle morphology, different scholars may have varied definitions on the quantitative parameters at each scale (Mitchell and Soga, 2005, Anochie-Boateng et al., 2011).

On an overall particle scale, the sphericity can be employed to characterise the global form of the particle (as shown by green dashed circle in Figure 2.15), which quantifies the shape such as flaky, blocky, elongated, branched, and rodlike. It represents the proximity of a particle to a sphere in three dimensions, or to a circle in two dimensions (Blott and Pye, 2008). The sphericity can be measured as the diameter of the largest sphere that fits inside the particle divided by the diameter of the smallest sphere that encloses the particle. However, due to the constraints in determining sphericity in three dimensions, many researchers have shifted their focus to calculating the circularity of particles based on their 2D projections (Riley, 1941,

Wadell, 1933). The initial attempt to represent particle form using a binary plot of width/length and thickness/width ratios was made by Zingg (1935), which was later improved by other researchers including Krumbein and Pettijohn (1938) and Krumbein (1941).

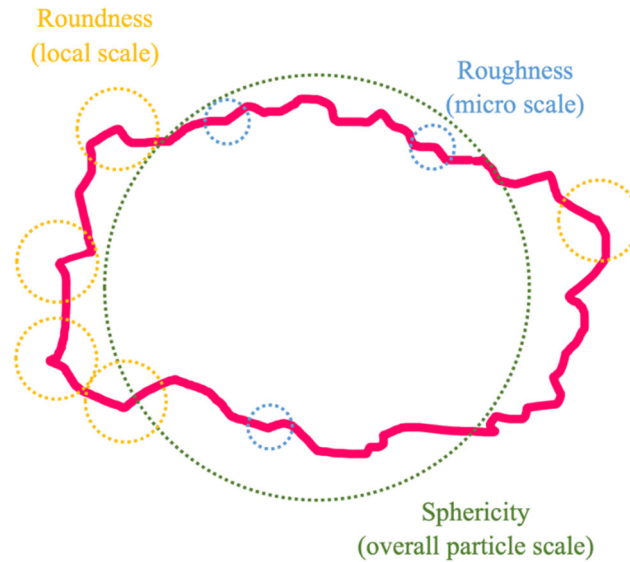


Figure 2.15. Shape descriptors at different scales.

In particle morphological analysis, several equations have been used to characterise particle form at over particle scale. The first one is $4\pi A/P_p^2$, which is usually employed to describe form and roughness (Cox, 1927, Kulu et al., 1998, Pons et al., 1999, Hentschel and Page, 2003, Russ, 2006, Ersoy et al., 2007, Coltelli et al., 2008, Liu et al., 2015), where A is particle area, and P_p is particle perimeter. This parameter is also termed as “sphericity” (Riley et al., 2003, Alfano et al., 2011, Beckett et al., 2014, Miwa et al., 2015), “roundness” (Mikli et al., 2001, Durant et al., 2009, Manga et al., 2011), “circularity” (Bjørk et al., 2009, Cioni et al., 2014, Heilbronner and Barrett, 2013), “HS circularity” (Leibrandt and Le Penneç, 2015), or “shape factor” (Bayhurst, 1995, Shea et al., 2010) by various researchers.

Additionally, equations including $P_p/(2\sqrt{\pi A})$ (Dellino et al., 2005, Büttner et al., 2006, Németh, 2010, Németh and Cronin, 2011, Dellino et al., 2012, Murtagh and White, 2013, Leibrandt and Le Penneç, 2015), $4A/\pi FL^2$ (Hentschel and Page, 2003, Wei et al., 2020, Wei et al., 2022), $4A/\pi A_{emi}^2$ (Ersoy et al., 2007), FW/FL (aspect ratio) (Pons et al., 1999, Hentschel and Page, 2003, Riley et al., 2003, Heilbronner and Keulen, 2006, Németh and Cronin, 2011, Andronico et al., 2014, Wei et al., 2020, Wei et al., 2022), and A_{emi}/A_{ema} (Polacci and Papale, 1997, Rust et al., 2003, Coltelli et al., 2008, Shea et al., 2010, Cioni et al., 2014) have also been

employed to describe particle form, where FL is particle length; FW is particle width; A_{ema} and A_{emi} are the major and minor axis of best-fit ellipse, respectively.

On a local scale, roundness (sometimes also known as angularity) is used to reflect surface irregularities that are basically one order of magnitude smaller than the particle size in two dimensions (Cho et al., 2006). Researchers initially believed that sphericity and roundness were synonymous. However, subsequent studies have shown that they actually represent distinct aspects of particle shape (Wadell, 1932). Roundness is mainly controlled by the sharpness of particle edges or corners, while it is unaffected by the overall geometric form of the particles themselves (Powers, 1953). As illustrated in Figure 2.15, irregularities including edges and corners within the yellow dashed circle along the particle perimeter are evaluated. Corners refer to the areas of the particle boundary where the local curvature is smaller than that of the largest inscribed circle (Wadell, 1932). Roundness, in this context, can be defined as the ratio between the average radius of curvature of surface irregularities and the radius of the largest inscribed circle. Several researchers have proposed that, rather than using the average curvature of all surface irregularities, it would be more precise to base roundness measurements on the curvature of the sharpest corner (Wentworth, 1919, Cailleux, 1947, Kuenen, 1956, Dobkins and Folk, 1970). Thus, it has been suggested that there is a need to create techniques for identifying the corners of particles and measuring their sharpness (Tafesse et al., 2013), with a specific focus on the sharpest corner (Roussillon et al., 2009).

Roughness (sometimes also known as smoothness) is used to conduct a similar analysis as the local scale introduced above, but at a micro scale (indicated by blue dashed circle in Figure 2.15). This parameter reflects the scale of surface texture comparing to the particle's overall radius. The texture of sand can undergo substantial modification due to both mechanical and chemical weathering processes, which gradually break down rocks and minerals during long-term geological processes (Das, 2021). In this context, the solidity and convexity are widely used to describe the textural roughness. Solidity is defined as A/A_c , where A_c is area of convex hull (Cioni et al., 2014, Liu et al., 2015), while convexity can be computed by equation P_c/P_p (Pons et al., 1999, Bjørk et al., 2009, Heilbronner and Barrett, 2013, Liu et al., 2015, Wei et al., 2020, Wei et al., 2022) and $A/(A+A_c)$ (Durant et al., 2009), where P_c is convex hull perimeter.

The particle abrasion process can increase both sphericity and roundness, while they do

not necessarily increase at the same rate. Additionally, particle breakage will result in an increase in sphericity, but a decrease in roundness (Wadell, 1932). It is noteworthy that particles that are not perfectly round can still exhibit non-spherical shapes, such as elliptical or disk-shaped particles. Similarly, particles that are equidimensional can have angular shapes, like a cube or hexahedron (Cho et al., 2006). The variations in shape that are easily discernible to the human eye may not be as easily identifiable to software algorithms, potentially resulting in imprecise quantitative results (Tafesse et al., 2013).

Although the quantitative characterisation of particle morphology by advanced testing equipment and mature theoretical frameworks has become the mainstream trend, some researchers such as Kleesment (2009), and Dadd and Foley (2016) still use qualitative methods to characterise particle morphology. This can be attributed to the fact that there is still no standardised methodology for analysing particle morphology up to now. In addition, there are numerous shape descriptors that have been presented by different researchers, but many of them are either theoretical in nature (Takashimizu and Iiyoshi, 2016) or can only be employed in independent software programs (Charpentier et al., 2013).

2.3.3 Influence of particle morphology on soil strength

Numerous laboratory and numerical studies have revealed that particle morphology is an important factor in controlling the mechanical properties of sandy soils, which has a considerable effect on stiffness, compressibility, permeability, strain localisation, critical state friction angle, dilation angle, strength, and anisotropy of strength (Dodds, 2003, Santamarina and Cho, 2004, de Bono and McDowell, 2016, Ren and Santamarina, 2018, Nasir et al., 2019, Daghistani and Abuel-Naga, 2023). Specimen composed of particles with various shapes have been extensively investigated, which include ellipses (Trulsson, 2018), polygon (Luo et al., 2017), rods (Trepanier and Franklin, 2010), squares (Jones et al., 2020), rhombus (Yao et al., 2021), T-shaped (Wang et al., 2021b), and star-shaped (Zhao, 2020).

2.3.3.1 Influence of particle morphology on the consolidation of sandy soil

Due to the complex geological origins of natural sands, it is often challenging to isolate and clearly identify the specific contributions of particle morphology or mineralogy to the macro-mechanical behavior of the sandy soil. By carrying out single particle crushing tests and

1-D consolidation tests on four types of sandy soil including completely decomposed granite, calcareous sand, standard Leighton Buzzard sand and pumice deposits, Zhang et al. (2020) concluded that particle morphology can significantly affect the survival possibility, yield stress, and the breakage degree of particles.

Cho et al. (2006) performed zero-lateral strain loading tests on natural ($R = 0.3-0.9$, $S = 0.5-0.9$) and crushed sands ($R = 0.2-0.3$, $S = 0.7-0.8$), and concluded that a reduction in particle regularity, which manifests as the decreased sphericity and/or roundness, would result in an increase in e_{max} , e_{min} , void ratio internal ($e_{max} - e_{min}$), and compression index. In their study, the morphological parameters including sphericity and roundness were determined by visual comparison with charts illustrated in Figure 2.10.

With the advancement in measurement technology, the use of high-resolution and more efficient equipment for quantifying particle morphology has become prevalent. This has significantly minimized the inaccuracy associated with the traditional manual measurements. The influence of particle morphology on particle fragmentation was investigated by Karatza et al. (2019) by performing the 1-D compression tests on industrially manufactured zeolite granules with high sphericity (average sphericity of 0.97). Based on the X-ray micro-computed tomography (μ CT) results, they concluded that the particle sphericity had the most pronounced effect on particle fragmentation compared to particle size, heterogeneity and density.

In the 1-D compression condition, the yielding implies the onset of particle breakage on a large scale. At this state, the effect of particle morphology was investigated by Cavarretta et al. (2010) on dry spherical and angular crushed glass ballotini. The relationships between the specific volume and vertical stress indicated that the yield stress and the NCL of spherical ballotini were achieved at higher vertical stresses than those of angular ones. The slope of the NCL line for the spherical ballotin is slightly larger than that for the angular ballotini, and the two lines tend to approach each other, suggesting that the influence of initial particle morphology diminishes progressively due to the occurrence of large-scale particle breakage under higher vertical pressures. The effect of particle roughness on loading-unloading processes was also studied in their study, but they concluded that the effect of particle roughness is not very significant compared to particle shape.

The change in particle morphology of sandy soil after 1-D compression tests has been

analysed by Zhao et al. (2020) by applying μ CT on Leighton Buzzard sands (LBS) characterized by round shapes and smooth surfaces. After compression, it was observed that the aspect ratio of the resultant fragments increased, while their roundness decreased. However, the morphological changes varied depending on the fragment size. Coarse fragments exhibited a more cubic shape, whereas finer fragments became increasingly flattened. Additionally, the sphericity and convexity of the finer fragments remained largely unchanged throughout the process. The conclusions drawn from the study were derived from 3D morphological data, and similar findings were reported by Altuhafi and Coop (2011) in experiments based on 2D morphology data obtained through laser image analysis. In both cases, it was observed that after 1-D compression, the particle form (aspect ratio), sphericity, and convexity of the LBS particles decreased. It is worth noting that in their studies the convexity was used to describe the particle compactness, a parameter quantified by the ratio of the projected area to the total area containing the concave portion.

In Altuhafi and Coop (2011)'s research, the surface roughness of LBS particles before and after the compression was quantified using an interferometer. The findings indicated an increase in roughness for sand specimens that experienced significant particle breakage, whereas the roughness of sand particles without substantial breakage exhibited a decrease. However, this method for roughness quantification has certain limitations. Firstly, the particle size must exceed a minimum diameter of 0.3 mm to ensure accurate measurement. Secondly, the technique is less effective when applied to particles with highly irregular surfaces.

2.3.3.2 Influence of particle morphology on the strength of sandy soil

The interlocking that occurs between angular particles is more pronounced, resulting in the increase both in the friction angle and the shear strength (Schanz and Vermeer, 1996). Holubec and D'appolonia (1973) reported that the internal friction angle, as observed in drained triaxial tests, experienced a more pronounced increase in granular soils with higher angularity. The same conclusion has also been obtained by Chan and Page (1997) by conducting ring shear tests on dry copper, and Shinohara et al. (2000) by performing triaxial tests on steel powder. According to Mair et al. (2002), it was found that the shearing resistance of sand particles increased with the angularity, due to the increase of particle slide-roll ratio at contact. The shear

band of angular particles generated at a greater axial strain. Additionally, the reduction in post-peak shear stress was not as evident for sand particles with subrounded to subangular shapes.

In addition, some empirical relationships between friction angle and roundness under various testing conditions have also been proposed. For example, Cho et al. (2006) proposed

$$\varphi_{cs} = 42 - 17R_1 \quad (2.12)$$

where φ_{cs} is the critical state friction angle; R_1 is the roundness determined by comparing the chart proposed by Krumbein and Sloss (1963) as shown in Figure 2.10.

Rousé et al. (2008) proposed

$$\varphi_{rep} = 41.7 - 14.4R_2 \quad (2.13)$$

$$\varphi_{MC} = 34.3 - 9.6R_2 \quad (2.14)$$

where φ_{rep} is the angle of repose, obtained by the observation of a saturated deposit in a water-filled cylinder (Santamarina and Cho, 2001). This value is equal to the constant-volume friction angle (Cho et al., 2006); φ_{MC} is the friction angle at the maximum contraction; R_2 is the roundness determined by employing the equation proposed by Wadell (1932) as below:

$$R_2 = \frac{\sum(r_i/N_f)}{r_{max}} \quad (2.15)$$

where r_i is the radius of curvature of surface features; N_f is the number of features examined; r_{max} is the radius of the largest inscribed circle.

Sukumaran and Ashmawy (2001) defined the following:

$$\varphi_{SF} = x_1 + x_2 \cdot \exp(x_3 \cdot SF) \quad (2.16)$$

$$\varphi_{AF} = y_1 + y_2 \cdot \exp(y_3 \cdot AF) \quad (2.17)$$

$$SF = \frac{\sum_{i=1}^{N_s} |\alpha_i|}{\sum_{i=1}^{N_s} |\alpha_{i-fp}|} \times 100\% \quad (2.18)$$

$$AF = \frac{\sum_{i=1}^{N_s} (\beta_i - 180)^2 - (360^2/N_s)}{3 \times (180)^2 - (360^2/N_s)} \times 100\% \quad (2.19)$$

where SF and AF are the abbreviation for normalised shape and angularity factor, respectively; α_i is the distortion angle, which represents the deviation of the particle outline from a perfect circle; α_{i-fp} is the value corresponding to a thin flat particle; N_s is the number of sampling points; β_i is the internal angles of the particle corner; φ_{SF} and φ_{AF} are the friction angle calculated based on SF and AF , respectively; x_i and y_i are Sukumaran coefficients.

The relationships between friction angle and roundness obtained by the aforementioned researchers are summarized by Zavala (2012) and plotted in Figure 2.16. The variations in the internal friction angle demonstrate a consistent decreasing trend when the soil particle becomes more rounded, or more spherical in the case of Sukumaran and Ashmawy (2001).

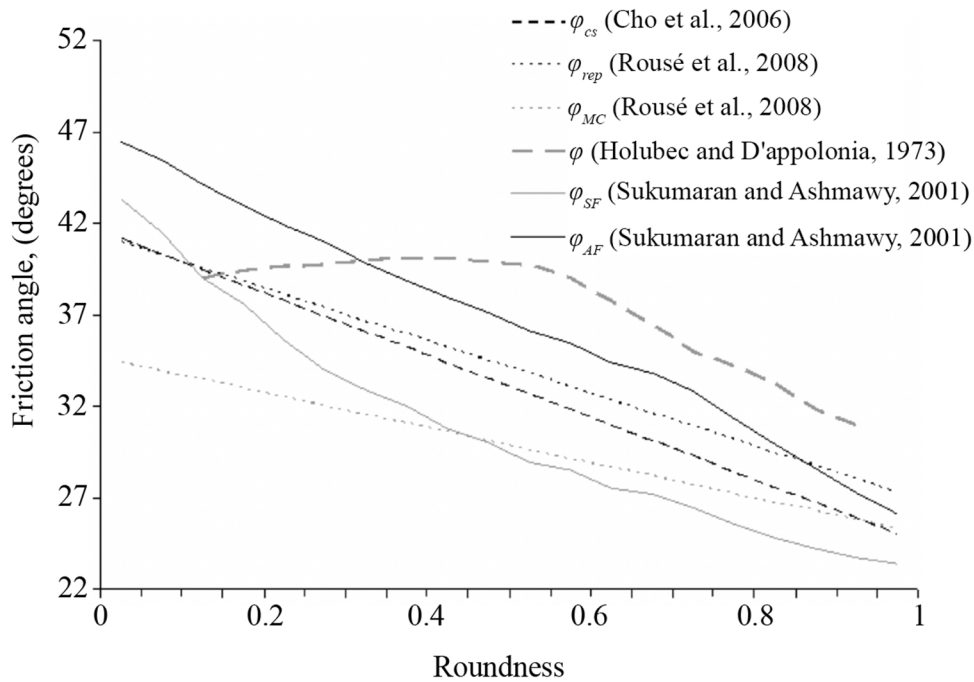


Figure 2.16. Relationship between friction angle and roundness (modified after Zavala (2012)).

The impact of particle roughness on shear strength and deformation behaviour was also investigated by various researchers. By performing a series of direct shear tests, Liu and Matsuoka (2003) found that sand particles with more angular shapes exhibit higher shear strength and mobilized friction angle during the initial stages of dilation. The same type of experiments are also extensively conducted by Siang and Wijeyesekera (2012), who concluded that Leighton Buzzard sand and Kahang sand particles with lower sphericity and roundness values are likely to exhibit higher dilatancy angles. This result was also confirmed by Siang et al. (2013) by performing tests subsequently on uniformly-graded sand specimens and glass beads. Li (2013) performed direct shear tests on particles with varying degrees of elongation and convexity, and concluded that the increasing elongation or decreasing convexity could lead to a higher residual friction angle. Guo and Su (2007) highlighted the influence of particle angularity on the shear strength and dilation by performing the triaxial compression tests on angular limestone particles and rounded Ottawa standard sands.

It is generally accepted that the cohesionless soil has no cohesive strength. The reason why cohesionless soils still exhibit a certain value of cohesion is due to the interlocking effect that occurs between particles, which is greatly influenced by the particle morphology. By performing triaxial tests on calcareous sands, Wang et al. (2019b) concluded that the interparticle interlocking increases the internal friction angle and lead to the shear dilatancy under low confining pressure, while it increases the apparent cohesion under high confining pressure. The similar conclusion was also obtained by Jiang et al. (2013) by conducting discrete element analysis on lunar regolith grains.

To provide more in-depth understanding of particle morphology on the mechanical behaviour of granular materials, numerical simulations using the discrete element method (DEM) have been widely employed by many researchers. By conducting both numerical and experimental direct shear tests on natural sands and polylactic acid particles, Ma et al. (2022) stated that the interlocking effect became pronounced as the modified shape parameter ($S_h = (A_s/V)L_s/6$) increased, where S_h is a modified shape parameter; A_s is the particle surface area; V is the particle volume; L_s is the diameter of a sphere with an equivalent volume to the particle. The increase in both the quantity and distribution of interparticle contacts could lead to a greater shear strength. O'Sullivan (2011) stated that non-convex particles exhibited greater shear strength and stiffness compared to convex particles, resulting from a larger number of contact points per particle. Similarly, Lu et al. (2019) observed higher peak shear strength in sand particles with more irregular shapes during the direct shear tests under normal stresses below 200 kPa. By conducting the same type of numerical and experimental tests, Peng et al. (2021) concluded that both peak shear stress and internal friction angle increased as the decrease of particle sphericity and roundness (as proposed by Krumbein and Sloss (1951)). By simulating the drained biaxial compression tests on the mixture of fine and coarse sands, Gong et al. (2019) stated that the internal friction angle increased with the aspect ratio (quantified as the inverse of sphericity) of fine sands. Mirghasemi et al. (2002) discovered that angular 2D polygon-shaped particles reached their highest shear strength at a greater axial strain compared to the rounded particles. Additionally, the reduction in post-peak strength was not as significant for angular materials. Based on their findings, they also reached the conclusion that the shear strength and dilation increased with the angularity of testing materials. Similar results were

also presented by Pena et al. (2007) by carrying out simulations on 2D convex polygon-shaped particles. Their analyses indicated that elongated particles exhibit higher critical-state shear strength compared to spherical particles.

Nonetheless, the simplified particle geometric models employed in these simulations such as spheres, pentagons or ovals (Ng, 2009, Härtl and Ooi, 2011, Azéma et al., 2012, de Bono and McDowell, 2016), cannot accurately represent the distinctive morphological features of real sand particles (Peng et al., 2021).

2.4 Particle breakage and its influence on the strength of sandy soils

When the applied external stress exceeds the material strength, partially or fully particle breakage will occur (Ovalle et al., 2015). As an important inherent soil characteristic, particle breakage plays a critical role in influencing the mechanical behaviour of sandy soil. At the macroscopic scale, the particle breakage will directly lead to alterations to the particle size distribution (PSD), which will have a non-negligible influence on the internal friction angle, porosity, pore water pressure, and permeability of granular materials (Yu, 2017c). At the microscopic scale, particle breakage changes the local contact relationship, causing the rearrangement of the granular microstructure. This significantly affects the development and transformation of soil properties over time, playing a critical role in the overall mechanical behaviour and response of the soil to various stress conditions (Karatza et al., 2017).

Furthermore, classical soil mechanics has traditionally assumed that soil particles are incompressible and non-breakable. Deformation of soil is caused by the discharge of air and water from pore spaces, along with the rearrangement of particles. The soil strength theory is based on the frictional sliding and rotating between particles (Cheng et al., 2004). This approach failed to account for the particle shape and breakage. Consequently, the study of particle breakage plays a pivotal role in advancing the understanding and development of soil mechanics theory (Bolton et al., 2008).

2.4.1 Definition and types of particle breakage

In the initial phase of soil mechanics, “particle breakage” was proposed by Terzaghi and Peck (1948) when considering the impact of soil structure on its mechanical performance.

Meanwhile, other concepts characterising soil microstructure including the distribution of void, the arrangement and connection state of soil particles were proposed as well (Yu, 2021). The term “particle breakage” is employed to describe the completely solid fracturing and volume decreasing process through repeated breakage of particles (John et al., 2023). During compression or shearing, particle breakage occurs when the loading stress exceeds the yielding stress of sands (Lade and Yamamuro, 1996, Hyodo et al., 2002, Lobo-Guerrero et al., 2006). This effect is particularly pronounced in uniformly graded samples (Bolton et al., 2008).

Particle breakage serves as a crucial factor in explaining the mechanical behaviour of granular materials, and the recognition of this mechanism further deepens the understanding of the performance of the material assembly at the macro level (Coop and Lee, 1992, Hyodo et al., 2002, Altuhafi and Coop, 2011). Particle breakage has been widely acknowledged as a critical factor shaping the overall behaviour of soils, significantly impacting their strength, deformation characteristics, and permeability (Wood and Maeda, 2008, Airey et al., 2011, Wang et al., 2017a). Therefore, identifying factors affecting particle breakage during loading is critical to explain the deformation of soil assembly. Among which, the external loading conditions, such as effective stress path, state of effective stress (Parab et al., 2014), effects of mineral composition (Leleu and Valdes, 2007), relative density (Shahnazari and Rezvani, 2013), particle size distribution (Gupta, 2017), and particle morphology (e.g. particle shape, sphericity, roundness, size, angularity, convexity, surface roughness) (Norazirah et al., 2016) are the most pronounced ones (Gao et al., 2021).

Depending on the factors such as the level of external force and the particle morphology, particle breakage usually occurs in three common ways including abrasion, breakoff, and splitting (Guyon and Trodec, 1994). As illustrated in Figure 2.17(a), “abrasion” generally refers to the process of rounding off the corners or surface asperities of particles, accompanied by the production of fine particles smaller than 0.075 mm, due to slight frictional contact between particles and other engineering materials they come into contact with. The process has a negligible impact on the overall size of the “parent” particle. As shown in Figure 2.17(b), “breakoff” is the term used to describe the rupture of the more prominent or irregular edge parts of the particle surface. This causes a small portion of solid to separate from the “parent” particle, resulting in the formation of smaller particles. As presented in Figure 2.17(c), “splitting” refers

to the development of cracks within a particle, extending throughout the entire particle, which ultimately leads to the complete rupture of the “parent” particle. As the “parent” particle breaks apart, multiple “daughter” particles of similar size are created.

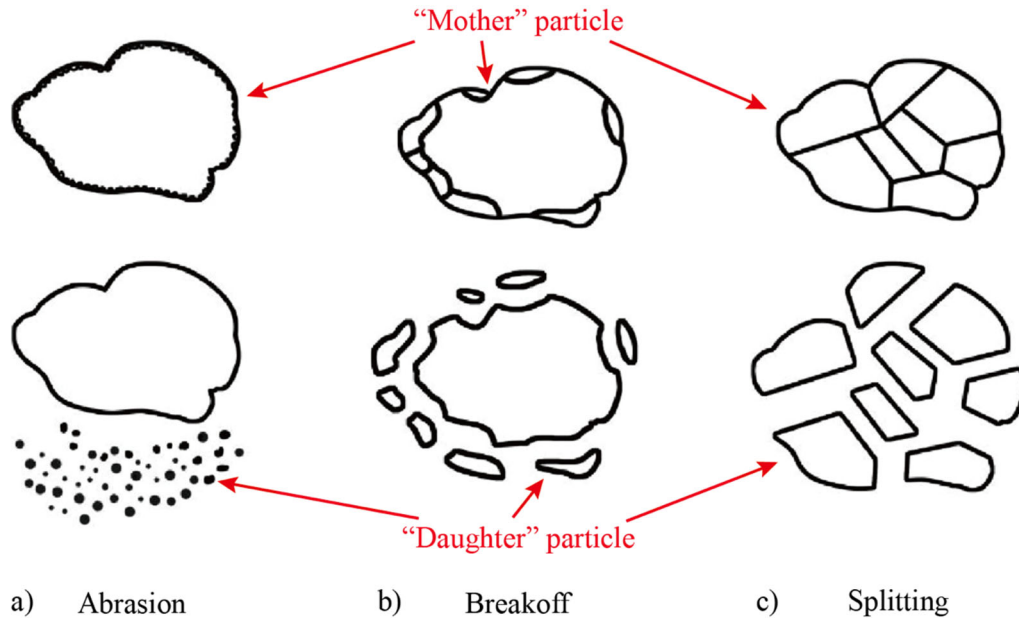


Figure 2.17. Schematic representation illustrating particle breakage under three different mechanisms (modified after Wang et al. (2022b)).

2.4.2 Quantification of particle breakage

To determine the magnitude of particle breakage and to compare it with findings from other researchers, a large number of different particle breakage indices have been developed. These indices capture the extent of breakage through various approaches, such as monitoring changes in the percentage of particles of a given size (Marsal, 1967, Lade and Yamamuro, 1996, Miura et al., 2003), changes in particle area (Miura and Sukeo, 1979, Nakata et al., 2001a), changes in particle perimeter (Wei et al., 2020), changes in PSD (Hardin, 1985, Einav, 2007a, Einav, 2007b, Indraratna et al., 2010, Indraratna and Nimbalkar, 2013, Yu, 2018), survival probability (Nakata et al., 1999), grading equation (Fukumoto, 1990, Fukumoto, 1992). Additionally, fractal theory (Turcotte, 1986, McDowell et al., 1996, Lobo-Guerrero and Vallejo, 2005a, Yu, 2018) and its integration with relative breakage (Einav, 2007a, Wood and Maeda, 2008) have also been employed to further refine breakage quantification method.

Most of the widely used methods to quantify particle breakage at present are based on comparing the changes in the PSD of the specimen before and after the experiment. To

characterise the influence of particle breakage and soil degradation on the design of gravel and soil filters in high earth dams, a series of anisotropic triaxial compression tests were performed by Lee and Farhoomand (1967). In their study, a particle breakage index, B_{15} was introduced, which can be obtained by using the following equation:

$$B_{15} = \frac{D_{15i}}{D_{15f}} \quad (2.20)$$

where D_{15i} and D_{15f} is the particle size (diameter) which is coarser than 15% of the total materials, for the initial and final grading of the tests, respectively (shown in Figure 2.18). Depending on the specific design requirements, B_{15} could range from 1 to infinity.

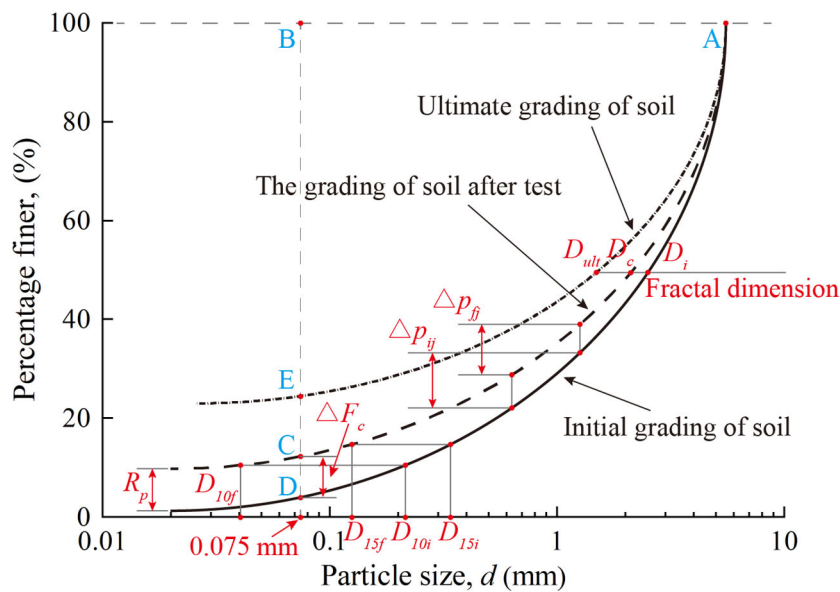


Figure 2.18. Calculation method of particle breakage indices proposed by various researchers (modified after Yu (2021)).

Similarly, to provide guidance on the design and construction of earth and rockfill dams, Marsal (1967) carried out large-scale triaxial compression tests on rockfill materials, and presented another particle breakage index, B_g , which can be calculated by employing the following equation:

$$B_g = 0.5 \sum_1^n |\Delta p_{ij} - \Delta p_{fj}| \quad (2.21)$$

where Δp_{ij} and Δp_{fj} is the difference of percentages at sieve size fraction j , for the initial and final grading, respectively (shown in Figure 2.18).

The relative breakage, B_r proposed by Hardin (1985), is defined as:

$$B_r = \frac{B_t}{B_p} \quad (2.22)$$

where B_t is total breakage, which is defined as the area between the initial and final particle size distribution ($Area_{ACDA}$); B_p is breakage potential, which is defined as the area between the initial PSD with particle size larger than 0.075 mm and the line defining the upper limit of the silt size (0.075 mm) ($Area_{ABDA}$ shown in Figure 2.18).

Based on the aforementioned Hardin's theory, a particle breakage index was specifically developed by Indraratna et al. (2005) to quantify the degradation intensity of railway ballast. As presented in Figure 2.19, by employing the initial PSD, final PSD, and a linear particle size axis, which is termed as "the arbitrary boundary of maximum breakage", the determination of the ballast breakage index (BBI) (ranges from 0 to 1) can be achieved by using the following equation:

$$BBI = \frac{A_{BBI}}{A_{BBI} + B_{BBI}} \quad (2.23)$$

where the method of defining parameters A_{BBI} and B_{BBI} are presented in Figure 2.19.

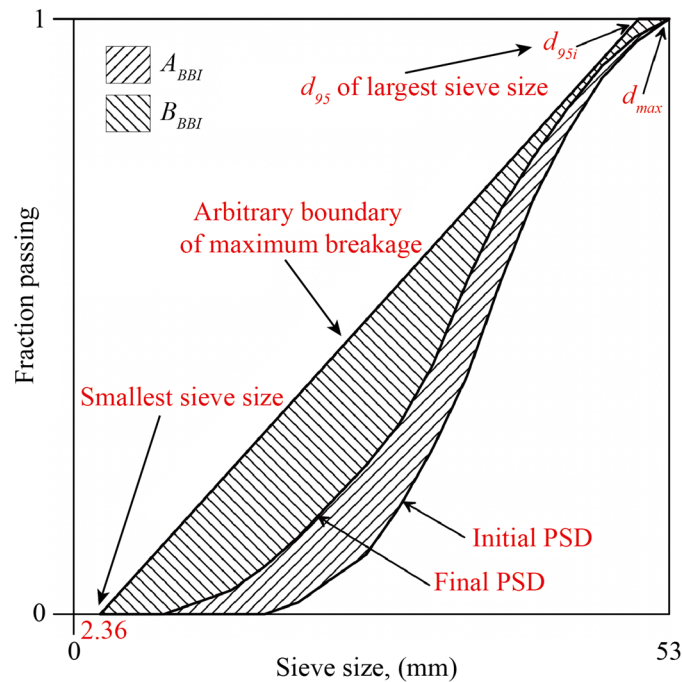


Figure 2.19. Calculation of ballast breakage index, BBI (modified after Indraratna et al. (2005)).

To estimate the permeability of sandy soil where particle breakage occurs, a hyperbolic model was built by Lade et al. (1996) by relating the particle breakage index, B_{10} to the total energy input per unit volume of the specimen. The value of B_{10} ranges from 0 to 1, and can be

obtained by using the following equation:

$$B_{10} = 1 - \frac{D_{10f}}{D_{10i}} \quad (2.24)$$

where D_{10i} and D_{10f} is the particle size (diameter) at which 10% of the material is finer, before and after the test, respectively (shown in Figure 2.18).

A particle breakage index based on the increase of fine contents, ΔF_c (0.075 mm or less) after test (shown in Figure 2.18) was proposed by Miura and Yagi (1997) to quantify particle crushing. The results demonstrated a distinct correlation between ΔF_c and other particle breakage indices introduced by Marsal (1965), Lee and Farhoomand (1967), Miura and Yamanouchi (1977), Lade et al. (1996).

A particle breakage index, B_f was introduced by Nakata et al. (1999), which can be determined by employing the following equation:

$$B_f = \frac{R_p}{100} \quad (2.25)$$

where R_p is the difference between the percentage of the finest particles after and before test (shown in Figure 2.18). The value of B_f ranges from 0 to 1, where 0 indicates no particle breakage and 1 represents complete breakage of all particles.

The process of particle breakage results in the generation of numerous fine particles, leading to a corresponding increase in particle surface area. By performing triaxial compression tests on decomposed granite soils, Miura and Sukeo (1979) analysed the effect of particle breakage on their shear behaviour, and found out that the increase in particle surface area is positively correlated to the input plastic work. Based on the comminution equation presented by Tanaka (1954), they suggested that the slope of the particle surface area-plastic work relationship (dA/dW) can be used to quantify the particle breakage under triaxial compression loading. It is also termed as the “particle-crushing rate”. However, the calculation of the particle area in their study is actually based only on the assumption that the particles are all spherical, and no quantification of the real particle areas has been conducted.

The concept of fractal theory has found its extensive use in the engineering practices in soil mechanics (Mandelbrot, 1983, Turcotte, 1986, Tyler and Wheatcraft, 1992, McDowell et al., 1996, McDowell and Bolton, 1998, Lobo-Guerrero and Vallejo, 2005a). The fractal characteristics of the soil PSD can be explained by a power law in the following form:

$$N(R_r > r) = k(r)^{-D_f} \quad (2.26)$$

where $N(R > r)$ is the number of particles with the radius R_r larger than the given value of r ; k is a proportionality constant; D_f is the fragmentation fractal dimension, which can be used to determine the soil PSD (Mandelbrot, 1983, Turcotte, 1986, Tyler and Wheatcraft, 1992, McDowell et al., 1996, McDowell and Bolton, 1998, Lobo-Guerrero and Vallejo, 2005a).

Based on the fractal theory and the B_r definition proposed by Hardin (1985), a particle breakage index was introduced by Einav (2007a) by employing the ultimate fractal PSD as a replacement of the sieve size of 0.075 mm ($Area_{ACDA}/Area_{AEDA}$ shown in Figure 2.18). As the breakage continues, the current PSD would move from the initial PSD to the ultimate fractal PSD. By extending Einav's theory, a grading state index, I_g (ranges from 0 to 1), was presented by Wood and Maeda (2008), suggesting that the current PSD would evolve from the single size grading to the fractal limiting grading.

Similar to Einav's theory, the relative fractal dimension, D_b was introduced by Yu (2018) to define breakage based on the fractal characteristics of soil particles. By employing the initial and ultimate PSD, D_b (ranges from 0 to 1) can be obtained by using the following equation:

$$D_b = \frac{D_c - D_i}{D_{ult} - D_i} \quad (2.27)$$

where D_c is the current fractal dimension; D_i is the initial fractal dimension of the initial PSD; D_{ult} is the ultimate fractal dimension of the ultimate PSD (shown in Figure 2.18).

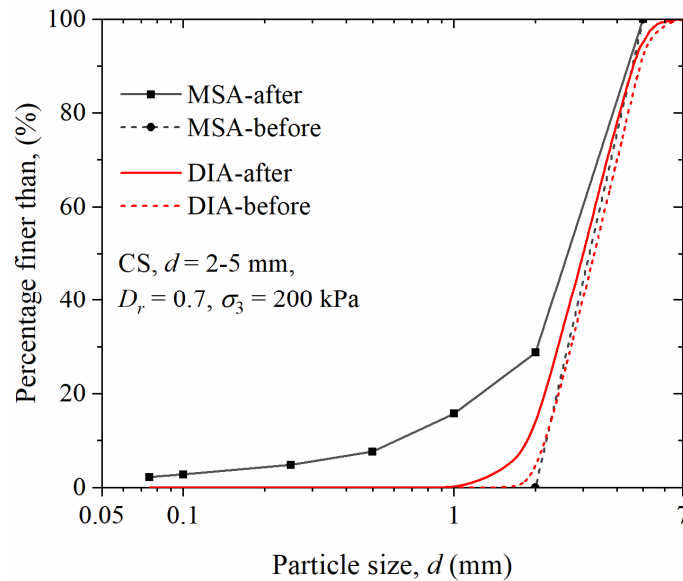


Figure 2.20. The mechanical sieving analysis (MSA, black lines) and dynamic image analysis (DIA, red curves) of PSD before (dashed lines) and after (solid lines) the CD triaxial compression tests.

The application of all the aforementioned theories relies heavily on accurately determining the PSD curve. As a simple and well-defined method, mechanical sieving analysis (MSA) has been extensively employed to determine the PSD of a specimen before and after the test. However, as indicated by the black polyline and the straight line in Figure 2.20, the resulting curve is typically determined by a limited number of coordinate points, which deviate somewhat from the results of a real, smooth curve.

As the technology advances, photographic and analytical techniques are increasingly being applied to the quantification of particle morphology. Based on the digital photos of sand particles, a breakage index, R_A , was proposed by Nakata et al. (2001a) by considering the changes in cross sectional areas. R_A can be obtained by using the following equation:

$$R_A = \frac{S_b - S_a}{S_b} \quad (2.28)$$

where S_b and S_a are the cross-sectional area of the particle before and after the test, respectively. However, the accuracy of this method is compromised due to the challenges associated with capturing photographs of the same sand particle before and after the experiment from exactly the same angle.

By employing the dynamic image analysis technique, a particle breakage index, B_{r-p} , was presented by Wei et al. (2020) recently by considering the changes in total particle perimeters based on 2D particle images. B_{r-p} can be obtained by using the following equation:

$$B_{r-p} = \frac{\sum P_a - \sum P_b}{2 \sum P_b} \quad (2.29)$$

where $\sum P_b$ and $\sum P_a$ are the total particle perimeters before and after the test, respectively.

The application of this method enables rapid and efficient acquisition of morphological data for a vast quantity of particles. In addition, the accuracy of the results has been significantly improved by the fact that for each individual sand particle, the results are averaged from 13 photographs taken from different angles.

2.4.3 Influence of particle breakage on soil strength

2.4.3.1 Influence of particle breakage on the consolidation of sandy soil

In the 1-D compression loading, the compressibility of sandy soil increased with particle breakage, and the onset of yielding phenomena signifies the initiation of large-scale particle

breakage. To investigate the relationship between the statistics of individual particle breakage and the change of compression lines, 1-D compression tests under the normal pressure up to 92 MPa were carried out by Nakata et al. (2001a) on Silica sands. 12 dyed sand particles were embedded in each specimen for particle identification purpose. Based on the change in particle area in 2D microscopic images, the single-particle damage mode was categorised into five classes. They concluded that approximately 50% of the particles experienced major splitting after yielding at the pressure of about 23 MPa. As the compression progressed, the compression index became gradually stabilized, indicating a steady rate of particle breakage. At the end of compression, nearly all of the marked particles had undergone some forms of damage, with about 60% experienced major particle splitting.

Similar tests were conducted by Nakata et al. (2001b) to investigate the effect of various factors on the yield stress. They observed that the yield stress for uniformly graded Silica sands increased linearly with the decrease of particle size or the initial void ratio. By testing the natural (rounded) and crushed (angular) glass ballotini, they concluded that the yield stress for rounded particles (20 MPa) is much higher than that of angular particles (6 MPa). It is also noteworthy that while the compression curve of angular particles exhibited a smooth, gradual reduction after the yielding, the compression behaviour of rounded particles demonstrated a more abrupt, near-vertical drop of stress immediately after yielding. They also reported that under the normal pressure up to 92 MPa, the contents of fine particles (less than 0.074 mm) after the test for all specimens have exceed 10%.

Different breakage modes during compression were also investigated by Bolton et al. (2008) by numerically simulating the isotropic compression tests on uniformly graded crushable agglomerates using DEM. The findings demonstrated that before yielding, agglomerate damage was primarily characterized by the degradation of surface asperities. At the yielding state, the grain splitting occurred. As the increase of normal pressure, both particle damage by asperity abrasion and grain splitting were observed across all particle sizes.

At higher normal loading pressures, the normal compression line of granular soils exhibits a linear decline. McDowell and Bolton (1998) attributed this behaviour to significant changes in the particle size distribution, which occurred as a result of ongoing fragmentation of fine particles under elevated pressures. In the consolidation tests on uniformly graded samples, the

increasing stress generates more fine particles through breakage, leading to a denser and more efficient packing. Coarser particles of higher coordination numbers due to interactions with numerous finer particles, are less prone to breakage, making fine particles with lower coordination numbers more susceptible to fragmentation. They stated that this phenomenon was to surpass the strengthening effect typically associated with the decrease of particle size.

Particle breakage is not an indefinite process during the 1-D consolidation, and under high stress conditions, a stable grading is expected to emerge (McDowell, 2002, Altuhafi and Coop, 2011). Research on various granular materials has demonstrated that this limiting grading often follows a fractal particle size distribution, with a fractal dimension typically ranging between 2.5 and 2.6 (McDowell et al., 1996, Coop et al., 2004).

In these studies, both the particle breakage index and its rate of increase exhibit a positive correlation with rising vertical stress levels. As noted by Xiao et al. (2017), these indices can be effectively computed by employing the following equation:

$$B_r = a_1(p'/p_{at})^{b_1} \quad (2.30)$$

where p' is the vertical stress; p_{at} is the atmospheric pressure; and a_1 and b_1 are fitting parameters.

By fitting the particle breakage data of coral sands at varying stress levels up to 3.2 MPa using Eq. 2.30, the values of parameter a_1 and b_1 for specimens of different initial relative densities were obtained by Wang et al. (2021a), as shown in Table 2.2. Their findings also indicated that the value of parameter a_1 decreased linearly with an increase in D_r , while the value of parameter b_1 shows a corresponding linear increase with the rising D_r , although the linear fit was obtained based on only three data points.

Table 2.2. The fitting parameters of coral sands with different initial relative densities.

| Parameter D_r | a_1 | b_1 | R^2 |
|--------------------|-------|-------|-------|
| 0.25 | 0.87 | 1.46 | 0.997 |
| 0.5 | 0.53 | 1.77 | 0.996 |
| 0.75 | 0.31 | 2.09 | 0.995 |

The influence of initial relative density on particle breakage during the 1-D consolidation has been investigated by various studies. Coop and Lee (1992) suggested that soils loaded on

the normal compression lines experienced a fixed amount of particle breakage at a given stress level. In their subsequent research, Altuhafi and Coop (2011) complemented this theory by introducing the effect of relative density on particle breakage. Based on PSD curves from Dog's Bay sands before and after the 1-D consolidation tests under a vertical stress up to 30 MPa, they found that the initial relative density played a significant role in particle breakage. Specifically, it was observed that specimens with a smaller initial relative density (higher initial void ratio) exhibited a greater degree of particle breakage. The relative breakage index proposed by Einav (2007a) tended to decrease as the increase of D_r as observed by Wang et al. (2021a) in their 1-D consolidation tests on non-uniformly graded coral sands with varying initial relative density (0.25, 0.5, and 0.75) and particle size (ranging from 0.25 to 2 mm).

2.4.3.2 Influence of particle breakage on the strength of sandy soil

In the literature, different types of laboratory tests have been conducted to explore the effect of particle breakage on the shear strength of sandy soil, including the ring shear tests, direct shear tests, and triaxial shear tests under drained and undrained conditions (Luzzani and MR, 2002, Sadrekarimi and Olson, 2010b, Ghafghazi et al., 2014).

The particle grading can be changed significantly during the loading process as fine particles are continuously generated through the successive breakage of coarser particles under the increasing loading stress. This process could significantly alter the granular packing structure, influencing both the shearing behaviour and dilatancy mechanics, which in turn results in dynamic variations in the overall strength of the soil (Yao et al., 2008, Sadrekarimi and Olson, 2010a, Yu, 2017b). Ever since the discovery and proposal of shear dilatancy phenomenon in granular materials by Reynolds (1885), there has been extensive research on how particle breakage or the presence of fine particles could affect the stress-dilatancy behaviour of soil particle specimens (Ueng and Chen, 2000, Hamidi et al., 2009, Xiao et al., 2014). In several previous research on the behaviour of mixed soil specimen, it has been observed that an increase in the content of non-plastic fines reduces the ability of soil expansion, i.e., the shear dilatancy becomes less pronounced (Been and Jefferies, 1985, Thevanayagam, 1998, Ni et al., 2004, Yu, 2017c). Contrary to these findings, certain researchers argued that the increase of the percentage of fine content can enhance both its strength and dilatancy (Murthy

et al., 2007, Sadrekarimi and Olson, 2011).

The excess friction angle, φ_{excess} ($\varphi_{excess} = \varphi_p - \varphi_{cs}$), together with the dilatancy angle, were extensively employed to describe the stress-dilatancy characteristics of sandy soil (Vaid and Sasitharan, 1992, Yu, 2017d). Taking into account of particle breakage, a linear relationship between the excess friction angle, void ratio, and dilatancy angle was presented by Yu (2017d) in the following form:

$$\frac{\psi_{max}}{\varphi_{excess}} = \Gamma - \lambda_p \log e_{skps} \quad (2.31)$$

where ψ_{max} is the maximum dilatancy angle, which is equal to the peak-state dilatancy angle; e_{skps} is the skeleton void ratio; Γ and λ_p are model parameters. This relation can be valuable in evaluating the changes in stress-dilatancy behaviour of sands during loading.

The occurrence of particle breakage inhibited the development of shear dilatancy, resulting in an overall contraction of the soil (Miura et al., 2003). The contractive behaviour in soils is typically characterized by a reduction in the dilatancy angle and void ratio during drained tests. In the undrained tests, the loading results in the development of excess pore water pressure within the soil assembly. These observations indicate that particle breakage has an intrinsic impact on soil behaviour (Bandini and Coop, 2011). Through carrying out direct shear tests on carbonate sands, Tarantino and Hyde (2005) observed that the apparent critical-state friction angle increased with the normalised particle breakage rate (defined as the reduction in particle surface area normalised with respect to the normal force).

The effect of particle breakage on the mobilized strength of sandy soil was explored by Yu and Su (2016) by performing a series of drained triaxial tests on pre-crushed Silica sand particles. The outcomes suggested that the occurrence of particle breakage changed the stress-dilatancy behaviour of the soil specimen, as evidenced by a parallel downward curve shift and rotation for the dilatancy factor ($1 - d\varepsilon_v/d\varepsilon_a$) - effective principal stress ratio (σ'_1/σ'_3) relationship as the amount of particle breakage increased. Both the mobilized friction and dilatancy angles decreased with the increase of particle breakage index. However, their difference, i.e., the mobilized basic friction angle, increased with the increase of particle breakage intensity.

Given the importance of particle breakage in the mechanical behaviour of granular soils, various constitutive models have been developed by taking into account the particle breakage,

which include the bounding surface models (Kan and Taiebat, 2014), the continuum breakage mechanics models (Einav, 2007a, Einav, 2007b), the disturb state concept models (Varadarajan et al., 2003), the elastoplastic models (Daouadji et al., 2001, Xiao and Liu, 2017), and the generalized plasticity models (Liu et al., 2014, Kong et al., 2016). For example, the conventional Cam-Clay model was enhanced by incorporating the concept of crushing energy to account for the influence of particle breakage on soil behaviour (McDowell et al., 1996). Russell (2011) further considered the energy dissipation mechanism during particle breakage in the Cam-Clay model, and proposed a closed-form expression for a limiting compression line in the double logarithmic voids ratio-stress plane. In this work, the fractals were employed to characterise particle and pore size distributions as particle fragmentation occurs. Similarly, a revised stress-dilatancy relationship for sand particles under triaxial loading conditions was presented by Ueng and Chen (2000), as well as Salim and Indraratna (2004) to characterise particle breakage and its effect on shear strength characteristics.

2.5 Summary

This chapter presents an in-depth review of the existing literature on the shear strength of granular soil and its key influencing factors. The key findings and identified research gap are listed below:

- The parameters characterising the strength of sandy soil include apparent cohesion and internal friction angle. The apparent cohesion is primarily governed by particle morphology, as the particle shape and surface characteristics play crucial roles in how they interlock together. The internal friction, on the other hand, can be categorized into sliding friction and particle interlocking, as controlled by surface roughness and particle morphology, respectively.
- Although the 1-D consolidation and triaxial compression tests on sand particles have been conducted to explore various factors influencing their mechanical behaviour, relatively few studies have thoroughly examined the effects of initial relative density. Expanding the range of D_r values in studies would enable researchers to gain a clearer understanding of its influence on the macroscopic mechanical properties, facilitating more detailed observations and analysis of soil behaviour under varying conditions.

- Furthermore, in analysing the impact of relative density on strength characteristics, the variation in findings across studies demonstrates significant differences depending on the type of sand particles, even under comparable experimental conditions. This discrepancy underscores the necessity of investigating the mechanical behaviour of various granular materials, particularly the underexplored ones like calcareous sands.
- Laboratory experiments, while advancing, continue to face constraints. Although 2D and 3D quantification methods have demonstrated reliability, many researchers still rely on traditional graphical comparisons, which are labour-intensive, time-consuming, and subjective, leading to potential inaccuracies.
- The image analysis based on 2D technology has become the preferred method for morphological quantification due to its efficiency in analysing the entirety of experimental specimens within a shorter timeframe. Nevertheless, 2D methods are constrained by the resolution of imaging equipment and the size of the particles under investigation.
- The mechanical sieving analysis is the predominant method employed to quantify particle breakage. This approach is not only time-consuming and labour-intensive but also constrained by the morphological characteristics of the granular materials being studied. Consequently, there is a pressing need to explore alternative methodologies that facilitate comprehensive monitoring of the entire spectrum of particle micro-activities, encompassing phenomena such as particle sliding, positional rearrangement, and breakage occurrences.

Chapter 3 Research Methodology

This chapter begins by outlining the two types of sandy soils used in this research, detailing the rationale for their selection, as well as their fundamental physical properties and the preparation procedures prior to experimentation. Next, the primary physical parameters of the materials including minimum and maximum dry index densities, specific gravity, and the necessary experimental apparatus are presented. The methods for quantifying particle morphology and breakage, along with the procedures for monitoring acoustic emission signals, are also thoroughly described. Finally, the chapter provides a comprehensive explanation of the experimental protocols and equipment employed in the 1-D consolidation and CD triaxial compression tests.

3.1 Testing materials

The calcareous and river sands were used for investigating the influence of particle morphology and particle breakage on the shear strength of sandy soils in this study. Both types of sands are formed in aquatic environments but have distinct particle morphological features and breakage characteristics.

3.1.1 Calcareous sands

The calcareous sands were sampled from one reclamation site on the Yongshu Reef (also known as the Fiery Cross Reef) in the Spratly Islands in the South China Sea. As a marginal sea in the western Pacific Ocean, the South China Sea covers an area of about 3.5×10^6 km², extending from 3 degrees south to 23 degrees north (Jilan, 2004). The coral reefs in the South China Sea cover an area of about 3.8×10^4 km², accounting for about 5% of the world's total coral reef amount (Wang et al., 2014). As shown in Figure 3.1(a), various sites including the Pratas Islands, the Paracel Islands, the Macclesfield Bank, the Scarborough Shoal, and the Spratly Islands are located in the South China Sea from north to south, with abundant resources of coral reefs. Among which, the southernmost Spratly Islands have the largest number of more than 100 widely distributed coral reef sites, which together constitute the largest coral reef system in the South China Sea (Dong et al., 2019).

Calcareous sand is a kind of geotechnical material with insoluble carbonates such as calcium carbonate and magnesium carbonate as the main mineral components (more than 50% of weight), which is formed by a series of physical, chemical, and biochemical effects after billions of years of deposition from the biological remains of dead hermatypic coral communities (Gourlay, 1988). Calcareous sand is also known as “coral sand” (Wang et al., 2019a), or “coral calcareous sand” (Gao and Ye, 2023), or “calcareous coral sand” (Ye et al., 2022). Nonetheless, the designation “coral” in the context of coral sand is somewhat broad, referring to limestone of recent biological origin. It should be noted that corals are not the primary contributors to these sand deposits. Instead, calcareous sand is typically a composite of coral fragments along with skeletal remnants of foraminifera, calcareous algae, molluscs, and crustaceans (Yamano et al., 2000).

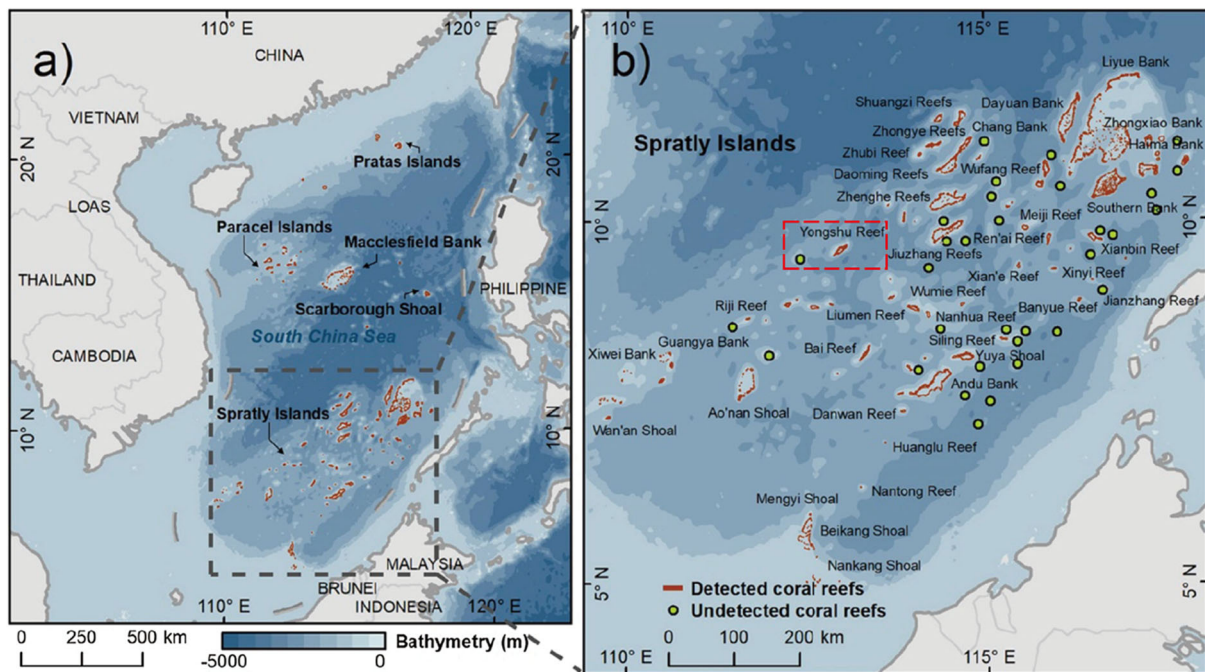


Figure 3.1. a) The location of the Spratly Islands in the South China Sea; b) Enlarged view of the Spratly Islands, showing the location of the Yongshu Reef (modified after Dong et al. (2019)).

Calcareous sands consisted of minerals mainly of aragonite, dolomite, and calcite (Wei et al., 2021). As presented in Table 3.1, the X-ray diffraction patterns showed that calcareous sands are mainly composed of CaCO_3 and MgCO_3 with the weight percentages of 81.08 and 11.55, respectively. The special marine origin and the deposition process without long-distance transportation, resulting in calcareous sands being characterized by extremely irregular particle

shapes (presented in Figure 3.2), high porosity, high brittleness, which make their mechanical properties different from the ordinary terrigenous soils (Hassanlourad et al., 2008). This also exhibits its unique property of particle breakage even under normal engineering conditions such as low stress or strain levels (Wei et al., 2021).

Table 3.1. The main minerals of calcareous sands (modified after Wang et al. (2017b)).

| Mineral | Chemical formula | Contents, (wt.%) |
|-----------|---|------------------|
| Aragonite | CaCO ₃ | 64 |
| Calcite | MgCO ₃ , CaCO ₃ | 14 |
| Feldspar | Al ₂ O ₃ , SiO ₂ | 8 |
| Calcite | CaCO ₃ | 7 |
| Quartz | SiO ₂ | 7 |
| Total | | 100 |

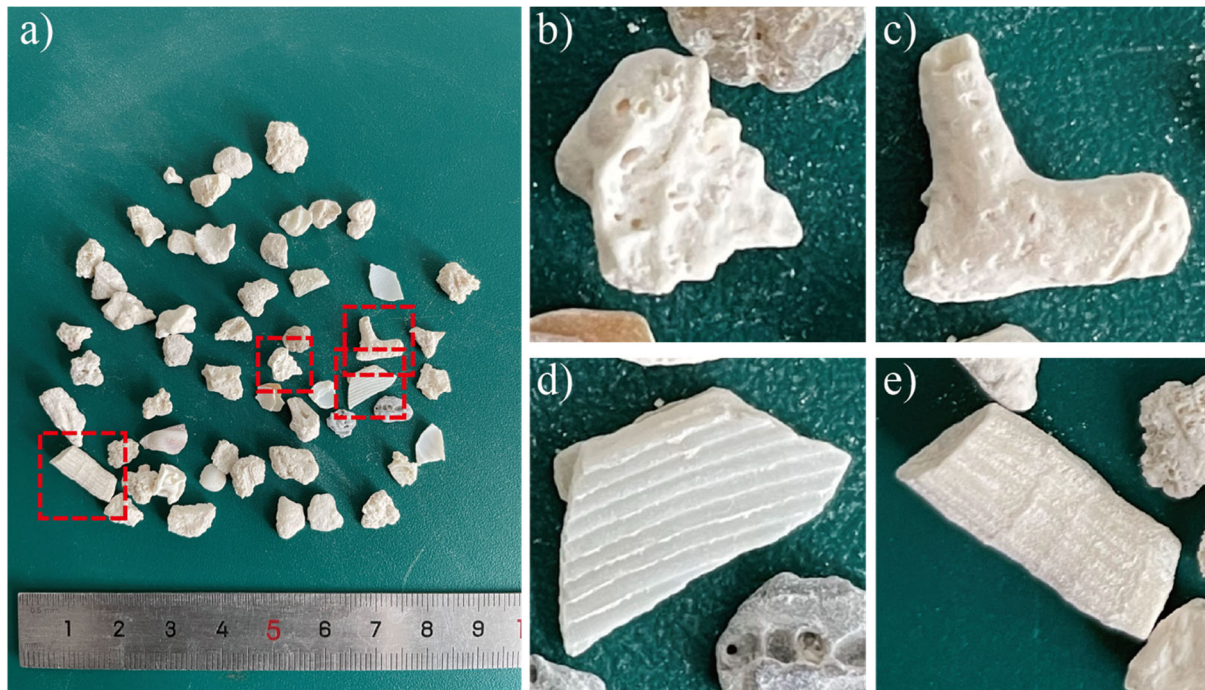


Figure 3.2. a) Calcareous sand particles of very diverse shapes, such as b) blocky; c) branched; d) flaky; and e) rodlike.

3.1.2 River sands

As a major source of natural sands, river sands are widely distributed on riverbanks or beds. They are made up of fine clean grains with rounded shape and smooth particle surface, which are formed by the transportation of residual sand from weathered rocks and mutual collision and attrition under the action of water current. River sands exhibit variability in their composition, yet are predominantly composed of silica (SiO₂), leading to their common

identification as silica sand. Their hardness, resistance to high temperatures, and chemical inertness make them extensively utilized in various civil engineering applications (Campbell, 2015). Since the change in the overall particle shape and the formation of their surface texture characteristics only occur during the geological transportation processes, their overall shape is basically blocky with high level of roundness. In addition, they have a significantly smoother surface (shown in Figure 3.3). The identification and quantitative analysis of the mineralogical phase components were carried out by applying the X-ray diffraction (XRD). As presented in Table 3.2, the results obtained by using a Bruker D8 ADVANCE (Bruker, 2023) show that river sand particles are dominated by quartz (39.44 wt.%) and albite (35.84 wt.%), which are chemically stable.



Figure 3.3. River sands with a round particle shape and a smooth surface.

Table 3.2. Quantitative mineralogy analysis results of river sands.

| Mineral | Chemical formula | Contents, (wt.%) |
|----------------------|---|------------------|
| Quartz | SiO_2 | 39.4 |
| Albite | $\text{NaAlSi}_3\text{O}_8$ | 35.8 |
| Microcline | KAlSi_3O_8 | 17.9 |
| Muscovite | $(\text{K,Na})\text{Al}_2(\text{Si,Al})_4\text{O}_{10}(\text{OH})_2$ | 3.3 |
| Magnesian-hornblende | $(\text{Ca,Na})_{2.26}(\text{Mg,Fe,Al})_{5.15}(\text{Si,Al})_8\text{O}_{22}(\text{OH})_2$ | 1.5 |
| Dolomite | $\text{CaMg}(\text{CO}_3)_2$ | 1.3 |
| Calcite | CaCO_3 | 0.7 |
| Total | | 100 |

3.1.3 Material preparation

The natural sands as received from the field were thoroughly mixed and washed by pure water to remove the fine impurities attached to their surfaces. Then, the two different sand particles were placed in separate trays in an oven to be dried at a uniform temperature of $110 \pm 5^\circ\text{C}$ for at least 24 hours to remove the moisture and make sure the samples were completely dried. After which, the sand samples were exposed to air at room temperature until they were completely cooled down.

A series of sieves with diameter of 200 mm and openings of 0.5 mm, 1 mm, 2 mm, and 5 mm along with a snug-fitting bottom pan and a top cover were selected and nested in the order of decreasing size of opening from top to bottom. The dried samples were divided into several portions in case of an overload of sand particles on the sieve. Each portion was placed on the top sieve, and the sieves were vibrated by a mechanical shaker (Figure 3.4) at a speed of 2,800 rpm (round per minute) for a sufficient period of 15 minutes. During sieving, the soil particles were completely separated. The masses of several portions retained on the same sieve were combined until particles of the size range of 2-5 mm, 1-2 mm and 0.5-1 mm have been prepared.

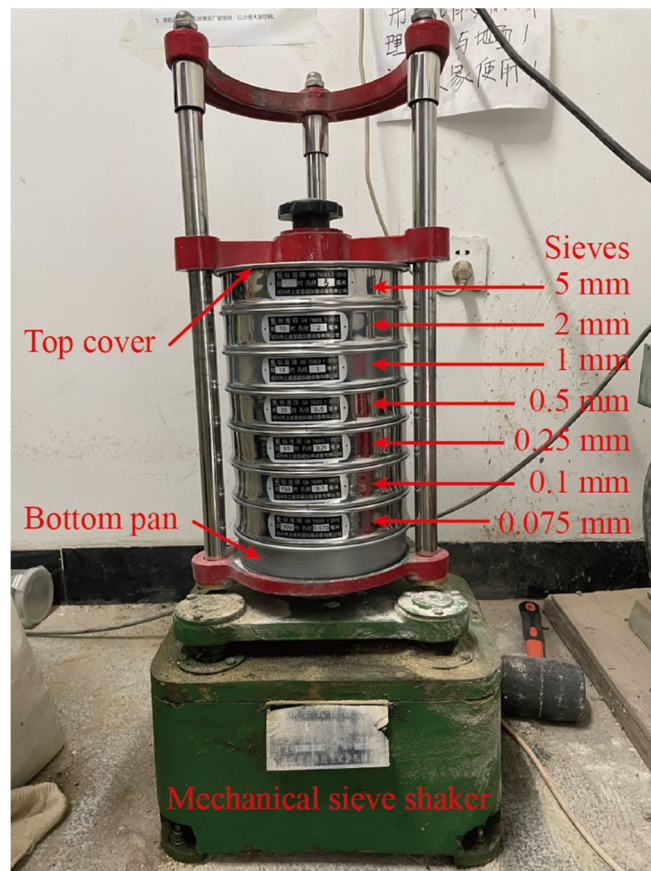


Figure 3.4. Series of sieves installed on the mechanical sieve shaker.

In this research, sand specimens were prepared for one-dimensional consolidation and triaxial compression tests. For each particle size range, specimen with initial relative density (D_r) of 0.5, 0.55, 0.6, 0.65, 0.7, 0.75, and 0.8 were prepared. The relationship between the maximum dry index density, minimum dry index density and initial relative density is given by the following equation:

$$D_r = \frac{(\rho_d - \rho_{dmin})\rho_{dmax}}{(\rho_{dmax} - \rho_{dmin})\rho_d} \quad (3.1)$$

where D_r is the initial relative density; ρ_d is the dry density; ρ_{dmax} and ρ_{dmin} are the maximum and minimum dry index density, respectively. Since the volume (V) of the specimen is known, the mass of specimens with different initial relative densities can be calculated as follows:

$$m = \frac{\rho_{dmax} \times \rho_{dmin}}{\rho_{dmax} - D_r \times (\rho_{dmax} - \rho_{dmin})} \times V \quad (3.2)$$

Each weighed specimen is stored separately in a resealable bag and clearly marked.

3.1.4 The physical parameters of the tested samples

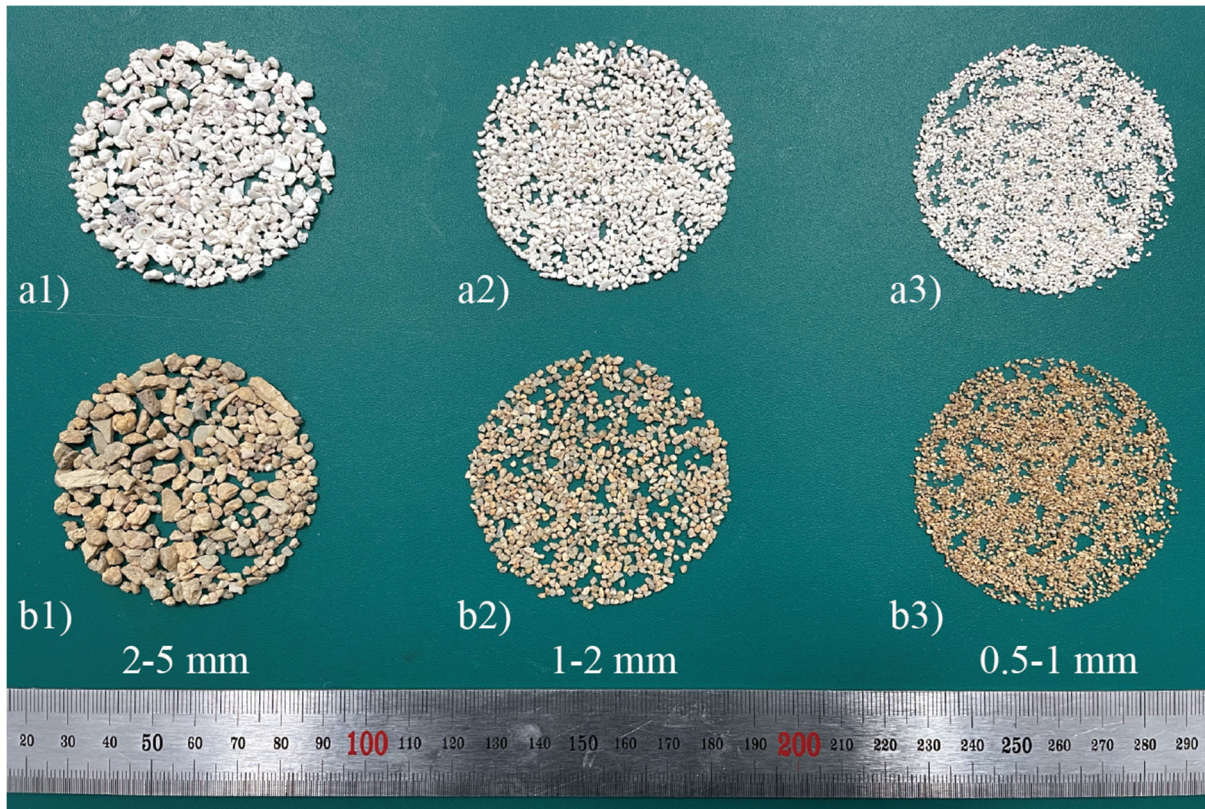


Figure 3.5. Tested materials: a) calcareous sands and b) river sands of particle size range of 2-5, 1-2, and 0.5-1 mm.

Considering the dimensions of the specimen positioned within the triaxial cell and the

purpose to study the influence of particle size on the characteristics of particle breakage and particle morphology, sand particles within the particle size range of 0.5-1 mm, 1-2 mm, and 2-5 mm were sieved and randomly selected (shown in Figure 3.5).

The basic physical parameters of the tested sands are indicated in Table 3.3. The coefficient of uniformity is one of the most commonly used parameters to describe the grading characteristics of soil, and can be calculated by the following equation:

$$C_u = \frac{D_{60}}{D_{10}} \quad (3.3)$$

where D_{60} is the sieve opening size (mm) through which 60% (by weight) of the aggregate passes, and D_{10} is the sieve opening size (mm) that allows 10% of the aggregate to pass. The C_u values were all less than 6, indicating that all the tested samples were classified as poorly graded according to the Unified Soil Classification System (USCS) (ASTM, 2020a). The choice of poorly graded specimens is due to the fact that the poorly graded specimens are more prone to breakage than the well-graded ones.

Table 3.3. The basic physical parameters of calcareous and river sands.

| | Particle size, d (mm) | Specific gravity, G_s | Maximum dry index density, ρ_{dmax} (g/cm³) | Minimum dry index density, ρ_{dmin} (g/cm³) | Coefficient of uniformity, C_u |
|-------------------------|---|---|---|---|--|
| Calcareous sands | 0.5-1 | 2.85 | 1.33 | 1.08 | 2.47 |
| | 1-2 | 2.85 | 1.32 | 1.04 | 1.59 |
| | 2-5 | 2.87 | 1.32 | 1.03 | 1.95 |
| River sands | 0.5-1 | 2.63 | 1.58 | 1.28 | 1.47 |
| | 1-2 | 2.63 | 1.61 | 1.28 | 1.34 |
| | 2-5 | 2.62 | 1.67 | 1.31 | 1.68 |

3.2 Determination of the basic physical parameters

For the testing materials, several basic physical parameters can be obtained from laboratory tests outlined below:

3.2.1 Minimum dry index density (ρ_{dmin})

As described in ASTM D4254-00 (ASTM, 2017), three alternative methods are provided to determine the minimum index density, as follows: Method A—Using a funnel pouring device or a hand scoop to place material in mould; Method B—Depositing material into a mould by extracting a soil filled tube; Method C—Depositing material by inverting a graduated

cylinder. Given the extensive material requirements of Methods A and B (both need cylindrical metal moulds having nominal volumes of 2,830 cm³ and 14,200 cm³, respectively), and their applicability to larger particle sizes (with Method A is applicable to soils in which 100%, by dry mass, of soil particles pass a 75 mm sieve and which may contain up to 30%, by dry mass, of soil particles retained on a 37.5 mm sieve; and Method B is applicable to soils in which 100%, by dry mass, of soil particles pass a 19 mm sieve), Method C (is applicable only to fine and medium sands in which 100%, by dry mass, of soil particles pass a 9.5 mm sieve) emerges as the most appropriate choice for determining the minimum index density in this research.

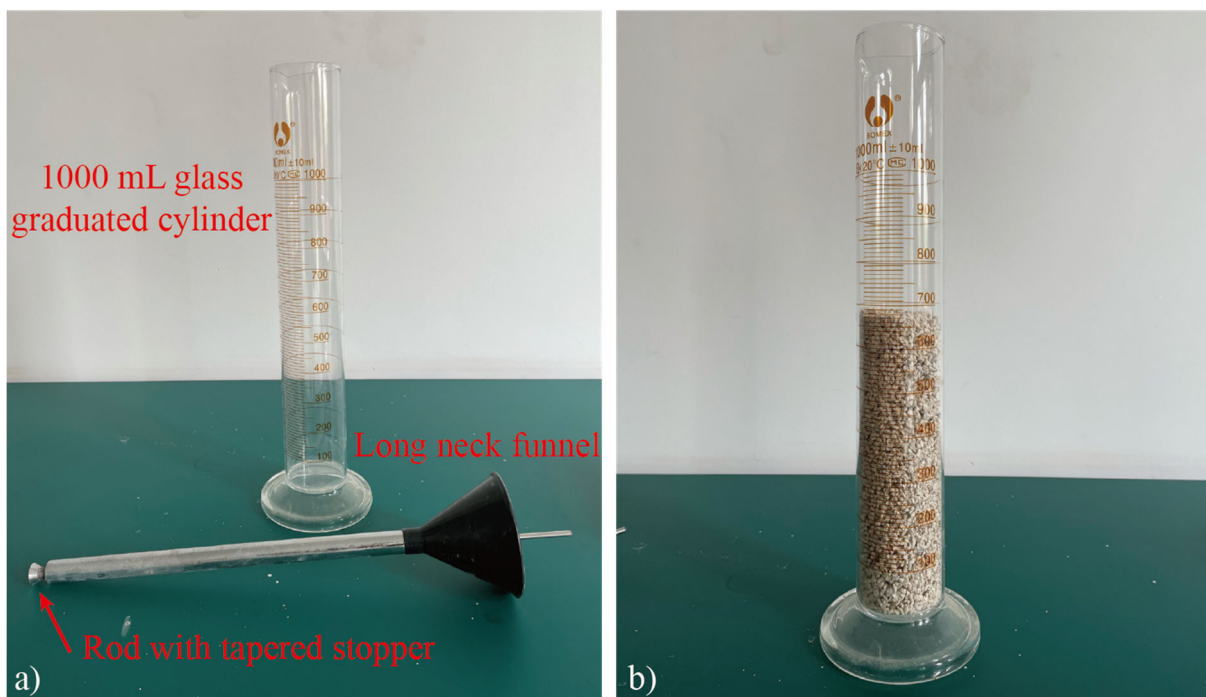


Figure 3.6. a) apparatuses for determining the ρ_{dmin} , including a glass graduated cylinder, a long neck funnel and a rod with tapered stopper; b) the glass cylinder loaded with 700 g of calcareous sands.

As shown in Figure 3.6, the testing device consists of a 1000 mL glass graduated cylinder, a long neck funnel, and a rod with tapered stopper. The rod was inserted through the lower opening of the long neck funnel, which was lifted upward until the lower opening was blocked. Then, they were put into a 1000 mL glass graduated cylinder together so that the lower end of the stopper was in contact with the inner bottom of the cylinder. 700 ± 1 g of sands were weighed. The funnel and the rod were raised at the same time, then the rod was lowered to make the stopper slightly away from the lower opening of the funnel. The lower opening was always kept 1-2 cm above the sand surface to make the sands fall into the cylinder slowly and

evenly distributed. The funnel and the rod were removed after all the sand particles have been poured into the cylinder (Figure 3.6(b)). The sand surface was levelled by using a rod, while avoiding the vibration of the cylinder. The volume that the sand occupies in the graduated cylinder was recorded with precision down to 5 ml. The opening of the cylinder was blocked with one hand or a rubber plate. After which, the cylinder was tipped upside down, and then it was tilted back to the original vertical position. This procedure was repeated several times, and the maximum value of the volume, V_{max} , was recorded. The minimum dry index density (ρ_{dmin}) can be calculated as follows:

$$\rho_{dmin} = \frac{M_s}{V_{max}} \quad (3.4)$$

where M_s is the mass of the tested-dry soil; V_{max} is the maximum volume of the tested-dry soil.

3.2.2 Maximum dry index density (ρ_{dmax})

As described in ASTM D4253-00 (ASTM, 2021b), four alternative methods for determining the maximum index density are provided as follows: Method 1A—Using oven-dried soil and an electromagnetic, vertically vibrating table; Method 1B—Using wet soil and an electromagnetic, vertically vibrating table; Method 2A—Using oven-dried soil and an eccentric or cam-driven, vertically vibrating table; Method 2B—Using wet soil and an eccentric or cam-driven vertically vibrating table. Due to the significantly higher results obtained by the wet method (Method 1B and 2B) for certain soil samples, when considered with the minimum index density, can significantly impact the subsequent calculation of relative density, and considering the time-consuming nature of the wet method, the dry method (Method 1A and 2A) was selected for this study. Additionally, according to ASTM (2021b), the results from the electromagnetic table used in Method 1A are marginally higher than those from the eccentric or cam-driven table used in Method 2A. Consequently, Method 2A was ultimately chosen for determining the maximum dry index density in this research.

The minimum mass of the tested specimen required for the measurement of ρ_{dmax} can be determined based on the volume of the mould as follows:

$$M_r = 0.0024 \times V_m \quad (3.5)$$

where M_r is the required sand mass, and V_m is the volume of the mould. Soil specimen with a total mass of 60 kg were prepared and placed in the cylindrical metal mould with the inner

diameter of 30 cm and height of 34 cm by using a small metal shovel. During loading, the height of the shovel was continuously adjusted to maintain a free fall distance of the sand particles of about 2 cm, and the shovel was moved in a spiral path from the outside to the centre of the mould to keep the thickness of each sand layer consistent. The spiralling movement should be just sufficient to minimize particle segregation. When the mould is filled to overflowing and the soil surface is about 25 mm higher than the top of the mould, the excess sands level is trimmed off by using a steel straightedge carefully. The mass of the empty mould was determined and recorded.



Figure 3.7. Apparatuses for determining the ρ_{dmax} , including a) a vibrating table, a mould, and a hoist; b) vibrator controller; c) surcharge weight.

As illustrated in Figure 3.7, a surcharge base plate was placed on the surface of the soil after the soil was levelled. To make sure the plate is uniformly in close contact with the soil, it was twisted slightly for several times. The handle of the plate was removed, and the mould was fixed to the vibrating table. A guide sleeve was firmly attached to the mould, and then a surcharge weight (surcharge pressure = 14 kPa) lifted by the hoist was placed onto the surcharge base plate. The vibrator controller was set to obtain a double amplitude of vertical

vibration of 0.5 mm at 50 Hz. The mould assembly and the specimen were vibrated for 12 min. After which, the surcharge weight and the guide sleeve were removed. Then, the surcharge base plate was checked to see if it is still uniformly and firmly in contact with the soil surface. The difference in elevation between the mould top surfaces and the upper side of the surcharge base plate was determined by using a dial indicator gage. The volume of the densified sands can be obtained by multiplying the average height by the area of the mould. Finally, the surcharge base plate was removed from the soil surface and the mould was detached from the vibrating table. The mass of the mould and the specimen was determined. The maximum dry index density (ρ_{dmax}) can be calculated as follows:

$$\rho_{dmax} = \frac{M_s}{V_{min}} \quad (3.6)$$

where M_s is the mass of the tested-dry soil; V_{min} is the minimum volume of the tested-dry soil.

3.2.3 Specific gravity (G_s)

The specific gravity (G_s) (true density) of sandy soils was determined by means of a gas pycnometer according to the ASTM D5550-14 (ASTM, 2023). Gas pycnometry is known as one of the most robust methods for determining the true (absolute), skeletal (apparent), envelope density of a material non-destructively by using gas displacement method. Compared to the traditional Archimedes water displacement method, the gas pycnometry technique can provide more accurate, faster, and reproducible measurements. An AccuPyc II 1340 (Gas pycnometer) (Micromeritics, 2023) located at Institute of Rock and Soil Mechanics, Chinese Academy of Sciences, Wuhan, China was used in this research.

As shown in Figure 3.8, a 100 cm³ cylindrical sample chamber with the diameter of 46.2 mm and height of 61.8 mm was prepared and its mass was determined. The chamber was filled with samples appropriately just over half the height. The mass of the chamber and the specimen was determined to obtain the mass of the loaded specimen. Then the chamber was put into the instrument compartment of known volume, which was sealed by using a self-aligning closure (shown in Figure 3.8(a)). High purity nitrogen was used as the displacement medium.

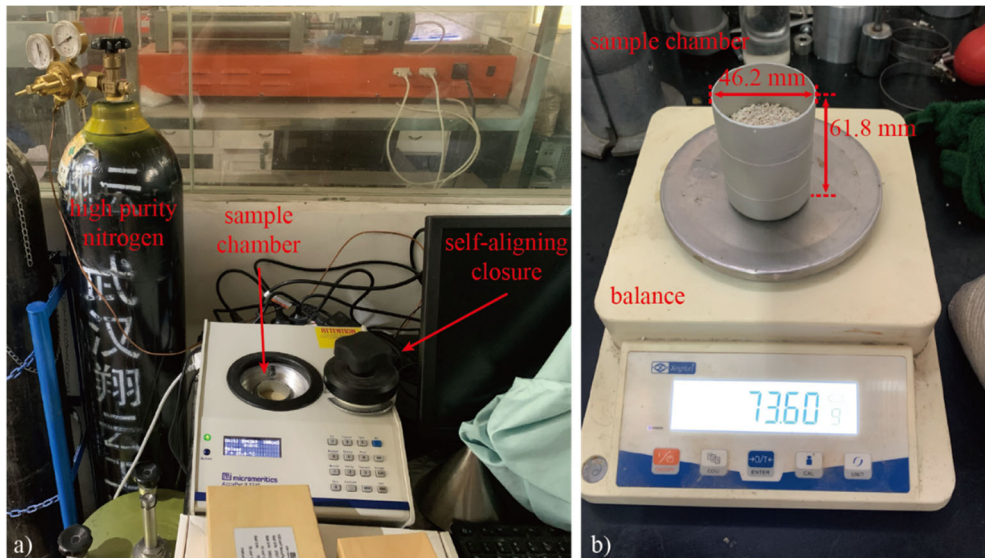


Figure 3.8. a) gas pycnometry system; b) sample chamber loaded with calcareous sands on a balance.

As illustrated in Figure 3.9, the main components of a gas pycnometry system include two chambers, three valves and a pressure gauge. The first step is to purge the sample and the instrument with the gas to remove any other gases that would otherwise interfere with the accuracy of the measurement. The fill and expansion valves are opened, and nitrogen is allowed to flow into both chambers to reach a pressure above atmospheric pressure (typically about 138 kPa). The gas fills up all the empty space inside the chambers, including sample pores. The fill valve is then closed, and the vent valve is opened, which allows nitrogen flows out of the instrument and return the whole system to atmospheric pressure. The purge cycle is then repeated a number of times (5-10 times) to ensure everything is flushed through and the sample is cleaned thoroughly before proceeding to analysis.

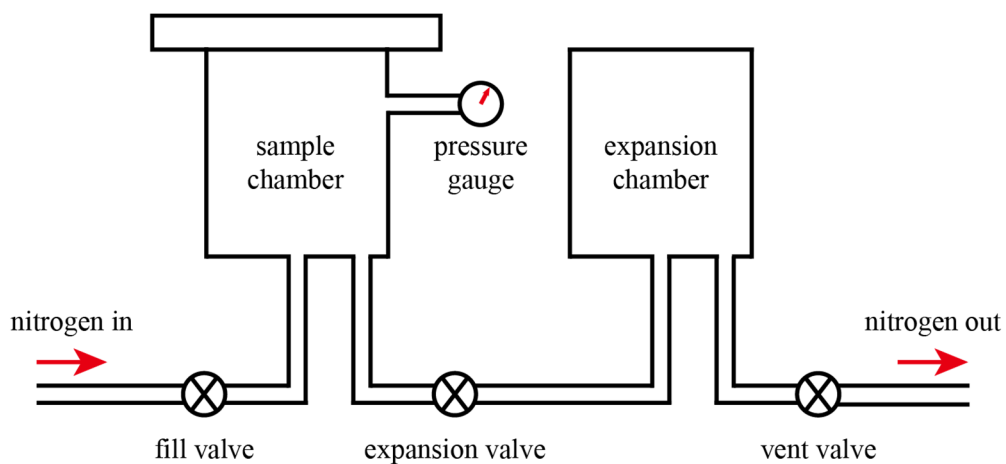


Figure 3.9. Schematic diagram of the measurement of specific gravity by gas pycnometry.

The first stage of analysis is to fill just the sample chamber with nitrogen, which is undertaken to a pressure typically around 138 kPa. The pressure is then allowed time to equilibrate or stabilize. A pressure change of less than 34 Pa is used as conditions for determining a stabilization. With the isolation of sample chamber, this pressure is then recorded and is applied as the value P_1 in the calculation of density. The expansion valve is opened, and gas can then flow from the sample chamber through to the expansion chamber. The pressure is then allowed to equilibrate at the same rate. The pressure recorded at this stage is P_2 . Finally, the vent valve is opened to ventilate the gas into the atmosphere. The measured values of P_1 and P_2 are then used in the following rearrangement of the Boyle's law equation to calculate the pycnometric volume (V_{sample}) occupied by the sample.

$$V_{sample} = V_{cell} - V_{exp} \left(\frac{P_2}{P_1 - P_2} \right) \quad (3.7)$$

where V_{sample} is the calculated sample volume; V_{cell} is the volume of sample chamber; V_{exp} is the volume of expansion volume.

The specific gravity can be determined by dividing the calculated sample volume into the sample weight as follows:

$$G_s = \frac{m}{V_{sample}} \quad (3.8)$$

where m is the sample mass.

3.3 Dynamic image analysis

Before and after the test, the morphological characteristics of individual sand particles can be quantified by applying the dynamic image analysis (DIA) (Microtrac, 2023b), which complies with the ISO 13322-2 (ISO, 2021). DIA characterizes sands by tracking and rapidly imaging individual sand particles during their free fall and storing the resulting digital pictures in computer in real time. Multiple images of each sand particle are acquired by using a high-speed digital camera, thereby the object tracking function allows the software to visualize each particle from numerous orientations. Consequently, the determination of length, width, and thickness for each particle can be achieved by utilizing the pixel size and position data from each image. Based on which, more than 40 morphological parameters can be obtained. In contrast to manual microscopy, the utilization of DIA technology could facilitate the automated

evaluation of a large number of particles within a limited timeframe (usually several minutes).

As illustrated in Figure 3.10(a), a particle size and shape analyser, PartAn^{3D} Maxi (now re-named as Camsizer Online XL) manufactured by Microtrac (2023a), was used in this research. A non-destructive scanning of dry particles with the particle size ranging from 0.16 to 135 mm can be achieved. The photographs of each particle were then digitised and processed by the software PartAn 3D (version: 7.1.2.236), which can analyse more than 100 frames in 1 s.

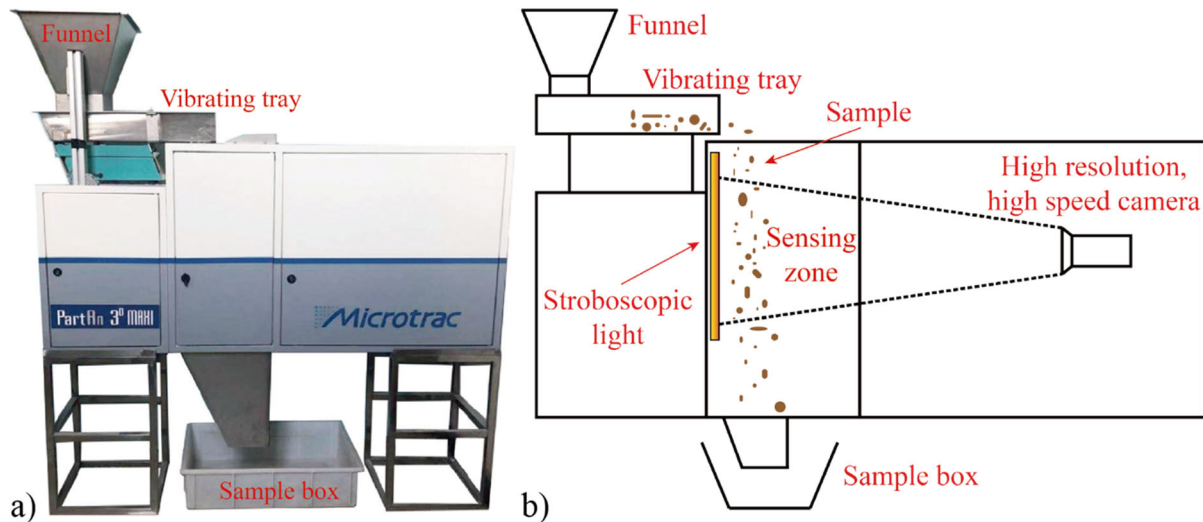


Figure 3.10. a) Particle size and shape analyser, PartAn^{3D} Maxi (modified after Wei et al. (2020)); b) schematic view of the particle size and shape analysing system.

The scanning process was initiated with the vibrating tray started to vibrate, the stroboscopic light was turned on and the high-speed camera entered the work-mode. The sand sample was held in hand at the height of about 2 cm above the central part of the tray, which was then gently poured onto the surface of the tray and evenly distributed each time. The sand particles were slowly moved to the edge with the vibration of the tray and tumbled down by gravity through the sensing zone. A stroboscopic light under the tray was used to light up the illuminated backdrop, and the projections from different orientations of each particle were captured by the high-speed camera on the other side (shown in Figure 3.10(b)). Although the continuous vibration of the tray can make the sand particles tumbling at a certain speed during falling to let different orientations of each particle be captured by the camera, the number of sand particles poured out of the bowl each time needs to be carefully controlled to prevent particle overlapping on the same shooting path on their way down. When the scanning is finished, the sand particles contained in each specimen that falls into the sample box placed

below the sensing zone were collected and bagged again. The whole scanning process was recorded and saved as a video file, which can be reloaded and analysed by the software. As shown in Figure 3.11, each particle has been imaged 13 times (one row per each particle) when they tumbled randomly through the sensing zone to provide abundant information. The images were then digitized to enable the calculation of morphological parameters through the precise determination of pixel size and positioning within the images.

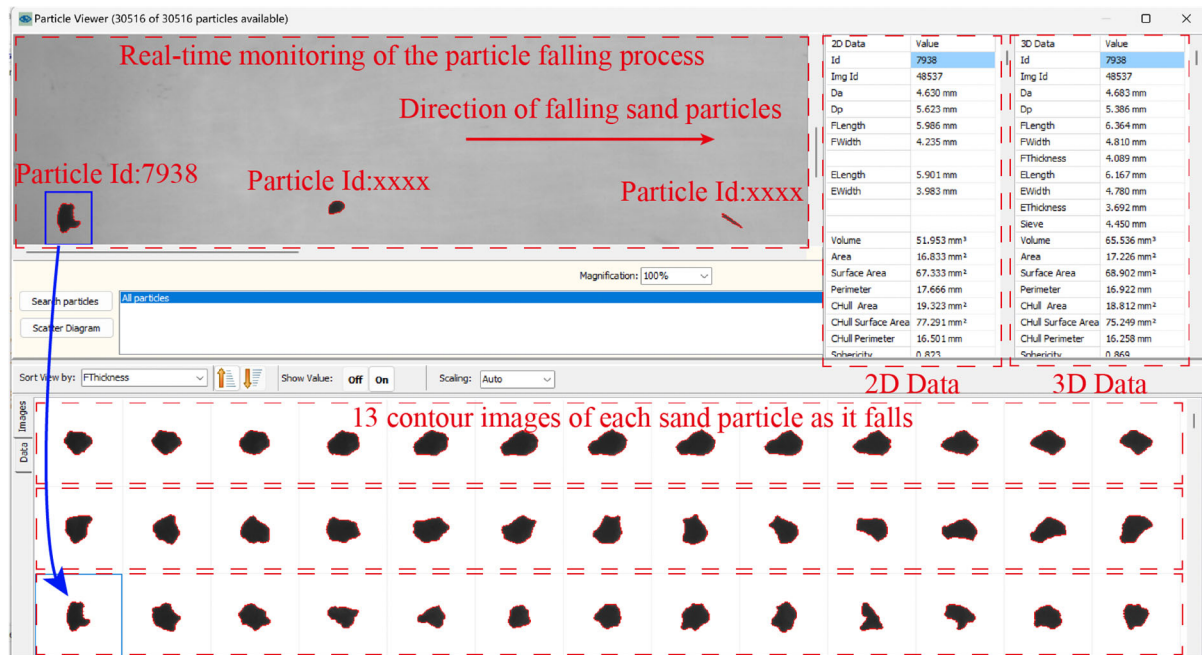


Figure 3.11. Successive snapshots of 3 particles (one row for each particle) during free falling.

As illustrated in Figure 3.12, for a typical particle projection image, the Feret size was computed as the distance between two parallel planes that bound closely to the particle and keep it perpendicular to the planes. Then, the particle length (FL) can be determined as the largest Feret size (F_{max}) obtained in a range of individual particle photos. The width (FW) was taken from the smallest Feret size (F_{min}). Thickness (FT) was not available in 2D mode, and it was determined as the minimum value of FW in a sequence of 3D images. The particle area (A) was determined by calculating the size of the pixels occupied by the 2D image of the particle. The particle perimeter (P_p) was taken as the perimeter of the projected image, while the convex hull perimeter (P_c) was assigned as the perimeter of the convex hull of the image. The convex hull can be visualized as a rubber band which is placed around the particle outline.

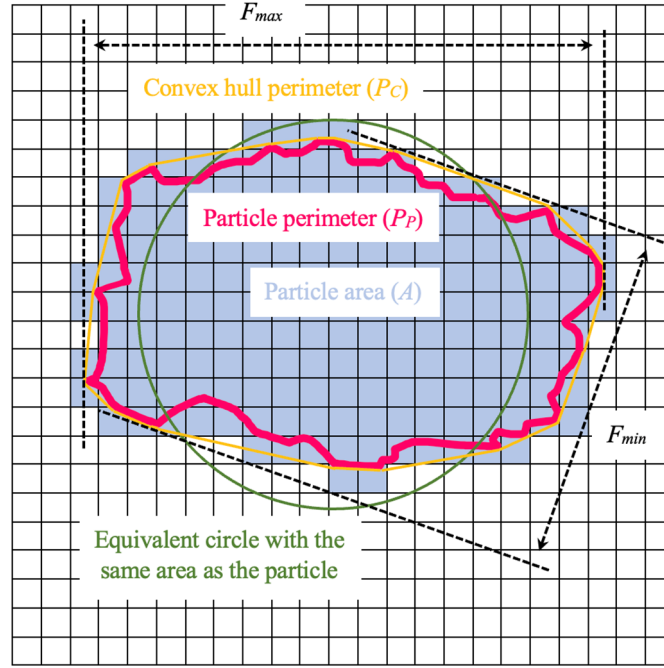


Figure 3.12. An image of digitized particle and definitions of a series of basic dimensions.

The particle dimensions can be characterised by these basic size parameters. Based on which, a series of key shape descriptors can be calculated using the following equations:

$$\text{Area equivalent diameter } Da = (4A/\pi)^{1/2} \quad (3.9)$$

$$\text{Aspect ratio } \alpha = FW/FL \quad (3.10)$$

$$\text{Flatness } \beta = FT/FW \quad (3.11)$$

$$\text{Roundness } R = 4A/\pi(FL)^2 \quad (3.12)$$

$$\text{Sphericity } S = Da/Pp \quad (3.13)$$

$$\text{Convexity } C = Pc/Pp \quad (3.14)$$

Da is determined as the diameter of the equivalent circle with the same area as the particle. Aspect ratio, flatness, roundness, and sphericity are form parameters that use the above basic values to quantitatively represent shape features of the particle. The aspect ratio and flatness range from 0 to 1, where 1 represents a circular shape. The values of roundness and sphericity are the measurement of proximity to a circle, which also range from 0 to 1, where the value 1 equals a perfect circle. As a scale-dependent parameter, roundness is typically characterized qualitatively (Altuhafi et al., 2013). Therefore, in lieu of roundness, sphericity was utilized in this research as one of a basic shape descriptor to quantitatively characterize particle form. Convexity is used to measure the surface roughness, with its value ranging from 0 to 1, where 1 represents a perfectly smooth particle surface. As a general rule, particles with smalls of α , β ,

and C tend to be elongated, flat, and rough (Wei et al., 2020).

3.4 Quantification of particle breakage

By comparing the DIA analysis results before and after the tests, the difference in statistical distribution of each particle morphology parameter and particle size distribution of the specimen can be obtained and analysed. DIA can also be applied in quantifying the degree of particle breakage during the two-dimensional analysis. A novel method using the following formula for characterising the particle breakage factor (B_{r-p}) based on the change of particle perimeters during tests proposed by Wei et al. (2020) was applied in this research.

$$B_{r-p} = \frac{\sum P_a - \sum P_b}{2 \sum P_b} \quad (3.15)$$

where $\sum P_b$ and $\sum P_a$ are the total particle perimeters before and after the test, respectively.

In addition to the innovative approach for determining the degree of particle breakage mentioned above, a traditional method developed by Hardin (1985) using the relative breakage, B_r was also applied in this research for comparison purpose. With its simplicity and robustness, this method has become the most popular and widely used method for quantifying particle breakage of sandy soils in civil engineering research.

The selection of Hardin's theory to quantify particle breakage among various traditional methods is primarily due to its exclusion of particles smaller than 0.074 mm. When processing the data obtained through the DIA method for quantifying particle breakage, the resolution limitation of the imaging equipment prevented the capture of very small particles. Consequently, particles with sizes below 0.074 mm were manually excluded in the subsequent data processing. This approach aligns with the assumptions of Hardin's theory, thereby facilitating a consistent and comparative analysis of particle breakage quantification using both methods. As illustrated in Figure 3.13, this method is applied by comparing the areas between the particle size distribution curves and the vertical line of 0.074 mm sieve size. The relative breakage, B_r can be expressed as a ratio of the total breakage, B_t over the breakage potential, B_p as follows:

$$B_r = \frac{B_t}{B_p} \quad (3.16)$$

where B_t is the area between the PSD curve before and after the test (Area_{ABCA}); B_p is the area

between the PSD curve before the test and the vertical line of 0.075 mm sieve size (Area_{ABDA}).

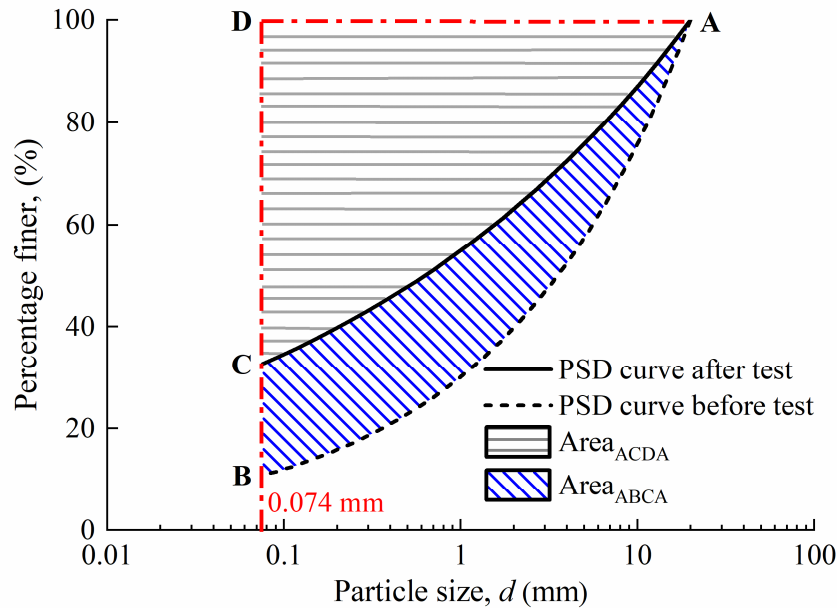


Figure 3.13. The calculation of relative breakage, B_r proposed by Hardin (1985).

3.5 Acoustic emission testing

In order to clarify the micro-mechanical behaviour of particle breakage and its influence on the macro-mechanical behaviour of sand assembly, the acoustic emission testing was carried out during the one-dimensional consolidation tests.

3.5.1 Technique principle

When the strain field of structures or materials is changed due to void formation and development, crack opening and closure, dislocation movement, interfacial failure, fatigue break and deformation, the abrupt redistribution of its internal stress will transform the mechanical energy into acoustic energy and generate transient elastic waves, which is termed as the acoustic emission (AE) (Sagasta et al., 2018). Since the AE signals have a close relationship with these activities, its acquisition, processing, and analysis can be applied to assess the dynamic behaviour of the object being detected and predict its failure. The acoustic emission testing, being a non-destructive testing (NDT) method, offers a significant benefit of allowing continuous in-situ testing, which facilitates the tracking and real-time representation of the initiation and progress of damage within the stressed materials or structures.

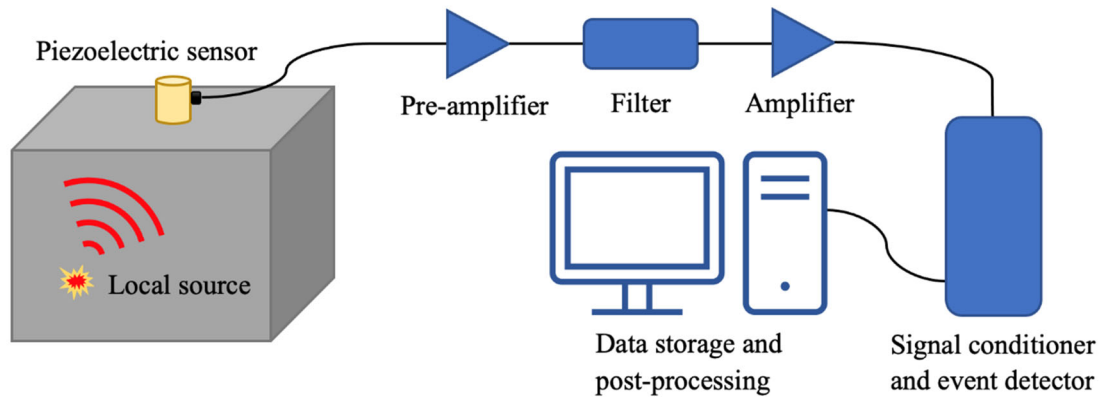


Figure 3.14. Schematic of an acoustic emission testing system.

As illustrated in Figure 3.14, the elastic waves emitted by local sources will propagate through the solid medium and eventually arrive at the material surface, leading to a small range of instantaneous displacement. Since these waves are of high frequency but low amplitude in ultrasonic range, the piezoelectric sensors with high sensitivity are necessary for accurate identifications. After the capture, a few more steps are needed to get useful data that can be identified and processed by the software. A preamplifier is required to amplify the signals to mitigate (as much as possible) the disturbance and avoid the signal loss. After which, a filter is applied to eliminate the unwanted noise and fix the desired frequency domain. Finally, the outputs are digitized and stored for later processing.

AE signals are usually categorized in two qualitative types as “continuous” and “burst”. Continuous emissions correspond to sustained signals resulted from time-overlapping and/or successive emission events such as the fracture processes of ductile metals and can be determined by Root-Mean-Squared (RMS) voltage (Muravin and Carlos, 2011). Burst emissions correspond to discrete AE signals generated by individual events, such as the fracture of non-metallic products or the breakage of corroded materials (Jayakumar, 2011). Most of the micromechanical behaviours of interest in this research are transient and result in burst type AE signals.

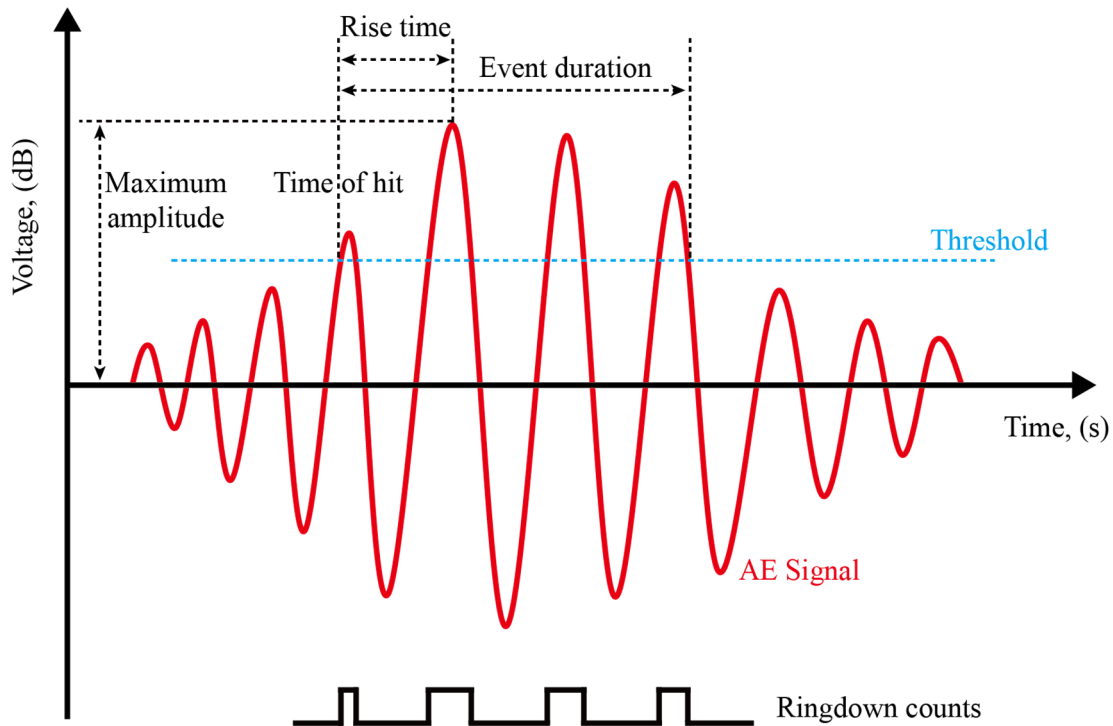


Figure 3.15. Parameters of an AE hit.

There are two main ways to deal with the AE signals: parameter-based (classical) method and waveform-based (quantitative) method (Grosse and Ohtsu, 2008). Nowadays, the characteristic parameter analysis method has been widely used (Gong et al., 2017). As shown in Figure 3.15, various AE hit-based parameters such as ringdown counts (RDC), event duration, rise time and amplitude can be obtained from a digitized AE signal in the time domain, which can be used to characterise the “burst” emissions. Time of hit refers to the time at which the AE signal exceeds the pre-set AE threshold. AE duration is defined as the time interval from the first threshold crossing to the end of the last threshold crossing of the AE signal. Rise time is the time between the time of hit and the peak amplitude. Ringdown counts is the number of times the AE signal excursions over the AE threshold. Because of its simplicity and practical effectiveness, it has become one of the most widely used AE parameters. However, when it is necessary to make the best possible use of the monitored data in some critical situations, it is not enough to analyse the RDC alone. AE amplitude is the largest voltage peak in the AE signal waveform, which relates to energy and can be greatly affected by material and deformation mechanism. It can be measured in dB relative to 1 microvolt at the preamplifier input assuming a 40 dB preamp as follows:

$$dB = 20 \log(V_{max}/1\mu - \text{volt}) - (\text{Preamplifier Gain in dB}) \quad (3.17)$$

AE energy is a relative parameter calculating by integrating the rectified voltage signal over the duration of the AE hit, which is quantitatively proportional to the true energy released from material. Therefore, this parameter is a better choice to characterize the AE intensity than using event hits since it is influenced by both the amplitude and the duration of the signals.

3.5.2 Testing apparatus

An AE testing system located at Institute of Rock and Soil Mechanics, Chinese Academy of Sciences, Wuhan, China was utilized in this research. As presented in Figure 3.16, it is mainly composed of 1 Micro-II Compact PCI AE chassis (PhysicalAcoustics, 2023c) using Express-8-PCI Express-based eight-channel AE boards (PhysicalAcoustics, 2023b), 6 2/4/6 preamplifiers (PhysicalAcoustics, 2023a), and 6 Nano-30 miniature sensors (PhysicalAcoustics, 2023d).

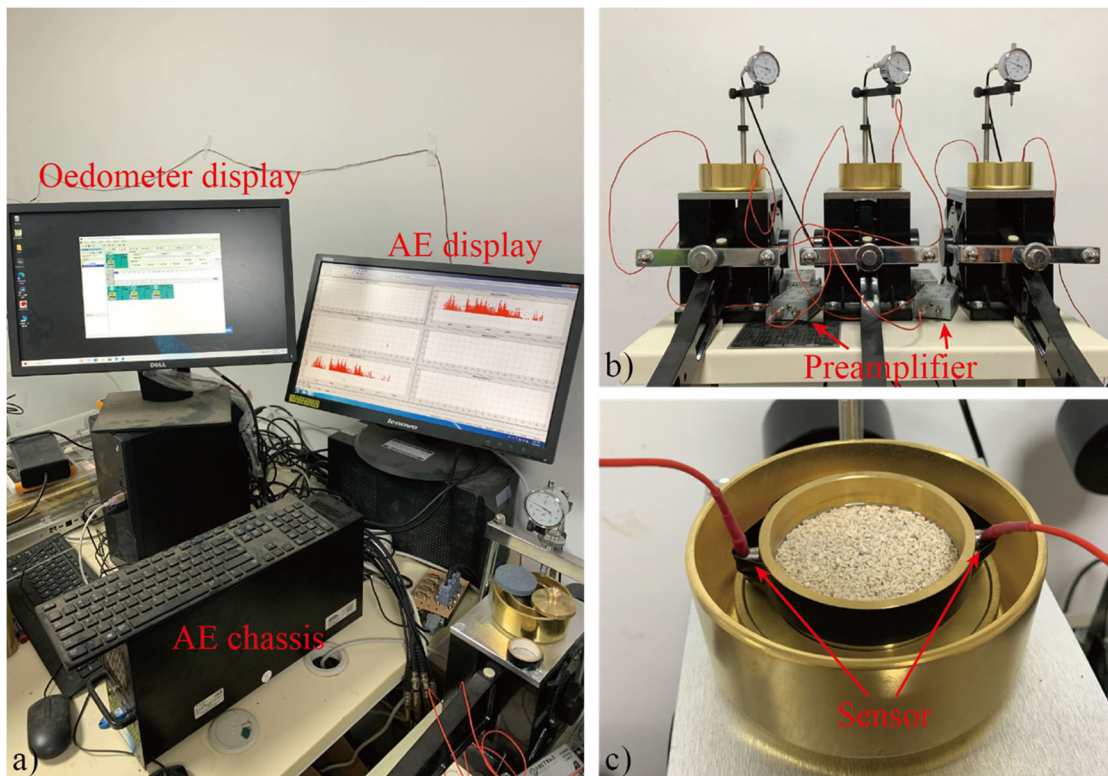


Figure 3.16. Acoustic emission testing set-up.

3.5.3 Operational procedure

Before running the system, all components of the preamplifier were properly connected. As shown in Figure 3.17, the end of the sensor cable was connected to the “SINGLE” input

port of the preamplifier, and the input selection was made by using the switch between two input ports. Then, the “POWER SIGNAL CABLEA” output port of the preamplifier was linked to the input port of the AE board on the back of the AE chassis, and the “GAIN” value of 40 dB was selected. After which, two sensors with couplant on the surface were fastened to the opposite faces of the guide ring by using electrical tapes as presented in Figure 3.16(c). After connecting all the cables, the relevant parameters shown in Table 3.4 were set up by using the software, AEwin.

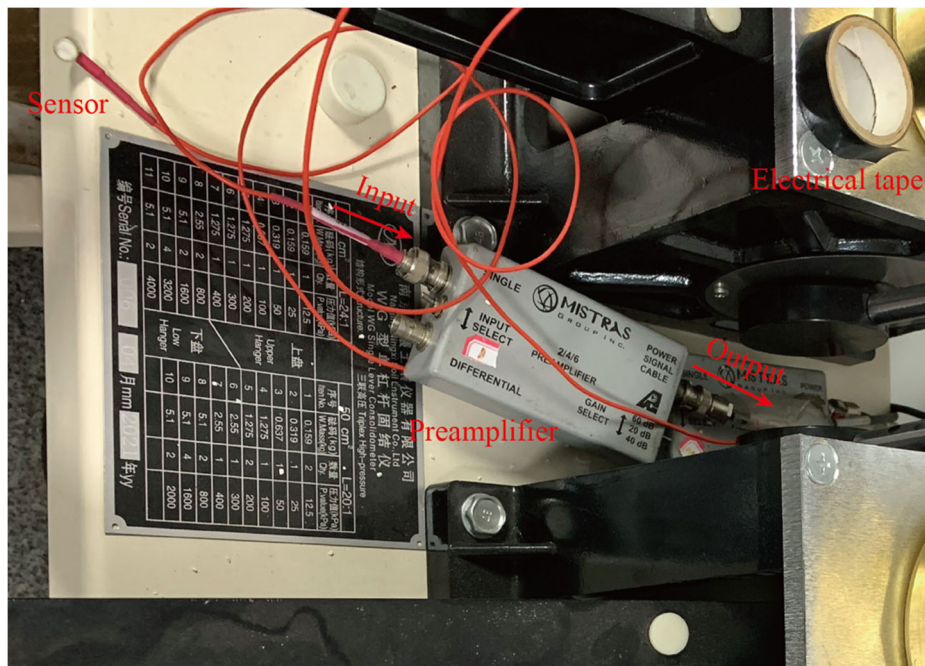


Figure 3.17. Cable connection of the preamplifier.

Table 3.4. Parameter settings by using AEwin.

| | | |
|-----------------------|-----------------|--------------------|
| AE Channel | Threshold type | Fixed |
| | Threshold value | 40 dB |
| Pre-Amp | Type | 2/4/6 |
| | Gain | 40 dB |
| Sensor | Sensor | 30 |
| Analog Filter | Lower | 100 kHz |
| | Upper | 400 kHz |
| Digital Filter | Lower | None |
| | Upper | None |
| Waveform | Sample rate | 5 MSPS |
| | Pre-Trigger | 256.0000 μ sec |
| | Length | 5 k (1 k = 1024) |

AE testing system was tested by conducting the pencil lead break (PLB) test according to

the ASTM E976-15 (ASTM, 2021a). A commercial mechanical propelling pencil with an in-house machined guide-ring was utilized to create artificial acoustic waves by carefully breaking a pencil lead (hardness degree: 2H) with the diameter of 0.5 mm and length between 2 and 3 mm in an angle of 45° against the guide ring ekstexine. The repeatability was examined by performing PLB tests three times for each sensor. During the test, the AE testing system should be kept synchronized with the other testing system. The simultaneous processing and display of the real-time AE features including waveform can be achieved by using the software, AEwin shown in Figure 3.18.

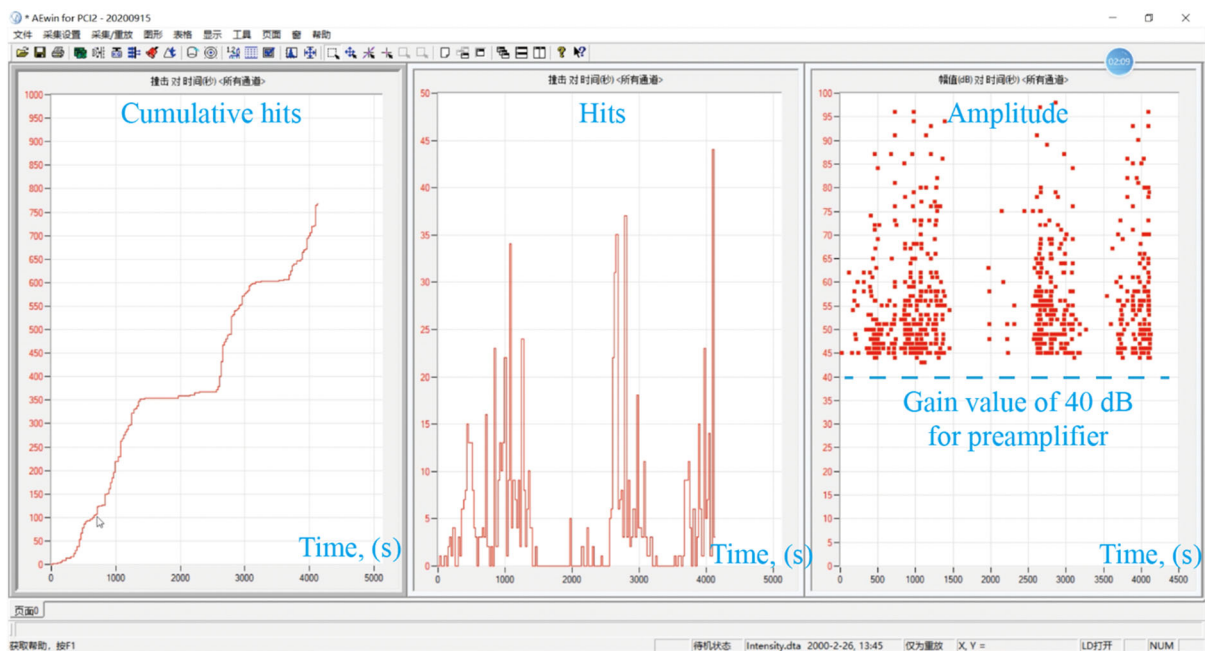


Figure 3.18. Typical real-time results of cumulative AE hits, hits, and amplitude by using AEwin.

3.6 One-dimensional consolidation test

To investigate the settlement characteristics of sandy soils under normal loading, the one-dimensional consolidation (oedometer) tests were carried out on calcareous and river sands. The primary objective is to investigate the settlement of a cylindrical and radially constrained soil sample subjected to a vertical loading. The influence of initial relative density and particle size on particle breakage and the consolidation characteristics of a soil mass were analysed. The changing trends of particle morphology were quantified by comparing the scanning results obtained by using the dynamic image analysis. During tests, acoustic emission testing was applied to characterize the particle breakage characteristics.

3.6.1 Testing apparatus

A single-lever consolidometer (triplex high-pressure) produced by Nanjing Ningxi Soil Instrument Co. (2023), located at Institute of Rock and Soil Mechanics, Chinese Academy of Sciences, Wuhan, China was used. The main components of the testing system include 1 set of loading device, 3 sets of consolidometer, a series of porous stone disks, 3 sets of dial gauges together with the fixed bars and clips, 3 sets of preload weight, a series of weights (ranging from 0.159 to 10 kg) and 3 sets of aluminium samples.

3.6.2 Testing procedure

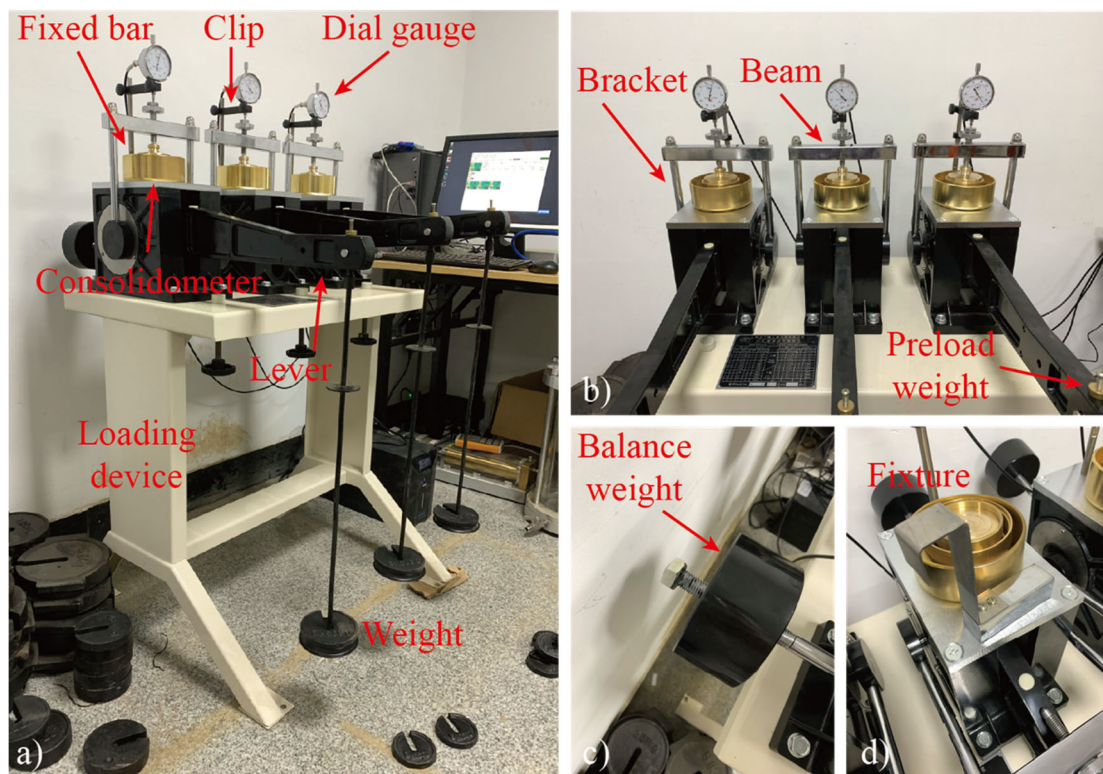


Figure 3.19. One-dimensional compression test set-up.

The one-dimensional compression (oedometer) tests were carried out by applying the “Test Method B” as described in ASTM D2435-04 (ASTM, 2011). Before starting the tests, the loading device should be calibrated and the deformation of the device itself by using aluminium samples under the same loading condition should be measured. A fixture presented in Figure 3.19(d) was used to lock the beam of the loading frame, while keeping the brackets on both sides upright. The screw and balance weight (Figure 3.19(c)) at the end of the lever was simultaneously positioned until the lower end of the lever became horizontal. Then, the screw

behind the balance weight was tightened. An aluminium sample of the same height as the test specimen and slightly smaller in diameter than the cutting ring was placed in the consolidometer. The exact loading and unloading of the consolidometer as in test were carried out, and the vertical deformation of the loading apparatus under each load was recorded, which was then subtracted from the total deformation results obtained in the following tests on specimens to determine the exact vertical deformation of the sand particles under loading.

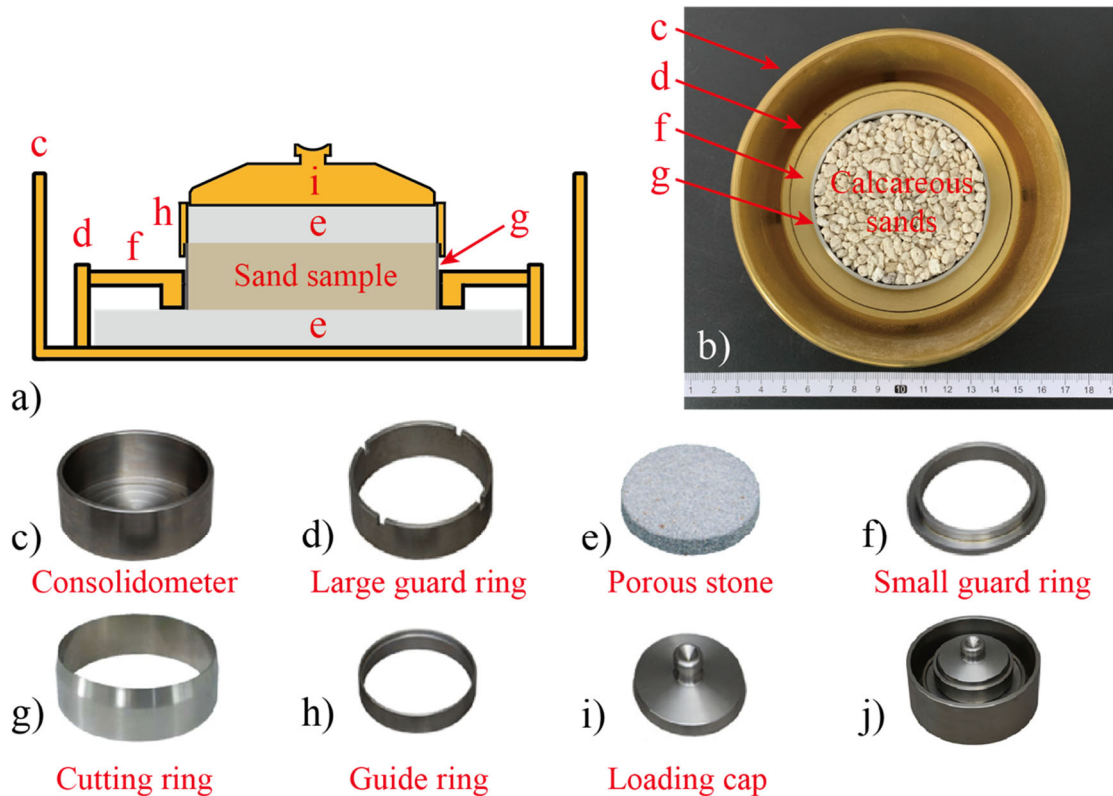


Figure 3.20. Components of a consolidometer.

The consolidometer was assembled as illustrated in Figure 3.20. A large guard ring (Figure 3.20(d)) was placed in the central bottom of the consolidometer (Figure 3.20(c)), and then a large porous disk (83 mm in diameter, 10 mm in height) (Figure 3.20(e)) was placed inside it. A small guard ring (Figure 3.20(f)) was placed on the porous disk against the inner wall of the large guard ring, followed by the placement of a cutting ring (61.8 mm in diameter, 20 mm in height) (Figure 3.20(g)). The entire inner space of the cutting ring was carefully and evenly loaded with the prepared dry sand samples layer by layer. After which, the consolidometer was placed in the centre of the loading platform as shown in Figure 3.19. A guide ring (Figure 3.20(h)) was snapped onto the upper edge of the cutting ring, followed by the placement of a

small porous disk (61.8 mm in diameter, 10 mm in height) on the top surface of the sand sample. Finally, a loading cap (Figure 3.20(i)) was put onto the small porous disk to finish the assembling. A consolidometer loaded with calcareous sands with the particle size ranging from 2 to 5 mm is presented in Figure 3.20(b).

A sitting pressure was applied on the specimen by placing a preload weight (13 g) on the lever (Figure 3.19(b)) to ensure the loading bracket has close contact with the loading cap. The dial gauge was positioned exactly at a right angle to the beam, which was then preloaded as the loading cap was pushed down during the test. A clip and a fixed bar as shown in Figure 3.19(a) were used to make sure the gauge is rigid. The initial reading was then recorded.

Table 3.5. Weight added and cumulative weight in each stage of the oedometer tests.

| Vertical pressure, P_o (kPa) | Weight, (kg) | Cumulative Weight, F_o (kg) | Vertical pressure, P_o (kPa) | Weight, (kg) | Cumulative Weight, F_o (kg) |
|--------------------------------|--------------|-------------------------------|--------------------------------|--------------|-------------------------------|
| 12.5 | 0.159 | 0.159 | 1600 | 10 | 20.199 |
| 25 | 0.159 | 0.318 | 2400 | 10 | 30.199 |
| 50 | 0.319 | 0.637 | 3200 | 10 | 40.199 |
| 100 | 0.637 | 1.274 | 4000 | 10 | 50.199 |
| 200 | 1.275 | 2.549 | 4800 | 10 | 60.199 |
| 300 | 1.275 | 3.824 | 5600 | 10 | 70.199 |
| 400 | 1.275 | 5.099 | 6400 | 10 | 80.199 |
| 800 | 5.1 | 10.199 | 7200 | 10 | 90.199 |

The specimen was then subjected to increments of constant total stress. The loading schedule was set as 12.5, 25, 50, 100, 200, 300, 400, 800, 1600, 2400, 3200, 4000, 4800, 5600, 6400, 7200 kPa. The vertical loading applied to the specimens was usually set to increase exponentially, but in this study more values were added to better observe the changes in the void ratios of the specimens. In particular, when the loading exceeded 3200 kPa, small increments (800 kPa) were applied for each stage since that intense particle breakage leads to a rapid decrease in the void ratio, which needs to be recorded more precisely. When the maximum load (7200 kPa) was reached, the unloading schedule was set in a descending order opposite to the loading schedule. To achieve a force applied to the specimen in a vertically downward direction that is consistent with the experimental design scheme, the weight of the weights to be loaded can be calculated by the following formula, provided that the beam ratio of the device is known to be 1:24 (i.e., 1 kg applied on the beam = 24 kg on the specimen).

$$F_o = \frac{P_o \times A_o}{0.0098 \times 24} \quad (3.18)$$

where F_o is the cumulative weight loaded on beam; P_o is the vertical pressure applied on the specimen, and A_o is the surface area of the specimen. The weight added and cumulative weight in each stage are listed in Table 3.5.

For each loading increment or decrement, the changes in height were recorded at time intervals of 1h. Once the disparity between consecutive readings became less than 0.01 mm, the sample deformation was considered to be stable. Then, the next level of loading could be implemented. The void ratio of the specimen during test can be determined as:

$$e = e_0 - (1 + e_0) \Delta h / h_0 \quad (3.19)$$

where h_0 is the initial height of the specimen; Δh is the vertical deformation of the loading frame; e_0 is the initial void ratio, defined as follows:

$$e_0 = \frac{h_0 - h_s}{h_s} \quad (3.20)$$

where h_s is the equivalent height of solid phase, defined as follows:

$$h_s = \frac{V_s}{A_o} \quad (3.21)$$

where A_o is the specimen area; V_s is the volume of solids, defined as follows:

$$V_s = \frac{M_d}{G_s \rho_w} \quad (3.22)$$

where M_d is the dry mass of specimen; G_s is the specific gravity; $\rho_w = 1.0 \text{ g/cm}^3$ is the water density.

After the test, the cutting ring and the specimen were removed from the consolidometer. The PSD of the specimen after test can be obtained by applying sieving analysis with a series of sieves of diameter 200 mm and openings ranging from 0.075 to 5 mm as presented in Figure 3.4. Then, particles smaller than 0.1 mm were removed from the sample and the remaining part was analysed by using DIA to get their morphological parameters after the test.

3.7 Consolidated drained triaxial compression test

The triaxial shear tests have been historically used to measure the strength parameters of soils. It yields comprehensive data on both the strength parameters and the stress-strain behaviour (Terzaghi and Peck, 1948, Hvorslev, 1960, Saada and Townsend, 1981, Potts et al.,

1987, Maccarini, 1993). Since calcareous sand particles have abundantly developed internal pores and relatively large particle sizes, the drainage condition is generally good. Thus, the consolidated and drained (CD) shearing is the most common stress condition for calcareous sands in practice (Wang et al., 2019c). Therefore, in this research, the CD triaxial compression tests have been carried out on calcareous and river sands to investigate the influence of particle breakage and morphology on the shear strength of sandy soils according to the ASTM D7181-20 (ASTM, 2020b). In this approach, the cylindrical specimen is consolidated and sheared under compression with drainage at a constant rate of axial deformation.

3.7.1 Testing apparatus

As presented in Figure 3.21, a TAS-LF fully automatic triaxial testing system produced by Xi'an KTL Instruments Co. (2023) and the software GeoSmartLab (version: 1.8.4.0) were used in this research. The system is mainly composed of a digital loading frame (model: LDF50), 2 standard volume pressure controllers (model: SVPC-1000-2 and SVPC-200-2), and a triaxial cell (model: TTC) equipped with a submersible force sensor.

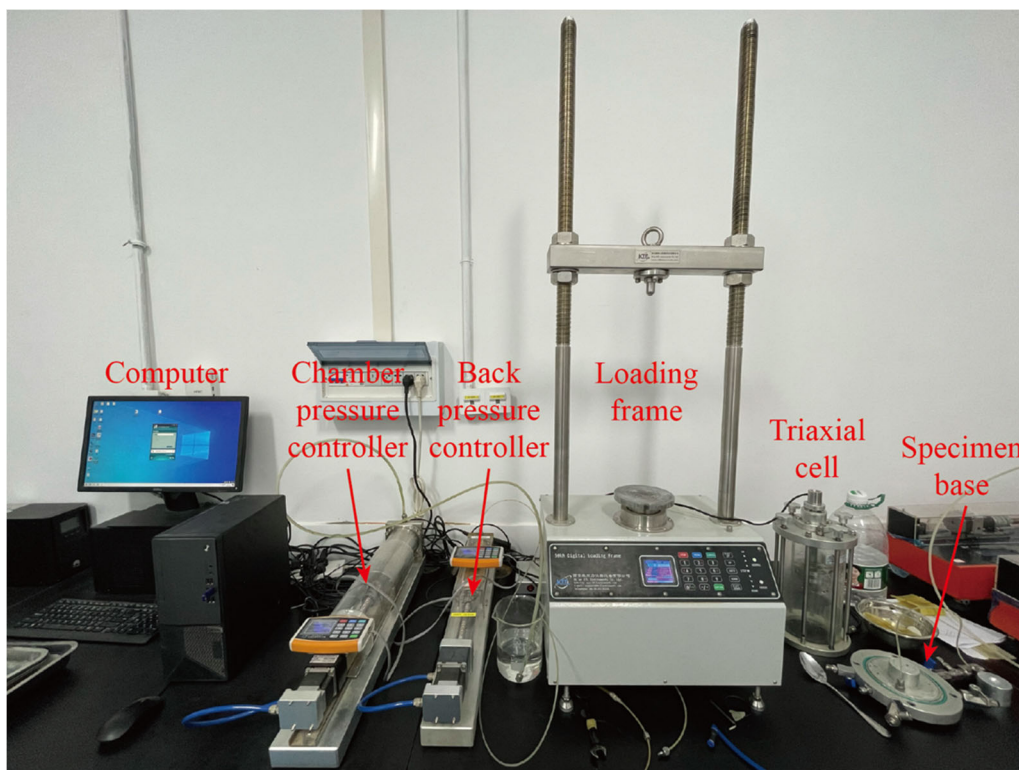


Figure 3.21. Consolidated and drained triaxial compression test set-up.

3.7.2 Sample preparation

The calcareous and river sands of different initial relative density ($D_r = 0.5, 0.55, 0.6, 0.65, 0.7, 0.75, 0.8$) and particle size (0.5-1, 1-2, 2-5 mm) were prepared. First, a porous disk with a diameter of 61.8 mm and height of 2 mm, a porous stone with the diameter of 61.8 mm and height of 10 mm, and a filter-paper disk of a diameter of 61.8 mm were placed on the specimen base from bottom up. A rubber membrane of thickness 1 mm was first inspected thoroughly to identify any potential defects such as flaws, leaks, or pinholes prior to use. Then, it was rolled on the base and sealed with 3 rubber bands. Subsequently, a customised split mould was placed on the base, the two halves of the mould were fit tightly together by 2 hose clamps to form a sleeve outside the rubber membrane. The membrane was tensioned and stucked tightly to the inner wall of the mould. The membrane above the top edge of the mould was then rolled down (Figure 3.22(a)). The cylindrical specimen with a diameter of 61.8 mm and height of 120 mm was prepared by compacting sand particles in 10 layers using a funnel, a tamper, and a steel ruler. Each layer of sands was weighed and placed in the mould by air pluviation. The specimen was compacted to the desired initial relative density by tamping each layer until the accumulative mass of the sand particles in the split mould was compacted to a known height (Figure 3.22(b)). After the final layer was compacted, a filter-paper disk, a porous stone, and the specimen cap were placed in the specimen surface in turn (Figure 3.22(c)). The preparation of the specimen was completed by releasing the folded membrane, placing the membrane ends over the specimen cap, and sealing the specimen cap with 3 rubber bands.

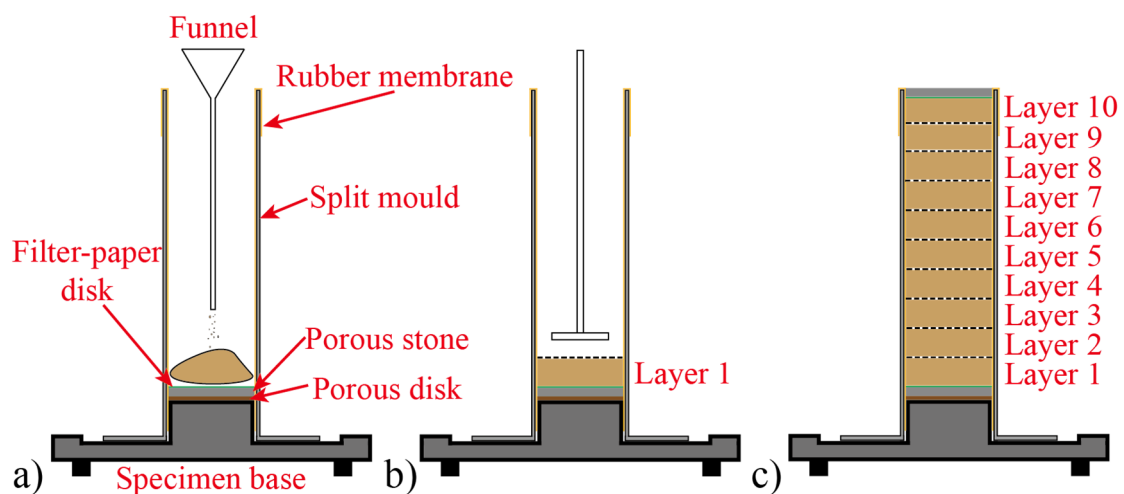


Figure 3.22. Illustration of specimen preparation for triaxial tests.

A partial vacuum of 20 kPa was applied to the specimen by using a vacuum pump to maintain its shape and size. The split mould was then removed. The preparation of a vacuumed specimen is shown in Figure 3.23(a) and (b).

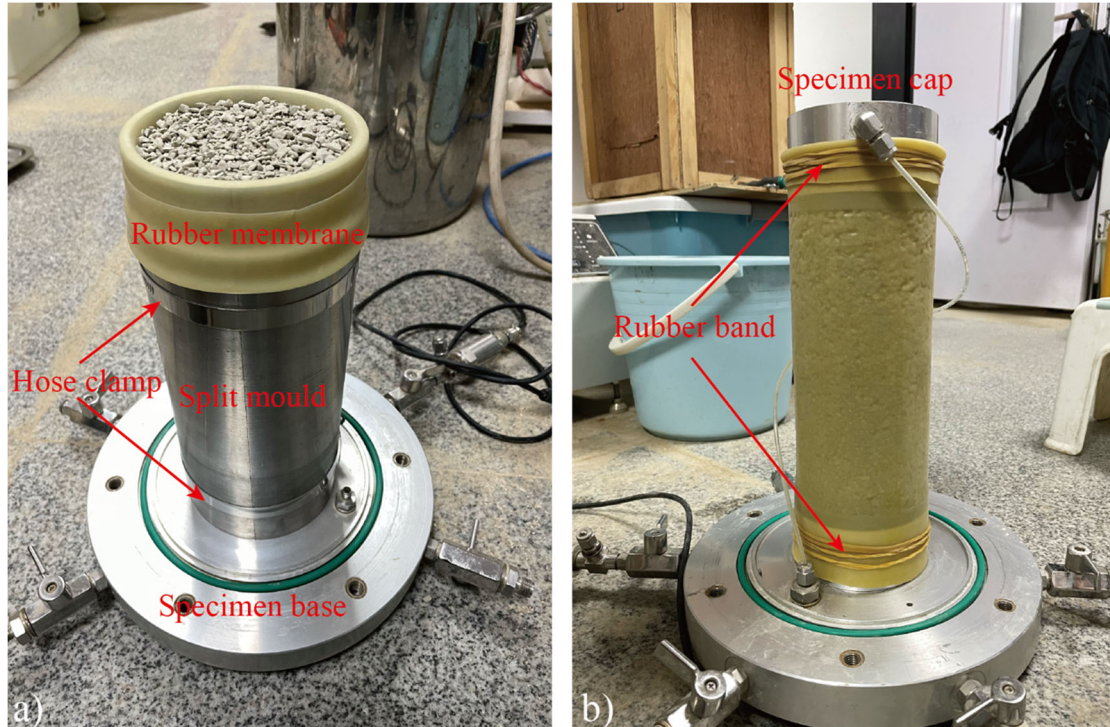


Figure 3.23. a) Sample preparation; b) Vacuumed specimen for triaxial tests.

The triaxial cell was then assembled, and the application of a modest amount of silicon grease onto the vertical surfaces of the cell and base will facilitate the secure sealing of the cell. After tightening the bolts, the axial load piston was lowered carefully to touch and in alignment with the specimen cap. The cell was placed on the platform of the loading frame and was then filled with water without trapping air by using a water pump.

3.7.3 Saturation

The aim of the saturation stage in the test is to effectively permeate the specimen with water, avoiding any unwanted distortions or agitations, and preventing any migration of fines. To help reduce the required pressure, the volume of water, and shorten the saturation duration, the sample can be flushed with carbon dioxide (CO_2) before water flushing, because CO_2 dissolves faster in water than air (Jefferies and Been, 2015, Lade, 2016, Naghavi, 2017, Naghavi and El Naggar, 2019, da Fonseca et al., 2021). In this research, both saturation methods, with and without the use of CO_2 were performed and subsequently compared.

Saturation without the use of CO₂ (applying vacuum to the specimen and dry drainage system, and then allowing deaired water to flow through the system and specimen, while maintaining the vacuum state) usually takes about 2 hours to complete (with 1 hour of vacuuming and 1 hour of allowing deaired water to flow through the system). However, when the method using CO₂ was employed, the saturation step was completed in just half an hour, and in addition, the completion time of the followed consolidation step was shortened as well. The primary benefit of employing CO₂ is the expedited attainment of full saturation in cohesionless soils compared to alternative methods. Therefore, carbon dioxide is used during saturation.

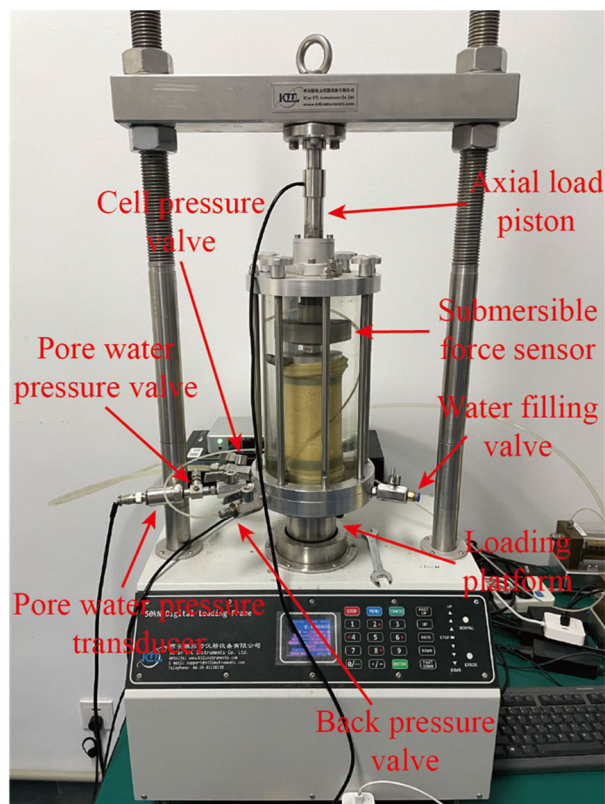


Figure 3.24. A prepared sand specimen before shearing.

During the saturation process, a pressure of 10 kPa was applied to the specimen by using the cell pressure controller, while a partial vacuum of 10 kPa was applied. Then, the cell pressure was adjusted to 20 kPa with the closure of the pump. At this point, there remains a consequential confining pressure of 20 kPa upon the sand specimen, notwithstanding its exposure to the outside air. The sand specimen was then flushed with carbon dioxide under a pressure about 3 kPa, smaller than the cell pressure. The CO₂ from a compressed gas cylinder entered through the pore water pressure valve is shown in Figure 3.24, circulating upwards in

the sand specimen, and finally out through the back pressure valve (shown in Figure 3.24) connected to the specimen cap. A tube attached to the back pressure valve, open and submerged in water contained in a beaker, enables the observation of both the bubbling rate and the volume of CO₂ percolated. To guarantee the complete displacement of air, CO₂ flushing is conducted for approximately 20 minutes. The deaired water with a volume of about 400 ml was then allowed to percolate slowly from the bottom to the top of the sand specimen by using the back pressure controller. The triaxial cell was then lifted by manually control, allowing the upper end of the axial load piston just touch and in alignment with the fixed head on the beam.

Tiny air bubbles may still adhere to the sand particles after flushing the deaired water. This has been proven to be challenging to remove. Full saturation is subsequently achieved by applying high pressures to the pore fluid, ensuring the complete dissolution of pore air into the pore water. As shown in Figure 3.25(a), the cell and back pressure is incrementally increased simultaneously in steps to high levels, while maintaining a low effective stress of 15 kPa.

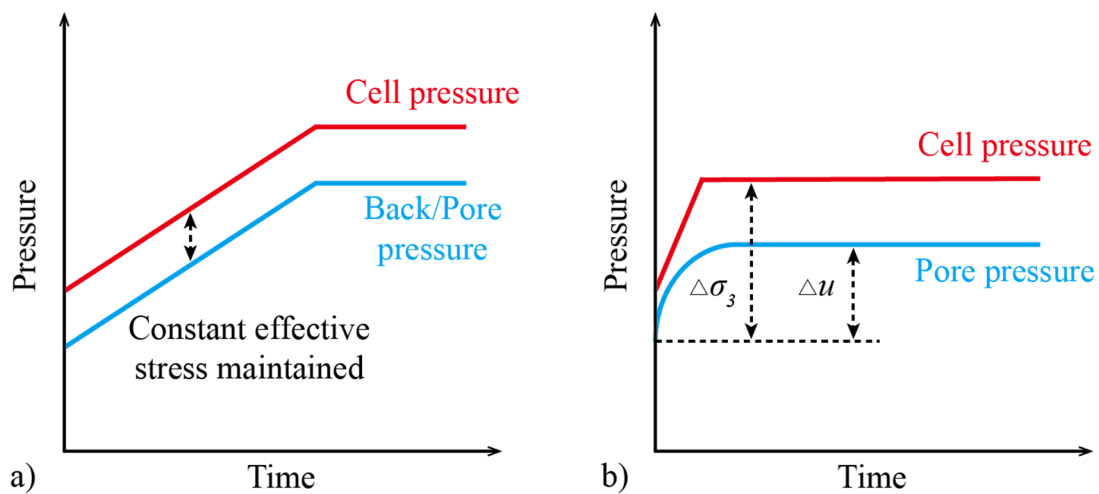


Figure 3.25. Pressure variation during stages of a) Specimen saturation; b) *B*-check.

To achieve a full saturation state, the required back pressure values vary depending on the experimental equipment and materials. da Fonseca et al. (2021) suggested that a back pressure of 300 kPa, in conjunction with CO₂ and deaired water flushing, can effectively achieve full saturation of cohesionless remoulded soils during triaxial testing. For certain soil samples, achieving a satisfactory level of saturation necessitates applying back pressures exceeding 500 kPa (Lowe, 1960, Soliman, 1983, Naghavi and El Naggar, 2019). By comparing various back pressure values, this research determined that a back pressure of 600 kPa is effective in

achieving full saturation of both calcareous and river sand specimens. Generally, the back pressure was increased to 600 kPa in the first ramp, followed by the determination of a pore pressure parameter, B to check if the specimen saturation is sufficiently high (Skempton, 1954). As presented in Figure 3.25(b), the cell pressure is increased to a specified value, whilst the back pressure valve is closed, which is the state where no drainage has occurred. The value of B can be obtained by using the following equation:

$$B = \frac{\Delta u}{\Delta \sigma_3} \quad (3.23)$$

where Δu is the change in the specimen pore pressure caused by the increase in cell pressure in the undrained state; and $\Delta \sigma_3$ is the isotropic pressure change in the cell pressure.

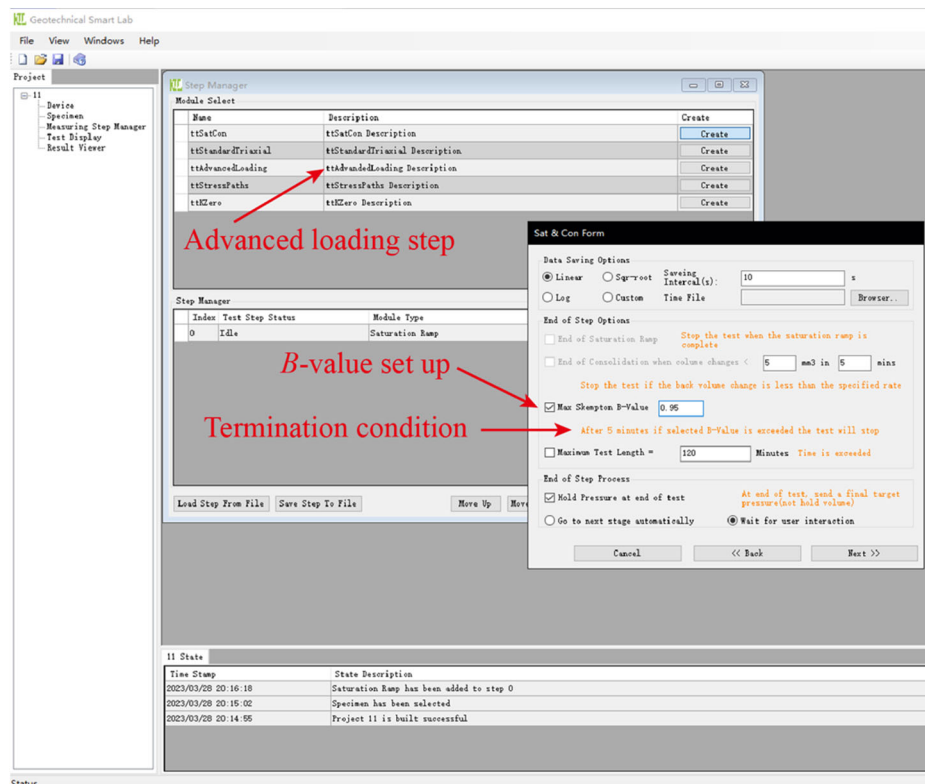


Figure 3.26. Set up of the “ B -check” step in the triaxial testing system using the software GeoSmartLab.

As shown in Figure 3.26, the “ B -check” step can be performed automatically through the software control, in which an increase of 20 kPa in cell pressure was used. When the termination condition, i.e., “the specified value of B (0.95) is exceeded after 5 minutes” is met, this step is automatically stopped and the next stage, i.e., consolidation is automatically initiated. If the condition is not satisfied, the same step prior to the “ B -check” needs to be

repeated by increasing the back pressure by setting a larger value of the cell pressure. These steps should be repeated until the value of B is equal to or greater than 0.95.

3.7.4 Consolidation

To achieve the equilibrium state in a drained state at the effective stress required for shearing, one commonly employed approach involves increasing the cell pressure to consolidate the sample, while maintaining a constant back pressure, which is typically equivalent to the pore pressure attained during “ B -check”.

The “Advanced loading” step can be run automatically through software control. The axial load piston and the specimen cap were in contact during the consolidation by applying a load of 0.01 kN. The consolidation is continued until the volume change-time curve becomes gradually horizontal. When the termination condition, i.e., “volume changes are less than 5 mm³ in 5 minutes” is met, this step is automatically stopped, and the consolidation is completed.

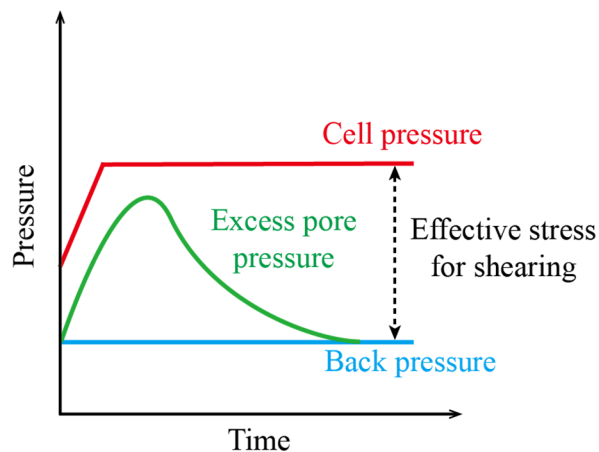


Figure 3.27. Pressure variation during the consolidation of test specimen.

3.7.5 Drained shear loading

The model configuration with prepared sand specimen before shearing is presented in Figure 3.24. The sand sample is sheared by applying an axial strain (ϵ_a) to the test specimen at a constant rate of 0.08 mm/min by upward movement of the loading platform. The velocity is sufficiently slow to produce an insignificant alteration to pore pressure. During shearing, the cell pressure and back pressure were maintained constant. The specimen drainage was allowed, and the volume change was recorded automatically. This step is continued until the axial strain of 30% has been reached. During shearing, the cross-sectional area of the specimen, A_{cs} , can

be calculated using the following equation:

$$A_{cs} = \frac{V_c - \Delta V_\varepsilon}{H_c - \Delta H_\varepsilon} \quad (3.24)$$

where V_c is the specimen volume after consolidation; ΔV_ε is the volume change from the beginning of shear; H_c is the specimen height after consolidation, and ΔH_ε is the height change from the beginning of shear.

The deviator stress, $\sigma_1 - \sigma_3$, can be calculated as follows:

$$\sigma_1 - \sigma_3 = \frac{P + \sigma_3(A_{cs} - a)}{A_{cs}} - \sigma_3 \quad (3.25)$$

where P is the value obtained by the submersible force sensor; σ_1 is the major principal stress; σ_3 is the minor principal stress (confining stress); A_{cs} is the cross-sectional area of the specimen; a is the cross-sectional area of axial load piston. In this research, since a force sensor of the submersible type was used, $a = 0$.

Three specimens of the same initial relative density and particle size were tested at different effective consolidation stresses from 100 kPa up to 800 kPa. The selection of the confining pressure level follows the practical engineering perspective for the loading condition of most offshore structures. For example, the fixed-foundation offshore wind farms are regularly deployed in water depths of up to 40 meters, with some installations extending to depths of 60 meters (Brears, 2024). Additionally, in terms of particle breakage, it has been observed that significant particle breakage had already occurred in calcareous sand specimens when the confining pressure reached 400 kPa (Liu et al., 2020, Wei et al., 2021). Consequently, the maximum confining pressure of 800 kPa was adopted in this research.

Chapter 4 One-Dimensional Consolidation Tests

This chapter presents a study of the consolidation behaviour of two types of sandy soils: calcareous sands and river sands, with the focus on investigating the effects of particle breakage and particle morphology on the compression and expansion of the sands. High-speed dynamic scanning was used to quantitatively determine the particle morphological parameters. Particle breakage was quantified by employing both mechanical sieving analysis and dynamic image analysis. Acoustic emission testing was used during tests, which provided useful insight into the fracturing mechanisms of sand particles. All experimental results under various test conditions are presented to analyse the occurrence and degree of particle breakage, trends in particle morphology, and their influence on the consolidation of the tested materials subjected to various affecting factors, including initial relative density, and particle size.

4.1 Experimental setup

Due to the long duration of the one-dimensional consolidation experiment and the need for manual application of weights in time, the time required for specimens to reach stability at each pressure varies slightly. The overall normal stress level of calcareous and river sand samples are basically the same, thus only the results of calcareous tests are shown. Figure 4.1(a) shows the duration of the loading and unloading processes for each level of effective normal stress during the 1-D consolidation test on calcareous sands with initial relative density of 0.7 in the size range of 2-5 mm. All individual experiments were completed within 5 to 6 days. The longer duration of the four phases, as indicated by the red arrows in Figure 4.1(a), is because the load was applied and kept constant on the specimen during the night. An enlarged view of the initial phase of the loading- and unloading-time relationships under vertical pressures smaller than 400 kPa are presented in Figure 4.1(b) and (c), respectively. At relatively low normal loading pressures, i.e., when the effective normal stress was less than 800 kPa, most of the testing stages reached stability in about 1 hour. As the experiments progressed, the time required to reach steady state for each stage under high pressure loading (i.e. between 1600 kPa and 7200 kPa) became significantly longer, taking approximately 2 to 8 hours. In the subsequent unloading

phase (i.e. from 7200 kPa to 12.5 kPa), all stages were able to reach stability within 1 hour.

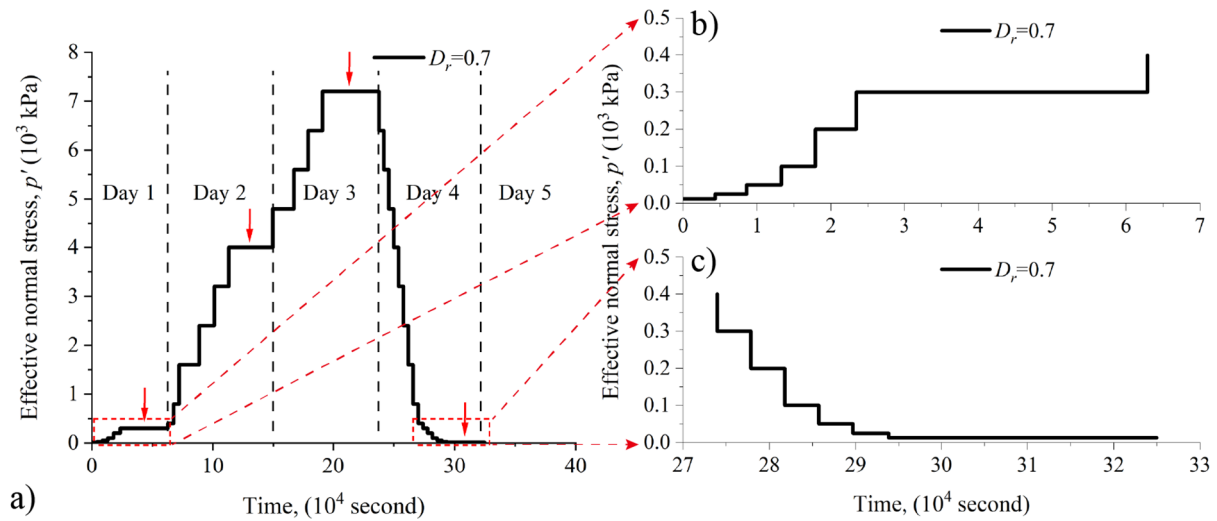


Figure 4.1. Effective normal stress-time relationships for calcareous sands with initial relative density of 0.7 in the size range of 2–5 mm during 1-D consolidation test. (b)(c): enlarged views.

4.2 Relationship between void ratio and effective normal stress

4.2.1 Influence of initial relative density on the evaluation of void ratio during compression

Figure 4.2 presents the evolution of void ratio (e) with the effective normal stress (p') for calcareous and river sands of the initial relative density ranging from 0.5 to 0.8 and particle size range of 2-5 mm during the one-dimensional consolidation. The evolution of soil void ratio under the incremental loads is characterized by obvious 3 stages. During the initial stage, designated as stage 1, the sand samples were gradually consolidated under a small level of normal stress with the value less than 400 kPa. This consolidation process resulted in only a small reduction in void ratio, a phenomenon that may be attributed to the high resistance by particle interlocking and internal friction, thereby hindering the void ratio reduction. In stage 2, a rapid increase in void ratio reduction can be observed with the increase of the normal stress. The curves underwent the maximum degree of “bending”, and the point of maximum curvature on the curves can be clearly observed. In stage 3, under the action of higher pressures (e.g. larger than 3000 kPa), the void ratio demonstrated a significant linear decrease trend in a semi-logarithmic plot as the loading stress increased. During the subsequent unloading stages, a small rebound of the specimen induced by the gradual reduction of the vertical pressure was observed, resulting in a minor increase in the void ratio in a nearly linear pattern.

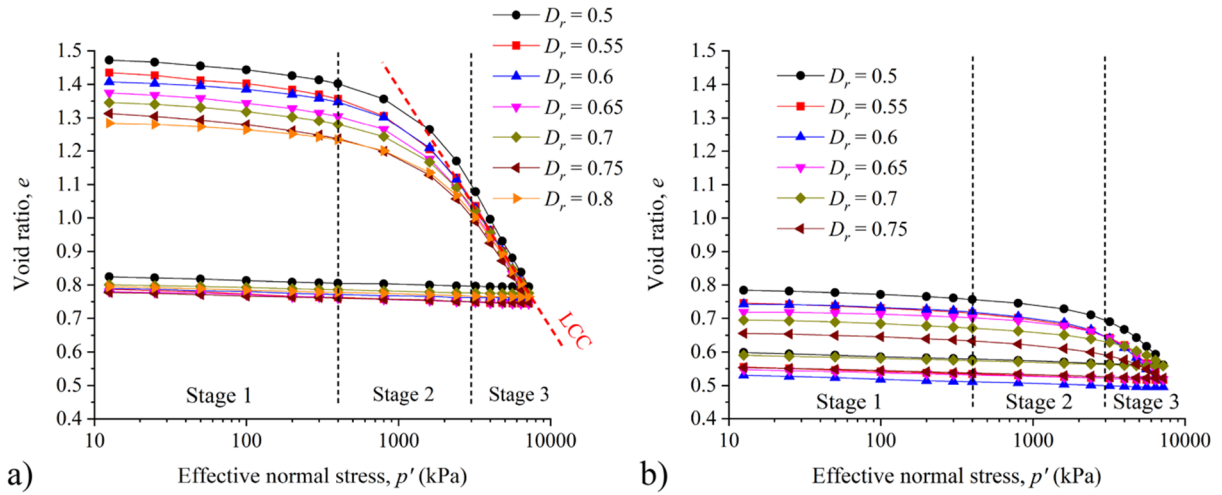


Figure 4.2. One-dimensional compression curves for (a) calcareous sands; and (b) river sands with different initial relative densities in the size range of 2-5 mm.

As illustrated in Figure 4.2(a), at the initial stage of the experiments, the specimens with varying initial relative densities showcased an initial void ratio range of 1.25 to 1.5, and the specimens with smaller initial relative density exhibit larger initial void ratio. The void ratios took on a synchronously decreasing trend with the increase of the vertical stress. During stage 2, as the decrease of the void ratio of the specimens with relatively small initial relative density accelerates, the multiple curves gradually show a tendency to merge together. During stage 3, all $e - \lg(p')$ curves of calcareous sands with different initial relative densities in particle size range of 2-5 mm gradually overlapped with each other and eventually merged into a single curve. For specimens with different initial relative densities, the high-level of vertical pressure would inevitably result in an equivalent level of void ratio, suggesting that void ratio is contingent on particle size, yet unaffected by the initial relative density of the sample. As indicated in Figure 4.2(a), the red dotted line is defined as the limiting compression curve (LCC) (Pestana and Whittle, 1995), which is also known as the normal compression line (NCL) (Coop, 1990) as the following equation:

$$e = N - \lambda_{NCL} \ln p' - 1 \quad (4.1)$$

where N and λ_{NCL} are the intercept and gradient of the NCL, respectively.

According to Figure 4.2, values of N and λ_{NCL} for calcareous sands in particle size range of 2-5 mm are 4.53 and 0.31, respectively, while they are 3.51 and 0.2 as obtained by Wu et al. (2022) for calcareous sands with D_{50} of 0.843 mm. Since these two values can be influenced by many factors including particle size, particle morphology, mineral composition, and particle

size distribution, and the maximum value of the vertical pressure is limited in this research, no further discussion about NCL is necessary. During the unloading stages, the curves of specimens with different initial relative densities were still overlapped, and the trends of their void ratios remain basically the same, with the final values ranging from 0.75 to 0.85.

Figure 4.2(b) presents the $e-\lg(p')$ curves of river sands under the same experimental conditions as those report in Figure 4.2(a). It is readily apparent that the initial void ratio of river sands with different initial relative densities ranges from 0.5 to 0.8, which is much smaller than that of calcareous sands. Since the shape of river sand particles is more regular than that of calcareous sands, the river sand particles are more closely assembled and therefore have smaller initial void ratios. During stage 1 of the loading process, the trend of the curves is basically the same as that of the calcareous sands, and the void ratios of river sands decreased at a relatively slower rate under small vertical pressures. In stage 2, the void ratios of the specimens continued to decrease slowly at a similar rate as in stage 1, and although there is a tendency for the curves to merge later in this stage, no point of maximum curvature is observed as in stage 2 for calcareous sands. During stage 3, the points of maximum curvature appeared, and the $e-\lg(p')$ curves of river sands also started to enter the linearly decreasing stage. However, the LCC of river sand still did not occur even under the highest vertical loading pressure of 7200 kPa in the experiment, characterizing that the river sands could effectively resist higher vertical pressures compared to the calcareous sands. The non-merging of the curves at the beginning of the unloading stage also resulted in a relatively wider distribution of the $e-\lg(p')$ curves throughout the unloading stages. Eventually, after the unloading is completed, the void ratios of river sands with initial relative densities ranging from 0.5 to 0.75 are distributed between 0.5 and 0.6.

4.2.2 Influence of particle size on the evaluation of void ratio during compression

The $e-\lg(p')$ curves of calcareous sands of the same initial relative density of 0.6 but in different particle size range of 2-5 mm, 1-2 mm, and 0.5-1 mm are illustrated in Figure 4.3. At the beginning of the test, specimen composed of sand particles with larger particle sizes exhibit higher initial void ratios due to the relatively larger volume of pore spaces between particles. As the applied vertical pressure increased, the void ratio of the specimens reduced accordingly.

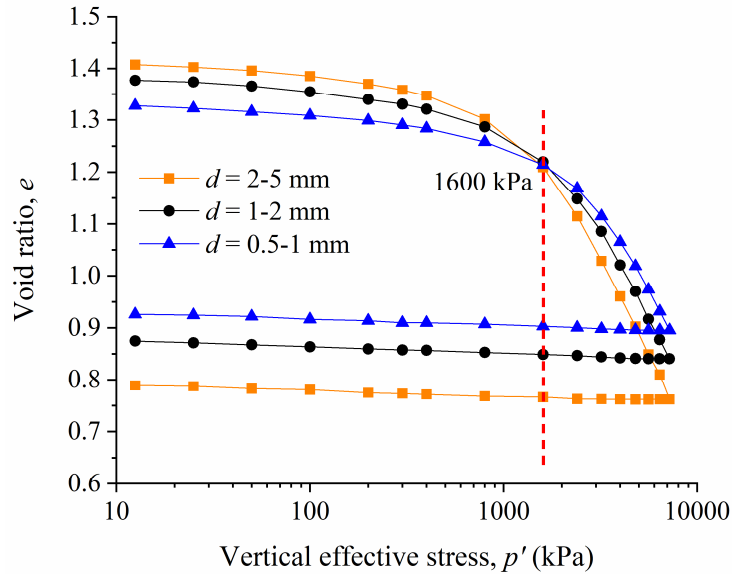


Figure 4.3. 1-D compression curves for CS in different size ranges. The initial relative density is 0.6.

However, specimen composed of coarser particles demonstrated a more pronounced reduction of void ratio, which can be attributable to the vertical pressure-induced particle rearrangement, which affected coarser particles to a greater extent. This in turn facilitated the filling of larger pore spaces by other fine particles, leading to substantial reductions in void ratio. The observed trend underwent a reversal as soon as the normal stress surpassed a value of 1600 kPa, primarily due to the emergence of significant particle breakage among the coarse particles. As a consequence, a substantial quantity of fine sand particles were produced, which rapidly occupied the interparticle pore spaces. A significantly faster reduction in the void ratio of the specimen made up of coarse sands can be observed. The decrease in the void ratio of samples with fine particles was comparatively slower, which is attributed to the lower rate of particle breakage of fine particles at a densely packed state. Upon attaining stability during the final loading stage under the vertical stress of 7200 kPa, a noteworthy difference in void ratio can be observed between specimens comprising coarse particles (2-5 mm), which exhibited void ratio below 0.8, and those consisting of fine particles (0.5-1 mm), which surpassed 0.9. The reason behind this is that coarse particles are more likely to be broken, generating a substantial quantity of fine particles that fill the void space previously present between the particles. This filling process finally resulted in a densely packed specimen.

4.3 Yield characteristics

As demonstrated in Figure 4.2, the void ratios of the specimens are reduced rapidly with the increase of normal loading pressure during stage 2. This post-elastic behaviour is usually described as the “yielding” of the granular media and the vertical pressure corresponding to the starting point where this process begins is termed as the yield stress (McDowell, 2002). As a key parameter that cannot be ignored in studying the performance of soil settlement in geotechnical engineering, yield stress can serve as an indicator of the onset of substantial particle breakage (McDowell et al., 1996, Nakata et al., 2001a, Karatza et al., 2019). Before the yield stress is reached, the micromechanical activities triggered by relatively small volume changes of the specimen are mainly include the rubbing of the particle surface against each other and the shearing of the asperities from the particle surface. Once the vertical pressure exceeds the yield stress, a considerable amount of particle breakage initiates and promptly dominates the numerous microscopic activities (Chuhan et al., 2003, Fernandes et al., 2010).

The determination of the yield stress can be performed either by using the graphic approach presented by Casagrande (1936) or finding the point where the deformation exhibits the most rapid change (Nakata et al., 2001b). The abscissa (effective normal stress) of the point corresponding to the maximum curvature on the $e-\lg(p')$ curves for sandy soils under one-dimensional compression was termed as the yield stress by McDowell (2002). This method was also applied in this research. The coordinate values of effective normal stress on the x-axis were about 1000 times more than those (void ratio) on the y-axis, which makes it difficult to perform the polynomial fitting directly on the $e-\lg(p')$ plots. Therefore, the logarithm to base 10 of the effective normal stress are presented as x-axis values. A 3rd order polynomial was used to fit the experimental data in the yielding region.

Figure 4.4 presents the polynomial fitting results of the void ratios of calcareous and river sands under the normal stress ranging from 200 kPa to 7200 kPa, and from 1600 kPa to 7200 kPa, respectively. The point with the maximum curvature on each curve was determined and shown as hollow dots. The yield stress for calcareous and river sands are listed in Table 4.1.

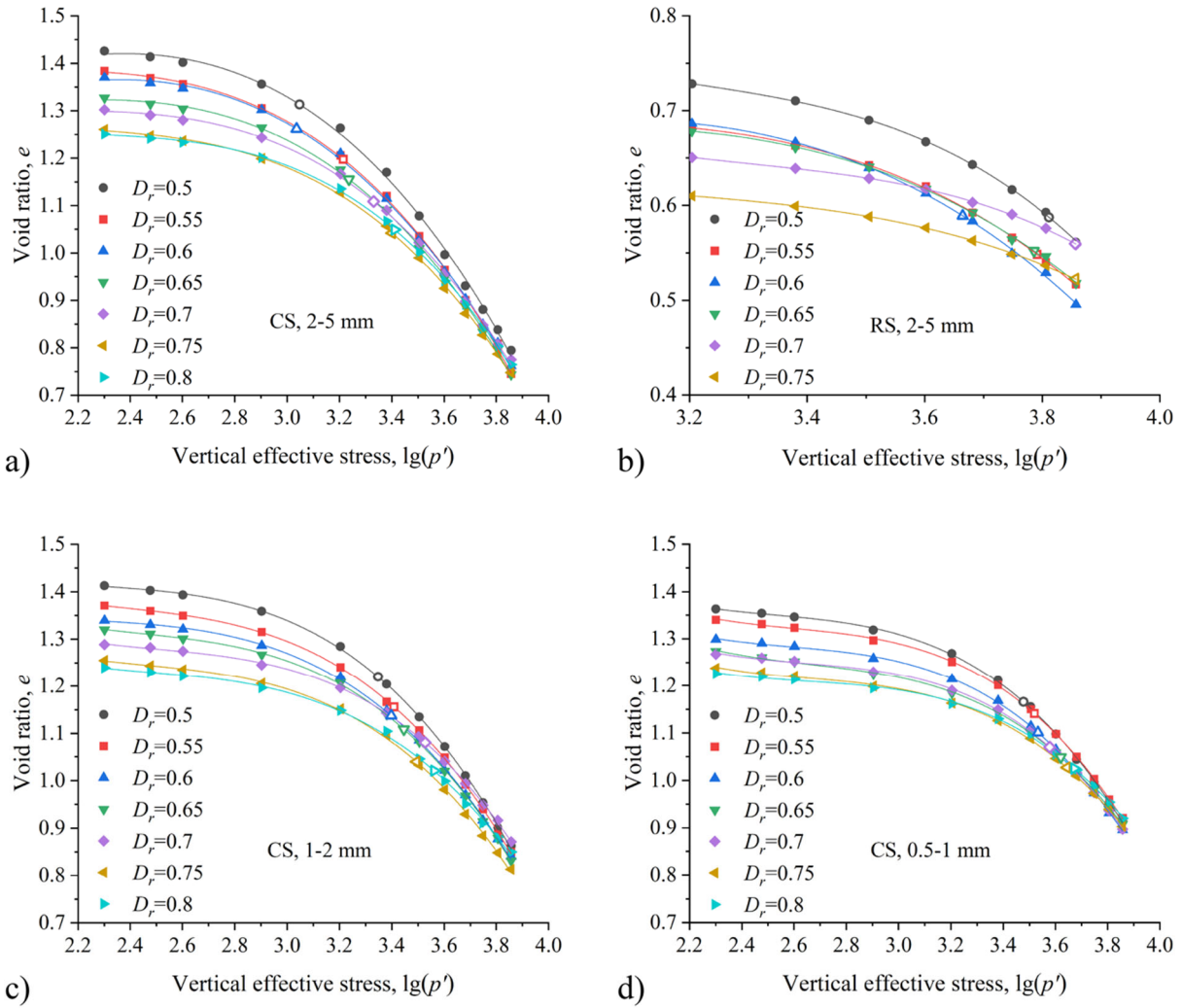


Figure 4.4. Yield points and fitting curves of (a) calcareous sands (CS) and (b) river sands (RS) with different initial relative densities and particle size of 2-5 mm, CS with different initial relative densities and particle size of (c) 1-2 mm and (d) 0.5-1 mm.

Table 4.1. Yield stress (unit: kPa) of calcareous and river sands.

| | Size \ D_r | 0.5 | 0.55 | 0.6 | 0.65 | 0.7 | 0.75 | 0.8 |
|--------------------|---------------|-------------------------|-----------------|---------|---------|---------|---------|---------|
| | | Calcareous sands | 0.5-1 mm | 3000.61 | 3305.83 | 3414.29 | 4173.88 | 3788.61 |
| | 1-2 mm | 2227.97 | 2562.54 | 2498.96 | 2792.93 | 3365.66 | 3121.40 | 3642.00 |
| | 2-5 mm | 1114.94 | 1642.44 | 1087.28 | 1720.88 | 2141.81 | 2516.98 | 2571.76 |
| River sands | 2-5 mm | 6479.78 | 6184.29 | 4617.85 | 6101.13 | 7178.27 | 7178.27 | - |

Figure 4.5 presents the yield stress for calcareous and river sands with different initial relative densities and particle sizes. As the initial relative density increased, the yield stresses of specimens with varying particle sizes exhibited an overall increasing trend, with the rate ranging from 4.4 to 5.5. This observation suggests that the sand specimens with higher density

can resist higher normal pressures, thereby delaying particle breakage at a certain threshold. For calcareous sands, it has been observed that the yield stress of specimens composed of coarser sand particles is significantly smaller than that of the fines. Since coarse grains have larger coordination numbers and more densely distributed inner pores among them, which greatly enhances the likelihood of particle breakage (Fonseca et al., 2013). For river sands with higher strength, their yield stress is significantly higher than that of calcareous sands.

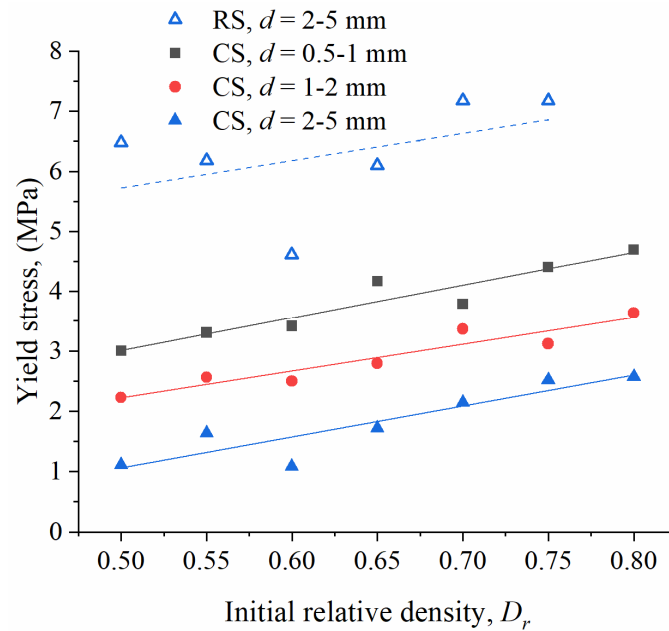


Figure 4.5. Influence of initial relative density and particle size on yield stress of calcareous sands (CS) and river sands (RS).

4.4 Particle breakage characteristics

4.4.1 Influence of initial relative density on particle size distribution change

The size of individual sand particles was measured during dynamic image analysis to obtain the particle size distribution (PSD) of specimens before and after the tests, thereby ensuring that the outcome is consistent with that determined through sieve analysis. Figure 4.6(a) and (b) demonstrates the PSD of calcareous and river sands, respectively with the initial relative density of 0.6 and 0.7 in the particles size range of 2-5 mm before and after the one-dimensional consolidation tests. The analyses of all tested specimens revealed a noticeable shift in the direction denoted by the black arrow in the figure, accompanied by an increase in the breadth of the curves. This observation indicates a reduction in the amount of larger sand

particles and a marked surge in the number of fine sand particles. The alterations in PSD positions among specimens with smaller initial relative densities ($D_r = 0.6$) were marginally more notable than those with larger relative densities ($D_r = 0.7$), suggesting that the sample with lower initial relative densities experienced more intense particle breakage, thereby producing a greater quantity of fine particles. By comparing Figure 4.6(a) and (b), it can be clearly seen that for sand specimens with the same initial relative density, the changes in the PSD of calcareous sands after the experiments are more pronounced than those of river sands, indicating that the amount of broken calcareous sands under the same experimental conditions is more than that of river sands.

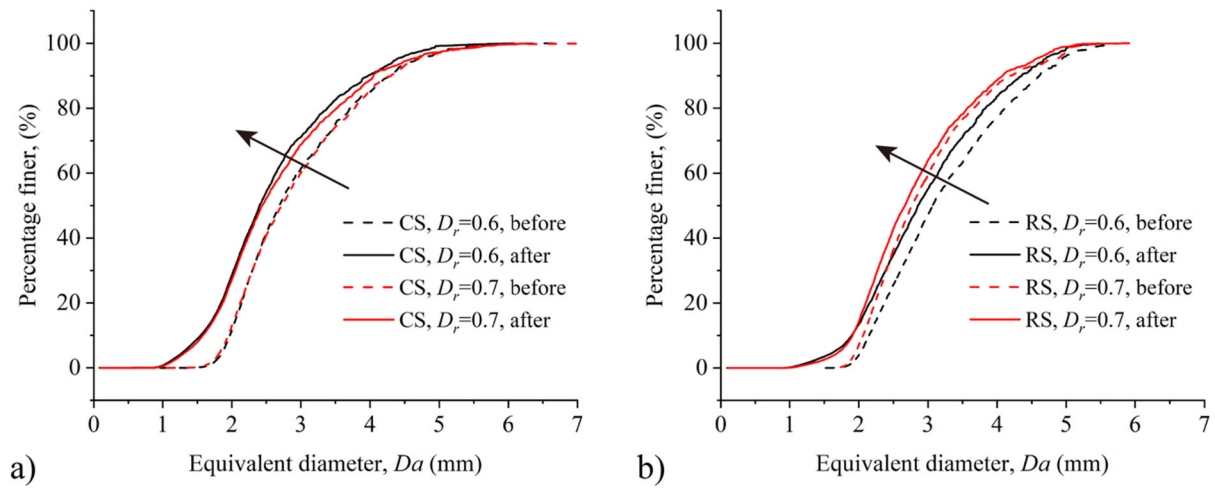


Figure 4.6. Initial (dashed curves) and final (solid curves) particle size distributions for (a) calcareous and (b) river sand samples with different initial relative densities in the particle size range of 2-5 mm.

The different patterns of variation can be more clearly distinguished from the statistical results of the frequency distribution of particle size. Figure 4.7(a) and (b) presents the statistical results of the frequency counts of particle size of calcareous sand specimens in the particle size range of 2-5 mm with the initial relative density of 0.55 and 0.8, respectively before and after the oedometer tests. The x-coordinate of the centre of the Gaussian distribution is represented by the mean (μ), while the extent of variation around the mean is indicated by the standard deviation (SD). As shown by the black bars, the particle size of calcareous sand specimens with different initial relative densities before the test ranged from 2 to 5 mm, following a Gaussian distribution with R^2 larger than 0.97. After the experiments, it was noted that the loading and unloading processes have produced a substantial reduction in the quantity of coarse particles

present in the tested samples, and an exponential distribution ($R^2 > 0.97$) revealed that a significant proportion of calcareous sands had been crushed, as evidenced by the fact that over 90% of the particles were smaller than 2 mm. As the rate parameter of an exponential distribution, λ determines the steepness of the curve, with a higher value indicating a faster rate of change in the data. Calcareous specimen with the D_r of 0.55 exhibit a higher λ -value of 0.86, while the sample with D_r of 0.8 had a λ -value of only 0.585. Furthermore, there was a notable decrease in the frequency counts of fine particles generated by the loose specimen, in contrast to the dense specimen. For specimen with D_r of 0.55, the frequency counts of fine particles in the size range of 0-0.5 mm and 0.5-1 mm were close to 40% and 30%, respectively, while these two values for specimen with D_r of 0.8 were significantly less than 35% and 30%, respectively. The results clearly demonstrate that the loose specimen exhibit a greater output of fine particles during the experiment when compared to the dense specimen.

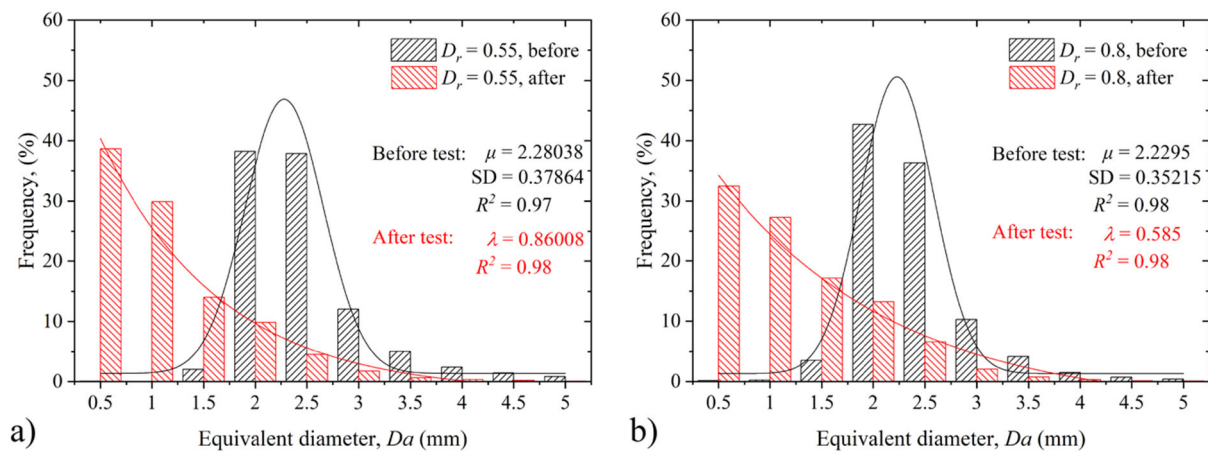


Figure 4.7. Statistics of particle sizes for calcareous sand specimens with the initial particle size range of 2-5 mm and initial relative density of (a) 0.55, and (b) 0.8 before and after the oedometer tests.

4.4.2 Influence of particle size on the particle size distribution change

The impact of particle size on the development of PSD of calcareous sands with a consistent initial relative density of 0.65 under one-dimensional consolidation test is illustrated in Figure 4.8. It is apparent that the impact of particle size on the PSD is much greater than that of the initial relative density. An increase in particle size resulted in a discernible shift in the PSD. There is a minimal alteration observed in the PSD for the 0.5-1 mm sample. A greater quantity of fine particles was produced by the specimen composed of coarser particles, suggesting a greater degree of particle breakage. The presence of irregularly shaped, rough-

surfaced coarse sand particles increases the probability of particle damage.

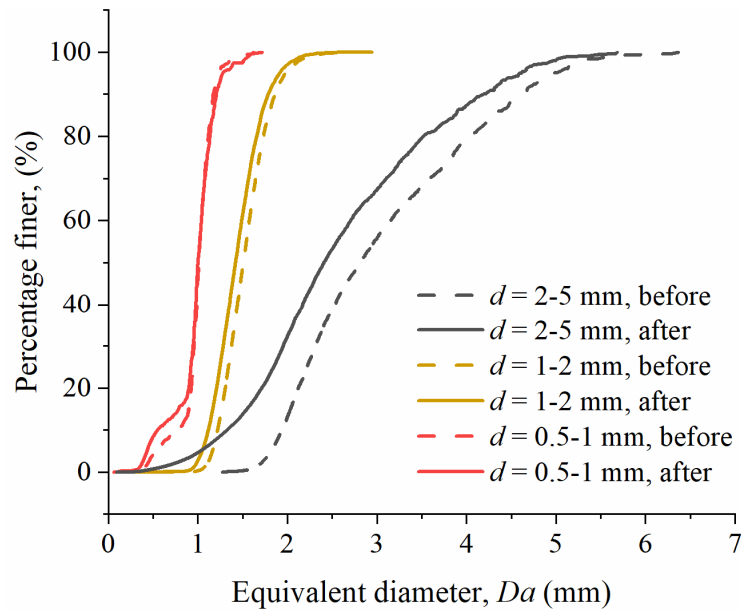


Figure 4.8. The initial (dashed curves) and final (solid curves) particle size distributions for calcareous sand samples of different particle size ranges. The initial relative density was 0.65.

Figure 4.9(a) and (b) presents the statistical results of the frequency counts of particle size of calcareous sand specimens with an initial relative density of 0.7 in the particle size range of 2-5 mm and 1-2 mm, respectively before and after the oedometer tests. Although these two specimens consisted of calcareous sand particles in different size ranges, the frequency counts of their particle size before the test followed well a Gaussian distribution with R^2 larger than 0.96. After the experiment, it was observed that the specimen with the initial particle size in 1-2 mm exhibited only a minor alteration in the frequency distribution when compared to that of the coarse specimen of particle size 2-5 mm. Namely, a decrease in the quantity of larger particles and an increase in the number of fine particles were observed. As shown in Figure 4.9(a), the frequency counts of particle size of specimen with particle size in the range of 2-5 mm after the test still demonstrated an exponential distribution, which is primarily due to the substantial production of fine particles from the specimen composed of coarser particles. However, as demonstrated in Figure 4.9(b), specimen comprised of finer particles displayed significantly reduced fines production throughout the experiment, leading to the observation of a Gaussian distribution in their particle size frequency distribution after the oedometer test.

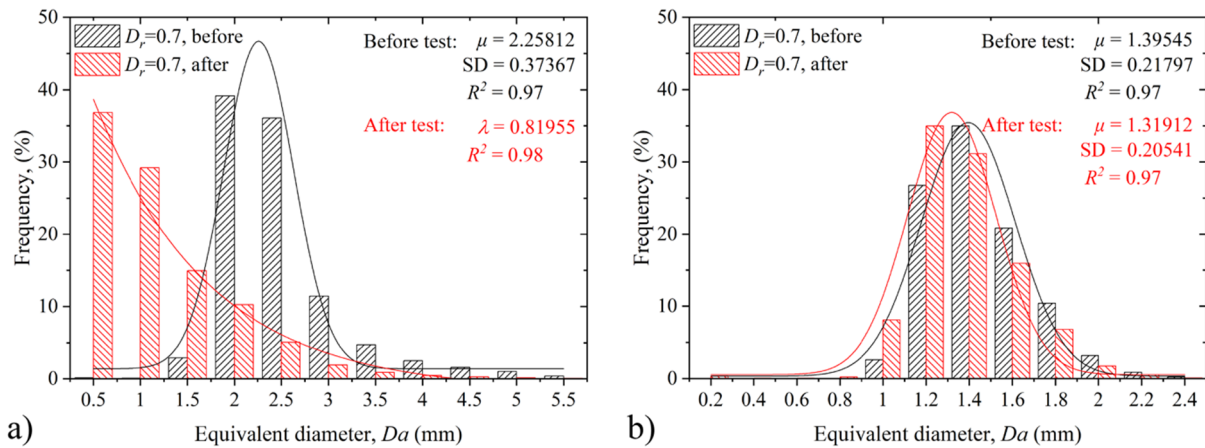


Figure 4.9. Statistics of individual particle size of calcareous sand specimens with the initial relative density of 0.7 and the particle size range of (a) 2-5 mm, and (b) 1-2 mm before and after the tests.

In addition, it is observed that the specimen with D_r of 0.7 followed an exponential distribution of particle size frequency after the test, with a λ -value of 0.82. It is noteworthy that this value falls between the outcomes recorded for the specimens with D_r of 0.55 (λ : 0.86) and 0.8 (λ : 0.585) showed in Figure 4.7, thus providing additional evidence to support the proposition that smaller specimen densities lead to greater generation of fine particles during the consolidation test. Further research is required to investigate the correlation between the rate parameter of an exponential distribution and the initial relative density of the specimens.

Traditional sieving analysis was also applied in this research. Particle size distribution of calcareous sand specimens with different initial relative densities in particle size range of 2-5 mm, and 1-2 mm before and after the oedometer tests are shown in Figure 4.10(a), and (b), respectively. Although the sieving method has constraints, the final PSD curves comprised a limited number of data points. Nonetheless, the trend of the PSD curves is readily discernible under various testing conditions, providing further validation for the reliability of the findings obtained by the DIA method. The post-test PSD curves are presented in decreasing order of initial relative density from bottom to top along the y-axis, indicating that the loose samples produced a greater number of fine particles. The values of the three curves at 0.1 in Figure 4.10(a) are significantly larger than those in Figure 4.10(b), suggesting that more pronounced particle breakage occurred in the specimen composed of coarser calcareous sand particles.

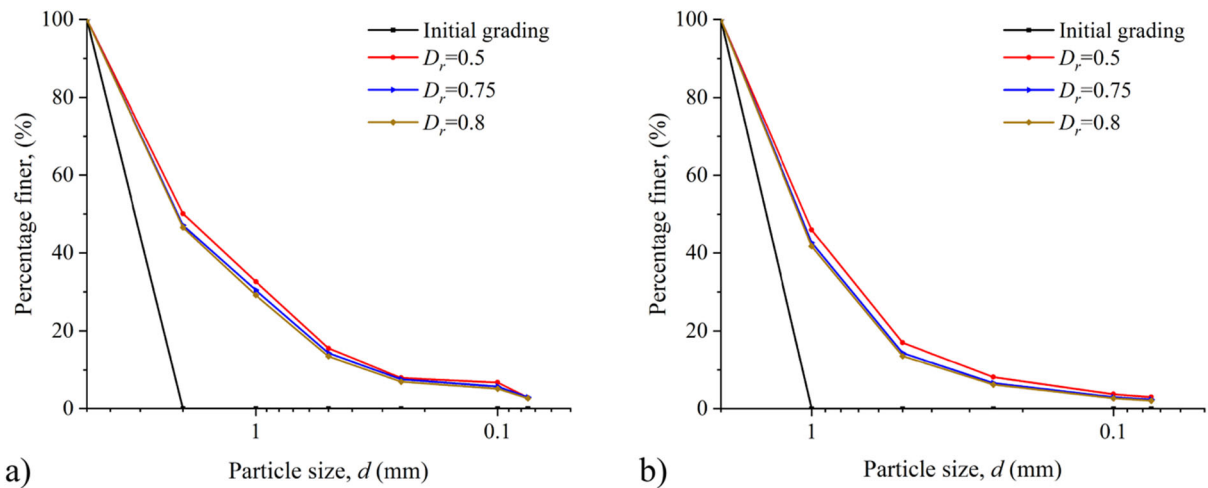


Figure 4.10. PSD of CS specimens with initial relative density of 0.5, 0.75, and 0.8 in particle size range of (a) 2-5 mm, and (b) 1-2 mm before and after the tests obtained by applying MSA.

4.4.3 Relationship between relative breakage and initial relative density

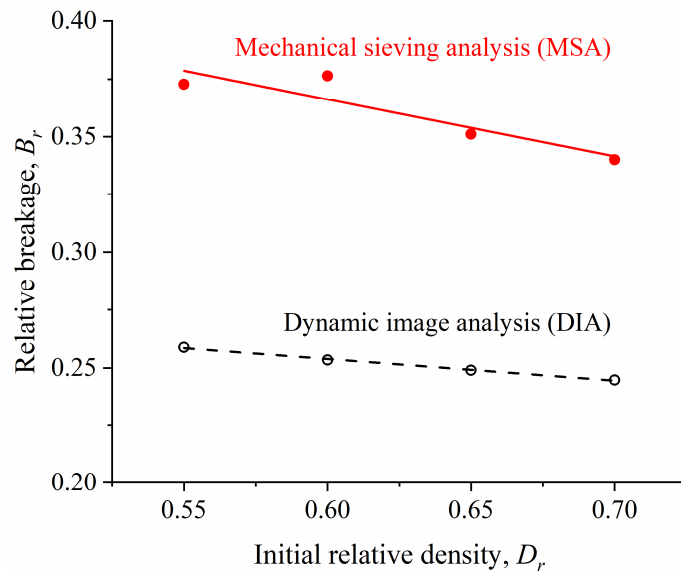


Figure 4.11. Relative breakage of CS specimen obtained by applying MSA and DIA.

A quantitative analysis was performed on particle breakage through comparison of the relative breakage (B_r) obtained from both sieving analysis and dynamic image analysis. Figure 4.11 presents the relative breakage of calcareous sand specimens of size in the range of 2-5 mm and initial relative density ranging from 0.55 to 0.7. The solid dots and hollow dots indicate the relative breakage values of the specimens composed of calcareous sand particles by using the sieve analysis and dynamic image analysis, respectively. The linear fitting results indicate that an increase in initial relative density leads to a small decrease in B_r , suggesting that loose specimens are more susceptible to breakage. The outcomes derived from implementing the

DIA demonstrate a significantly reduced level of variability with R^2 equal to 0.996 compared to those obtained by using the sieve analysis.

4.4.4 Relationship between particle breakage and compression deformation

Based on the analyses in the previous subsections, it is clear that the reduction of void ratio of sand specimens in the one-dimensional consolidation tests is mainly caused by two micro-mechanical behaviours of the particles, i.e., particle rearrangement and particle breakage, which can be expressed in the following equation:

$$\Delta e = e_r + e_b \quad (4.2)$$

where Δe is the change in void ratio under vertical loading; e_r is the change in void ratio due to particle rearrangement; e_b is the change in void ratio due to particle breakage.

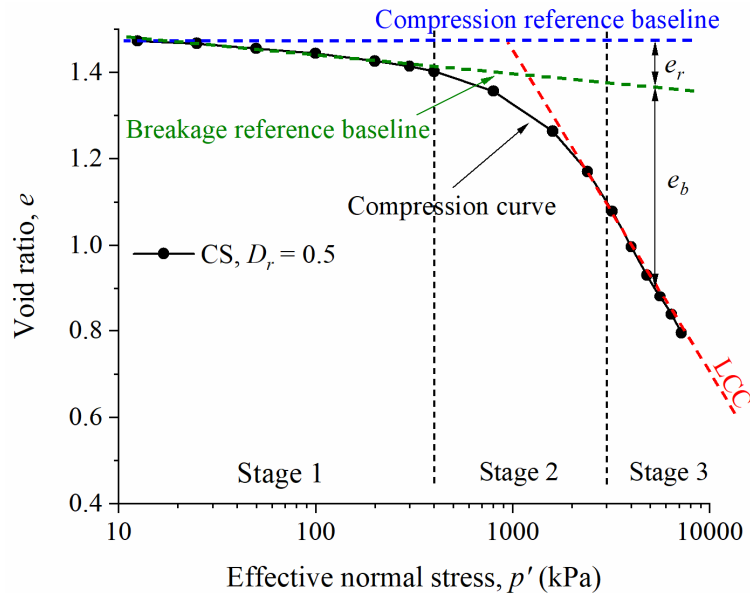


Figure 4.12. Definition of the change in void ratio due to particle rearrangement and breakage.

Figure 4.12 illustrates how e_r and e_b are defined in the e - $\lg(p')$ plot, where the black compression curve is the result of experiment on calcareous sands with an initial relative density of 0.5 and initial particle size range of 2-5 mm. The blue horizontal line through the initial void ratio before loading is defined as the “compression reference baseline”. During stage 1 of the compression experiments, the void ratio decreased slowly and nearly linearly with the increasing vertical stress. In the realm of one-dimensional compression behaviour of cohesive soils, the compression curve for normally consolidated clay exhibits a linear relationship between the void ratio and vertical stress in a semi-logarithmic plot, as delineated

by the following equation:

$$e = e_c - \lambda_c \log(p') \quad (4.3)$$

where e_c represents the void ratio corresponding to a vertical stress of 1 MPa; and λ_c denotes the slope of the compression curve within e - $\log(p')$ plot. Therefore, the alteration in void ratio resulting from particle rearrangement can be quantified by the following equation:

$$e_r = e_0 - e_c - \lambda_c \log(p') \quad (4.4)$$

As the compression progress to stage 2, the yielding of the specimen occurs, implying that particle breakage occurs on a large scale, causing the compression line of the calcareous sands to show a curved downward development trend, which is consistent with the behaviour of over consolidated clay in the same type of experiment. The following equation was presented by Luo et al. (2024) to characterise the compression curve.

$$e = e_0 - b \left(\frac{p'}{p_0} \right)^f \quad (4.5)$$

where b represents the difference between the void ratio and the initial void ratio under the vertical stress of 1 MPa; p_0 is equal to 1 MPa; and f signifies the test parameter. The extension of the straight line (i.e., the green line in Figure 4.12) in stage 1 is referred to as the “breakage reference baseline”. Therefore, the alteration in void ratio attributable to particle breakage can be determined by the difference between the compression curve and the breakage reference baseline, as:

$$e_b = e_c - \lambda_c \log(p') - \left(e_0 - b \left(\frac{p'}{p_0} \right)^f \right) \quad (4.6)$$

By substituting the experimental results of calcareous sands with an initial relative density of 0.5 and particle size of 2-5 mm under vertical stresses larger than 300 kPa into Equation 4.6 for an example, the experimental parameters can be obtained and summarized in Table 4.2. The results on the relationship between e_b and p' are presented in Figure 4.13. The change in void ratio due to particle breakage under different levels of vertical pressure can be well reflected.

Table 4.2. Experimental parameters of Eq. 4.6.

| Parameter | e_c | λ_c | e_0 | b | f |
|-----------|-------|-------------|-------|-------|-------|
| Value | 0.595 | 0.212 | 1.478 | 0.958 | 0.344 |

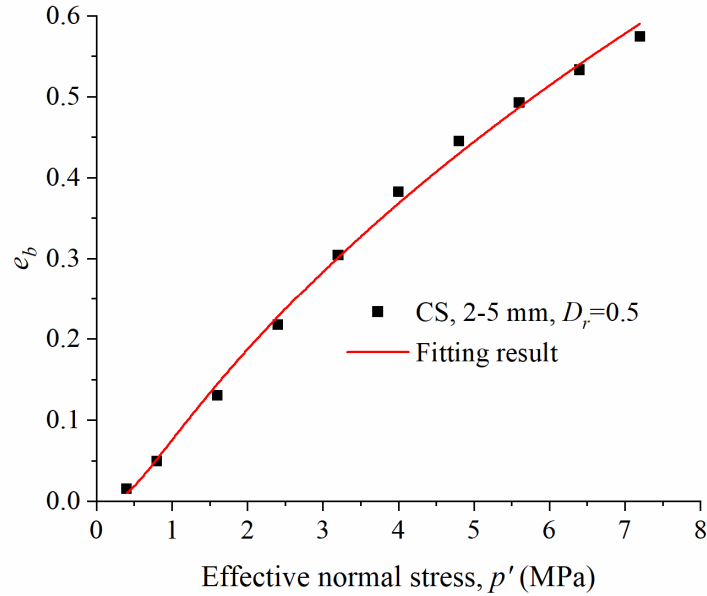


Figure 4.13. The change in void ratio due to breakage under the normal stress ranging from 0.3 to 7.2 MPa of CS with the initial relative density of 0.5 and in particle size range of 2-5 mm.

4.5 Acoustic emission characteristics

Relative breakage can only be used to quantify the changes in the number of fine and coarse particles by comparing the changes in PSD curves after the experiments. However, the identification of the onset or development patterns of micromechanical behaviour, as well as the determination of specific types of micromechanical behaviours during the test, cannot be achieved by analysing the B_r alone. The AE ringdown counts (RDC) and peak frequency were used to characterize the intensity and identify various modes of micromechanical behaviours during the one-dimensional consolidation tests, respectively.

4.5.1 Evolutions of AE ringdown counts

The evolution of AE ringdown counts and vertical effective stress with time during the oedometer on the specimen with an initial relative density of 0.6 and in the particle size range of 1-2 mm is presented in Figure 4.14. The chart illustrates that nearly all the notable increase tended to rise at the beginning of the time interval for applying each level of vertical pressure, i.e., the moment of loading or unloading. In instances where the applied vertical pressure upon the specimen remains below the threshold of 400 kPa, i.e., during stage 1 in Figure 4.2(a), a limited amount of RDC results can be observed due to inadequate compression of the inter-particle void spaces within the specimen under a lower vertical pressure, and particle sliding

governed the micromechanical response exhibited by the calcareous sand particles.

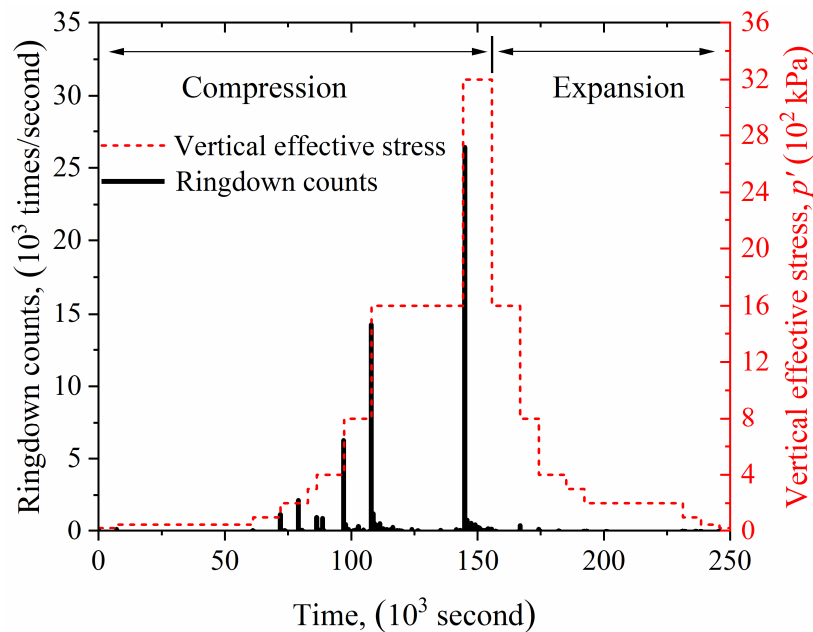


Figure 4.14. Evolutions of AE ringdown counts and vertical effective stress over time of CS specimen with an initial relative density of 0.6 and in particle size range of 1-2 mm.

Upon the vertical pressure reaching 800 kPa, there is a noticeable increase in RDC due to the force chain provided by the densely packed sand particles becoming incapable of resisting the applied load. This, thereby resulted in the substantial microcracking of the calcareous sand particles, accompanied by the abrasion of the asperities on their surfaces. When the vertical pressure reached its maximum value of 3200 kPa, the RDC exhibited a significant increase and concurrently reached its peak due to a considerable amount of calcareous sand particles undergoing breakage in a more intensive way. During the expansion (unloading) stage, only smaller RDC values can be observed at the moment of unloading the weights, since acoustic waves are closely tied to irreversible deformations (Lin et al., 2019).

The effects of initial relative density and particle size on the evolutions of cumulative AE RDC with vertical effective stress are presented in Figure 4.15(a) and (b). As demonstrated in Figure 4.15, the cumulative RDC-vertical effective stress curves for different tests showed a consistent pattern of development throughout all the oedometer tests. During the initial loading phase, no significant acoustic emission signals was generated as the micromechanical behaviour of calcareous sand particles is primarily characterized by sliding and positional rearrangement under a relatively small level of vertical pressure, leading to a minor increase in

the cumulative RDC. A considerable increase in vertical pressure to levels exceeding 400 kPa led to the occurrence of large-scale particle breakage, resulting in an exponential surge in the cumulative RDC value. The cumulative RDC results during compression stages are represented by the solid scattered symbols, which are optimally fitted through deployment of the logistic function (solid lines) with R^2 larger than 0.93. The results obtained during the unloading stages of the experiment are depicted as hollow scatter dots. The micromechanical behaviour of calcareous particles at these stages are mainly dominated by particle sliding and rearrangement with minimal particle breakage taking place. As such, the cumulative RDC does not undergo significant variation, and can be accurately represented by the dashed linear fitting lines.

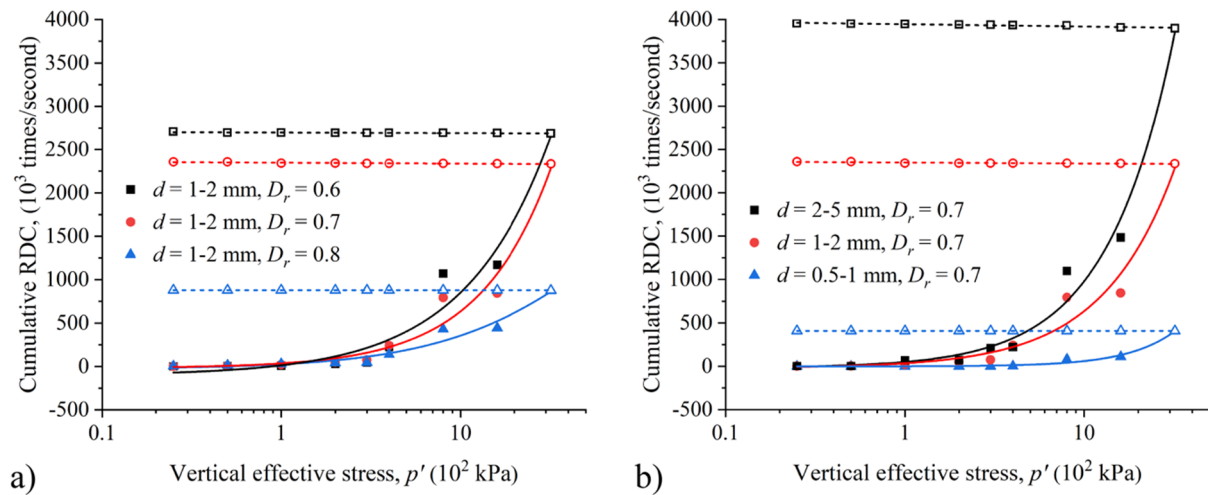


Figure 4.15. Evolutions of cumulative AE RDC with vertical effective stress during of CS (a) with different initial relative densities in the same particle size range of 1-2 mm, (b) with the same initial relative density of 0.7 in different particle size ranges.

As illustrated in Figure 4.15(a), it was observed that loose calcareous sand specimens with D_r of 0.6 and 0.7 exhibited a more rapid growth in the cumulative RDC when subjected to a normal stress greater than 400 kPa. This phenomenon can be attributed to the occurrence of intense asperity abrasion on particle surfaces and particle sliding or rearrangement in loose sands, causing such an effect to be more pronounced in comparison to denser specimen ($D_r = 0.8$). When subjected to vertical loading stresses higher than 800 kPa, the dense specimen demonstrated greater resistance to loading and exhibited fewer instances of sand particle breakage, which subsequently led to a lower numbers of detectable AE counting signals.

Based on the findings presented in Figure 4.15(b), it is apparent that the initial particle size range of the calcareous sand particles composing the specimen has a more significant effect on

the variation of the cumulative RDC. Specifically, as the vertical pressures increased, calcareous sands specimens with larger initial particle sizes produced a greater amount of AE signals, leading to a more rapid accumulation of RDC. Due to the abundant internal pores and defects in coarser calcareous sands, along with the unevenly shaped surface asperities, the likelihood of incurring catastrophic failure of the particles is considerably magnified. In the case of the specimen composed of fine calcareous sands (0.5-1 mm), the impact of irregular surfaces on them was significantly reduced, resulting in minimal variation in strength due to their spatial arrangement. Consequently, it became more challenging to instigate particle breakage, which ultimately led to lower increasing rate of the cumulative RDC values.

4.5.2 Evolutions of AE peak frequency

Figure 4.16(a) and (b) illustrate the results of peak frequency of all acoustic emission waveforms obtained during the one-dimensional consolidation tests conducted on calcareous sands with the particle size range of 1-2 mm and initial relative density of 0.6 and 0.8, respectively. The duration required for the specimen to reach stability at each vertical pressure level is also shown. The results of both the loose and dense specimen demonstrate that the acoustic emission hits recorded during tests under a load of less than 800 kPa are predominated by low-frequency AE components at approximately 0.02 MHz. Whilst the average frequency values of the low-frequency contents generated by specimens with varying initial relative densities remain identical, it is noteworthy that there exists a slight difference in the quantity of low-frequency contents produced by loose and dense specimens during the initial loading stages. The compression of inter-particle voids in the loose specimen resulted in a relatively small amount of low-frequency signals. Conversely, the calcareous sand particles of dense specimen were already in close contact with each other before the vertical load was applied. Subsequently, a significant amount of particle friction occurred among the particles subjected to the vertical pressure, resulting in the production of a substantial quantity of low-frequency signal contents. As summarized by Mao and Towhata (2015) that particle sliding and interparticle friction are generally characterized by low-frequency AE components with the value less than 100 kHz, whereas particle breakage is dominated by significantly high-frequency components greater than 100 kHz.

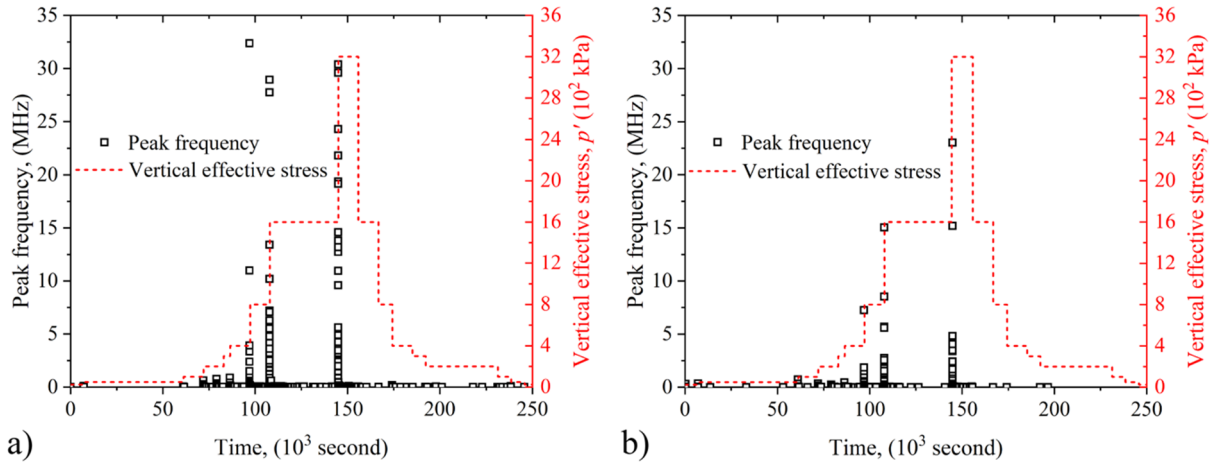


Figure 4.16. Evolutions of AE peak frequency and vertical effective stress with time of calcareous sands with particle size range of 1-2 mm and initial relative density of (a) 0.6, and (b) 0.8.

The loose specimen ($D_r = 0.6$) demonstrated a rapid increase in peak frequency values as the load reached 800 kPa. The majority of these results were concentrated in the intervals of 0-4, 0-7.5, and 0-15 MHz with the maximum value of around 32.5, 29, and 30 MHz under the vertical stress of 800, 1600 and 3200 kPa, respectively. However, as illustrated in Figure 4.16(b), it can be observed that the denser specimen encountered a considerable drop in its high-frequency range as well as its maximum value. The significant decline in high-frequency AE components appears to have a strong correlation with the decrease in particle breakage incidents. This can be attributed to the fact that denser specimens are more capable of resisting greater loading stresses, thereby limiting the likelihood of particle breakage (Lin et al., 2019, Muñoz-Ibáñez et al., 2019). Furthermore, a reduction in the low-frequency AE components implies the particle rearrangement within specimen with larger initial relative density.

4.6 Changes of particle morphological characteristics

The frequency distribution of representative particle shape descriptors for a specimen composed of calcareous sands with a size range of 2-5 mm and the initial relative density of 0.65 are illustrated in Figure 4.17. Before the vertical load is applied to the specimen, the frequency distribution of all descriptors including sphericity, convexity, aspect ratio, and flatness exhibited a Gaussian distribution. After the oedometer tests, the distribution of morphological parameters remained consistent with the initial observations and still of a Gaussian distribution, with the exception of convexity (Figure 4.17(b)), which displayed an

exponential distribution after the test due to the considerable increase observed in the convexity value of the majority of the particles, which closely approximates 1. This indicates that the surface of most particles has undergone a significant smoothing process during the experiment.

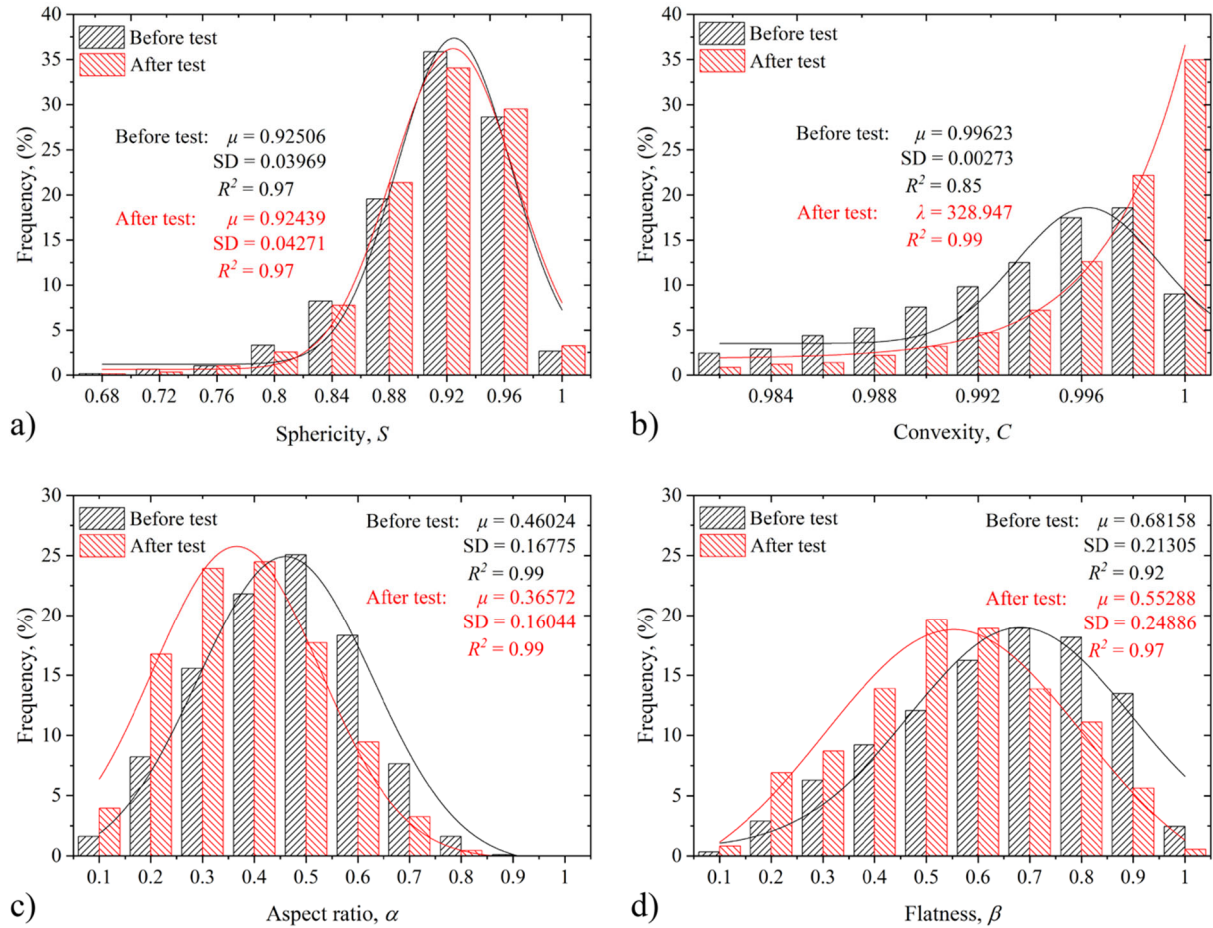


Figure 4.17. Frequency counts of particle shape descriptors including (a) sphericity, (b) convexity, (c) aspect ratio, and (d) flatness before and after the one-dimensional consolidation tests.

The testing process resulted in a slight decrease in particle sphericity as shown in Figure 4.17(a), indicating that the fine particles produced by either the abrasion of the particle surface or the rupture of the calcareous sand particles are characterised by more angular shapes. As the vertical pressure reaches elevated levels, the intact sand particles and newly produced fine particles resulting from particle abrasion and splitting experience tightly arrangement and consequent frictional interaction. This, thereby resulted in the smoothing or worn off of the asperities on the particle surface, ultimately leading to a smoother surface of the particles (see Figure 4.17(b)). The mean (μ) of aspect ratio shown in Figure 4.17(c) and flatness presented in Figure 4.17(d) experienced a reduction following the test, suggesting that there is a higher

degree of elongation and a lower degree of flatness in the shape of newly generated particles. During the step-by-step loading and unloading process of the 1-D consolidation test, the smoothing or worn off of the extensive but irregularly distributed asperities on the particle surface have made the particle surface significantly smoother. The breakage of single particles resulted in large amounts of fine particles with elongated, flatter, and more angular shapes.

4.7 Summary

This chapter investigated the consolidation characteristics of calcareous sands by conducting the one-dimensional consolidation tests. A vertical effective stress up to 7200 kPa was applied on sandy soil specimens with initial relative densities ranging from 0.5 to 0.8, and particle size range of 0.5-1 mm, 1-2 mm, and 2-5 mm. To enable a meaningful comparison of the experimental outcomes, results on river sands were also included. The morphological parameters of single particles were quantified and analysed. The particle breakage was investigated by applying both the dynamic image analysis and the sieving analysis. The acoustic emission testing was applied during the oedometer tests, parameters including AE ringdown counts and peak frequency were used. The major conclusions of this work are summarized as follows:

- A greater consolidation can be observed in sandy soil specimens with smaller initial relative density and larger particle size. The consolidation of calcareous sands is significantly larger than that of river sands.
- The one-dimensional compression of calcareous sand particles of various initial relative densities leads to the creation of a unique limiting compression curve resulting from the particle breakage.
- The yield stress of calcareous sands typically falls within the range of 1 to 4.7 MPa. It demonstrates an increasing trend with the initial relative density; conversely, the yield stress exhibits a decline with the particle size.
- The extent of particle breakage for calcareous sands is related to particle size and inversely related to initial relative density.
- The dynamic image analysis presents a clear advantage over the sieving analysis in terms of the quantification of particle breakage. The latter solely yields a line graph based only

on the change in particle weight over a limited number of particle size intervals, while the former presents smooth PSD curves based on the particle size of each individual particle in a much shorter period of time.

- A relationship for predicting the consolidation of calcareous sand under specific loading conditions is proposed. Within this framework, the parameter e_b , indicative of the change in void ratio due to particle breakage, is introduced.
- The acoustic emission test has been proved to be a powerful tool for characterizing micromechanical behaviours during the oedometer tests for calcareous sands. The AE ringdown counts and peak frequency of the corresponding acoustic waveform have the potential to characterize the intensity and distinguish different types of micromechanical activities, respectively. During the oedometer tests on calcareous sands, a majority of the RDC results were identified during the experimental loading stages, and their quantity experienced a notable rise after the vertical pressure exceeded 400 kPa. The observed trend depicted an increase in values as particle size increased, conversely, a decrease was evident as the initial relative density increased.
- The peak frequency results indicate that there has been a near-constant occurrence of particle sliding or rearrangement throughout the duration of the experimental process, producing lower-frequency AE components typically at around 0.02 MHz. High-frequency AE components can only be observed under normal stress larger than 800 kPa, which is evidently linked to the breakage of calcareous sand particles.
- The DIA outcomes indicate that the frequency counts of particle sphericity, aspect ratio and flatness before and after experiments closely followed the Gaussian distribution, except for the frequency counts of convexity after the test followed an exponential distribution as the surface of most particles becomes smoother after tests. The fine calcareous sand particles produced during the one-dimensional consolidation tests are more elongated and flattened, but less spherical and convex.

Chapter 5 Consolidated and Drained Triaxial Compression Tests

This chapter presents a study of the shearing behaviour of two types of sandy soils: calcareous sands and river sands, with the focus on investigating the effects of particle breakage and particle morphology on the shear strength of the sands. High-speed dynamic scanning was used to determine the particle morphological parameters quantitatively. Particle breakage was quantified by calculating the change in particle size distribution before and after shearing, which provided useful insight into the cracking mechanisms of sand particles. All experimental results under various test conditions are presented to analyse the occurrence and degree of particle breakage, trends in particle morphology, and their influence on the strength of the tested materials subjected to various affecting factors, including initial relative density, effective pressure, and particle size.

5.1 The mechanical behaviour of soil

5.1.1 Influence of initial relative density on the shear response

For tests using calcareous sands of various relative density, the deviatoric stress (q)-axial strain (ε_a) relationship is illustrated in Figure 5.1(a). In the tests, the particle size ranged from 2 mm to 5 mm and the effective confining pressures was set as 200 kPa. In all tests, the deviatoric stresses increased rapidly with the axial strain, and the denser specimens had a quicker increasing rate during this process. The peak shear strength was achieved at an axial strain of approximately 15%. It is noteworthy that, the loose specimens reached the peak stress at relatively large axial strains. After reaching the peak shear strength, the deviatoric stress decreased gradually due to shear softening at relatively low effective confining pressure.

The corresponding volumetric strain (ε_v)-axial strain (ε_a) relationship is shown in Figure 5.1(b). In this study, a reduction in the values on the Y-axis is specified as the contraction of the specimen volume. The volumetric strain of the specimens decreased continuously with increasing axial strain, showing a clear shear contraction behaviour. After reaching the peak deviatoric stresses, ε_v increased slightly due to shear-induced dilation, and the incremental

magnitude increased with the relative density of sand specimens. This phenomenon indicates that the denser calcareous specimens are more sensitive to shear induced dilation due to its densely packed granular state.

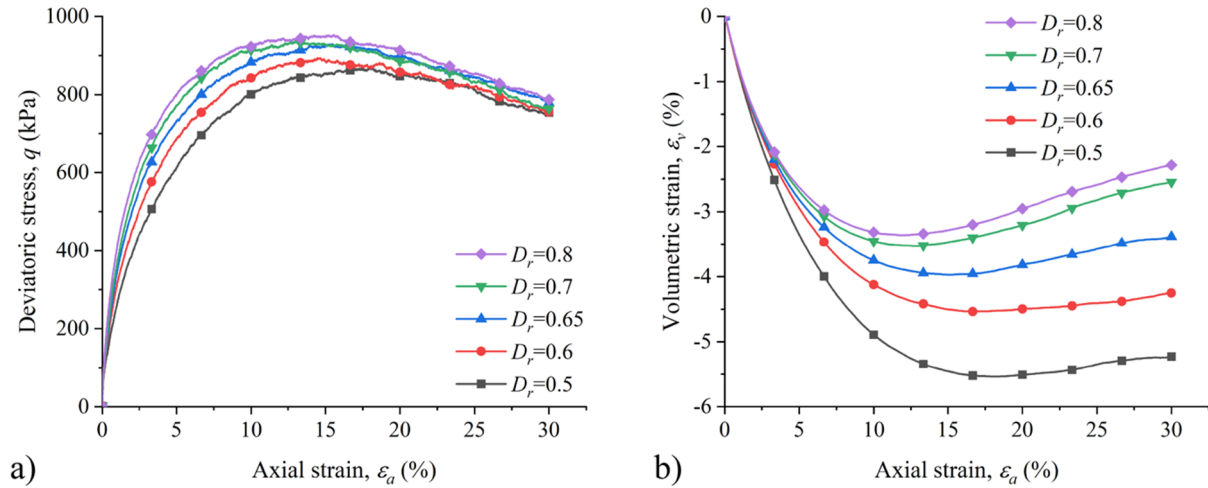


Figure 5.1. Evolutions of a) deviatoric stress; and b) volumetric strain with axial strain of CS specimen in particle size range of 2-5 mm under the effective confining pressures of 200 kPa.

5.1.2 Influence of particle size on shear response

Figure 5.2(a) compares the stress-strain relationship between calcareous sand (CS) and river sand (RS) specimens with an initial relative density of 0.7 and under the effective confining pressures of 200 kPa. As shown by the solid curves, the deviatoric stress of the calcareous sand specimens in different particle size ranges increased rapidly with the increase of axial strain. Furthermore, it was observed that fine specimen had a higher growth rate during this process. The peak of q - ϵ_a curve occurs at a relatively small axial strain for the specimen consists of fine calcareous sand particles. The fine particle specimens also exhibited higher peak shear strength due to smaller internal pores and less defects when compared to the coarse particle samples. The small internal pore volume also allowed the particles to closely align with each other at high coordinate number. After reaching the peak strength, the deviatoric stress exhibited a decline in all three specimens, manifesting evident strain softening behaviour. It is noteworthy that as the size of the particles reduces, there was a corresponding increase in the rate at which the deviatoric stress decreased. Once the axial strain reaches approximately 18%, a complete alteration in the behaviour of the deviatoric stress of specimens featuring three distinct particle sizes is observed. More specifically, the residual deviatoric stress of coarse

particles became higher than that of the fine particle specimen. The observed phenomenon could be attributed to the breakage of a significant number of coarse calcareous sand particles, leading to the creation of fine particles that can occupy the interparticle void spaces. As a result, the overall specimen experienced an increase in relative density, leading to a comparatively elevated shear strength.

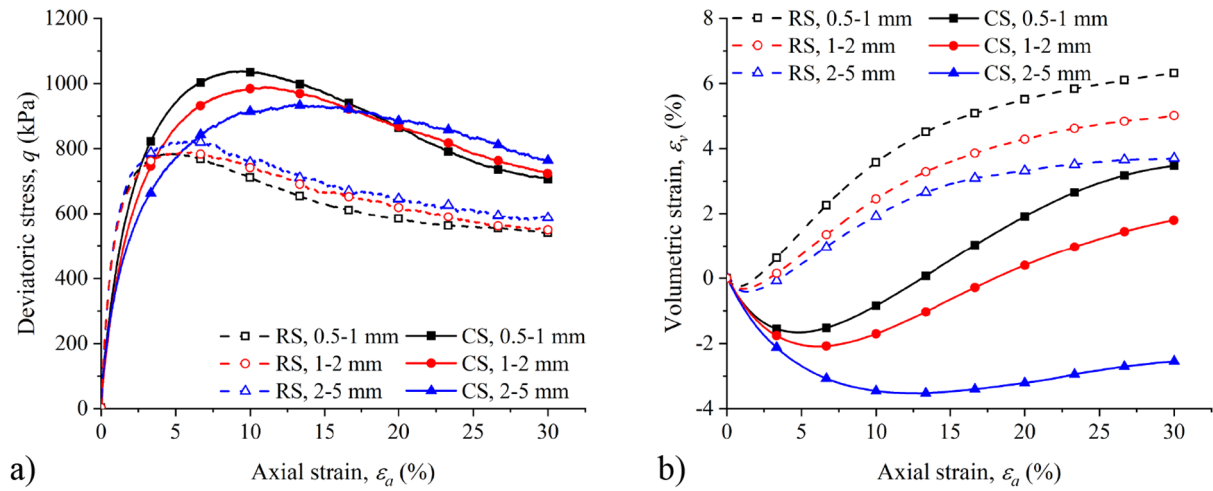


Figure 5.2. Evolutions of a) deviatoric stress; and b) volumetric strain with axial strain of calcareous sand (CS) and river sand (RS) specimens, at the initial relative density of 0.7 under the effective confining pressure of 200 kPa.

As presented by the dashed curves in Figure 5.2(a), at the initial shear stage, the deviatoric stress of river sand increased rapidly, surpassing the corresponding increasing rate of calcareous sands. This observation indicates that the inter-particle pores within the river sands were comparatively less and more stable than those of the calcareous sands. The axial strain corresponding to the peak deviatoric stress of river sands is smaller than that of calcareous sands. Additionally, the peak shear strength of river sands is significantly lower than that of calcareous sands due to the relatively smooth particle surface texture, resulting in lower inter-particle friction and weaker interlocking effect. As the axial strain increased, the river sands also exhibited strain softening behaviour. However, in contrast to calcareous sands, it was noted that the rate of deviatoric stress reduction remained almost consistent across various grain sizes of river sands. Additionally, river sands with larger particle sizes consistently exhibited higher shear strength. The observed outcome can be attributed to the considerably low level of particle breakage in river sands. This, in turn, ensures the structural integrity and stability of river sands throughout the shear process.

Figure 5.2(b) presents the relationships between volumetric strain (ϵ_v) and axial strain (ϵ_a) for calcareous sand (CS) and river sand (RS) specimens. The calcareous sand specimen with a larger particle size ($d = 2-5$ mm) exhibited a tendency of shear contraction, while those composed of fine calcareous sands underwent significant shear dilatation. For coarse grain specimen, intense particle breakages dominated the micromechanical behaviour, reducing the intensity of particle rearrangement, and thus the volumetric dilation. For fine grain specimens, the particle breakage intensity was low and particle rearrangement was significant due to particle shape irregularity. As a result, the specimen exhibited clear shear dilation after the peak stress was reached.

For river sands, the specimens exhibited a more prominent degree of shear dilation than the calcareous sands. The finer river sands exhibited had higher final volumetric strain after a negligible initial shear contraction. Furthermore, the onset of shear dilation was observed in the river sands at a significantly lower value of axial strain ($< 2\%$). This can be attributed to much less particle breakage occurred in river sands than that of calcareous sands. Additionally, the particle surface of river sands is much smoother than that of calcareous sands, such that the particle arrangement is more likely to occur, resulting in more evident shear dilation.

5.1.3 Influence of effective confining pressure on shear response

In the drained triaxial compression tests conducted on calcareous sand (CS) and river sand (RS) specimens, varied responses under different effective confining pressures ranging from 25 kPa to 800 kPa were observed, as illustrated in Figure 5.3(a) and (b). These tests were carried out with an initial relative density of 0.7 and particle sizes between 2 mm and 5 mm. The results, represented by solid curves, indicate that under low effective confining pressures, the calcareous sand specimens exhibited pronounced strain softening and shear dilation. Consequently, these specimens reached shear strengths at relatively low axial strains. This behaviour is attributed to the rapid attainment of a steady state through interparticle friction and interlocking, accompanied by minimal particle breakage. Conversely, as the effective confining pressure increased, the specimens underwent more extensive consolidation. This led to significant enhancements in peak deviatoric stress at higher shear strains. Furthermore, it is worth noting that the calcareous sand specimens exhibit strain softening under an effective

confining pressure below 400 kPa. As the pressure increased, the shear dilatancy occurred in the specimen was gradually suppressed, causing the q - ε_a relationship curves to transit from strain-softening to strain-hardening. Under an effective confining pressure of 800 kPa, the specimen no longer experiences shear dilation and clearly displays strain hardening behaviour.

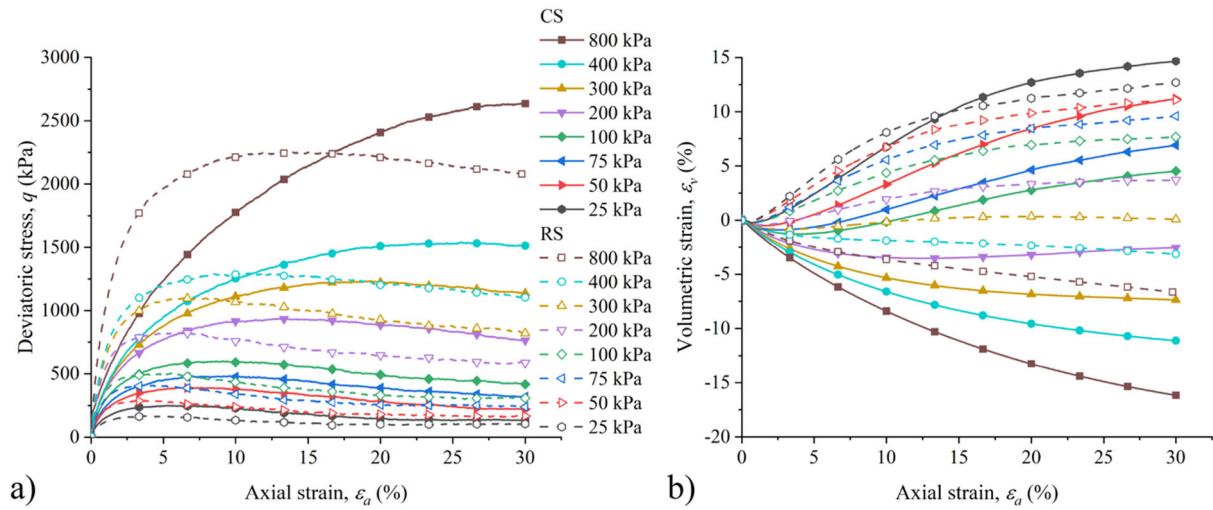


Figure 5.3. Evolutions of a) deviatoric stress; and b) volumetric strain with axial strain for calcareous sand (CS) and river sand (RS) specimens, at an initial relative density of 0.7 and in particle size range of 2-5 mm under different effective confining pressures.

Compared to calcareous sands, the river sand specimens consistently exhibited strain softening and shear dilation under both low and high confining pressures. They reached peak deviatoric stress at relatively low axial strains. This contrast was particularly evident under a high effective confining pressure of 800 kPa. The river sand specimen exhibited its maximum deviatoric stress at 15% of axial strain, while the calcareous sand specimen only reached the peak by the end of the experiment (30% of the axial strain). The significant divergence of sample response observed under high confining pressures can be attributed to particle breakage and the resultant alteration in granular packing. Under equivalent confining pressures, calcareous sands exhibited substantially higher breakage intensity than river sands. Consequently, calcareous sands achieved a denser consolidation due to the filling of void spaces by the generated fine grains, leading to higher shear strengths. In contrast, river sand grains were robust enough to withstand shear-induced breakage, resulting in a micromechanical behavior dominated by particle sliding and rearrangement.

Figure 5.3(b) presents the evolution of volumetric strain in both calcareous and river sand

specimens. Under effective confining pressures lower than 200 kPa, both sands exhibited significant shear-induced dilatancy. Particle breakage occurred less frequently, while the particles demonstrate a high degree of mobility. The extensive particle rearrangement resulted in marked shear dilatancy. However, with increasing confining pressure, calcareous sands displayed a transition from shear dilation to contraction, attributable to substantial particle breakage. In contrast, river sand specimens experienced less particle breakage and retained most of their smooth-surfaced particles, which tended to slide under low confining pressure. At higher confining pressures (> 300 kPa), the river sands initially contracted, followed by a trend towards dilatation. As confining pressure increased, some river sand particles were crushed, producing fine, irregularly shaped particles that filled interparticle voids, thus enhancing the material's relative density. Consequently, only minor dilation was observed with continued shearing. Notable shear contraction of river sands was observed only under the confining pressure of 400 and 800 kPa.

5.2 Particle breakage

5.2.1 Changes in particle size distribution

To investigate the influence of initial relative density on the evolutions of particle size distribution of calcareous sand specimens after the consolidated drained triaxial compression tests, the initial (dashed curves) and final (solid curves) particle size distribution for calcareous sand samples with different initial relative densities in the particle size range of 2-5 mm under the effective confining pressures of 200 kPa are presented in Figure 5.4(a). It is evident that all the final PSD curves of calcareous sand specimens with different initial relative densities shifted towards leftwards compared to the initial ones, suggesting that the experiments have crushed coarse particles, producing more fines. Whilst the particle sizes of the three specimens fall within the same range, the quantity of particles sharing identical sizes within that range is not uniform. Consequently, the initial PSD curves presented in dashed lines for the three specimens exhibit slight variations in position. Although the difference is not particularly pronounced, it can be seen from the figure that the contrast between the initial and final PSD curves is more evident in specimens with higher initial relative densities. This suggests that more intense particle breakage occurred in the dense calcareous sands during shearing.

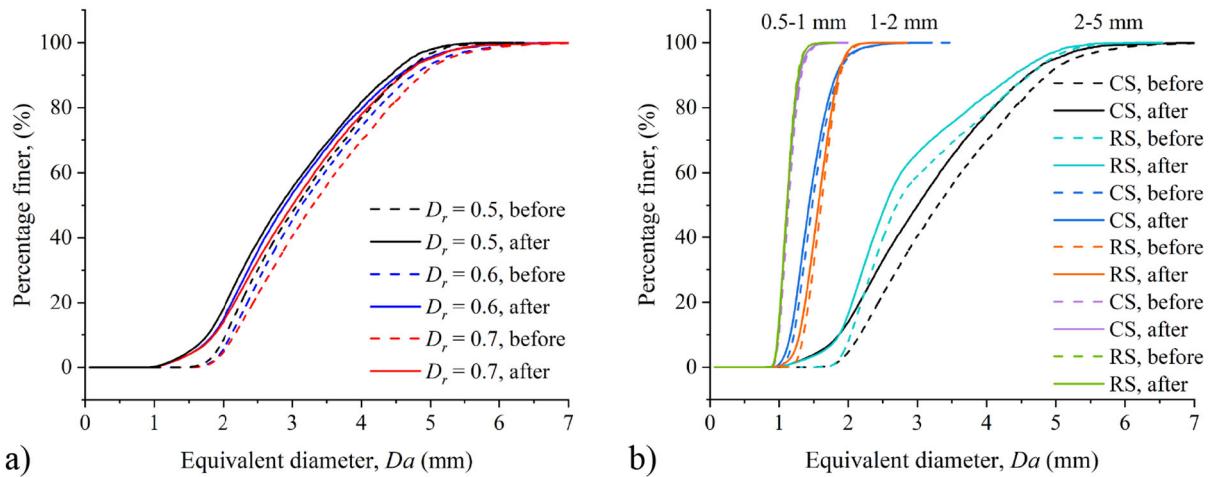


Figure 5.4. Initial (dashed curves) and final (solid curves) PSD for (a) CS with different initial relative densities but uniform particle size in the range of 2-5 mm; (b) CS and RS with initial relative density of 0.7 but different particle size ranges under the effective confining pressure of 200 kPa.

The influence of initial particle size on the evolutions of particle size distribution after the CD triaxial compression tests were investigated through the initial (dashed curves) and final (solid curves) particle size distributions for calcareous and river sand specimens as shown in Figure 5.4(b). In the tests, all tests had the same initial relative density as 0.7, but different particle size ranges under the effective confining pressures of 200 kPa. It can be clearly seen from the figure that the effect of particle size on the evolutions of PSD curves is much more pronounced than that of the initial relative density for both calcareous and river sands. The results revealed that specimens composed of coarser particles underwent more pronounced changes in particle size distributions compared to those consisting of particles in finer ranges, suggesting that larger particles experienced greater crushing. This finding aligns with the trend identified from the one-dimensional consolidation tests in section 4.4.2. By comparing the results for two types of sand particles in the size range of 2-5 mm, it becomes apparent that calcareous sands experience a much higher degree of particle breakage during shearing.

To investigate the influence of effective confining pressure on the evolutions of particle size distribution after the compression tests, initial (dashed curves) and final (solid curves) particle size distributions for calcareous and river sand samples are presented in Figure 5.5(a) and (b), respectively. It is obvious from the results that the change in PSD curve positions before and after the tests under relatively high confining pressures are pronounced for both calcareous and river sand specimens. When the sand specimen is subjected to a relatively high

effective confining pressure during the shearing process, the sand particles are closely packed, significantly increasing the inter-particle interactions. Consequently, the particle sliding is obviously suppressed, leading to extensive particle breakage as the experiment progresses. However, the micromechanical behaviour of sand particles under lower confining pressures is mainly characterised by particle rearrangement, with reduced particle breakage. As a result, the position of their initial and final PSD curves shows less pronounced changes. Nevertheless, the findings presented in the figure do not exhibit a distinct disparity in the outcomes between calcareous and river sand samples under the same level of confining pressure, thus necessitating a more thorough examination of the distribution statistics on particle size.

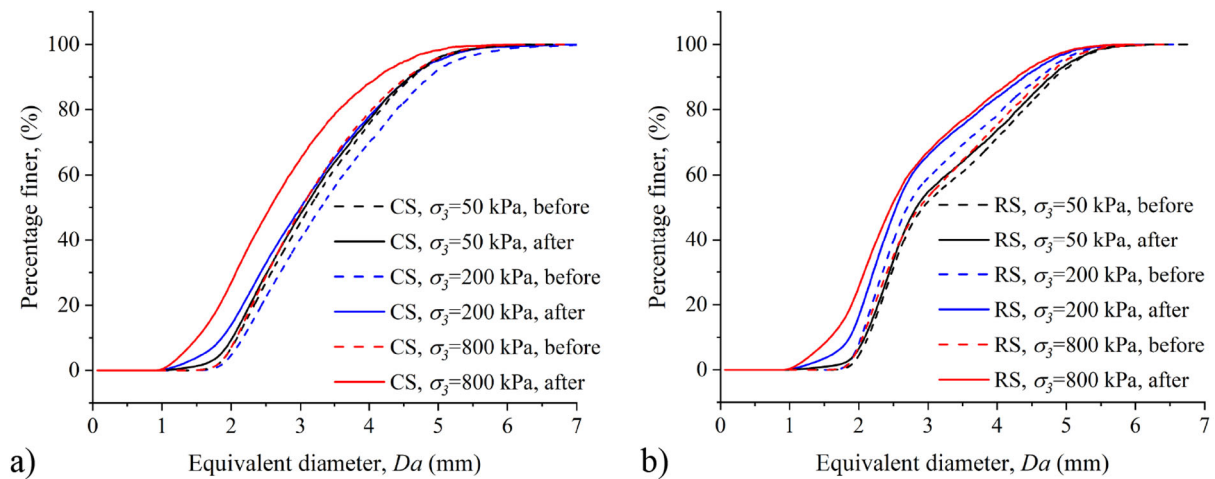


Figure 5.5. Initial (dashed curves) and final (solid curves) PSD for (a) CS samples, and (b) RS samples with initial relative density of 0.7 and in particle size range of 2-5 mm under different effective confining pressures.

5.2.2 Statistics of particle size distribution

The different patterns of particle size distribution can be clearly distinguished from the statistical analysis of particle size frequency distribution, as shown in Figure 5.6(a) and (b). Before the tests, the particle size of calcareous sands of different initial relative densities ranged from 2 to 5 mm, following a Gaussian distribution. After the shearing tests, a substantial reduction in the frequency counts of particles larger than 2 mm, as well as an evident increase in the fine particles of size 1-1.5 mm can be observed, revealing that a significant proportion of calcareous sands were crushed.

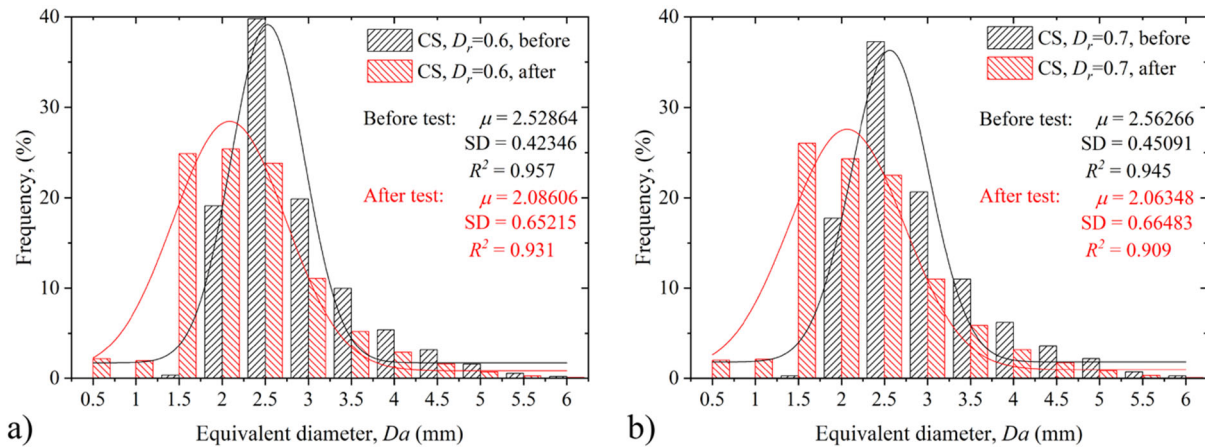


Figure 5.6. Statistics of individual particle size of calcareous sands with the initial particle size range of 2-5 mm and initial relative density of (a) 0.6, and (b) 0.7 before and after the tests under the effective confining pressure of 200 kPa.

In Figure 5.6(b), the denser specimen ($D_r = 0.7$) exhibit 26% of particles with equivalent diameter measuring between 1 and 1.5 mm, a slightly higher than that obtained for the loose specimen with the initial relative density of 0.6 (24%). Furthermore, it should be noted that the change of mean particle size was negligibly small for different tests, indicating that the impact of different initial relative densities on the degree of particle breakage is not particularly pronounced. Nonetheless, it is noteworthy that the specimen with higher initial relative density experienced a slightly higher level of particle breakage, which quantitatively justifies the results obtained from Figure 5.4(a).

Figure 5.7(a) and (b) present the statistical results of the frequency counts of particle size distribution for specimens with different initial particle sizes in the ranges of 2-5 mm and 1-2 mm, respectively. Before the tests, the frequency counts of equivalent particle diameter of calcareous sands followed well the Gaussian distributions. After shearing, as shown in Figure 5.7(a), coarser calcareous sands underwent more pronounced breakage, as evidenced by the decrease in the number of larger particles and a significant increase in the fine particles of size smaller than 2 mm. The standard deviation (SD) of the Gaussian distribution increased from 0.45 to 0.66, indicating that the breakage has produce particles of a wider size range. Conversely, Figure 5.7(b) illustrates that calcareous sands of size 1-2 mm underwent minimal breakage, with only a slight reduction in coarse particle frequency and increase of smaller particles. Furthermore, after the test, the change in the standard deviation of the Gaussian

distribution is not significant compared to that in Figure 5.7(a). The results further validate the conclusions reached in Figure 5.4(b).

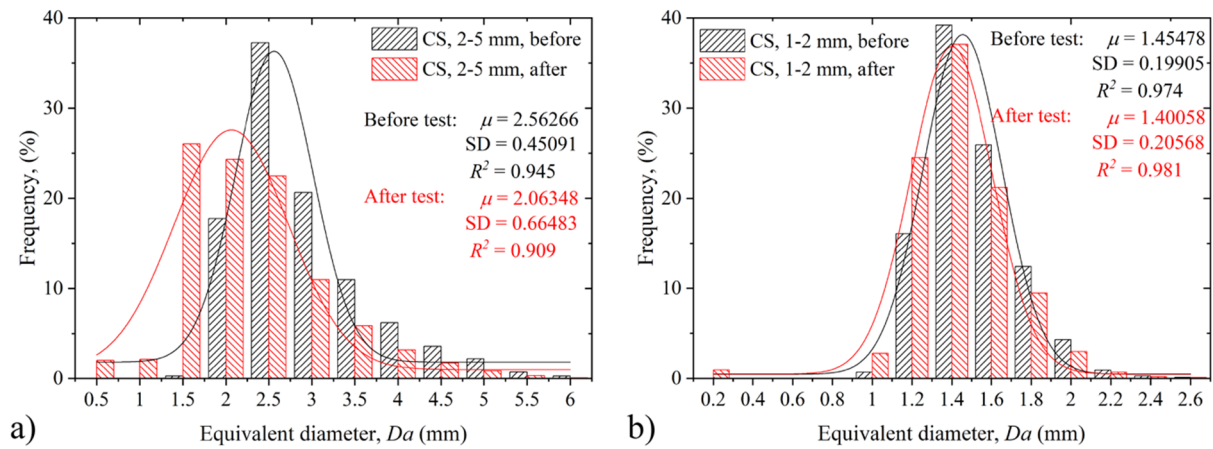


Figure 5.7. Statistics of individual particle size of calcareous sands with initial relative density of 0.7 in initial particle size range of (a) 2-5 mm, and (b) 1-2 mm before and after the tests under the effective confining pressure of 200 kPa.

As a comparison, the statistical results of river sand size distributions are shown in Figure 5.8(a) and (b). By comparing the results presented in Figure 5.8(a) and (b), it is evident that after shearing, the particle size frequency distribution for fine and coarse specimens exhibit a more significant difference than that of the calcareous sands. Specimens comprised of relatively large-sized river sand particles experienced a greater degree of particle breakage, resulting in a notable reduction in the number of larger particles and a significant increase in the number of finer particles.

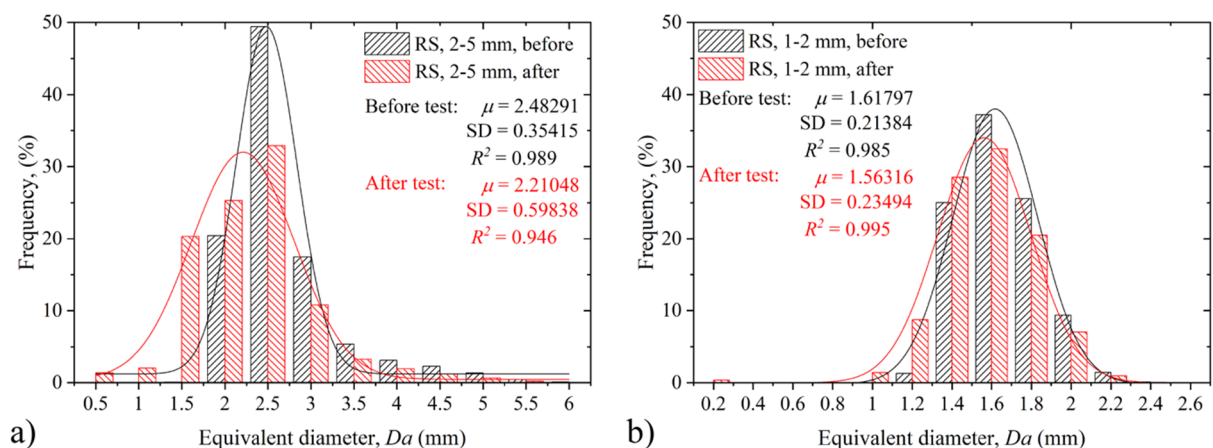


Figure 5.8. Statistics of individual particle size of river sands with initial relative density of 0.7 in initial particle size range of (a) 2-5 mm, and (b) 1-2 mm before and after the tests under the effective confining pressure of 200 kPa.

By comparing the data depicted in Figure 5.8(a) and Figure 5.7(a), it is apparent that the calcareous sand specimens underwent a higher degree of particle breakage than the river sand samples when exposed to identical experimental conditions. Specifically, after shearing, sand particles with diameter less than 1.5 mm (i.e. newly produced fines) accounted for 23% of the river sand specimen, whereas the proportion exceeded 30% in the calcareous sand specimen. The same changing trends can also be obtained by comparing Figure 5.7(b) and Figure 5.8(b), with sand particles finer than 1 mm accounted for 1.76% of the river sand specimen after shearing, whereas the proportion exceeded 3.72% in the calcareous sand specimen.

Figure 5.9(a) and (b) demonstrate the statistical results of the particle size frequency for calcareous sand specimens tested under the effective confining pressure of 50 kPa and 800 kPa, respectively. The frequency counts of equivalent particle diameter followed well Gaussian distributions. As depicted in Figure 5.9(a), the statistical mean value of equivalent diameter only decreased by about 0.11 mm after shearing, indicating that the particle size of most of the calcareous sand particles could remain concentrated between 2 and 2.5 mm under a relatively low confining pressure. The overall particle size distribution remained fairly consistent and experienced no significant changes during the test. The observed increase in the SD value suggests a rise in size variability. The particle breakage also makes the particle size distribution closer to the Gaussian distribution along with the augmentation of the associated R^2 value.

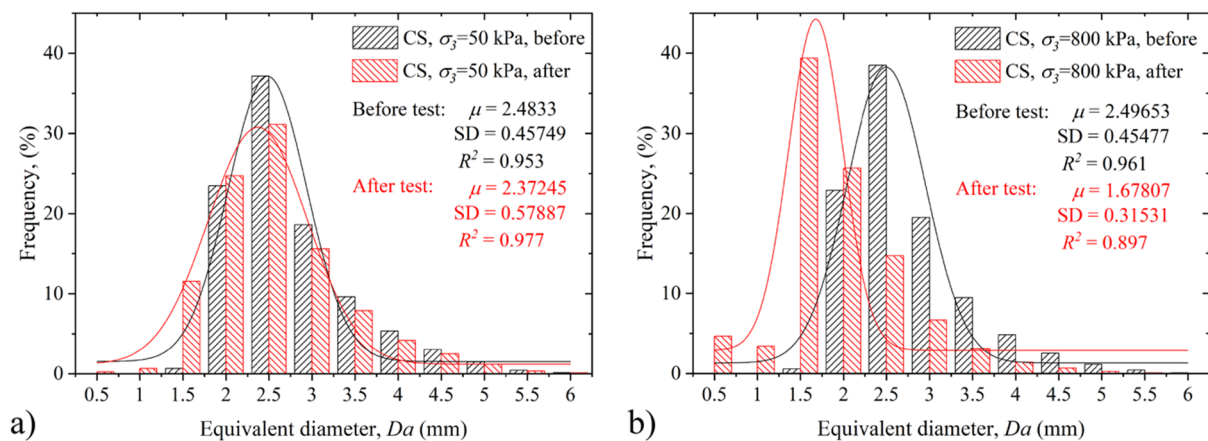


Figure 5.9. Statistics of individual particle size of calcareous sands with initial relative density of 0.7 in initial particle size range of 2-5 mm before and after the tests under the effective confining pressure of (a) 50 kPa, and (b) 800 kPa.

As shown in Figure 5.9(b), the notable shift of equivalent particle size distribution to the

fine size range can be observed. This decrease in particle size under high confining pressure can be attributed to the intense breakage of coarse particles. As the fine grains can resist further breakage, the SD value after shearing is smaller than that before the test. However, the increase in the quantity of calcareous sands smaller than 0.5 mm also gives rise to a deviation from a Gaussian distribution in the particle size frequency distribution, thereby causing a significant decrease in the R^2 value. By comparing the above two figures, it is clear that intense particle breakage has occurred in the calcareous sand sample under relatively high confining pressure, which matches the results reported in Figure 5.5(a).

Figure 5.10(a) and (b) demonstrate the statistical results of particle size for river sands tested under the effective confining pressure of 50 kPa and 800 kPa, respectively. The frequency counts of equivalent diameter of river sands before and after shearing under different confining pressures followed well a Gaussian distribution with R^2 larger than 0.9. As demonstrated in Figure 5.10(a), the slight decrease in mean and increase in SD indicate that small-scale particle breakage occurred in the river sand specimen during the triaxial shearing under the lower confining pressure. By comparing with Figure 5.9(a), it can be find that the frequency counts of particles finer than 1.5 mm in calcareous sand specimen reached 11.74% after the test, which is slightly higher than that of river sand specimen (9.59%), indicating that calcareous sands are more susceptible to breakage under low confining pressure shearing.

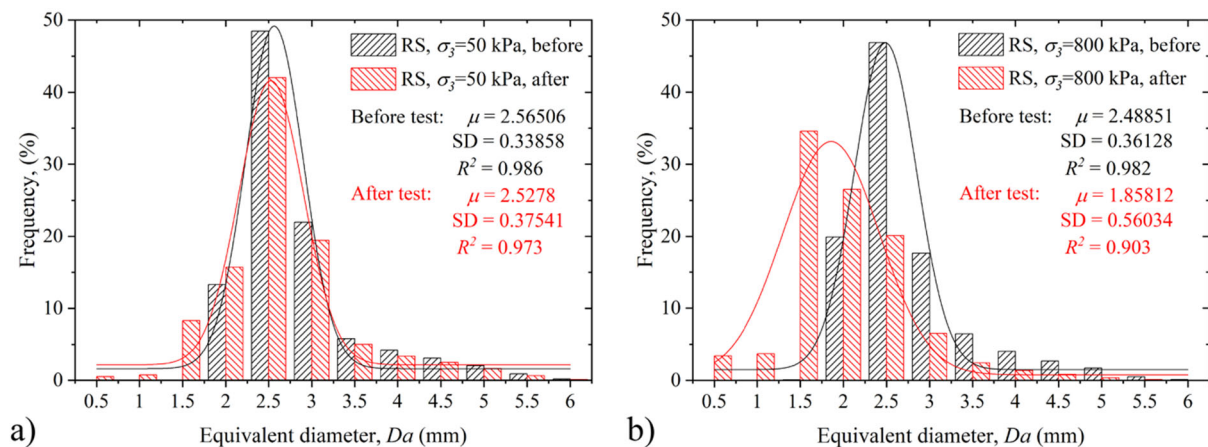


Figure 5.10. Statistics of individual particle size of river sands with initial relative density of 0.7 in initial particle size range of 2-5 mm before and after the tests under the effective confining pressure of (a) 50 kPa, and (b) 800 kPa.

As presented in Figure 5.10(b), the mean particle size reduced significantly from 2.49 mm

to 1.86 mm after the shearing under a confining pressure of 800 kPa. The presence of a large number of river sand particles finer than 2 mm also led to a significant increase in SD. Fine river sand particles in particle size range of 0-0.5 mm and 0.5-1 mm exhibited similar frequencies. As a result, deviation from the Gaussian distribution was observed in the frequency distribution of the post-test results, leading to a decrease in the R^2 value. The change in the parameters of the Gaussian distribution before and after the test provide clear evidence that the river sand samples under high confining pressure during shearing experience more pronounced particle breakage than those under low confining pressure.

5.2.3 Changes in particle size distribution obtained by applying sieving analysis

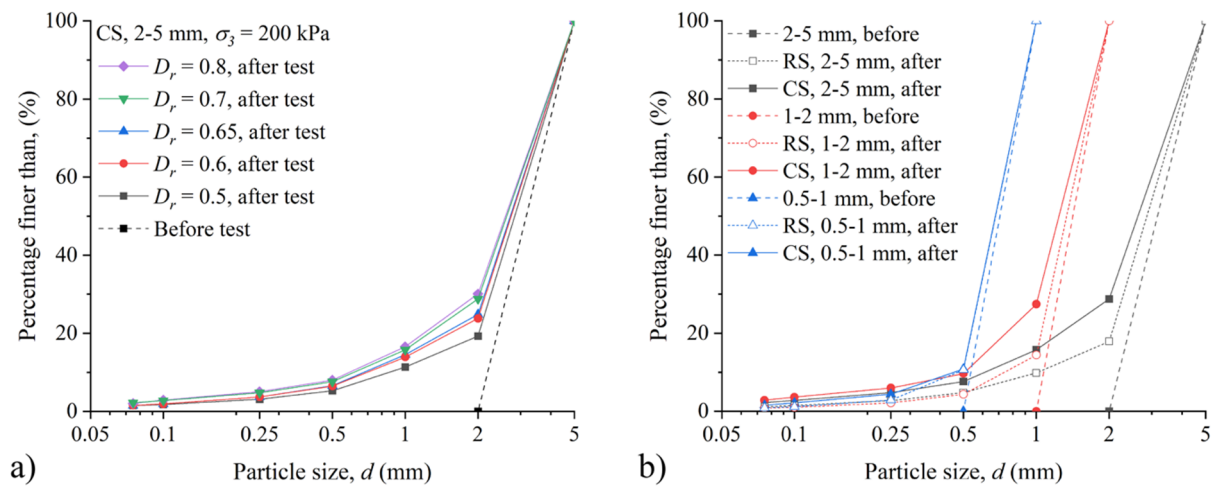


Figure 5.11. PSD for (a) calcareous sands in particle size range of 2-5 mm but with different initial relative densities; (b) calcareous and river sands with initial relative density of 0.7 but in different particle size ranges before (dashed lines) and after (solid lines) the tests under the effective confining pressure of 200 kPa. The results were obtained by applying sieving analysis.

To complement the findings derived from implementing the DIA method, the traditional sieving analysis was also performed. Figure 5.11(a) presents the particle size distribution of calcareous sand specimens in particle size range of 2-5 mm but with different initial relative densities before and after the consolidated drained triaxial compression tests under the effective confining pressure of 200 kPa. The figure demonstrates that the particle size distribution of the calcareous sand specimens before shearing are identical for varying levels of initial relative densities, as represented by the dashed line. While there is a notable consistency in the cumulative mass percentages across the various calcareous sand specimens with different initial relative densities after shearing, slight discrepancies are discernible. It is evident that,

across the particle size range of 0.075 to 2 mm, the cumulative mass percentage increased with D_r . Notably, particles in the size range of 1-2 mm exhibited a more substantial increase in the cumulative mass percentage of the denser specimen. This observation indicates a higher degree of particle breakage in the denser specimens during the shearing process.

Figure 5.11(b) illustrates the particle size distribution of calcareous and river sand specimens with initial relative density of 0.7 but in different particle size ranges before (dashed lines) and after (solid lines) the consolidated drained triaxial compression tests under the effective confining pressure of 200 kPa. The two different types of sand specimens exhibited an identical behaviour, whereby an increase in particle size led to greater variations in their initial and final PSD lines. This finding provides further evidence that larger sand particles are subject to more intense breakage mechanisms. By comparing the results of two different types of sands in the same particle size range, it is evident that calcareous sand specimen consistently yields more fine particles when compared to the river sand specimen within the same particle size interval. This discrepancy is particularly noticeable for the specimen composed of sand particles in size range of 1-2 mm and 2-5 mm. The findings sufficiently demonstrate that calcareous sand particles experience more severe particle breakage, producing greater quantities of finer particles.

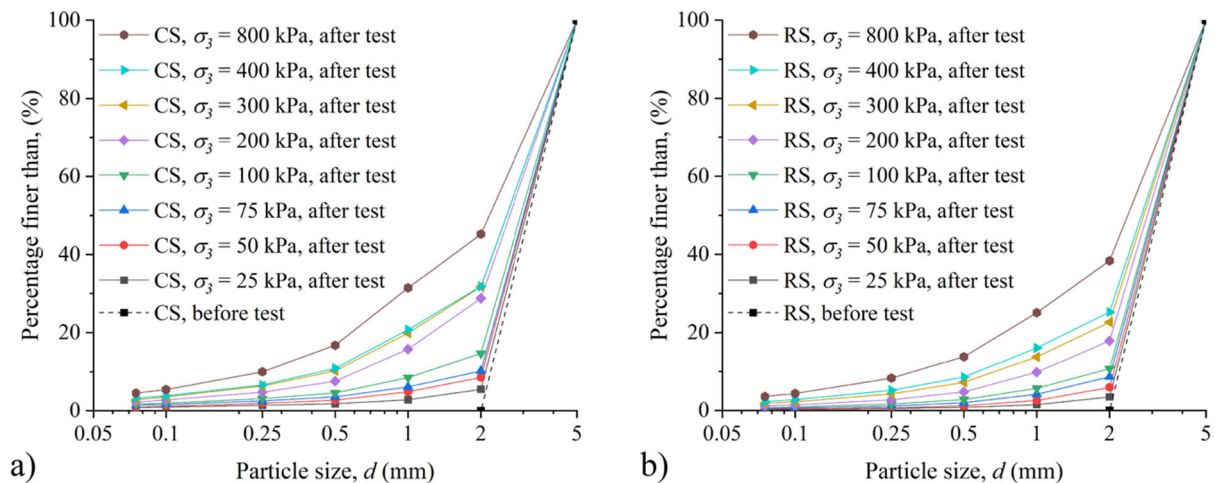


Figure 5.12. PSD for (a) calcareous sands; and (b) river sands in particle size range of 2-5 mm and with initial relative density of 0.7 before (dashed lines) and after (solid lines) the tests under different effective confining pressures. . The results were obtained by applying sieving analysis.

Figure 5.12(a) and (b) present the particle size distribution for calcareous and river sand specimens, with the initial particle size range of 2-5 mm and relative density of 0.7. When the

confining pressure is relatively low (< 200 kPa), the cumulative particle size distribution after shearing are very close, but it can still be observed that the post-test and the pre-test PSD lines for sand specimen under a relatively high confining pressure has higher portion of fines. This indicates a more substantial scale of particle breakage. When the effective confining pressure exceeded 200 kPa, a noteworthy level of particle breakage in specimens occurs, increasing rapidly the portion of fines.

By comparing the results of two different types of sand specimens under the same confining pressure, it is evident that calcareous sand specimen consistently yields higher percentage of fines when compared to river sand specimen within the same particle size interval. This discrepancy is particularly noticeable for the specimens under the confining pressure higher than 200 kPa. The findings sufficiently demonstrate that calcareous sands experience more severe particle breakage, resulting in greater quantities of finer particles being produced.

5.2.4 Quantification of particle breakage

The traditional method to quantify the degree of particle breakage proposed by Hardin (1985) was applied in this study, and the results for calcareous and river sand specimens are shown in the following table.

Table 5.1. Relative breakage for CS in different particle size ranges and with different initial relative densities after the tests under different effective confining pressures obtained by applying MSA.

| Particle size, d (mm) | Effective confining pressure, σ_3 (kPa) | Initial relative density, D_r | | | | |
|-------------------------|--|---------------------------------|-------|-------|-------|-------|
| | | 0.5 | 0.6 | 0.65 | 0.7 | 0.8 |
| 2-5 | 100 | 0.116 | 0.121 | 0.123 | 0.127 | 0.124 |
| | 200 | 0.145 | 0.153 | 0.177 | 0.153 | 0.224 |
| | 300 | 0.208 | 0.229 | 0.241 | 0.243 | 0.256 |
| 1-2 | 100 | 0.052 | 0.066 | 0.084 | 0.088 | 0.096 |
| | 200 | 0.074 | 0.104 | 0.126 | 0.126 | 0.126 |
| | 300 | 0.107 | 0.136 | 0.157 | 0.157 | 0.163 |
| 0.5-1 | 100 | 0.040 | 0.045 | 0.051 | 0.051 | 0.051 |
| | 200 | 0.087 | 0.083 | 0.084 | 0.081 | 0.090 |
| | 300 | 0.107 | 0.119 | 0.115 | 0.116 | 0.122 |

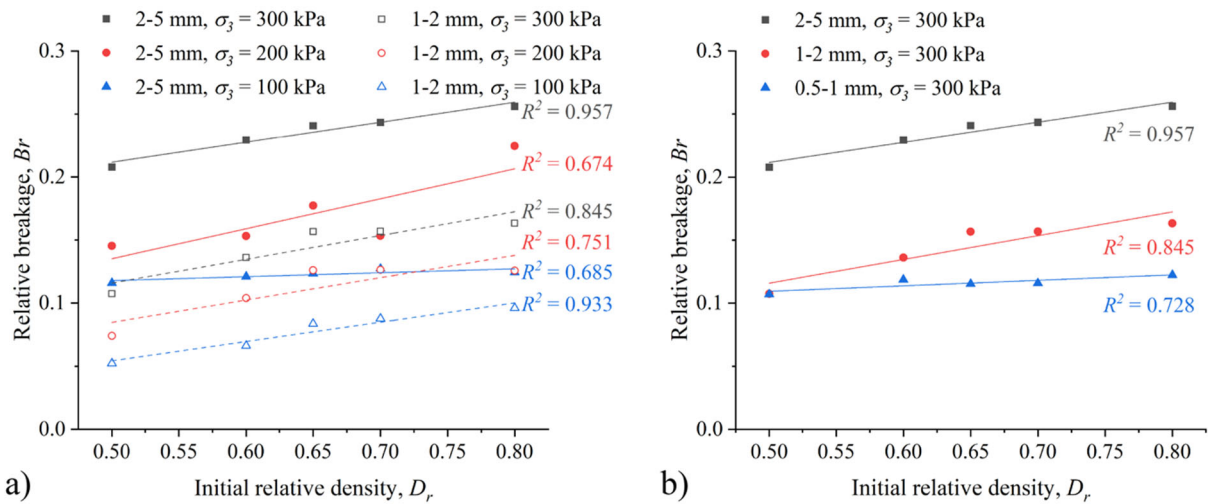


Figure 5.13. Relative breakage for calcareous sands with different initial relative densities (a) in particle size range of 2-5 mm and 1-2 mm after the tests under the effective confining pressure of 100, 200 and 300 kPa; and (b) in different particles size ranges after the tests under the same effective confining pressure of 300 kPa obtained by applying sieving analysis.

Figure 5.13(a) presents the evolutions of relative breakage (B_r) with the increase of initial relative density for calcareous sand specimens under various testing conditions. Regardless of the initial particle size ranges of the calcareous sand specimens or the amount of the effective confining pressure applied during shearing, there is a linear positive correlation between relative breakage and the initial relative density. This indicates that the closely packed calcareous sand particles are more likely to experience the stripping of surface asperities and the complete breakage of single particles during shearing. The rate of growth in relative breakage among specimens composed of calcareous sand particles, which initially measured between 1-2 mm, exhibited nearly uniform results, with values ranging from 0.15 to 0.18.

However, there is a marked difference in the growth rate of relative breakage of calcareous sand specimens with the initial size range of 2-5 mm. In particular, the growth rate of the linear fitting results represented by the solid blue line under the confining pressure of 100 kPa is significantly lower than those under greater confining pressures. This can be attributed to two factors: the large dispersion of the data results with small R^2 , and the slow growth of B_r under lower confining pressures. Coarse calcareous sands are more prone to be crushed, thus resulting in a more significant effect of the change in the confining pressure on their breakage characteristics. Conversely, smaller-sized particles are much stronger to resist damage, thus exhibiting a less pronounced rate of change in the B_r under the same confining pressure.

Figure 5.13(b) shows the B_r - D_r relationship of calcareous sand specimens in different particle size ranges under the same testing confining pressure of 300 kPa. There is also a clear linear positive correlation between the relative breakage and the initial relative density for calcareous sand specimen in each particle size range. For calcareous sand specimens with the same initial relative density of 0.5 but in different particle size ranges, the B_r values of the specimens in the particle size range of 1-2 mm and 0.5-1 mm is the same, but is much smaller than the value of the specimens in the size range of 2-5 mm. This can be attributed to the larger pore volume found between coarse particles, which allows for particle sliding even under a relatively high confining pressure (300 kPa), and enhanced the breakage. In comparison, smaller-sized particles tend to have smaller void volumes. In addition, the effects of the asperities on their surface are greatly weakened by the size effect, thus resulting in their B_r values be closer and significantly smaller than that of the 2-5 mm sand particles. The increase in B_r values for the specimen composed of calcareous sands within the size range of 0.5-1mm is not considerably substantial as the initial relative density increases, due to the inherently limited amount of particle breakage that takes place in smaller-sized sand particles.

Table 5.2. Relative breakage of calcareous and river sand specimens in the particle size range of 2-5 mm and with initial relative density of 0.7 after the tests under different effective confining pressures obtained by applying MSA.

| | Effective confining pressure, σ_3 (kPa) | | | | | | | |
|----|--|-------|-------|-------|-------|-------|-------|-------|
| | 25 | 50 | 75 | 100 | 200 | 300 | 400 | 800 |
| CS | 0.042 | 0.065 | 0.079 | 0.111 | 0.214 | 0.245 | 0.248 | 0.359 |
| RS | 0.025 | 0.042 | 0.063 | 0.079 | 0.133 | 0.174 | 0.196 | 0.300 |

Table 5.2 and Figure 5.14 present the B_r - σ_3 relationships for calcareous and river sand specimens in the same particle size range of 2-5 mm and with the same initial relative density of 0.7 after the tests obtained by conducting sieving analysis. For both types of sands, the relative particle breakage increased with the effective confining pressure, following an exponential relationship. When the confining pressure was less than 0.2 MPa, the relative breakage increased rapidly with the increase of confining pressure in an approximately linear relationship. When the confining pressure exceeds 200 kPa, the rate of increase of the B_r of the sand particle specimens decreases significantly with the continuous increase of the confining pressure. For the same level of confining pressure, the B_r of calcareous sands is always greater

than that of river sands. This discrepancy increased as the confining pressure increased.

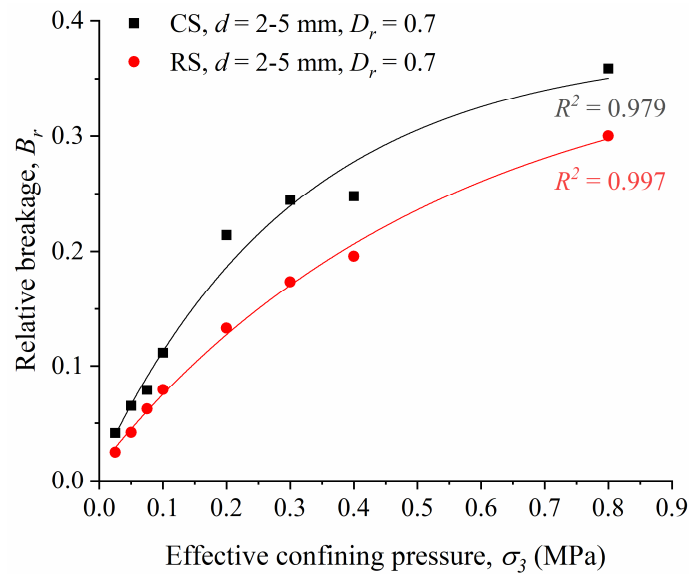


Figure 5.14. Evolutions of B_r with effective confining pressure for CS and RS in particle size range of 2-5 mm with initial relative density of 0.7. The data was obtained by applying MSA.

5.3 Changes of particle morphological characteristics

5.3.1 Morphological characteristics of calcareous sands

Figure 5.15 illustrates the distribution of particle shape descriptors — sphericity, convexity, aspect ratio, and flatness — for calcareous sand specimens in the 2-5 mm particle size range with an initial relative density of 0.7. These distributions show results both before and after the consolidated drained triaxial compression tests, which were conducted under an effective confining pressure of 400 kPa, as analysed by Dynamic Image Analysis (DIA). The fitting curves indicate that the distributions of sphericity, aspect ratio, and flatness, both before and after the tests, followed well the Gaussian distributions. In contrast, the distribution of convexity followed an Exponential distribution.

As shown in Figure 5.15(a), a slight increase in the mean and decrease in the standard deviation of particle sphericity distribution after the test can be observed, indicating that the sphericity of most of the individual calcareous sand particles are increased, with most values fell into a narrow range closer to 1. Such changes imply that the particle surface asperities were worn off, and the rough edges are smoothed, resulting in an overall transformation of the calcareous sand particles towards a more spherical shape.

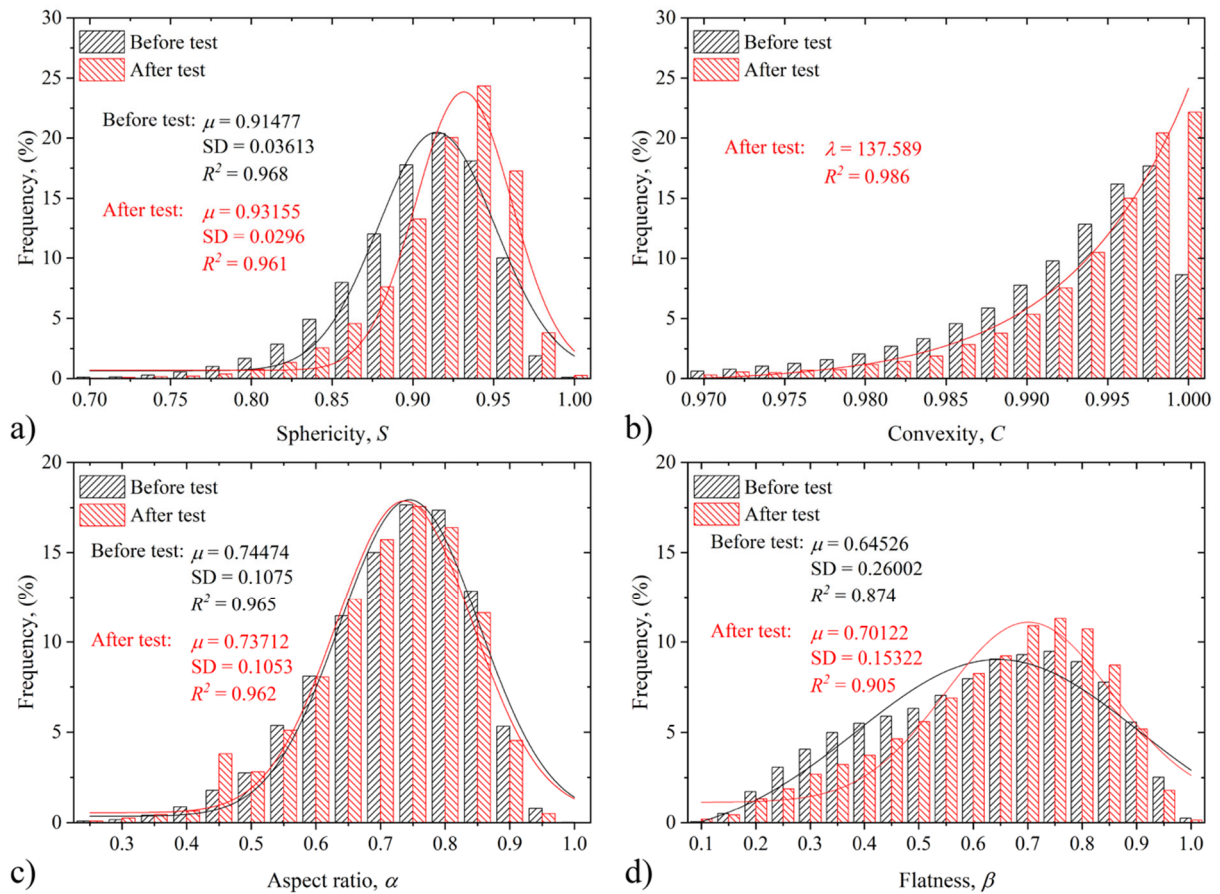


Figure 5.15. Frequency of particle shape descriptors: (a) sphericity, (b) convexity, (c) aspect ratio, and (d) flatness for calcareous sands before and after the tests. The specimens were in particle size range of 2-5 mm, initial relative density of 0.7 and under an effective confining pressure of 400 kPa.

As presented in Figure 5.15(b), the frequency of convexity for calcareous sand particles before test is not of exponential distribution due to the fact that a larger percentage of particles, approximately 17.67%, have convexity values within a range of 0.996 to 0.998, while only 8.62% fall within the range of 0.998 to 1, which is closer to 1. After shearing, a higher number of particles are found to have convexity values close to 1, with particles located in the range of 0.998 to 1 occupying 22.18%. Consequently, an exponential distribution is observed in the frequency distribution. The increase in the convexity of a majority of calcareous sand particles, resulting in a value closer to 1, suggests that the uneven asperities on the particle surfaces have been smoothed out and the particle angles rounded, leading to significantly smoother surfaces.

As shown in Figure 5.15(c), despite the similarity in the position and shape of the distribution curves before and after the test, there exists a slight reduction in the distribution's mean after the test. Additionally, a noteworthy observation is the marked increase in the

percentage of particles with aspect ratios ranging from 0.4 to 0.45, which increased from 1.7% before to 3.7% after shearing test. The slight decrease in aspect ratio after the test indicates that the particle breakage during shearing has produced a number of more elongated particles.

As presented in Figure 5.15(d), the results display a significant increase in the mean and a decrease in the standard deviation of the frequency distribution of flatness of calcareous sands after shearing. This pattern suggests a shift towards less flat particle shapes, with a majority of the values tightly grouped in a range nearer to 1. This is likely because during breakage, the particle width tends to decrease more than thickness, leading to an increase in flatness values.

5.3.2 Morphological characteristics of river sands

As a comparison, Figure 5.16 presents the frequency counts of particle shape descriptors for river sands under the same experimental conditions as the calcareous sand specimens. The fitting curves clearly demonstrate that the frequency counts of sphericity, aspect ratio, and flatness, both before and after the test, adhered to a Gaussian distribution. In contrast, the frequency counts of convexity aligned with the exponential distribution.

As shown in Figure 5.16(a), a relatively small increase in the mean and a decrease in the standard deviation of the frequency distribution after the test can be observed, indicating that the sphericity of most of the individual river sand particles are slightly increased, with the majority of values distributed in a narrow range closer to 1. This implies that the asperities on the particle surface were worn off, and the rough edges are smoothed, resulting in an overall transformation of the particle shape towards a more spherical form.

As presented in Figure 5.16(b), the frequency of convexity for river sand particles before the test approximately 46.45% of particles have convexity values within a range of 0.995 to 0.9975, while only 16.57% fall within the range of 0.9975 to 1. After shearing, a higher number of particles are found within the interval range of convexity values that is closer to 1, with particles located in the range of 0.9975 to 1 occupying 38.23%. Consequently, an exponential distribution is observed in the frequency distribution. The increase in the convexity of a majority of river sand particles, resulting in a value closer to 1, suggests that the uneven asperities on particle surfaces have been smoothed out and the angles of the particles have been rounded, ultimately making their surfaces much smoother.

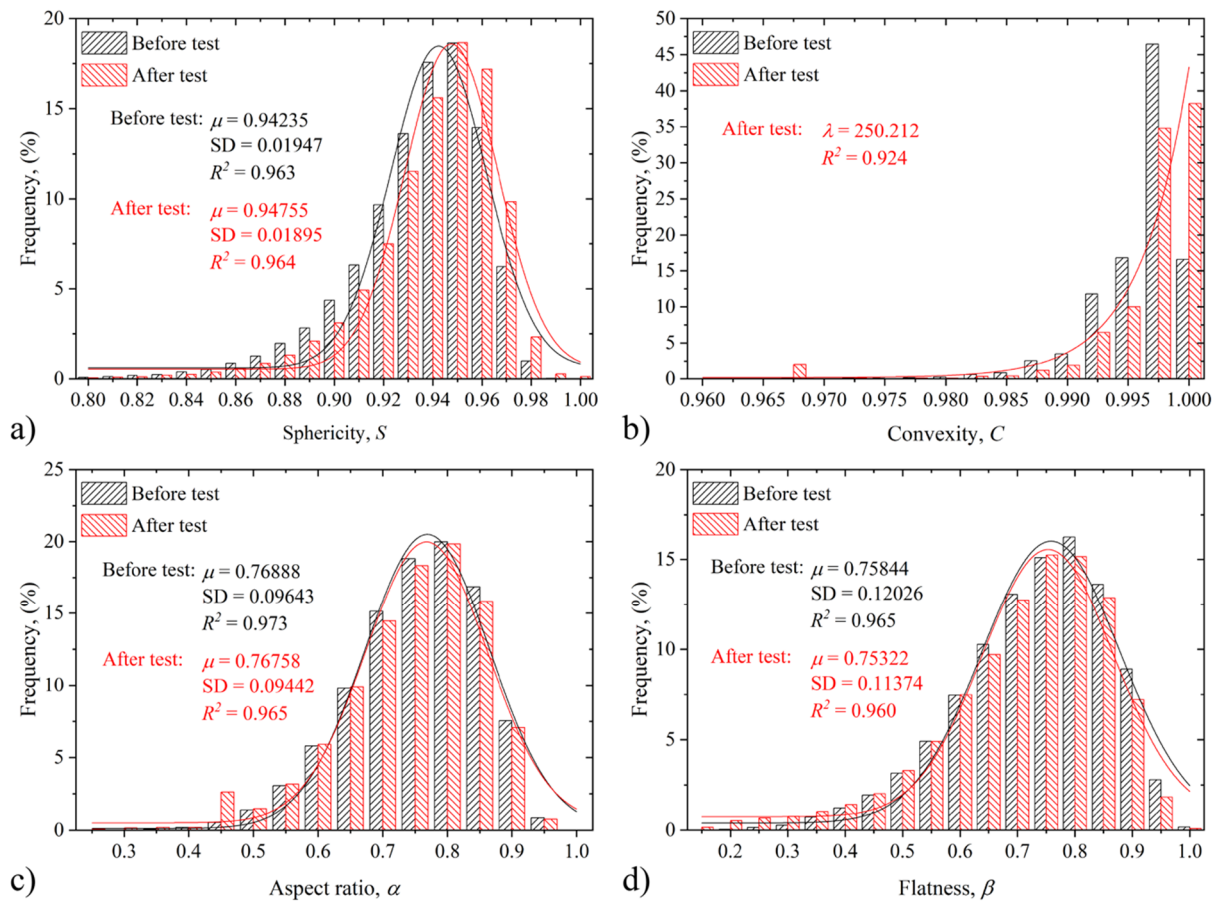


Figure 5.16. Frequency distribution of particle shape descriptors of (a) sphericity, (b) convexity, (c) aspect ratio, and (d) flatness for river sand specimens. The specimens have the particle size in the range of 2-5 mm, initial relative density of 0.7, under the effective confining pressure of 400 kPa.

As shown in Figure 5.16(c), despite the similarity in position and shape of the distribution curves before and after the experiment, there exists a slight reduction in the distribution's mean observed after the test. Additionally, a noteworthy observation is the marked increase in the percentage of particles with aspect ratios ranging from 0.4 to 0.45, which increased from 0.53% before to 2.63% after the shearing. The slight decrease in aspect ratio after shearing indicates that the shearing process has produced a number of river sand particles that exhibit a more elongated particle shape.

As presented in Figure 5.16(d), the results display a small decrease in the mean and the standard deviation of the frequency distribution of flatness of river sand particles after shearing. This suggests a small shift towards a flat shape of the individual river sand particles, with the majority of values clustering within a narrow range of 0.7-0.8. The rationale behind this is that during the crushing process of each particle, its thickness is more prone to be reduced in

comparison to its width. Consequently, when the thickness of the particle is divided by its width, a slightly smaller flatness value is obtained.

5.3.3 Comparison of particle morphological characteristics

By comparing the statistical results shown in Figure 5.15(a) and Figure 5.16(a), it is evident that the pre-shearing mean sphericity of river sand is 0.942, which is higher than that of calcareous sands (0.915). This suggests that undisturbed calcareous sands possess a more irregular shape compared to river sands.

Post-shearing, calcareous sands demonstrated a greater increase in the mean sphericity relative to river sands, attributable to the shearing-induced breakage of their irregular surfaces. Consequently, this leads to a morphology that is more spherical and exhibits increased variability from its original form. Conversely, prior to the test, river sand particles exhibited higher strength and a more uniform shape, accompanied by fewer surface irregularities. This resulted in less particle fragmentation and an insignificant change in sphericity following shearing. The sphericity of the calcareous sands is still smaller than that of the river sands after shearing, indicating that most of the river sand particles have a more spherical shape than the calcareous sand particles after the tests.

By comparing the statistical results shown in Figure 5.15(b) and Figure 5.16(b), it can be observed that most of the convexity values of the calcareous sands before the shearing test are distributed in the range of 0.97 to 0.998, where the percentage of each interval gradually increased as the interval range get closer to 1. The greatest number of calcareous sand particles, accounting for 17.67%, fell within the convexity range of 0.996 to 0.998. In contrast, prior to testing, river sands exhibited notably higher convexity values compared to calcareous sands, with 46.45% of their particle convexity falling between 0.996 and 0.998. This statistical trend suggests that in their natural state, the surface of river sand particles is significantly smoother than that of calcareous sand particles.

Post-shearing, the convexity of both calcareous and river sands transitioned into exponential distributions. The frequency of intervals with convexity values less than 0.996 decreased for calcareous sands, while a notable increase is noted for particles with convexity exceeding this threshold. The percentage of calcareous particles falling within the range of

0.998-1 increased from 8.62% before to 22.18% after the test. The rate parameter (λ) of the exponential distribution for river sands was significantly higher than that for calcareous sands, signifying a marked rise in the proportion of values in intervals approaching 1. There was a decrease in the frequency of river sand intervals with convexity values below 0.998. Conversely, a noticeable increase from 16.57% to 38.23% was observed for river sand particles with convexity values in the 0.998-1 range. These findings suggest that, following the tests, the surface texture of river sands becomes relatively smoother compared to that of calcareous sands.

A comparison of the statistical data in Figure 5.15(c) and Figure 5.16(c) reveals that the mean aspect ratio of river sands before the test exceeds that of calcareous sands. This suggests that individual calcareous sand particles in their natural state tend to have more elongated shapes compared to those of river sands. After shearing, the mean aspect ratio of calcareous sands shows a more pronounced decrease compared to that of river sands. This difference indicates that calcareous sand particles experienced more extensive particle breakages, leading to the formation of new, finer particles with elongated shapes. The generation of these elongated particles could be attributed to several factors: a relative reduction in the width of the original calcareous sand particles due to friction at specific points, the detachment of rod-like asperities from the particle surfaces, or the complete bifurcation of individual particles.

Additionally, a comparison between Figure 5.15(d) and Figure 5.16(d) clearly shows that the mean flatness of calcareous sands prior to shearing is less than that of river sands. This implies that, on average, individual CS particles in their natural state are flatter in shape compared to those of RS. After shearing, the flatness of the two different types of sand particles undergoes different changes. The fitted results indicate a significant increase in the mean of the calcareous sand particles' flatness, suggesting that the calcareous sand withstands greater stress along the “width” direction relative to the “thickness” direction during the crushing process, which results in its width becoming smaller relative to its thickness, ultimately making it less flat. The flatness of the river sands is slightly reduced after shearing, indicating that the particle sliding has resulted in a relatively smaller thickness, making it appear flatter.

5.4 Influence on shear strength characteristics

5.4.1 Influence on peak friction angle and cohesion

The strength parameters including peak friction angle and apparent cohesion of calcareous sands were obtained using the Mohr-Coulomb theory. Figure 5.17(a) demonstrates that the peak friction angle of calcareous specimens tends to decrease with the increasing particle size range under the CD condition. Specifically, calcareous specimens with an initial particle size range of 0.5-1 mm exhibited a peak friction angle of approximately 40° . This angle slightly decreased to 39° for specimens with a larger initial particle size range of 1-2 mm. Most notably, the peak friction angle for specimens with an even larger initial particle size range of 2-5 mm showed a significant decrease to about 37° . This can be attributed to the relatively large size of the void spaces between the coarse particles, which makes inter-particle sliding more likely to occur. Conversely, smaller particles have smaller void space volumes, leading to closer alignment and reduced susceptibility to self-displacement. These findings align with those presented by Wang et al. (2022a). It is also clear from the figure that the calcareous sands with large initial relative densities also exhibited relatively large friction angles, due to the fact that the more closely packed distributions could greatly enhance the friction between the sand particles.

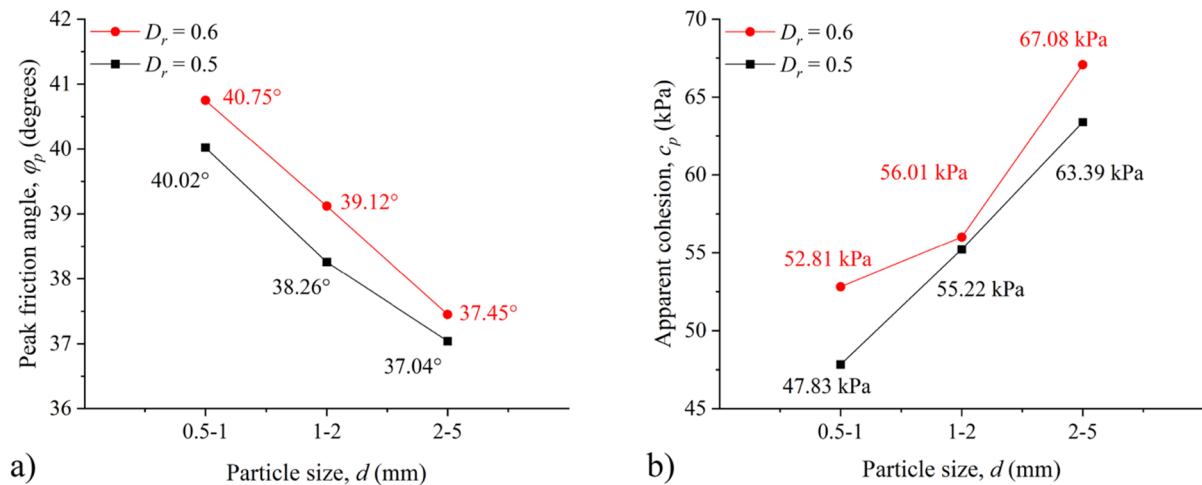


Figure 5.17. Variation of a) peak friction angle; and b) apparent cohesion with particle size for calcareous sand specimen with initial relative density of 0.5 and 0.6.

During shearing, “apparent cohesion” was used to represent the strong interlocking behaviour that occurred between angular sand particles. Figure 5.17(b) reveals that specimens composed of calcareous sand particles in the same particle size range exhibited a slight increase

in peak cohesion as their initial relative densities increased. Due to the closely packed particle structures of the denser specimens, there was a greater degree of interlocking and complete contact among them. The peak cohesion for calcareous specimens tended to decrease with decreasing particle size range under the CD condition. The reason behind this can be attributed to the irregular shapes and asperities distributed on the surface of the coarse calcareous sand particles which are more prominent and thus, facilitate greater degree of interlocking. Conversely, the smaller particles being of a relatively smaller size, experienced a decreased effect of its irregular shape, ultimately resulting in a reduced likelihood of interlocking.

5.4.2 Influence on dilatancy angle

As can be seen from the volumetric strain-axial strain relationships presented in Figure 5.1(b), Figure 5.2(b), and Figure 5.3(b), the shear-induced soil dilatation was more likely to occur in sand specimens composed of fine grains with higher initial relative densities, or those subjected to relatively small effective confining pressures. The dilatancy angle can be obtained by using the following equation proposed by Schanz and Vermeer (1996):

$$\psi = \sin^{-1} \frac{d\varepsilon_v/d\varepsilon_a}{d\varepsilon_v/d\varepsilon_a - 2} \quad (5.1)$$

where ψ is the dilatancy angle; ε_v is the volumetric strain; ε_a is the axial strain, $d\varepsilon_v/d\varepsilon_a$ is the slope of volumetric strain-axial strain curve at the point of maximum curvature.

As shown in Table 5.3, for calcareous sand specimens composed of coarse particles with diameter in the range of 2-5 mm, the shear dilation only occurred during the CD shearing tests under a relatively small confining pressure of 100 kPa. Shear dilation in calcareous sands with particle sizes of 1-2 mm and an initial relative density below 0.65 was only observed during shearing at a confining pressure of 100 kPa. Conversely, specimens in the same size range but with a higher initial relative density (≥ 0.65) exhibited shear dilation at both confining pressures of 100 kPa and 200 kPa. For specimens composed of smaller particles (0.5-1 mm), the shear dilation occurred under both 100 kPa and 200 kPa. Additionally, dense specimens with an initial relative density of 0.8 also demonstrated shear dilation. For specimens in the same particle size range, river sands always exhibit higher dilatancy angle than calcareous sands.

Table 5.3. Dilatancy angle of CS and RS specimens with different initial relative densities and initial particle size ranges after the tests under different effective confining pressures.

| Particle type | Particle size range, d (mm) | Initial relative density, D_r | Effective confining pressure, σ_3 (kPa) | Dilatancy angle, ψ (degrees) |
|------------------|-------------------------------|---------------------------------|--|-----------------------------------|
| Calcareous sands | 2-5 | 0.5 | 100 | 5.08 |
| | | 0.6 | | 6.51 |
| | | 0.65 | | 7.29 |
| | | 0.7 | | 7.90 |
| | | 0.8 | | 9.95 |
| | 1-2 | 0.5 | 100 | 7.76 |
| | | 0.6 | 100 | 8.55 |
| | | 0.65 | 100 | 8.82 |
| | | | 200 | 2.87 |
| | | 0.7 | 100 | 10.00 |
| | | | 200 | 5.51 |
| | | 0.8 | 100 | 12.68 |
| | | | 200 | 6.43 |
| | 0.5-1 | 0.5 | 100 | 9.42 |
| | | | 200 | 3.47 |
| | | 0.6 | 100 | 10.62 |
| | | | 200 | 6.20 |
| | | 0.65 | 100 | 11.43 |
| | | | 200 | 7.09 |
| | | 0.7 | 100 | 12.78 |
| | | | 200 | 7.33 |
| | | 0.8 | 100 | 12.70 |
| | | | 200 | 8.66 |
| | | | 300 | 4.54 |
| River sands | 2-5 | 0.7 | 200 | 7.98 |
| | 1-2 | | | 9.00 |
| | 0.5-1 | | | 11.56 |

Figure 5.18(a) presents the relationship between ψ and D_r for calcareous sand specimens of different initial particle sizes. For each specimen, a linear increase in the dilatancy angle with initial relative density was observed, suggesting that denser specimens, whose particles were initially in closer contact, experienced more pronounced volume increases due to particle sliding. Among different specimens, those with finer sand displayed higher dilatancy angles. This is attributed to two main factors: first, the void spaces between coarser sand particles are comparatively higher, making their rearrangement less impactful on the specimen's overall volume. Second, the smaller, irregularly shaped asperities on the surface of calcareous sand particles have a reduced effect on particle interlocking, facilitating easier particle sliding, thereby leading to more pronounced shear dilation.

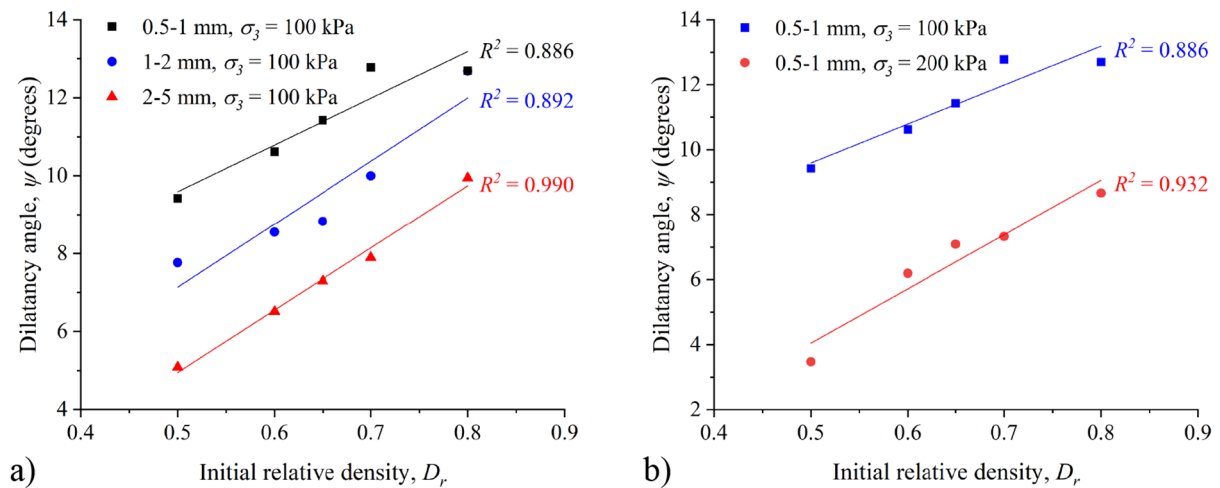


Figure 5.18. Variation of dilatancy angle in calcareous sand specimens: (a) in different initial particle size ranges, but under the effective confining pressure of 100 kPa; (b) in the same initial particle size range of 0.5-1 mm, but under different effective confining pressures.

Figure 5.18(b) illustrates the relationship between ψ and D_r for calcareous sand specimens in the same initial particle size range of 0.5-1 mm after the consolidated drained triaxial compression tests under different effective confining pressures. It is obvious that specimens under lower effective confining pressures exhibit larger dilatancy angle. It can be attributed to the fact that under a lower effective confining pressure during shearing, the overall external forces on the calcareous sand specimen are relatively low and less particle breakage could occur, allowing the sand particles to be more easily rearranged and thus cause volume expansion.

The dilatancy angle of calcareous and river sand specimens, both with an initial relative density of 0.7 and particle size range of 2-5 mm, tested under varying effective confining pressures are summarized in Table 5.4. The relationships between dilatancy angle (ψ) and effective confining pressure (σ_3) are displayed in Figure 5.19. It is clear that the dilatancy angle of the distinct sand particle specimens decreased linearly with the increase of effective confining pressure. Under a low confining pressure of 25 kPa, both sands exhibited very close dilatancy angles. However, for calcareous sands, the dilatancy angle decreased more rapidly, which disappear at effective confining pressures above 100 kPa. In contrast, river sand specimens could maintain the dilation effect until the confining pressure exceeding 300 kPa.

The shear dilation of the calcareous sands has ceased at lower confining pressures due to significant particle breakage. The minor volume increase from shear-induced particle rearrangement was outweighed by the volume decrease resulting from particle breakage and

the subsequent filling of void space with fines. Another pattern that can be seen is that under the same effective confining pressure, river sands exhibit a greater shear dilatancy angle compared to calcareous sands. This difference is attributed to the high strength and smoother surface of river sands, which makes them inherently less susceptible to fracturing and thus more prone to pronounced shear dilation than calcareous sands.

Table 5.4. Dilatancy angle of CS and RS specimens with the initial relative density of 0.7 and in initial particle size range of 2-5 mm under different effective confining pressures.

| | Effective confining pressure, σ_3 (kPa) | | | | | |
|----|--|-------|-------|-------|------|------|
| | 25 | 50 | 75 | 100 | 200 | 300 |
| CS | 17.98 | 13.21 | 9.21 | 7.90 | | |
| RS | 20.14 | 17.16 | 15.57 | 12.97 | 7.98 | 2.91 |

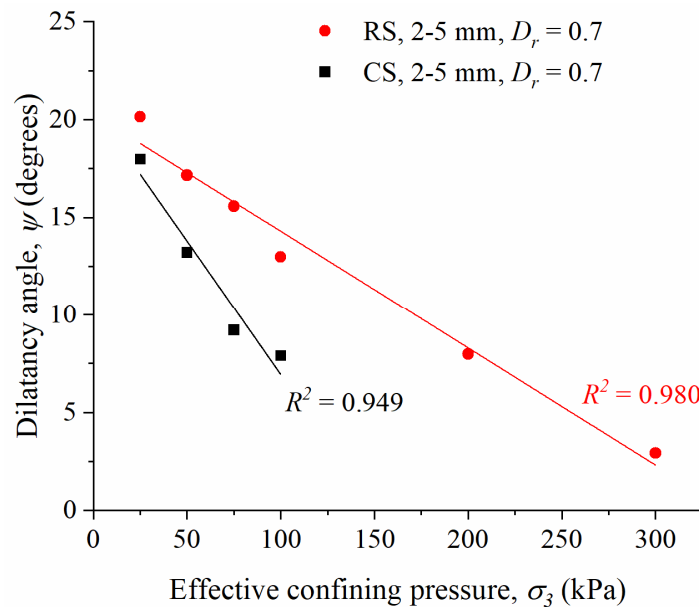


Figure 5.19. Variation of soil dilatancy angle with the effective confining pressure for CS and RS specimens. The initial relative density was 0.7 and initial particle size range was 2-5 mm.

5.5 Summary

This chapter investigated the shear strength characteristics of calcareous and river sands by conducting consolidated drained triaxial compression tests. Effective confining pressure of 100 kPa, 200 kPa, and 300 kPa were applied on sandy soil specimens with different initial relative densities ranging from 0.5 to 0.8, and particle size range of 0.5-1 mm, 1-2 mm, and 2-5 mm. In order to gain a more comprehensive understanding of the impact of varied confining pressures on factors such as strength parameters, a series of tests were conducted under the

effective confining pressure ranging from 25 kPa to 800 kPa. The morphological parameters of single particles were quantified and analysed. The particle breakage was investigated by applying the sieving analysis. The major conclusions of this work are summarized as followed:

- The deviatoric stress-axial strain relationships for the two types of sand specimens exhibited strain-softening behaviour under the effective confining pressure less than 400 kPa. However, the CS demonstrated a gradual transition to strain-hardening behaviour with the increase in confining pressure. Conversely, the RS continued to exhibit strain-softening behaviour until the effective confining pressure reached 800 kPa.
- The peak deviatoric stress of calcareous sands increased with the initial relative density. Moreover, the denser the specimen, the faster the deviatoric stress reached its peak.
- Sand specimens composed of smaller-sized particles exhibited higher deviatoric stress. However, the trend in the results for calcareous sands reversed when the axial strain reaches around 18%, i.e., the deviatoric stress became greater for coarser particles.
- Sand specimens composed of finer sand particles with a greater initial relative density and subjected to a lower confining pressure were more susceptible to exhibit shear dilation behaviour. River sand specimens were more prone to demonstrate shear dilation than calcareous sand specimens.
- The extent of particle breakage for calcareous sands was related to particle size, initial relative density, and effective confining pressure. The relative breakage increased linearly with the initial relative density, but exponentially with the effective confining pressure. Under the same experimental conditions, the amount of particle breakage that occurred in river sand specimen was less than that of a calcareous sand specimen.
- The DIA outcomes indicate that the frequency counts of particle sphericity, aspect ratio and flatness before and after experiments closely followed the Gaussian distribution, except that the frequency counts of convexity after test follow an exponential distribution as the surface of most particles became smoother after tests.
- The overall shape of the calcareous sand particles and river sands were closer to a spherical shape with a smoother particle surface after the consolidation and drainage shear process. The calcareous sand particles became elongated but no longer flat, while the river sand particles became slightly elongated and flat.

- The peak friction angle for calcareous specimens tended to increase with decreasing particle size range under the CD condition. For calcareous specimen with an initial particle size range of 2-5 mm, 1-2 mm, and 0.5-1 mm, the mean peak friction angle was roughly 37.9°, 38.1°, and 40.8°, respectively.
- The peak cohesion for calcareous sand specimens under different testing conditions ranged from 47 kPa to 94 kPa. A slight increase in peak cohesion could be observed as their initial relative densities increase. The peak cohesion tended to decrease with decreasing particle size range under the CD condition. Under the same experimental conditions, both the peak friction angle and the peak cohesion of RS was less than those of the CS specimens.
- The dilatancy angle increased linearly with the initial relative density but decreased linearly with the effective confining pressure. Under the same experimental conditions, the dilatancy angle of river sands was larger than that of calcareous sands.

Chapter 6 Conclusions and Future Research

6.1 Conclusions

The objective of this research was to investigate the influence of particle breakage and morphology on the strength of sandy soil. Two primary experimental approaches, namely the one-dimensional consolidation and consolidated drained triaxial compression tests, were conducted to investigate the consolidation and strength characteristics of calcareous sands (CS). To enable a meaningful comparison of the experimental outcomes, results on river sands (RS) were also included. Given that the initial relative density and particle size are two critical factors influencing particle breakage, this research has prepared sand samples with the initial relative densities ranging from 0.5 to 0.8, and particle size in the ranges of 0.5-1 mm, 1-2 mm, and 2-5 mm. To maximize the degree of particle breakage, all samples had uniform particle size distributions. To enhance clarity and readability, this section has two subsections, each dedicated to summarizing the findings from these two experimental studies.

6.1.1 One-dimensional consolidation tests

A series of vertical stresses, up to 7.2 MPa, were systematically applied to the sand particle specimens to investigate the particle breakage and morphology change. Relationships between void ratio and effective normal stress shows that a greater consolidation can be observed in sandy soil specimens with smaller initial relative density and larger particle size. The consolidation-induced settlement of CS is significantly larger than that of RS. The one-dimensional compression of CS of various initial relative densities leads to the creation of a unique limiting compression curve resulting from the particle breakage.

The “yielding” of the specimen is characterised by the occurrence of concentrated particle breakage. The yield stress of CS typically falls within the range of 1 to 4.7 MPa. It demonstrates an increasing trend with the initial relative density, while reduces with the particle size. The extent of particle breakage for calcareous sands is related to particle size and inversely related to initial relative density. The particle breakage was investigated by applying both the dynamic image analysis and the mechanical sieving analysis. The dynamic image analysis presents a clear advantage over the mechanical sieving analysis regarding the particle breakage

quantification. The latter solely yields a broken-line graph based only on the change in particle weight over a limited number of particle size intervals, while the former presents smooth PSD curves based on the size of each individual particle in a much shorter period of time. A relationship for predicting the consolidation of CS under specific loading conditions is proposed. Within this framework, the parameter e_b , indicative of the change in void ratio due to particle breakage, is introduced.

The acoustic emission testing has been proved to be a powerful tool for characterizing micromechanical behaviours during the oedometer tests for CS. The AE ringdown counts and peak frequency of the corresponding acoustic waveform have the potential to characterize the intensity and distinguish different types of micromechanical activities, respectively. During the tests, a majority of the RDC results were identified during the loading stages, and their quantity experienced a notable rise after the vertical pressure exceeding 400 kPa. The observed trend depicted an increase in cumulative RDC as particle size increased, conversely, a decrease was evident as the initial relative density increased. The peak frequency results indicate that there has been a near-constant occurrence of particle sliding or rearrangement throughout the duration of the experimental process, producing lower-frequency AE components typically at around 0.02 MHz. High-frequency AE components can only be observed under normal stresses larger than 800 kPa, which is closely linked to the breakage of CS particles.

The morphological parameters of single particles were quantified and analysed. The DIA outcomes indicate that the frequency counts of particle sphericity, aspect ratio and flatness before and after the experiments followed closely the Gaussian distribution, except for the frequency counts of convexity for an exponential distribution as the surface of most particles becomes smoother after tests. The fine CS particles produced during the one-dimensional consolidation tests are more elongated and flattened, but less spherical and convex.

6.1.2 Consolidated drained triaxial compression tests

The deviatoric stress-axial strain relationships for the two types of sand specimens exhibited strain-softening behaviour under the effective confining pressure less than 400 kPa. However, the CS demonstrated a gradual transition to strain-hardening behaviour with the increase of confining pressure. Conversely, the RS continued to exhibit strain-softening

behaviour for the effective confining pressure less than 800 kPa. The peak deviatoric stress of CS increased with the initial relative density. Furthermore, the denser the specimen is, the faster the deviatoric stress could reach its peak. Sand specimens composed of finer particles exhibited higher deviatoric stress. However, this trend reversed when the axial strain reached around 18%, indicating that the deviatoric stress became greater for specimens composed of coarser particles.

The volumetric strain-axial strain relationships showed that sand specimens composed of finer sand particles with a greater initial relative density and subjected to a lower confining pressure were more susceptible to exhibit shear dilation behaviour. RS specimens were more prone to demonstrate shear dilation than CS specimens.

The particle breakage was investigated by applying the sieving analysis. The relative breakage increased linearly with the initial relative density, but exponentially with the effective confining pressure. Under the same experimental conditions, the amount of particle breakage occurred in RS specimen was less than that in a CS specimen. The DIA outcomes indicate that the frequency counts of particle sphericity, aspect ratio and flatness before and after the experiments closely followed the Gaussian distribution, except that the frequency counts of convexity after the test followed an exponential distribution as the surface of most particles became smoother after the tests. The overall shape of the CS and RS particles were closer to a spherical shape with a smoother particle surface after the shear process. The CS particles became elongated and blocky, while the RS particles became slightly elongated and flat.

Studies on the strength parameters of sand particles have shown that the peak friction angle of CS tended to increase with the decreasing particle size range under the CD condition. For CS with an initial particle size range of 2-5 mm, 1-2 mm, and 0.5-1 mm, the mean peak friction angle was roughly 37.9°, 38.1°, and 40.8°, respectively. The peak apparent cohesion of CS specimens under different testing conditions ranged from 47 kPa to 94 kPa. A slight increase in peak cohesion could be observed as their initial relative densities increased. The peak cohesion tended to decrease with the decreasing particle size range under the CD condition. Under the same experimental conditions, both the peak friction angle and the peak cohesion of RS specimen were less than those of the CS specimen. The dilatancy angle increased linearly with the initial relative density but decreased linearly with the effective confining pressure. Under the same experimental conditions, the dilatancy angle of RS was larger than that of CS.

6.2 Publications

During my PhD studies, I have contributed to the publication of three academic articles. The first article, entitled “Influence of particle breakage on drained shear strength of calcareous sands”, involved my responsibilities in data compilation and drafting the manuscript.

- Wei, H., Li, X., Zhang, S., Zhao, T., Yin, M. and Meng, Q. (2021) 'Influence of Particle Breakage on Drained Shear Strength of Calcareous Sands', *International Journal of Geomechanics*, 21(7), pp. 04021118.

The second article, entitled “Particle breakage and morphology changes of calcareous sands under one-dimensional compression loading”, the whole content of which is from Chapter 4 of this thesis, where I have overseen the experimental design, data organization, and manuscript preparation, including addressing reviewers' comments.

- Wei, H., Liu, H., Zhao, T., Zhang, S., Ma, L., Yin, M. and Meng, Q. (2022) 'Particle breakage and morphology changes of calcareous sands under one-dimensional compression loading', *Marine Geophysical Research*, 43(4), pp. 45.

The third article, entitled “Effect of particle shape and breakage on the shear strength of calcareous soils”, is currently under review and is derived from Chapter 5 of this thesis. I was responsible for the experimental design, data management, drafting the manuscript, with further revisions also being managed by me.

6.3 Future research

In examining the influence of particle morphology and breakage on the mechanical behaviour of sandy soil, which remains the focal point of this study. The future work can be divided into two primary areas: first, it involves the analysis of data already collected in this study, which has yet to be processed and interpreted due to time constraints; and second, it includes the design and performance of new experimental investigations to further explore these phenomena.

6.3.1 Data already collected

As many as 34 morphological parameters of single sand particles obtained by dynamic image analysis techniques contain both two-dimensional and three-dimensional data. However,

this research has only studied four of these data including sphericity, convexity, aspect ratio and flatness. These four parameters could offer a relatively thorough representation of particle morphology across different dimensions, from overall shape to surface texture. Nonetheless, there remains a wide array of morphological parameters yet to be explored. A broader range of parameters would enable geotechnical specialists to achieve a more detailed understanding of particle morphological changes, thereby providing a richer foundation for interpreting the implications on the macroscopic mechanical properties of sandy soils.

In addition to expanding the scope of morphological parameters under investigation, it is crucial to conduct a more in-depth analysis of the existing data to accurately quantify their relationship with the macroscopic mechanical properties of sand particles, such as settlement and strength. A deeper investigation should aim to establish an intrinsic model that could serve as a more robust guide to practical engineering applications.

In analysing the results obtained from one-dimensional consolidation tests, this research has demonstrated that the dynamic image analysis can be successfully applied to quantify particle breakage, and the obtained results are consistent with those obtained using the traditional sieving method. However, due to time limitations, the results of triaxial tests could not be similarly analysed using the morphological data to quantify particle breakage, an area that could be investigated to further validate the method's accuracy and applicability. Furthermore, while this research has quantified particle breakage based on the changes in the perimeter of sand particle projections, future work should explore additional morphological parameters, such as particle volume or area, to enhance the robustness and comprehensiveness of the particle breakage quantifications.

6.3.2 New experiments

In analysing the one-dimensional consolidation tests, this research has demonstrated the successful application of acoustic emission monitoring technique for distinguishing and quantifying micromechanical behaviours. These real-time data could offer researchers an enhanced understanding of these mechanical processes, providing insights into otherwise "invisible" phenomena. However, due to time constraints, the necessary modifications to the triaxial specimen chamber for the installation of acoustic emission probes were not completed,

preventing the monitoring of acoustic signals during triaxial testing. Future work should focus on integrating this monitoring technique to capture the real-time data on particle sliding or breakage throughout the experiments. Additionally, in the one-dimensional consolidation tests, only two acoustic emission probes were positioned around each specimen due to the limited specimen size. For upcoming triaxial tests, it is recommended to deploy at least six probes around each specimen chamber, arranged vertically from top to bottom. This setup would enable 3D signal localization, allowing for precise quantification of acoustic emissions and real-time determination of signal origin within the specimen. Such an approach would facilitate targeted analysis of microscopic activities, particularly in critical areas like shear zones.

With the rapid advancements in non-destructive testing (NDT) techniques, researchers now have the capability to directly observe the microscopic activities within soil specimens. Among these techniques, X-ray micro-tomography stands out, gradually gaining recognition and being increasingly applied to the study of rock materials. This technique holds the potential for parallel application in one-dimensional consolidation tests, enabling detailed examining the change of local pore space distributions, force chain evolution, coordination number variations, and the initiation and progression of particle breakage.

To investigate the impact of particle morphology on the macroscopic mechanical behaviour of sandy soil, it is essential to first prepare the sand samples with well-quantified morphological characteristics. While the current study has emphasized that the sphericity, surface roughness of particles—particularly its smoothness—play critical roles in inter-particle interactions. Thus, future research will be directed towards examining the influence of particle surface roughness on the mechanical behaviour of sandy soil, with corresponding experiments designed to explore this aspect in greater detail. By rounding the sand particles to different degrees prior to the experiment, sand particles with different degrees of smoothness (i.e., different surface roughness) will be prepared. The influence of particle roughness on the mechanical properties of sandy soil can be then quantitatively investigated.

References

- Airey, D. W., Carter, J. P. and Liu, M. D. (2011) 'Sydney soil model. II: Experimental validation', *International Journal of Geomechanics*, 11(3), pp. 225-238.
- Al-Taie, A. J. and Al-Shakarchi, Y. J. (2017) 'Shear strength, collapsibility and compressibility characteristics of compacted Baiji dune soils', *Journal of Engineering Science and Technology*, 12(3), pp. 767-779.
- Aldefae, A. H. H. (2016) 'Prediction of One-Dimensional Compression Test using Finite Elements Model', *International Journal of Engineering Research*, 5(05).
- Alfano, F., Bonadonna, C., Delmelle, P. and Costantini, L. (2011) 'Insights on tephra settling velocity from morphological observations', *Journal of Volcanology and Geothermal Research*, 208(3-4), pp. 86-98.
- Alshibli, K. A. and Cil, M. B. (2018) 'Influence of particle morphology on the friction and dilatancy of sand', *Journal of Geotechnical and Geoenvironmental Engineering*, 144(3), pp. 04017118.
- Altuhafi, F. and Coop, M. R. (2011) 'Changes to particle characteristics associated with the compression of sands', *Géotechnique*, 61(6), pp. 459-471.
- Altuhafi, F., O'sullivan, C. and Cavarretta, I. (2013) 'Analysis of an image-based method to quantify the size and shape of sand particles', *Journal of Geotechnical and Geoenvironmental Engineering*, 139(8), pp. 1290-1307.
- Altuhafi, F. N., Coop, M. R. and Georgiannou, V. N. (2016) 'Effect of particle shape on the mechanical behavior of natural sands', *Journal of Geotechnical and Geoenvironmental Engineering*, 142(12), pp. 04016071.
- Amirpour Harehdasht, S., Karray, M., Hussien, M. N. and Chekired, M. (2017) 'Influence of particle size and gradation on the stress-dilatancy behavior of granular materials during drained triaxial compression', *International Journal of Geomechanics*, 17(9), pp. 04017077.
- Andersson, T. (2010) *Estimating particle size distributions based on machine vision*. Doctoral, Luleå tekniska universitet.
- Andronico, D., Scollo, S., Castro, M. D. L., Cristaldi, A., Lodato, L. and Taddeucci, J. (2014) 'Eruption dynamics and tephra dispersal from the 24 November 2006 paroxysm at South-East Crater, Mt Etna, Italy', *Journal of volcanology and geothermal research*, 274, pp. 78-91.
- Anochie-Boateng, J., Komba, J. J. and Mvelase, G. M. (2011) 'Advanced and automated laser-based technique to evaluate aggregates'.
- Anusree, K. and Latha, G. M. (2023) 'Characterization of sand particle morphology: state-of-the-art', *Bulletin of Engineering Geology and the Environment*, 82(7), pp. 269.
- Arasan, S., Hasiloglu, A. S. and Akbulut, S. (2010) 'Shape properties of natural and crushed aggregate using image analysis', *International Journal of Civil & Structural Engineering*, 1(2), pp. 221-233.
- Aschenbrenner, B. C. (1956) 'A new method of expressing particle sphericity', *Journal of Sedimentary Research*, 26(1), pp. 15-31.
- ASTM (2011) *D2435-04:2011 Standard Test Methods for One-Dimensional Consolidation Properties of Soils Using Incremental Loading*. West Conshohocken: ASTM. Available

- at: <https://www.astm.org/d2435-04.html> (Accessed: 23 March 2023).
- ASTM (2017) *D4254-00:2017 Standard Test Methods for Minimum Index Density and Unit Weight of Soils and Calculation of Relative Density*. West Conshohocken: ASTM. Available at: <https://www.astm.org/d4254-00.html> (Accessed: 1 March 2023).
- ASTM (2018) *D2488-17e1:2018 Standard Practice for Description and Identification of Soils (Visual-Manual Procedures)*. West Conshohocken: ASTM. Available at: <https://www.astm.org/d2488-17e01.html> (Accessed: 16 Jul 2023).
- ASTM (2020a) *D2487-17:2020 Standard Practice for Classification of Soils for Engineering Purposes (Unified Soil Classification System)*. West Conshohocken: ASTM. Available at: <https://www.astm.org/d2487-17.html> (Accessed: 22 February 2023).
- ASTM (2020b) *D7181-20:2020 Standard Test Method for Consolidated Drained Triaxial Compression Test for Soils*. West Conshohocken: ASTM. Available at: <https://www.astm.org/d7181-20.html> (Accessed: 29 March 2023).
- ASTM (2021a) *E976-15:2021 Standard Guide for Determining the Reproducibility of Acoustic Emission Sensor Response*. West Conshohocken: ASTM. Available at: <https://www.astm.org/e0976-15r21.html> (Accessed: 3 April 2023).
- ASTM (2021b) *D4253-00:2021 Standard Test Methods for Maximum Index Density and Unit Weight of Soils Using a Vibratory Table*. West Conshohocken: ASTM. Available at: <https://www.astm.org/d4253-00.html> (Accessed: 1 March 2023).
- ASTM (2023) *D5550-14:2023 Standard Test Method for Specific Gravity of Soil Solids by Gas Pycnometer*. West Conshohocken: ASTM. Available at: <https://www.astm.org/d5550-14.html> (Accessed: 15 March 2023).
- Atkinson, J. (1993) *An introduction to the mechanics of soils and foundations: through critical state soil mechanics*. McGraw-Hill Book Company (UK) Ltd.
- Azéma, E., Estrada, N. and Radjai, F. (2012) 'Nonlinear effects of particle shape angularity in sheared granular media', *Physical Review E*, 86(4), pp. 041301.
- Azéma, E., Estrada, N. and Radjai, F. 'Shear strength, force distributions and friction mobilization in sheared packings composed of angular particles', Vol. 1542. *AIP Conference Proceedings*, American Institute of Physics, 511-514.
- Bagheri, G., Bonadonna, C., Manzella, I. and Vonlanthen, P. (2015) 'On the characterization of size and shape of irregular particles', *Powder Technology*, 270, pp. 141-153.
- Bales, B., Pollock, T. and Petzold, L. (2017) 'Segmentation-free image processing and analysis of precipitate shapes in 2D and 3D', *Modelling and Simulation in Materials Science and Engineering*, 25(4), pp. 045009.
- Bandini, V. and Coop, M. R. (2011) 'The influence of particle breakage on the location of the critical state line of sands', *Soils and foundations*, 51(4), pp. 591-600.
- Bayhurst, G. K. 'A METHOD FOR CHARACTERIZING VOLCANIC ASH FROM THE DECEMBER 15, 1989, ERUPTION OF REDOUBT VOLCANO, ALASKA', Vol. 2047. *Volcanic Ash and Aviation Safety: Proceedings of the First International Symposium on Volcanic Ash and Aviation Safety*, DIANE Publishing, 13.
- Beckett, F., Witham, C., Hort, M., Stevenson, J., Bonadonna, C. and Millington, S. (2014) 'The sensitivity of NAME forecasts of the transport of volcanic ash clouds to the physical characteristics assigned to the particles', *UK Met Off. Forecast. Res. Tech. Rep.*, 592, pp. 1-39.

- Been, K. and Jefferies, M. G. (1985) 'A state parameter for sands', *Géotechnique*, 35(2), pp. 99-112.
- Bjørk, T., Mair, K. and Austrheim, H. (2009) 'Quantifying granular material and deformation: Advantages of combining grain size, shape, and mineral phase recognition analysis', *Journal of Structural Geology*, 31(7), pp. 637-653.
- Blatt, H. (1973) 'Origin of sedimentary rocks', *Soil Science*, 115(5), pp. 400.
- Blatt, H. (1982) 'Sedimentary petrology'.
- Blott, S. J. and Pye, K. (2008) 'Particle shape: a review and new methods of characterization and classification', *Sedimentology*, 55(1), pp. 31-63.
- Bolton, M. (1986) 'The strength and dilatancy of sands', *Geotechnique*, 36(1), pp. 65-78.
- Bolton, M., Nakata, Y. and Cheng, Y. (2008) 'Micro-and macro-mechanical behaviour of DEM crushable materials', *Géotechnique*, 58(6), pp. 471-480.
- Bond, A. J., Schuppener, B., Scarpelli, G., Orr, T. L., Dimova, S., Nikolova, B. and Pinto, A. V. 'Eurocode 7: geotechnical design worked examples', Vol. 7. *Workshop "Eurocode*.
- Bono, J. D., McDowell, G. R. and Wanatowski, D. (2014) 'DEM of triaxial tests on crushable cemented sand', *Granular Matter*, 16, pp. 563-572.
- Bowman, E. T., Soga, K. and Drummond, W. (2001) 'Particle shape characterisation using Fourier descriptor analysis', *Geotechnique*, 51(6), pp. 545-554.
- Brears, R. C. (2024) *Offshore Wind Power: Harnessing the Wind for a Greener Future: Global Climate Solutions*. Available at: <https://medium.com/global-climate-solutions/offshore-wind-power-harnessing-the-wind-for-a-greener-future-5f240f6e1c3a> (Accessed: 29 July 2024).
- British Standards Institution (2008) *BS EN 933-4:2008:4 Feb 2008 Tests for geometrical properties of aggregates*: British Standards Institution (Accessed: 15 Jul 2023).
- British Standards Institution (2012) *BS EN 933-3:2012:29 Feb 2012 Tests for geometrical properties of aggregates*: British Standards Institution (Accessed: 19 Jul 2023).
- Bruker (2023) *D8 ADVANCE*. X-RAY DIFFRACTION (XRD). Available at: <https://www.bruker.com/en/products-and-solutions/diffractometers-and-scattering-systems/x-ray-diffractometers/d8-advance-family/d8-advance.html> (Accessed: 21 February 2023).
- Burmister, D. M. 'The importance and practical use of relative density in soil mechanics', Vol. 48. *Proceedings-American Society for Testing and Materials*, AMER SOC TESTING MATERIALS 100 BARR HARBOR DR, W CONSHOCKEN, PA 19428-2959, 1249-1268.
- Büttner, R., Dellino, P., Raue, H., Sonder, I. and Zimanowski, B. (2006) 'Stress-induced brittle fragmentation of magmatic melts: Theory and experiments', *Journal of Geophysical Research: Solid Earth*, 111(B8).
- Cailleux, A. (1947) 'L'indice d'emousse: definition et premiere application', *CR Somm. Soc. Geol. France*, 10, pp. 251-252.
- Callahan, P., Simmons, J. and De Graef, M. (2012) 'A quantitative description of the morphological aspects of materials structures suitable for quantitative comparisons of 3D microstructures', *Modelling and Simulation in Materials Science and Engineering*, 21(1), pp. 015003.

- Cambridge Dictionary (2023) *shape*: Cambridge University Press.
- Campbell, J. (2015) 'Chapter 15 - Moulding', in Campbell, J. (ed.) *Complete Casting Handbook (Second Edition)*. Boston: Butterworth-Heinemann, pp. 797-819.
- Carpenter, R. (1960) 'Principles and procedures of statistics, with special reference to the biological sciences', *The Eugenics Review*, 52(3), pp. 172.
- Casagrande, A. 'The determination of preconsolidation load and its practical significance', Vol., *Proceedings of the International Conference on Soil Mechanics and Foundation Engineering*, USA, 22-26 June, 60-64.
- Casella, G. and Berger, R. (2024) *Statistical inference*. CRC Press.
- Cavarretta, I., Coop, M. and O'SULLIVAN, C. (2010) 'The influence of particle characteristics on the behaviour of coarse grained soils', *Géotechnique*, 60(6), pp. 413-423.
- Cepuritis, R., Jacobsen, S., Pedersen, B. and Mørtzell, E. (2016) 'Crushed sand in concrete—effect of particle shape in different fractions and filler properties on rheology', *Cement and concrete composites*, 71, pp. 26-41.
- Chan, L. C. and Page, N. W. (1997) 'Particle fractal and load effects on internal friction in powders', *Powder Technology*, 90(3), pp. 259-266.
- Charpentier, I., Sarocchi, D. and Sedano, L. A. R. (2013) 'Particle shape analysis of volcanic clast samples with the Matlab tool MORPHEO', *Computers & Geosciences*, 51, pp. 172-181.
- Chen, X. and Zhang, J. (2016) 'Influence of relative density on dilatancy of clayey sand–fouled aggregates in large-scale triaxial tests', *Journal of Geotechnical and Geoenvironmental Engineering*, 142(10), pp. 06016011.
- Cheng, Y., Bolton, M. and Nakata, Y. (2004) 'Crushing and plastic deformation of soils simulated using DEM', *Geotechnique*, 54(2), pp. 131-141.
- Cho, G.-C., Dodds, J. and Santamarina, J. C. (2006) 'Particle shape effects on packing density, stiffness, and strength: natural and crushed sands', *Journal of geotechnical and geoenvironmental engineering*, 132(5), pp. 591-602.
- Choudhury, K. R., Meere, P. A. and Mulchrone, K. F. (2006) 'Automated grain boundary detection by CASRG', *Journal of Structural Geology*, 28(3), pp. 363-375.
- Chuhan, F. A., Kjeldstad, A., Bjørlykke, K. and Høeg, K. (2003) 'Experimental compression of loose sands: relevance to porosity reduction during burial in sedimentary basins', *Canadian Geotechnical Journal*, 40(5), pp. 995-1011.
- Cil, M. B. and Alshibli, K. A. (2012) '3D assessment of fracture of sand particles using discrete element method', *Géotechnique Letters*, 2(3), pp. 161-166.
- Cioni, R., Pistolesi, M., Bertagnini, A., Bonadonna, C., Hoskuldsson, A. and Scateni, B. (2014) 'Insights into the dynamics and evolution of the 2010 Eyjafjallajökull summit eruption (Iceland) provided by volcanic ash textures', *Earth and Planetary Science Letters*, 394, pp. 111-123.
- Clark, N. (1987) 'A new scheme for particle shape characterization based on fractal harmonics and fractal dimensions', *Powder Technology*, 51(3), pp. 243-249.
- Coltelli, M., Miraglia, L. and Scollo, S. (2008) 'Characterization of shape and terminal velocity of tephra particles erupted during the 2002 eruption of Etna volcano, Italy', *Bulletin of volcanology*, 70, pp. 1103-1112.
- Consoli, N. C., Prietto, P. D. and Ulbrich, L. A. (1998) 'Influence of fiber and cement addition

- on behavior of sandy soil', *Journal of geotechnical and geoenvironmental engineering*, 124(12), pp. 1211-1214.
- Coop, M. (1990) 'The mechanics of uncemented carbonate sands', *Géotechnique*, 40(4), pp. 607-626.
- Coop, M. and Lee, I. 'The behaviour of granular soils at elevated stresses', Vol., *Predictive soil mechanics: Proceedings of the Wroth Memorial Symposium held at St Catherine's College, Oxford, 27-29 July 1992*, Thomas Telford Publishing, 186-198.
- Coop, M., Sorensen, K., Bodas Freitas, T. and Georgoutsos, G. (2004) 'Particle breakage during shearing of a carbonate sand', *Géotechnique*, 54(3), pp. 157-163.
- Coulomb, C. A. (1773) 'Essai sur une application des regles de maximis et minimis a quelques problemes de statique relatifs a l'architecture', *Mem. Div. Sav. Acad.*
- Cox, E. (1927) 'A method of assigning numerical and percentage values to the degree of roundness of sand grains', *Journal of Paleontology*, 1(3), pp. 179-183.
- Cuccovillo, T. and Coop, M. (1999) 'On the mechanics of structured sands', *Géotechnique*, 49(6), pp. 741-760.
- da Fonseca, A. V., Cordeiro, D. and Molina-Gómez, F. (2021) 'Recommended procedures to assess critical state locus from triaxial tests in cohesionless remoulded samples', *Geotechnics*, 1(1), pp. 95-127.
- Dadd, K. and Foley, K. (2016) 'A shape and compositional analysis of ice-rafted debris in cores from IODP Expedition 323 in the Bering Sea', *Deep Sea Research Part II: Topical Studies in Oceanography*, 125, pp. 191-201.
- Daghistani, F. and Abuel-Naga, H. (2023) 'Evaluating the Influence of Sand Particle Morphology on Shear Strength: A Comparison of Experimental and Machine Learning Approaches', *Applied Sciences*, 13(14), pp. 8160.
- Dan, G., Sultan, N. and Savoye, B. (2007) 'The 1979 Nice harbour catastrophe revisited: trigger mechanism inferred from geotechnical measurements and numerical modelling', *Marine Geology*, 245(1-4), pp. 40-64.
- Daouadji, A., Hicher, P.-Y. and Rahma, A. (2001) 'An elastoplastic model for granular materials taking into account grain breakage', *European Journal of Mechanics-A/Solids*, 20(1), pp. 113-137.
- Das, B. M. (2021) *Principles of geotechnical engineering*. Cengage learning.
- de Bono, J. P. and McDowell, G. R. (2016) 'Investigating the effects of particle shape on normal compression and overconsolidation using DEM', *Granular Matter*, 18(3), pp. 55.
- De Mello, J., Amaral, C., da Costa, A. M., Rosas, M., Coelho, P. D. and Porto, E. 'Closed-ended pipe piles: testing and piling in calcareous sand', Vol., *Offshore Technology Conference*, OTC, OTC-6000-MS.
- Dellino, P., Gudmundsson, M., Larsen, G., Mele, D., Stevenson, J., Thordarson, T. and Zimanowski, B. (2012) 'Ash from the Eyjafjallajökull eruption (Iceland): Fragmentation processes and aerodynamic behavior', *Journal of Geophysical Research: Solid Earth*, 117(B9).
- Dellino, P., Mele, D., Bonasia, R., Braia, G., La Volpe, L. and Sulpizio, R. (2005) 'The analysis of the influence of pumice shape on its terminal velocity', *Geophysical Research Letters*, 32(21).
- Det Norske Veritas (2022) *ENERGY TRANSITION OUTLOOK 2022*. Norway: Det Norske

- Veritas,. Available at: https://www.dnv.com/energy-transition-outlook/download.html?utm_source=Google&utm_medium=Search&utm_campaign=eto22&gad=1&gclid=Cj0KCCQjw7aqkBhDPARIsAKGa0oIpOIsGL17_QtR-R9bvHzTzknq2-wlXUOQhFi91zt7DRSHchdctkywaAh_MEALw_wcB#downloadform (Accessed: 16 Jun 2023).
- Dobkins, J. E. and Folk, R. L. (1970) 'Shape development on Tahiti-nui', *Journal of Sedimentary Research*, 40(4), pp. 1167-1203.
- Dodds, J. S. (2003) *Particle shape and stiffness: effects on soil behavior*. Civil and Environmental Engineering, Georgia Institute of Technology.
- Dolwin, J., Khorshid, M. and GOUDOEVER, E. 'Evaluation of driven pile capacity. Methods and results', Vol., *International conference on calcareous sediments*, 409-428.
- Dong, Y., Liu, Y., Hu, C. and Xu, B. (2019) 'Coral reef geomorphology of the Spratly Islands: A simple method based on time-series of Landsat-8 multi-band inundation maps', *ISPRS Journal of Photogrammetry and Remote Sensing*, 157, pp. 137-154.
- Dowdeswell, J. A. (1982) 'Scanning electron micrographs of quartz sand grains from cold environments examined using Fourier shape analysis', *Journal of Sedimentary Research*, 52(4), pp. 1315-1323.
- Draper, N. R. and Smith, H. (1998) *Applied regression analysis*. John Wiley & Sons.
- Dunlop, D. G., Brewster, N. T., Madabhushi, S. G., Usmani, A. S., Pankaj, P. and Howie, C. R. (2003) 'Techniques to improve the shear strength of impacted bone graft: the effect of particle size and washing of the graft', *JBJs*, 85(4), pp. 639-646.
- Durant, A. J., Rose, W. I., Sarna-Wojcicki, A., Carey, S. and Volentik, A. (2009) 'Hydrometeor-enhanced tephra sedimentation: Constraints from the 18 May 1980 eruption of Mount St. Helens', *Journal of Geophysical Research: Solid Earth*, 114(B3).
- Dutt, R. N., Ingram, W. B. and Lhuillier, B. (2021) 'Bearing capacity of jack-up footings in carbonate granular sediments', *Engineering for Calcareous Sediments*: CRC Press, pp. 291-296.
- Einav, I. (2007a) 'Breakage mechanics—part I: theory', *Journal of the Mechanics and Physics of Solids*, 55(6), pp. 1274-1297.
- Einav, I. (2007b) 'Breakage mechanics—Part II: Modelling granular materials', *Journal of the Mechanics and Physics of Solids*, 55(6), pp. 1298-1320.
- Ersoy, O., Gourgaud, A., Aydar, E., Chinga, G. and Thouret, J.-C. (2007) 'Quantitative scanning-electron microscope analysis of volcanic ash surfaces: Application to the 1982–1983 Galunggung eruption (Indonesia)', *Geological Society of America Bulletin*, 119(5-6), pp. 743-752.
- Estrada, N., Azéma, E., Radjai, F. and Taboada, A. (2011) 'Identification of rolling resistance as a shape parameter in sheared granular media', *Physical Review E*, 84(1), pp. 011306.
- Fannin, R., Eliadorani, A. and Wilkinson, J. (2005) 'Shear strength of cohesionless soils at low stress', *Géotechnique*, 55(6), pp. 467-478.
- Fernandes, F., Syahrial, A. I. and Valdes, J. R. (2010) 'Monitoring the oedometric compression of sands with acoustic emissions', *Geotechnical Testing Journal*, 33(5), pp. 410-415.
- Fernlund, J. M. (1998) 'The effect of particle form on sieve analysis: a test by image analysis',

- Engineering Geology*, 50(1-2), pp. 111-124.
- Fernlund, J. M. R. (2005) 'Image analysis method for determining 3-D shape of coarse aggregate', *Cement and Concrete Research*, 35(8), pp. 1629-1637.
- Folk, R. L. (1955) 'Student operator error in determination of roundness, sphericity, and grain size', *Journal of Sedimentary Research*, 25(4), pp. 297-301.
- Fonseca, J., O'Sullivan, C., Coop, M. R. and Lee, P. (2013) 'Quantifying the evolution of soil fabric during shearing using directional parameters', *Géotechnique*, 63(6), pp. 487-499.
- Fujima, K., Shigihara, Y., Tomita, T., Honda, K., Nobuoka, H., Hanzawa, M., Fujii, H., Ohtani, H., Orishimo, S. and Tatsumi, M. (2006) 'Survey results of the Indian Ocean tsunami in the Maldives', *Coastal Engineering Journal*, 48(02), pp. 81-97.
- Fukumoto, T. (1990) 'A grading equation for decomposed granite soil', *Soils and Foundations*, 30(1), pp. 27-34.
- Fukumoto, T. (1992) 'Particle breakage characteristics of granular soils', *Soils and foundations*, 32(1), pp. 26-40.
- Gao, C., Xu, L., Coop, M. R., Huang, C. and Zuo, L. (2021) 'An investigation of particle breakage in loess', *Engineering Geology*, 286, pp. 106083.
- Gao, R. and Ye, J. (2023) 'Mechanical behaviors of coral sand and relationship between particle breakage and plastic work', *Engineering Geology*, 316, pp. 107063.
- Garboczi, E. J. and Bullard, J. W. (2004) 'Shape analysis of a reference cement', *Cement and concrete research*, 34(10), pp. 1933-1937.
- Ghafghazi, M., Shuttle, D. and DeJong, J. (2014) 'Particle breakage and the critical state of sand', *Soils and Foundations*, 54(3), pp. 451-461.
- Glantz, S. A., Slinker, B. K. and Neilands, T. B. (1990) 'Primer of applied regression and analysis of variance McGraw-Hill', *Inc., New York*.
- Gong, J., Nie, Z., Zhu, Y., Liang, Z. and Wang, X. (2019) 'Exploring the effects of particle shape and content of fines on the shear behavior of sand-fines mixtures via the DEM', *Computers and Geotechnics*, 106, pp. 161-176.
- Gong, Y., Song, Z., He, M., Gong, W. and Ren, F. (2017) 'Precursory waves and eigenfrequencies identified from acoustic emission data based on singular spectrum analysis and laboratory rock-burst experiments', *International Journal of Rock Mechanics and Mining Sciences*, 91, pp. 155-169.
- Gorsevski, P. V., Onasch, C. M., Farver, J. R. and Ye, X. (2012) 'Detecting grain boundaries in deformed rocks using a cellular automata approach', *Computers & Geosciences*, 42, pp. 136-142.
- Gourlay, M. 'Coral cays: products of wave action and geological processes in a biogenic environment', Vol. 2. *Proceedings of the 6th international coral reef symposium*, Great Barrier Reef Committee Townsville, 491-496.
- Grosse, C. U. and Ohtsu, M. (2008) *Acoustic emission testing*. Springer Science & Business Media.
- Guo, P. and Su, X. (2007) 'Shear strength, interparticle locking, and dilatancy of granular materials', *Canadian Geotechnical Journal*, 44(5), pp. 579-591.
- Gupta, V. (2017) 'Effect of size distribution of the particulate material on the specific breakage rate of particles in dry ball milling', *Powder Technology*, 305, pp. 714-722.
- Guyon, É. and Troadec, J.-P. (1994) *Du sac de billes au tas de sable*. Odile Jacob.

- Hagenaar, J. 'The use and interpretation of SPT results for the determination of axial bearing capacities of piles driven into carbonate soils and coral', Vol., *Penetration Testing*, Routledge, 51-55.
- Hamidi, A., Alizadeh, M. and Soleymani, S. (2009) 'Effect of particle crushing on shear strength and dilation characteristics of sand-gravel mixtures'.
- Hamidi, A. and Hooresfand, M. (2013) 'Effect of fiber reinforcement on triaxial shear behavior of cement treated sand', *Geotextiles and Geomembranes*, 36, pp. 1-9.
- Hanley, K. J., Huang, X. and O'Sullivan, C. (2018) 'Energy dissipation in soil samples during drained triaxial shearing', *Géotechnique*, 68(5), pp. 421-433.
- Hardin, B. O. (1985) 'Crushing of soil particles', *Journal of geotechnical engineering*, 111(10), pp. 1177-1192.
- Härtl, J. and Ooi, J. Y. (2011) 'Numerical investigation of particle shape and particle friction on limiting bulk friction in direct shear tests and comparison with experiments', *Powder Technology*, 212(1), pp. 231-239.
- Hassanlourad, M., Salehzadeh, H. and Shahnazari, H. (2008) 'Dilation and particle breakage effects on the shear strength of calcareous sands based on energy aspects', *International Journal of Civil Engineering*, 6(2), pp. 108-119.
- Heilbronner, R. and Barrett, S. (2013) *Image analysis in earth sciences: microstructures and textures of earth materials*. Springer Science & Business Media.
- Heilbronner, R. and Keulen, N. (2006) 'Grain size and grain shape analysis of fault rocks', *Tectonophysics*, 427(1-4), pp. 199-216.
- Hentschel, M. L. and Page, N. W. (2003) 'Selection of descriptors for particle shape characterization', *Particle & Particle Systems Characterization: Measurement and Description of Particle Properties and Behavior in Powders and Other Disperse Systems*, 20(1), pp. 25-38.
- Holtz, R. D., Kovacs, W. D. and Sheahan, T. C. (1981) *An introduction to geotechnical engineering*. Englewood Cliffs: Prentice-Hall.
- Holubec, I. and D'appolonia, E. (1973) 'Effect of particle shape on the engineering properties of granular soils', *Evaluation of relative density and its role in geotechnical projects involving cohesionless soils*: ASTM International.
- Houston, W. N. and Herrmann, H. G. (1980) 'Undrained cyclic strength of marine soils', *Journal of the Geotechnical Engineering Division*, 106(6), pp. 691-712.
- Hvorslev, M. J. 'Physical components of the shearstrength of saturated clay', Vol., *Proceedings of the Res. Conf. Shear Strength of Cohesive Soils*, ASCE, Boulder, CO, 169-273.
- Hyodo, M., Hyde, A. F., Aramaki, N. and Nakata, Y. (2002) 'Undrained monotonic and cyclic shear behaviour of sand under low and high confining stresses', *Soils and Foundations*, 42(3), pp. 63-76.
- Hyslip, J. P. and Vallejo, L. E. (1997) 'Fractal analysis of the roughness and size distribution of granular materials', *Engineering geology*, 48(3-4), pp. 231-244.
- Ideozu, R. and Ikoro, D. (2015) 'Sedimentology of Conglomeratic Beds within Odoro Ikpe–Arochukwu Axis: Afikpo Basin Southeastern Nigeria', *Int J Min Geol*, 5(2), pp. 1-15.
- IEA (2022) *Global Energy Crisis*: IEA. Available at: <https://www.iea.org/topics/global-energy-crisis> (Accessed: 19 Jun 2023).
- Igwe, O., Fukuoka, H. and Sassa, K. (2012) 'The effect of relative density and confining stress

- on shear properties of sands with varying grading', *Geotechnical and Geological Engineering*, 30, pp. 1207-1229.
- Indraratna, B., Lackenby, J. and Christie, D. (2005) 'Effect of confining pressure on the degradation of ballast under cyclic loading', *Geotechnique*, 55(4), pp. 325-328.
- Indraratna, B. and Nimbalkar, S. (2013) 'Stress-strain degradation response of railway ballast stabilized with geosynthetics', *Journal of geotechnical and geoenvironmental engineering*, 139(5), pp. 684-700.
- Indraratna, B., Sun, Q. D. and Nimbalkar, S. (2015) 'Observed and predicted behaviour of rail ballast under monotonic loading capturing particle breakage', *Canadian Geotechnical Journal*, 52(1), pp. 73-86.
- Indraratna, B., Thakur, P. K. and Vinod, J. S. (2010) 'Experimental and numerical study of railway ballast behavior under cyclic loading', *International Journal of Geomechanics*, 10(4), pp. 136-144.
- ISO (2021) *13322-2:2021 Particle size analysis — Image analysis methods — Part 2: Dynamic image analysis methods*. Geneva: ISO. Available at: <https://www.iso.org/standard/72566.html> (Accessed: 21 March 2023).
- Iwata, H. and Ukai, Y. (2002) 'SHAPE: a computer program package for quantitative evaluation of biological shapes based on elliptic Fourier descriptors', *Journal of heredity*, 93(5), pp. 384-385.
- Jamiolkowski, M., Lo Presti, D. and Manassero, M. (2003) 'Evaluation of relative density and shear strength of sands from CPT and DMT', *Soil behavior and soft ground construction*, pp. 201-238.
- Jang, H.-S., Zhang, Q.-Z., Kang, S.-S. and Jang, B.-A. (2018) 'Determination of the basic friction angle of rock surfaces by tilt tests', *Rock Mechanics and Rock Engineering*, 51(4), pp. 989-1004.
- Janoo, V. C. (1998) 'Quantification of shape, angularity, and surface texture of base course materials'.
- Jayakumar, T. (2011) 'Ndt techniques: Acoustic emission', *Encyclopedia of Materials: Science and Technology*, pp. 6001-6003.
- Jefferies, M. and Been, K. (2015) *Soil liquefaction: a critical state approach*. CRC press.
- Jiang, M., Shen, Z. and Thornton, C. (2013) 'Microscopic contact model of lunar regolith for high efficiency discrete element analyses', *Computers and Geotechnics*, 54, pp. 104-116.
- Jilan, S. (2004) 'Overview of the South China Sea circulation and its influence on the coastal physical oceanography outside the Pearl River Estuary', *Continental Shelf Research*, 24(16), pp. 1745-1760.
- Jin, Y.-F., Wu, Z.-X., Yin, Z.-Y. and Shen, J. S. (2017) 'Estimation of critical state-related formula in advanced constitutive modeling of granular material', *Acta Geotechnica*, 12, pp. 1329-1351.
- Johansson, J. and Vall, J. 2011. Friktionsjords kornform: Inverkan på geotekniska egenskaper, beskrivande storheter och bestämningsmetoder.
- John, N. J., Khan, I., Kandalai, S. and Patel, A. (2023) 'Particle breakage in construction materials: A geotechnical perspective', *Construction and Building Materials*, 381, pp. 131308.

- Jones, R. P., Ottino, J. M., Umbanhowar, P. B. and Lueptow, R. M. (2020) 'Remarkable simplicity in the prediction of nonspherical particle segregation', *Physical Review Research*, 2(4), pp. 042021.
- Kan, M. E. and Taiebat, H. A. (2014) 'A bounding surface plasticity model for highly crushable granular materials', *Soils and Foundations*, 54(6), pp. 1188-1201.
- Kappraff, J. (1986) 'The geometry of coastlines: a study in fractals', *Computers & mathematics with applications*, 12(3-4), pp. 655-671.
- Karatza, Z., Andò, E., Papanicolopoulos, S.-A., Viggiani, G. and Ooi, J. Y. 'Evolution of particle breakage studied using x-ray tomography and the discrete element method', Vol. 140. *EPJ Web of Conferences*, EDP Sciences, 07013.
- Karatza, Z., Andò, E., Papanicolopoulos, S.-A., Viggiani, G. and Ooi, J. Y. (2019) 'Effect of particle morphology and contacts on particle breakage in a granular assembly studied using X-ray tomography', *Granular Matter*, 21, pp. 1-13.
- Karimpour-Fard, M., Rezvani, R. and Selakjani, S. G. (2021) 'Crushability and compressibility of carbonate and siliceous sands in the one-dimensional oedometer test', *Arabian Journal of Geosciences*, 14(23), pp. 2536.
- Keller, G. H. 'Shear Strength and Other Physical Properties of: Of Sediments from Some Ocean Basins', Vol., *Civil Engineering in the Oceans*, ASCE, 391-417.
- Kleesment, A. (2009) 'Roundness and surface features of quartz grains in Middle Devonian deposits of the East Baltic and their palaeogeographical implications', *Estonian Journal of Earth Sciences*, 58(1).
- Kong, X., Liu, J., Zou, D. and Liu, H. (2016) 'Stress-dilatancy relationship of Zipingpu gravel under cyclic loading in triaxial stress states', *International Journal of Geomechanics*, 16(4), pp. 04016001.
- Krumbein, W. C. (1941) 'Measurement and geological significance of shape and roundness of sedimentary particles', *Journal of Sedimentary Research*, 11(2), pp. 64-72.
- Krumbein, W. C. and Pettijohn, F. J. (1938) *Manual of sedimentary petrography*. New York, London: D. Appleton-Century Company, incorporated, p. 549.
- Krumbein, W. C. and Sloss, L. L. (1951) *Stratigraphy and sedimentation*. LWW.
- Krumbein, W. C. and Sloss, L. L. (1963) *Stratigraphy and sedimentation*. 2nd edn. San Francisco: W. H. Freeman and Company.
- Kuenen, P. H. (1956) 'Experimental abrasion of pebbles: 2. Rolling by current', *The Journal of Geology*, 64(4), pp. 336-368.
- Kulu, P., Tumanok, A., Mikli, V., Kaerdi, H., Kohutek, I. and Besterci, M. (1998) 'Possibilities of evaluation of powder particle granulometry and morphology by image analysis', *Proceedings of the Estonian Academy of Sciences: Engineering(Estonia)*, 4(1), pp. 3-17.
- Lade, P. V. (2016) *Triaxial testing of soils*. John Wiley & Sons.
- Lade, P. V. and Yamamuro, J. A. (1996) 'Undrained sand behavior in axisymmetric tests at high pressures', *Journal of Geotechnical Engineering*, 122(2), pp. 120-129.
- Lade, P. V., Yamamuro, J. A. and Bopp, P. A. (1996) 'Significance of particle crushing in granular materials', *Journal of Geotechnical Engineering*, 122(4), pp. 309-316.
- Lambe, T. W. and Whitman, R. V. (1991) *Soil mechanics*. John Wiley & Sons.
- Lanaro, F. and Tolppanen, P. (2002) '3D characterization of coarse aggregates', *Engineering*

- Geology*, 65(1), pp. 17-30.
- Lee, J.-S., Park, G., Byun, Y.-H. and Lee, C. (2020) 'Modified fixed wall oedometer when considering stress dependence of elastic wave velocities', *Sensors*, 20(21), pp. 6291.
- Lee, K. L. and Farhoomand, I. (1967) 'Compressibility and crushing of granular soil in anisotropic triaxial compression', *Canadian geotechnical journal*, 4(1), pp. 68-86.
- Lees, G. (1964) 'The measurement of particle shape and its influence in engineering materials', *Journ. Brit. Granite and Whinstone Federation*, 4(2).
- Leibrandt, S. and Le Pennec, J.-L. (2015) 'Towards fast and routine analyses of volcanic ash morphometry for eruption surveillance applications', *Journal of Volcanology and Geothermal Research*, 297, pp. 11-27.
- Leleu, S. and Valdes, J. (2007) 'Experimental study of the influence of mineral composition on sand crushing', *Géotechnique*, 57(3), pp. 313-317.
- Li, D., Minner, D. D. and Christians, N. E. 'Quantitative evaluation of sand shape and roundness and their potential effect on stability of sand-based athletic fields', Vol., *I International Conference on Turfgrass Management and Science for Sports Fields 661*, 159-170.
- Li, X., Zhao, S., He, S., Yan, Q. and Lei, X. (2019) 'Seismic stability analysis of gravity retaining wall supporting c- ϕ soil with cracks', *Soils and Foundations*, 59(4), pp. 1103-1111.
- Li, Y. (2013) 'Effects of particle shape and size distribution on the shear strength behavior of composite soils', *Bulletin of Engineering Geology and the Environment*, 72, pp. 371-381.
- Lieberman, E., Rollett, A., Lebensohn, R. and Kober, E. (2015) 'Calculation of grain boundary normals directly from 3D microstructure images', *Modelling and Simulation in Materials Science and Engineering*, 23(3), pp. 035005.
- Lin, W., Liu, A. and Mao, W. (2019) 'Use of acoustic emission to evaluate the micro-mechanical behavior of sands in single particle compression tests', *Ultrasonics*, 99, pp. 105962.
- Liu, E., Cashman, K., Rust, A. and Gislason, S. (2015) 'The role of bubbles in generating fine ash during hydromagmatic eruptions', *Geology*, 43(3), pp. 239-242.
- Liu, H., Zeng, K. and Zou, Y. (2020) 'Particle breakage of calcareous sand and its correlation with input energy', *International Journal of Geomechanics*, 20(2), pp. 04019151.
- Liu, H., Zou, D. and Liu, J. (2014) 'Constitutive modeling of dense gravelly soils subjected to cyclic loading', *International Journal for Numerical and Analytical Methods in Geomechanics*, 38(14), pp. 1503-1518.
- Liu, S. and Matsuoka, H. (2003) 'Microscopic interpretation on a stress-dilatancy relationship of granular materials', *Soils and Foundations*, 43(3), pp. 73-84.
- Lobo-Guerrero, S. and Vallejo, L. E. (2005a) 'Analysis of crushing of granular material under isotropic and biaxial stress conditions', *Soils and foundations*, 45(4), pp. 79-87.
- Lobo-Guerrero, S. and Vallejo, L. E. (2005b) 'Discrete element method evaluation of granular crushing under direct shear test conditions', *Journal of Geotechnical and Geoenvironmental Engineering*, 131(10), pp. 1295-1300.
- Lobo-Guerrero, S., Vallejo, L. E. and Vesga, L. F. (2006) 'Visualization of crushing evolution in granular materials under compression using DEM', *International Journal of Geomechanics*, 6(3), pp. 195-200.
- Lowe, J. 'Use of back pressure to increase degree of saturation of triaxial test specimens', Vol.,

- Proc., ASCE Research Conf. on Shear Strength of Cohesive Soils*, 819-836.
- Lu, N., Kim, T.-H., Sture, S. and Likos, W. J. (2009) 'Tensile strength of unsaturated sand', *Journal of engineering mechanics*, 135(12), pp. 1410-1419.
- Lu, N. and Likos, W. J. (2006) 'Suction stress characteristic curve for unsaturated soil', *Journal of geotechnical and geoenvironmental engineering*, 132(2), pp. 131-142.
- Lu, N., Wu, B. and Tan, C. P. (2007) 'Tensile strength characteristics of unsaturated sands', *Journal of Geotechnical and Geoenvironmental Engineering*, 133(2), pp. 144-154.
- Lu, Z., Yao, A., Su, A., Ren, X., Liu, Q. and Dong, S. (2019) 'Re-recognizing the impact of particle shape on physical and mechanical properties of sandy soils: a numerical study', *Engineering Geology*, 253, pp. 36-46.
- Luo, M., Liu, X., Zhong, L., Wang, X. and Wu, C. (2024) 'Effects of Particle Breakage on the Mechanical Behavior of Calcareous Sand Under Confined Compression Tests', *International Journal of Civil Engineering*, pp. 1-18.
- Luo, T., Ooi, E., Chan, A. and Shao-jun, F. (2017) 'A combined DEM-SBFEM for particle breakage modelling of rock-fill materials'.
- Luzzani, L. and MR, C. (2002) 'On the relationship between particle breakage and the critical state of sands', *Soils and foundations*, 42(2), pp. 71-82.
- Ma, X., Lei, H. and Kang, X. (2022) 'Effects of particle morphology on the shear response of granular soils by discrete element method and 3D printing technology', *International Journal for Numerical and Analytical Methods in Geomechanics*, 46(11), pp. 2191-2208.
- Maccarini, M. (1993) 'A comparison of direct shear box tests with triaxial compression tests for a residual soil', *Geotechnical & Geological Engineering*, 11, pp. 69-80.
- Maeda, K. and Miura, K. (1999) 'Relative density dependency of mechanical properties of sands', *Soils and Foundations*, 39(1), pp. 69-79.
- Mair, K., Frye, K. M. and Marone, C. (2002) 'Influence of grain characteristics on the friction of granular shear zones', *Journal of Geophysical Research: Solid Earth*, 107(B10), pp. ECV 4-1-ECV 4-9.
- Mandelbrot, B. B. (1983) *The fractal geometry of nature*. WH freeman New York.
- Manga, M., Patel, A. and Dufek, J. (2011) 'Rounding of pumice clasts during transport: field measurements and laboratory studies', *Bulletin of Volcanology*, 73, pp. 321-333.
- Mao, W. and Towhata, I. (2015) 'Monitoring of single-particle fragmentation process under static loading using acoustic emission', *Applied Acoustics*, 94, pp. 39-45.
- Marsal, R. 'Soil properties-shear strength and consolidation', Vol. 3. *Proc. 6th Int. Conf., SMFE, 1965*, 310-316.
- Marsal, R. J. (1967) 'Large scale testing of rockfill materials', *Journal of the Soil Mechanics and Foundations Division*, 93(2), pp. 27-43.
- Marsal, R. J. (1973) 'Mechanical properties of rockfill', *Publication of: Wiley (John) and Sons, Incorporated*.
- Mashiri, M., Vinod, J., Sheikh, M. N. and Tsang, H.-H. (2015) 'Shear strength and dilatancy behaviour of sand-tyre chip mixtures', *Soils and Foundations*, 55(3), pp. 517-528.
- Matsushima, T., Saomoto, H., Matsumoto, M., Toda, K. and Yamada, Y. 'Discrete element simulation of an assembly of irregularly-shaped grains: Quantitative comparison with experiments', Vol., *16th ASCE Engineering Mechanics Conference*, American Society

- of Civil Engineers, 1-8.
- McClelland, B. 'Calcareous sediments: an engineering enigma', Vol., *International conference on calcareous sediments*, 777-784.
- McDowell, G. (2002) 'On the yielding and plastic compression of sand', *Soils and foundations*, 42(1), pp. 139-145.
- McDowell, G. and Bolton, M. (1998) 'On the micromechanics of crushable aggregates', *Géotechnique*, 48(5), pp. 667-679.
- McDowell, G., Bolton, M. and Robertson, D. (1996) 'The fractal crushing of granular materials', *Journal of the Mechanics and Physics of Solids*, 44(12), pp. 2079-2101.
- Meloy, T. (1977) 'Fast Fourier transforms applied to shape analysis of particle silhouettes to obtain morphological data', *Powder Technology*, 17(1), pp. 27-35.
- Mesri, G. and Funk, J. (2015) 'Settlement of the Kansai international airport islands', *Journal of Geotechnical and Geoenvironmental Engineering*, 141(2), pp. 04014102.
- Mesri, G. and Vardhanabhuti, B. (2009) 'Compression of granular materials', *Canadian Geotechnical Journal*, 46(4), pp. 369-392.
- Micromeritics (2023) *AccuPyc II*. Gas Displacement Pycnometry System. Available at: <https://www.micromeritics.com/accupyc-ii/> (Accessed: 15 March 2023).
- Microtrac (2023a) *CAMSIZER® ONLINE XL*. Dynamic Image Analysis. Available at: <https://www.microtrac.com/products/particle-size-shape-analysis/dynamic-image-analysis/camsizer-online-xl/> (Accessed: 21 March 2023).
- Microtrac (2023b) *Dynamic Image Analysis*. Particle Size & Shape Analysis. Available at: <https://www.microtrac.com/files/79556/dynamic-image-analysis.pdf> (Accessed: 21 March 2023).
- Mikli, V., Kaerdi, H., Kulu, P. and Besterci, M. (2001) 'Characterization of powder particle morphology', *Proceedings of the Estonian Academy of Sciences: Engineering(Estonia)*, 7(1), pp. 22-34.
- Mingireanov Filho, I., Spina, T. V., Falcão, A. X. and Vidal, A. C. (2013) 'Segmentation of sandstone thin section images with separation of touching grains using optimum path forest operators', *Computers & geosciences*, 57, pp. 146-157.
- Mirghasemi, A., Rothenburg, L. and Matyas, E. (2002) 'Influence of particle shape on engineering properties of assemblies of two-dimensional polygon-shaped particles', *Geotechnique*, 52(3), pp. 209-217.
- Mishra, B. and Thornton, C. (2001) 'Impact breakage of particle agglomerates', *International Journal of Mineral Processing*, 61(4), pp. 225-239.
- Mitchell, J. K. and Soga, K. (2005) *Fundamentals of soil behavior*. John Wiley & Sons New York.
- Miura, N. and Sukeo, O. (1979) 'Particle-crushing of a decomposed granite soil under shear stresses', *Soils and foundations*, 19(3), pp. 1-14.
- Miura, N. and Yamanouchi, T. 'Effect of particle-crushing on the shear characteristics of a sand', Vol. 1977. *Proceedings of the Japan Society of Civil Engineers*, Japan Society of Civil Engineers, 109-118.
- Miura, S. and Yagi, K. (1997) 'Particle breakage of volcanic coarse-grained soils and its evaluation', *Doboku Gakkai Ronbunshu*, 1997(561), pp. 257-269.
- Miura, S., Yagi, K. and Asonuma, T. (2003) 'Deformation-strength evaluation of crushable

- volcanic soils by laboratory and in-situ testing', *Soils and Foundations*, 43(4), pp. 47-57.
- Miwa, T., Shimano, T. and Nishimura, T. (2015) 'Characterization of the luminance and shape of ash particles at Sakurajima volcano, Japan, using CCD camera images', *Bulletin of Volcanology*, 77, pp. 1-13.
- Mohr, O. (1900) 'Welche Umstände bedingen die Elastizitätsgrenze und den Bruch eines Materials', *Zeitschrift des Vereins Deutscher Ingenieure*, 46(1524-1530), pp. 1572-1577.
- Mora, C. and Kwan, A. (2000) 'Sphericity, shape factor, and convexity measurement of coarse aggregate for concrete using digital image processing', *Cement and concrete research*, 30(3), pp. 351-358.
- Muñoz-Ibáñez, A., Delgado-Martín, J. and Grande-García, E. (2019) 'Acoustic emission processes occurring during high-pressure sand compaction', *Geophysical Prospecting*, 67(4), pp. 761-783.
- Muravin, B. and Carlos, M. F. (2011) 'Guide for development of acoustic emission application for examination of metal structure', *Acoustic Emission*, 29, pp. 142-148.
- Murison, R. (2023) 'The Influence of Oedometer Sample Aspect Ratio on the 1-D Compression Behaviour of Silica Sand', Vol., *10th South African Young Geotechnical Engineers Conference*, Oubaai Hotel, 406 Herolds Bay Road, George, Western Cape, 13, 14 & 15 September.
- Murtagh, R. M. and White, J. D. (2013) 'Pyroclast characteristics of a subaqueous to emergent Surtseyan eruption, Black Point volcano, California', *Journal of Volcanology and Geothermal Research*, 267, pp. 75-91.
- Murthy, T., Loukidis, D., Carraro, J., Prezzi, M. and Salgado, R. (2007) 'Undrained monotonic response of clean and silty sands', *Géotechnique*, 57(3), pp. 273-288.
- Naghavi, N. (2017) *Liquefaction Assessment of Carbonate-Silica Silty Sands Using Energy, State Parameter and Shear Wave Velocity*. The University of Western Ontario (Canada).
- Naghavi, N. and El Naggar, M. H. (2019) 'Application of back pressure for saturation of soil samples in cyclic triaxial tests', *Geotechnical Engineering in the XXI Century: Lessons learned and future challenges*: IOS Press, pp. 115-123.
- Nakata, A., Hyde, M., Hyodo, H. and Murata (1999) 'A probabilistic approach to sand particle crushing in the triaxial test', *Géotechnique*, 49(5), pp. 567-583.
- Nakata, Y., Hyodo, M., Hyde, A. F., Kato, Y. and Murata, H. (2001a) 'Microscopic particle crushing of sand subjected to high pressure one-dimensional compression', *Soils and foundations*, 41(1), pp. 69-82.
- Nakata, Y., Kato, Y., Hyodo, M., Hyde, A. F. and Murata, H. (2001b) 'One-dimensional compression behaviour of uniformly graded sand related to single particle crushing strength', *Soils and foundations*, 41(2), pp. 39-51.
- Nam, S., Gutierrez, M., Diplas, P. and Petrie, J. (2011) 'Determination of the shear strength of unsaturated soils using the multistage direct shear test', *Engineering Geology*, 122(3-4), pp. 272-280.
- Nanjing Ningxi Soil Instrument Co., L. (2023) *Single lever consolidation instrument (triple high pressure)*. Consolidation test. Available at: <http://en.ningxi.com/product/122.html>

(Accessed: 23 March 2023).

- Nasir, M., Megat Johari, M. A., Yusuf, M. O., Maslehuddin, M., Al-Harthi, M. A. and Dafalla, H. (2019) 'Impact of slag content and curing methods on the strength of alkaline-activated silico-manganese fume/blast furnace slag mortars', *Arabian Journal for Science and Engineering*, 44, pp. 8325-8335.
- Nauroy, J. and Le Tirant, P. 'Model Tests of Piles in Calcareous Sands', Vol., *Geotechnical Practice in Offshore Engineering*, ASCE, 356-369.
- Németh, K. (2010) 'Volcanic glass textures, shape characteristics and compositions of phreatomagmatic rock units from the Western Hungarian monogenetic volcanic fields and their implications for magma fragmentation', *Central European Journal of Geosciences*, 2, pp. 399-419.
- Németh, K. and Cronin, S. J. (2011) 'Drivers of explosivity and elevated hazard in basaltic fissure eruptions: the 1913 eruption of Ambrym Volcano, Vanuatu (SW-Pacific)', *Journal of volcanology and geothermal research*, 201(1-4), pp. 194-209.
- Ng, T. T. (2009) 'Particle shape effect on macro-and micro-behaviors of monodisperse ellipsoids', *International journal for numerical and analytical methods in geomechanics*, 33(4), pp. 511-527.
- Ni, Q., Tan, T., Dasari, G. and Hight, D. (2004) 'Contribution of fines to the compressive strength of mixed soils', *Géotechnique*, 54(9), pp. 561-569.
- Norazirah, A., Fuad, S. and Hazizan, M. (2016) 'The effect of size and shape on breakage characteristic of mineral', *Procedia Chemistry*, 19, pp. 702-708.
- O'Sullivan, C. (2011) *Particulate discrete element modelling: a geomechanics perspective*. CRC Press.
- Ovalle, C., Dano, C., Hicher, P.-Y. and Cisternas, M. (2015) 'Experimental framework for evaluating the mechanical behavior of dry and wet crushable granular materials based on the particle breakage ratio', *Canadian Geotechnical Journal*, 52(5), pp. 587-598.
- Parab, N. D., Claus, B., Hudspeth, M. C., Black, J. T., Mondal, A., Sun, J., Fezzaa, K., Xiao, X., Luo, S. and Chen, W. (2014) 'Experimental assessment of fracture of individual sand particles at different loading rates', *International Journal of Impact Engineering*, 68, pp. 8-14.
- Park, L. K., Suneel, M. and Chul, I. J. (2008) 'Shear strength of Jumunjin sand according to relative density', *Marine Georesources and Geotechnology*, 26(2), pp. 101-110.
- Patel, S. K. and Singh, B. (2019) 'Shear strength response of glass fibre-reinforced sand with varying compacted relative density', *International Journal of Geotechnical Engineering*, 13(4), pp. 339-351.
- Pena, A., Garcia-Rojo, R. and Herrmann, H. J. (2007) 'Influence of particle shape on sheared dense granular media', *Granular matter*, 9(3-4), pp. 279-291.
- Peng, Z., Chen, C. and Wu, L. (2021) 'Numerical investigation of particle shape effect on sand shear strength', *Arabian Journal for Science and Engineering*, 46(11), pp. 10585-10595.
- Pentland, A. (1927) 'A method of measuring the angularity of sands', *Proceedings and Transactions of the Royal Society of Canada*, 21(3), pp. 43.
- Persson, A.-L. (1998) 'Image analysis of shape and size of fine aggregates', *Engineering Geology*, 50(1-2), pp. 177-186.

- Pestana, J. M. and Whittle, A. (1995) 'Compression model for cohesionless soils', *Géotechnique*, 45(4), pp. 611-631.
- Pettijohn, F. J. (1949) *Sedimentary rocks*. New York: Harper & Brothers.
- PhysicalAcoustics (2023a) 2/4/6 - SWITCH SELECTABLE GAIN SINGLE ENDED AND DIFFERENTIAL PREAMPLIFIER. Preamplifiers. Available at: <https://www.physicalacoustics.com/by-product/2-4-6/> (Accessed: 2 April 2023).
- PhysicalAcoustics (2023b) EXPRESS-8 – PCI EXPRESS-BASED EIGHT-CHANNEL AE BOARD & SYSTEM. Boards. Available at: <https://www.physicalacoustics.com/by-product/express-8/> (Accessed: 2 April 2023).
- PhysicalAcoustics (2023c) Micro-II – Compact PCI AE Chassis. Chassis. Available at: <https://www.physicalacoustics.com/by-product/micro-ii/> (Accessed: 2 April 2023).
- PhysicalAcoustics (2023d) NANO30 - 150-750 KHZ MINIATURE AE SENSOR WITH INTEGRAL COAXIAL CABLE. Sensors. Available at: <https://www.physicalacoustics.com/by-product/nano30-150-750-khz-miniature-ae-sensor-with-integral-coaxial-cable/> (Accessed: 2 April 2023).
- Polacci, M. and Papale, P. (1997) 'The evolution of lava flows from ephemeral vents at Mount Etna: insights from vesicle distribution and morphological studies', *Journal of Volcanology and Geothermal Research*, 76(1-2), pp. 1-17.
- Pons, M.-N., Vivier, H., Belaroui, K., Bernard-Michel, B., Cordier, F., Oulhana, D. and Dodds, J. A. (1999) 'Particle morphology: from visualisation to measurement', *Powder Technology*, 103(1), pp. 44-57.
- Potts, D., Dounias, G. and Vaughan, P. (1987) 'Finite element analysis of the direct shear box test', *Geotechnique*, 37(1), pp. 11-23.
- Powers, M. C. (1953) 'A new roundness scale for sedimentary particles', *Journal of Sedimentary Research*, 23(2), pp. 117-119.
- Rahaman, M. N. (2017) *Ceramic processing and sintering*. CRC press.
- Ren, X. and Santamarina, J. (2018) 'The hydraulic conductivity of sediments: A pore size perspective', *Engineering Geology*, 233, pp. 48-54.
- Research Nester (2023) *Global Supply & Demand Analysis & Opportunity Outlook 2023-2035*: Research Nester. Available at: <https://www.researchnester.com/reports/offshore-drilling-market/4895> (Accessed: 19 Jun 2023).
- Reynolds, O. (1885) 'LVII. On the dilatancy of media composed of rigid particles in contact. With experimental illustrations', *The London, Edinburgh, and Dublin Philosophical Magazine and Journal of Science*, 20(127), pp. 469-481.
- Riley, C. M., Rose, W. I. and Bluth, G. J. (2003) 'Quantitative shape measurements of distal volcanic ash', *Journal of Geophysical Research: Solid Earth*, 108(B10).
- Riley, N. A. (1941) 'Projection sphericity', *Journal of Sedimentary Research*, 11(2), pp. 94-95.
- Rodriguez, J., Edeskär, T. and Knutsson, S. (2013) 'Particle shape quantities and measurement techniques: a review', *The Electronic journal of geotechnical engineering*, 18, pp. 169-198.
- Rousé, P., Fannin, R. and Shuttle, D. (2008) 'Influence of roundness on the void ratio and strength of uniform sand', *Géotechnique*, 58(3), pp. 227-231.
- Roussillon, T., Piégay, H., Sivignon, I., Tougne, L. and Lavigne, F. (2009) 'Automatic computation of pebble roundness using digital imagery and discrete geometry',

- Computers & Geosciences*, 35(10), pp. 1992-2000.
- Rowe, P. (1954) 'A stress-strain theory for cohesionless soil with applications to earth pressures at rest and moving walls', *Geotechnique*, 4(2), pp. 70-88.
- Rozenblat, Y., Portnikov, D., Levy, A., Kalman, H., Aman, S. and Tomas, J. (2011) 'Strength distribution of particles under compression', *Powder Technology*, 208(1), pp. 215-224.
- Russ, J. C. (2006) *The image processing handbook*. CRC press.
- Russell, A. R. (2011) 'A compression line for soils with evolving particle and pore size distributions due to particle crushing', *Géotechnique Letters*, 1(1), pp. 5-9.
- Russell, R. D. and Taylor, R. E. (1937) 'Roundness and shape of Mississippi River sands', *The Journal of Geology*, 45(3), pp. 225-267.
- Rust, A., Manga, M. and Cashman, K. V. (2003) 'Determining flow type, shear rate and shear stress in magmas from bubble shapes and orientations', *Journal of Volcanology and Geothermal Research*, 122(1-2), pp. 111-132.
- Saada, A. and Townsend, F. (1981) 'State of the art: laboratory strength testing of soils'.
- Sadrekarami, A. and Olson, S. (2011) 'Critical state friction angle of sands', *Géotechnique*, 61(9), pp. 771-783.
- Sadrekarami, A. and Olson, S. M. (2010a) 'Particle damage observed in ring shear tests on sands', *Canadian Geotechnical Journal*, 47(5), pp. 497-515.
- Sadrekarami, A. and Olson, S. M. (2010b) 'Shear band formation observed in ring shear tests on sandy soils', *Journal of geotechnical and geoenvironmental engineering*, 136(2), pp. 366-375.
- Sagasta, F., Zitto, M. E., Piotrkowski, R., Benavent-Climent, A., Suarez, E. and Gallego, A. (2018) 'Acoustic emission energy b-value for local damage evaluation in reinforced concrete structures subjected to seismic loadings', *Mechanical Systems and Signal Processing*, 102, pp. 262-277.
- Salim, W. and Indraratna, B. (2004) 'A new elastoplastic constitutive model for coarse granular aggregates incorporating particle breakage', *Canadian Geotechnical Journal*, 41(4), pp. 657-671.
- Santamarina, J. C. and Cho, G.-C. 'Soil behaviour: The role of particle shape', Vol., *Advances in geotechnical engineering: The Skempton conference: Proceedings of a three day conference on advances in geotechnical engineering, organised by the Institution of Civil Engineers and held at the Royal Geographical Society, London, UK, on 29–31 March 2004*, Thomas Telford Publishing, 604-617.
- Santamarina, J. C. and Cho, G. C. (2001) 'Determination of critical state parameters in sandy soils—simple procedure', *Geotechnical testing journal*, 24(2), pp. 185-192.
- Schäfer, M. (2002) 'Digital optics: Some remarks on the accuracy of particle image analysis', *Particle & Particle Systems Characterization: Measurement and Description of Particle Properties and Behavior in Powders and Other Disperse Systems*, 19(3), pp. 158-168.
- Schanz, T. and Vermeer, P. (1996) 'Angles of friction and dilatancy of sand', *Géotechnique*, 46(1), pp. 145-151.
- Schwarcz, H. and Shane, K. (1969) 'Measurement of particle shape by Fourier analysis', *Sedimentology*, 13(3-4), pp. 213-231.

- Shahnazari, H. and Rezvani, R. (2013) 'Effective parameters for the particle breakage of calcareous sands: An experimental study', *Engineering geology*, 159, pp. 98-105.
- Shea, T., Houghton, B. F., Gurioli, L., Cashman, K. V., Hammer, J. E. and Hobden, B. J. (2010) 'Textural studies of vesicles in volcanic rocks: an integrated methodology', *Journal of Volcanology and Geothermal Research*, 190(3-4), pp. 271-289.
- Shen, W., Zhao, T., Dai, F., Crosta, G. B. and Wei, H. (2020) 'Discrete element analyses of a realistic-shaped rock block impacting against a soil buffering layer', *Rock Mechanics and Rock Engineering*, 53, pp. 3807-3822.
- Shenzhen Stereo3D Technology (2023) *PTS-A series (binocular) photographic white light 3D scanner*. Photo 3D scanner. Available at: <https://www.3doe.net.cn/detail/1327.html> (Accessed: 23 Jul 2023).
- Shi, W.-c., Zhu, J.-g., Chiu, C.-f. and Liu, H.-l. (2010) 'Strength and deformation behaviour of coarse-grained soil by true triaxial tests', *Journal of Central South University of Technology*, 17(5), pp. 1095-1102.
- Shinohara, K., Oida, M. and Golman, B. (2000) 'Effect of particle shape on angle of internal friction by triaxial compression test', *Powder technology*, 107(1-2), pp. 131-136.
- Shipton, B. and Coop, M. R. (2012) 'On the compression behaviour of reconstituted soils', *Soils and Foundations*, 52(4), pp. 668-681.
- Siang, A. J. L. M. and Wijeyesekera, D. C. (2012) 'Effect of particle grading size and shape on density, dilatancy and shear strength of sands', *Malaysian Journal of Science*, 31(2), pp. 161-174.
- Siang, A. J. L. M., Wijeyesekera, D. C. and Zainorabidin, A. (2013) 'The effect of particle morphology of sand on the relationship between shear strength and dilatancy characteristics', *Electronic Journal of Geotechnical Engineering*, 18, pp. 1537-1546.
- Skempton, A. (1986) 'Standard penetration test procedures and the effects in sands of overburden pressure, relative density, particle size, ageing and overconsolidation', *Geotechnique*, 36(3), pp. 425-447.
- Skempton, A. W. (1954) 'The Pore-Pressure Coefficients A and B', *Géotechnique*, 4(4), pp. 143-147. DOI: 10.1680/geot.1954.4.4.143.
- Smith, G. N. (1982) *Elements of soil mechanics for civil and mining engineers*.
- Soliman, N. 'Effect of Geologic History on the Design Parameters of Heavily Overconsolidated Till', Vol., *Geological Environmental and Soil Properties*, ASCE, 246-268.
- Spalding, M., Spalding, M. D., Ravilious, C. and Green, E. P. (2001) *World atlas of coral reefs*. Univ of California Press.
- Sukumaran, B. and Ashmawy, A. (2001) 'Quantitative characterisation of the geometry of discret particles', *Geotechnique*, 51(7), pp. 619-627.
- Suzuki, K., Fujiwara, H. and Ohta, T. (2015) 'The evaluation of macroscopic and microscopic textures of sand grains using elliptic Fourier and principal component analysis: implications for the discrimination of sedimentary environments', *Sedimentology*, 62(4), pp. 1184-1197.
- Szadeczky-Kardoss, E. v. (1933) 'Die Bestimmung des Abrollungsgrades', *Zentralblatt für Mineralogie, Geologie und Paläontologie, Abt. B*, pp. 389-401.
- Tafesse, S., Robison Fernlund, J. M., Sun, W. and Bergholm, F. (2013) 'Evaluation of image analysis methods used for quantification of particle angularity', *Sedimentology*, 60(4),

- pp. 1100-1110.
- Takashimizu, Y. and Iiyoshi, M. (2016) 'New parameter of roundness R: circularity corrected by aspect ratio', *Progress in Earth and Planetary Science*, 3(1), pp. 1-16.
- Tamsir, P. C., Arafianto, A. and Rahardjo, P. P. 'Study on the performance of coastal reclamation and qc/N correlation of calcareous sands in Makassar', Vol., *Geotechnics for Sustainable Infrastructure Development*, Springer, 1375-1381.
- Tanaka, T. (1954) 'A new concept applying a final fineness value to gringing mechanism-grinding test with frictional and impulsive force', *J. Chem. Eng. Jpn.*, 18, pp. 160-171.
- Tarantino, A. and Hyde, A. F. (2005) 'An experimental investigation of work dissipation in crushable materials', *Géotechnique*, 55(8), pp. 575-584.
- Terzaghi, K. and Peck, R. B. (1948) *Soil mechanics in engineering practice*. New York, NY: John Wiley & Sons, Inc.
- Thakur, P. K. (2011) 'Cyclic densification of ballast and associated deformation and degradation'.
- Thevanayagam, S. (1998) 'Effect of fines and confining stress on undrained shear strength of silty sands', *Journal of geotechnical and geoenvironmental engineering*, 124(6), pp. 479-491.
- Thevanayagam, S., Ravishankar, K. and Mohan, S. (1997) 'Effects of fines on monotonic undrained shear strength of sandy soils', *Geotechnical testing journal*, 20(4), pp. 394-406.
- Thomas, M., Wiltshire, R. and Williams, A. (1995) 'The use of Fourier descriptors in the classification of particle shape', *Sedimentology*, 42(4), pp. 635-645.
- Trepanier, M. and Franklin, S. V. (2010) 'Column collapse of granular rods', *Physical Review E*, 82(1), pp. 011308.
- Trulsson, M. (2018) 'Rheology and shear jamming of frictional ellipses', *Journal of Fluid Mechanics*, 849, pp. 718-740.
- Tsegaye, A. B. and Benz, T. (2014) 'Plastic flow and state-dilatancy for geomaterials', *Acta Geotechnica*, 9, pp. 329-342.
- Tunwal, M. (2018) *Quantitative textural analysis of sedimentary grains and basin subsidence modelling*. University College Cork.
- Turcotte, D. L. (1986) 'Fractals and fragmentation', *Journal of Geophysical Research: Solid Earth*, 91(B2), pp. 1921-1926.
- Tyler, S. W. and Wheatcraft, S. W. (1992) 'Fractal scaling of soil particle-size distributions: Analysis and limitations', *Soil Science Society of America Journal*, 56(2), pp. 362-369.
- Ueng, T.-S. and Chen, T.-J. (2000) 'Energy aspects of particle breakage in drained shear of sands', *Géotechnique*, 50(1), pp. 65-72.
- (2004) *General Design and Construction Considerations for Earth and Rock-Fill Dams*. Washington, DC. Available at: https://www.publications.usace.army.mil/portals/76/publications/engineermanuals/em_1110-2-2300.pdf (Accessed: 6 Jul 2023).
- Uygar, E. and Doven, A. G. (2006) 'Monotonic and cyclic oedometer tests on sand at high stress levels', *Granular Matter*, 8(1), pp. 19-26.
- Vaid, Y., Fisher, J., Kuerbis, R. and Negussey, D. (1990) 'Particle gradation and liquefaction',

- Journal of Geotechnical Engineering*, 116(4), pp. 698-703.
- Vaid, Y. and Sasitharan, S. (1992) 'The strength and dilatancy of sand', *Canadian Geotechnical Journal*, 29(3), pp. 522-526.
- Van Olphen, H. (1964) 'An introduction to clay colloid chemistry', *Soil Science*, 97(4), pp. 290.
- Varadarajan, A., Sharma, K., Venkatachalam, K. and Gupta, A. (2003) 'Testing and modeling two rockfill materials', *Journal of geotechnical and geoenvironmental engineering*, 129(3), pp. 206-218.
- Vesic, A. S. and Clough, G. W. (1968) 'Behavior of granular materials under high stresses', *Journal of Soil Mechanics & Foundations Div.*
- Wadell, H. (1932) 'Volume, shape, and roundness of rock particles', *The Journal of Geology*, 40(5), pp. 443-451.
- Wadell, H. (1933) 'Sphericity and roundness of rock particles', *The Journal of Geology*, 41(3), pp. 310-331.
- Wadell, H. (1935) 'Volume, shape, and roundness of quartz particles', *The Journal of Geology*, 43(3), pp. 250-280.
- Wang, C., Ding, X., Xiao, Y., Peng, Y. and Liu, H. (2021a) 'Effects of relative densities on particle breaking behaviour of non-uniform grading coral sand', *Powder Technology*, 382, pp. 524-531.
- Wang, L., Yu, K., Zhao, H. and Zhang, Q. (2014) 'Economic valuation of the coral reefs in South China Sea', *Trop. Geogr*, 34, pp. 44-49.
- Wang, W., Li, W. and Yao, Z. 'Experimental study on shear characteristics of reef coral sand', Vol. 358. *IOP Conference Series: Earth and Environmental Science*, IOP Publishing, 052042.
- Wang, X., Niu, X., Wang, X., Qiu, X. and Wang, L. (2021b) 'Effects of filler distribution and interface thermal resistance on the thermal conductivity of composites filling with complex shaped fillers', *International Journal of Thermal Sciences*, 160, pp. 106678.
- Wang, X., Wang, X., Shen, J. and Zhu, C. (2022a) 'Particle size and confining-pressure effects of shear characteristics of coral sand: An experimental study', *Bulletin of Engineering Geology and the Environment*, 81(3), pp. 97.
- Wang, X., Wang, Y., Liao, C., Cui, J., Shen, J.-H., Wang, X.-Z. and Zhu, C.-Q. (2022b) 'Particle breakage mechanism and particle shape evolution of calcareous sand under impact loading', *Bulletin of Engineering Geology and the Environment*, 81(9), pp. 372.
- Wang, X., Weng, Y., Wei, H., Meng, Q. and Hu, M. (2019b) 'Particle obstruction and crushing of dredged calcareous soil in the Nansha Islands, South China Sea', *Engineering Geology*, 261, pp. 105274.
- Wang, X., Zhu, C.-Q., Wang, X.-Z. and Qin, Y. (2019c) 'Study of dilatancy behaviors of calcareous soils in a triaxial test', *Marine Georesources & Geotechnology*, 37(9), pp. 1057-1070.
- Wang, X.-Z., Wang, X., Jin, Z.-C., Meng, Q.-S., Zhu, C.-Q. and Wang, R. (2017a) 'Shear characteristics of calcareous gravelly soil', *Bulletin of Engineering Geology and the Environment*, 76(2), pp. 561-573.
- Wang, X.-Z., Wang, X., Jin, Z.-C., Zhu, C.-Q., Wang, R. and Meng, Q.-s. (2017b) 'Investigation of engineering characteristics of calcareous soils from fringing reef', *Ocean Engineering*, 134, pp. 77-86.

- Wei, H., Li, X., Zhang, S., Zhao, T., Yin, M. and Meng, Q. (2021) 'Influence of Particle Breakage on Drained Shear Strength of Calcareous Sands', *International Journal of Geomechanics*, 21(7), pp. 04021118.
- Wei, H., Liu, H., Zhao, T., Zhang, S., Ma, L., Yin, M. and Meng, Q. (2022) 'Particle breakage and morphology changes of calcareous sands under one-dimensional compression loading', *Marine Geophysical Research*, 43(4), pp. 45.
- Wei, H., Zhao, T., Meng, Q., Wang, X. and Zhang, B. (2020) 'Quantifying the morphology of calcareous sands by dynamic image analysis', *International Journal of Geomechanics*, 20(4), pp. 04020020.
- Wentworth, C. K. (1919) 'A laboratory and field study of cobble abrasion', *The Journal of Geology*, 27(7), pp. 507-521.
- Wentworth, C. K. (1923) *Method of measuring and plotting the shapes of pebbles*. US Government Printing Office Washington, DC.
- Wiltsie, E., Hulett, J., Murff, J., Brown, J., Hyden, A. and Abbs, A. (2021) 'Foundation design for external strut strengthening system for Bass Strait first generation platforms', *Engineering for Calcareous Sediments*: CRC Press, pp. 321-330.
- Witt, K.-J. and Brauns, J. (1983) 'Permeability-anisotropy due to particle shape', *Journal of geotechnical engineering*, 109(9), pp. 1181-1187.
- Wood, D. M. and Belkheir, K. (1994) 'Strain softening and state parameter for sand modelling', *Géotechnique*, 44(2), pp. 335-339.
- Wood, D. M. and Maeda, K. (2008) 'Changing grading of soil: effect on critical states', *Acta Geotechnica*, 3, pp. 3-14.
- Wu, Y., Wu, Y., Liu, J., Li, N. and Li, S. (2022) 'The evolution and influence of particle breakage on the compression behavior of calcareous sand', *Marine Georesources & Geotechnology*, 40(6), pp. 668-678.
- Wu, Y., Zhou, X., Gao, Y., Zhang, L. and Yang, J. (2019) 'Effect of soil variability on bearing capacity accounting for non-stationary characteristics of undrained shear strength', *Computers and Geotechnics*, 110, pp. 199-210.
- Xi'an KTL Instruments Co., L. (2023) *TAS-LF Fully Automatic Triaxial Testing System*. Triaxial Testing System. Available at: http://www.ktlinstruments.com/?post_type=products&page_id=7293 (Accessed: 27 March 2023).
- Xiao, Y. and Liu, H. (2017) 'Elastoplastic constitutive model for rockfill materials considering particle breakage', *International Journal of Geomechanics*, 17(1), pp. 04016041.
- Xiao, Y., Liu, H., Chen, Q., Ma, Q., Xiang, Y. and Zheng, Y. (2017) 'Particle breakage and deformation of carbonate sands with wide range of densities during compression loading process', *Acta Geotechnica*, 12(5), pp. 1177-1184.
- Xiao, Y., Liu, H., Chen, Y. and Chu, J. (2014) 'Strength and dilatancy of silty sand', *Journal of Geotechnical and Geoenvironmental Engineering*, 140(7), pp. 06014007.
- Xu, L.-J., Wang, X.-z., Wang, R., Zhu, C.-q. and Liu, X.-p. (2022) 'Physical and mechanical properties of calcareous soils: A review', *Marine Georesources & Geotechnology*, 40(6), pp. 751-766.
- Xu, W., Xu, Q. and Hu, R. (2011) 'Study on the shear strength of soil-rock mixture by large scale direct shear test', *International Journal of Rock Mechanics and Mining Sciences*,

- 48(8), pp. 1235-1247.
- Yamamuro, J. A. and Lade, P. V. (1996) 'Drained sand behavior in axisymmetric tests at high pressures', *Journal of Geotechnical Engineering*, 122(2), pp. 109-119.
- Yamano, H., Miyajima, T. and Koike, I. (2000) 'Importance of foraminifera for the formation and maintenance of a coral sand cay: Green Island, Australia', *Coral Reefs*, 19, pp. 51-58.
- Yang, G., Chen, Z., Sun, Y. and Jiang, Y. (2022) 'Effects of Relative Density and Grading on the Particle Breakage and Fractal Dimension of Granular Materials', *Fractal and Fractional*, 6(7), pp. 347.
- Yang, Y., Fei, W., Yu, H.-S., Ooi, J. and Rotter, M. (2015) 'Experimental study of anisotropy and non-coaxiality of granular solids', *Granular Matter*, 17(2), pp. 189-196.
- Yao, J., Li, W., Ou, D., Lei, L., Asif, M. and Liu, Y. (2021) 'Performance and granular characteristics of salt-tolerant aerobic granular reactors response to multiple hypersaline wastewater', *Chemosphere*, 265, pp. 129170.
- Yao, Y.-P., Yamamoto, H. and Wang, N.-D. (2008) 'Constitutive model considering sand crushing', *Soils and foundations*, 48(4), pp. 603-608.
- Ye, J., Haiyilati, Y., Cao, M., Zuo, D. and Chai, X. (2022) 'Creep characteristics of calcareous coral sand in the South China Sea', *Acta Geotechnica*, 17(11), pp. 5133-5155.
- Yu, F. (2017a) 'Characteristics of particle breakage of sand in triaxial shear', *Powder technology*, 320, pp. 656-667.
- Yu, F. (2017b) 'Particle breakage and the critical state of sands', *Géotechnique*, 67(8), pp. 713-719.
- Yu, F. (2017c) 'Particle breakage and the drained shear behavior of sands', *International Journal of Geomechanics*, 17(8), pp. 04017041.
- Yu, F. (2017d) 'Stress-dilatancy behavior of sand incorporating particle breakage', *Acta Geotechnica Slovenica*, 14(1), pp. 55-61.
- Yu, F. (2018) 'Particle breakage in triaxial shear of a coral sand', *Soils and foundations*, 58(4), pp. 866-880.
- Yu, F. (2021) 'Particle breakage in granular soils: a review', *Particulate Science and Technology*, 39(1), pp. 91-100.
- Yu, F.-w. and Su, L.-j. (2016) 'Particle breakage and the mobilized drained shear strengths of sand', *Journal of Mountain Science*, 13(8), pp. 1481-1488.
- Zavala, J. M. R. (2012) 'Particle shape quantities and influence on geotechnical properties—A review', *Lulea University of Technology*.
- Zeidan, M., Jia, X. and Williams, R. A. (2007) 'Errors implicit in digital particle characterisation', *Chemical engineering science*, 62(7), pp. 1905-1914.
- Zhang, D., Luo, F., Zhu, Z., Liu, J., Li, J., Li, B. and Xue, T. (2021) 'Study on mechanical properties of gravelly sand under different stress paths', *Advances in Civil Engineering*, 2021, pp. 1-21.
- Zhang, H., Ren, H., Mu, C., Wu, X., Huang, K. and Wang, F. (2023) 'Experiment study on the influence of density and confining pressure on triaxial shear properties of calcareous sand', *Materials*, 16(4), pp. 1683.
- Zhang, X., Baudet, B. A. and Yao, T. (2020) 'The influence of particle shape and mineralogy on the particle strength, breakage and compressibility', *International Journal of Geo-*

- Engineering*, 11, pp. 1-10.
- Zhao, B., Wang, J., Andò, E., Viggiani, G. and Coop, M. R. (2020) 'Investigation of particle breakage under one-dimensional compression of sand using X-ray microtomography', *Canadian Geotechnical Journal*, 57(5), pp. 754-762.
- Zhao, Y. (2020) *Characterization and Mechanism of Rigidity in Columns of Star-shaped Granular Particles*. Duke University.
- Zheng, H. (2012) 'A three-dimensional rigorous method for stability analysis of landslides', *Engineering Geology*, 145, pp. 30-40.
- Zheng, J., Hryciw, R. D. and Ventola, A. (2017) 'Compressibility of sands of various geologic origins at pre-crushing stress levels', *Geotechnical and Geological Engineering*, 35, pp. 2037-2051.
- Zingg, T. (1935) *Beitrag zur schotteranalyse*. ETH Zurich.